The Astrophysical Journal, 982:79 (54pp), 2025 April 1 https://doi.org/10.3847/1538-4357/adb39f

New Cold Subdwarf Discoveries from Backyard Worlds and a Metallicity Classification System for T Subdwarfs

Adam J. Burgasser[1], Adam C. Schneider[2], Aaron M. Meisner[3], Dan Caselden[4], Chih-Chun Hsu[5], Roman Gerasimov[6], Christian Aganze[7,8,20], Emma Softich[1], Preethi Karpoor[1], Christopher A. Theissen[1], Hunter Brooks[9], Thomas P. Bickle[10], Jonathan Gagné[11], Ètienne Artigau[12], Michaël Marsset[13], Austin Rothermich[4,14,15], Jacqueline K. Faherty[16], J. Davy Kirkpatrick[17], Marc J. Kuchner[18], Nikolaj Stevnbak Andersen[19], Paul Beaulieu[19], Guillaume Colin[19], Jean Marc Gantier[19], Leopold Gramaize[19], Les Hamlet[19], Ken Hinckley[19], Martin Kabatnik[19], Frank Kiwy[19], David W. Martin[19], Diego H. Massat[19], William Pendrill[19], Arttu Sainio[19], Jörg Schümann[19], Melina Thévenot[19], Jim Walla[19], Zbigniew Wędracki[19]The Backyard Worlds: Planet 9 Collaboration
[1] Department of Astronomy & Astrophysics, UC San Diego, La Jolla, CA, USA; aburgasser@ucsd.edu
[2] US Naval Observatory, Flagstaff Station, Flagstaff, AZ, USA
[3] NSF's National Optical-Infrared Astronomy Research Laboratory, 950 North Cherry Avenue, Tucson, AZ 85719, USA
[4] Department of Astrophysics, American Museum of Natural History, Central Park West at 79th Street, NY 10024, USA
[5] Center for Interdisciplinary Exploration and Research in Astrophysics (CIERA), Northwestern University, 1800 Sherman, Evanston, IL 60201, USA
[6] Department of Physics & Astronomy, University of Notre Dame, Notre Dame, IN 46556, USA
[7] Center for Astrophysics and Space Sciences, Department of Physics, UC San Diego, La Jolla, CA, USA
[8] Department of Physics & Astronomy, Stanford University, Stanford, CA 94305, USA
[9] Department of Astronomy and Planetary Science, Northern Arizona University, Flagstaff, AZ 86011, USA
[10] School of Physical Sciences, The Open University, Milton Keynes, MK7 6AA, UK
[11] Planétarium Rio Tinto Alcan, Espace pour la Vie, 4801 av. Pierre-de Coubertin, Montréal, Québec, Canada
[12] Institut Trottier de recherche sur les exoplanètes, Département de Physique, Université de Montréal, Montréal, Québec, Canada
[13] European Southern Observatory, Alonso de Cordova 3107, 1900 Casilla Vitacura, Santiago, Chile
[14] Department of Physics, Graduate Center, City University of New York, 365 5th Avenue, New York, NY 10016, USA
[15] Department of Physics and Astronomy, Hunter College, City University of New York, 695 Park Avenue, New York, NY 10065, USA
[16] Department of Astrophysics, American Museum of Natural History, New York, NY, USA
[17] IPAC, Mail Code 100-22, Caltech, 1200 East California Boulevard, Pasadena, CA 91125, USA
[18] Exoplanets and Stellar Astrophysics Laboratory, NASA Goddard Space Flight Center, 8800 Greenbelt Road, Greenbelt, MD 20771, USA
[19] Backyard Worlds: Planet 9
Received 2024 March 26; revised 2024 October 30; accepted 2024 November 5; published 2025 March 20

Abstract

We report the results of a spectroscopic survey of candidate T subdwarfs identified by the Backyard Worlds: Planet 9 program. Near-infrared spectra of 31 sources with red $J - W2$ colors and large J-band reduced proper motions show varying signatures of subsolar metallicity, including strong collision-induced H_2 absorption, obscured methane and water features, and weak K I absorption. These metallicity signatures are supported by spectral model fits and 3D velocities, indicating thick disk and halo population membership for several sources. We identify three new metal-poor T subdwarfs ([M/H] $\lesssim$ –0.5), CWISE J062316.19+071505.6, WISEA J152443.14−262001.8, and CWISE J211250.11-052925.2; and 19 new "mild" subdwarfs with modest metal deficiency ([M/H] $\lesssim -0.25$). We also identify three metal-rich brown dwarfs with thick disk kinematics. We provide kinematic evidence that the extreme L subdwarf 2MASS J053253.46+824646.5 and the mild T subdwarf CWISE J113010.07+313944.7 may be part of the Thamnos population, while the T subdwarf CWISE J155349.96+693355.2 may be part of the Helmi stream. We define a metallicity classification system for T dwarfs that adds mild subdwarfs (d/sdT), subdwarfs (sdT), and extreme subdwarfs (esdT) to the existing dwarf sequence. We also define a metallicity spectral index that correlates with metallicities inferred from spectral model fits and iron abundances from stellar primaries of benchmark T dwarf companions. This expansion of the T dwarf classification system supports investigations of ancient, metal-poor brown dwarfs now being uncovered in deep imaging and spectroscopic surveys.

Unified Astronomy Thesaurus concepts: Brown dwarfs (185); L dwarfs (894); L subdwarfs (896); T subdwarfs (1680); T dwarfs (1679); Stellar classification (1589)

Materials only available in the online version of record: data behind figures

1. Introduction

Over the past 25 yr, wide-field red optical and near-infrared surveys have dramatically expanded our census of the lowest-mass stars, brown dwarfs, and free-floating exoplanets, uncovering thousands of low-temperature ultracool dwarfs (UCDs) that span the late-M, -L, -T, and -Y dwarf spectral classes (J. D. Kirkpatrick et al. 1999; A. J. Burgasser et al. 2006b; M. C. Cushing et al. 2011). This sequence is well-sampled

[20] Stanford Science Fellow and Rubin Fellow.

among solar-metallicity objects down to effective temperatures $T_{\rm eff} \approx 300$ K (K. L. Luhman 2014), providing a rich sample for studying the formation, evolution, atmospheres, structures, and spatial distribution of objects that bridge the gap between the lowest-mass stars and gas giant planets.

Metal-poor ultracool subdwarfs, including members of the thick disk and halo populations of the Milky Way, remain a very small fraction ($\lesssim$0.1%) of the currently known population. The rarity of these sources can be directly attributed to the sparsity of metal-poor halo stars in the vicinity of the Sun (≈0.5%; M. Jurić et al. 2008), the long-term cooling of brown dwarfs that makes old metal-poor objects cold and faint, and the relatively small distances ($\lesssim$30 pc) to which low-temperature brown dwarfs can be detected. Nevertheless, metallicity variety among the known brown dwarf population is crucial for understanding how composition influences atmospheric chemistry, thermal evolution, interior structure, and the hydrogen burning mass threshold (D. Saumon et al. 1994; I. Baraffe et al. 1997; A. Burrows et al. 2011; R. Gerasimov et al. 2020). In addition, since UCDs have either long hydrogen fusion lifetimes ($\gtrsim 10^{12}$ yr; G. Laughlin et al. 1997) or never fuse, these objects record the conditions and chemical abundances of the earliest generations of star formation in the Milky Way (A. J. Burgasser 2009; N. Lodieu et al. 2015; I. Caiazzo et al. 2017).

While metal-poor M-type subdwarfs have been known for over 75 yr (A. H. Joy 1947; J. R. Mould & D. B. McElroy 1978; J. E. Gizis 1997; S. Lépine et al. 2007), significantly metal-poor brown dwarfs are a recent discovery. The first serendipitous discoveries of metal-poor L-type subdwarfs (A. J. Burgasser et al. 2003; R.-D. Scholz et al. 2004; T. Sivarani et al. 2009; N. Lodieu et al. 2010) were made with data from the Two Micron All-Sky Survey (2MASS; M. F. Skrutskie et al. 2006), the Sloan Digital Sky Survey (SDSS; D. G. York et al. 2000), and the UKIRT Infrared Deep Sky Survey (UKIDSS; A. Lawrence et al. 2007). These sources have distinct near-infrared colors and spectra compared to solar-metallicity L dwarfs, shaped by enhanced collision-induced H_2 absorption (J. L. Linsky 1969; A. J. Burgasser et al. 2003) and metallicity-induced variations in optical molecular absorption and condensate formation (J. E. Gizis & J. Harvin 2006; A. J. Burgasser et al. 2007a; E. C. Gonzales et al. 2021). However, most L subdwarfs are low-mass stars, since brown dwarfs at the age of the Galactic thick disk and halo ($\gtrsim$8 Gyr; M. Kilic et al. 2017) have temperatures $\lesssim$1500 K, within the late-L and -T dwarf regime (A. Burrows et al. 2001; I. Baraffe et al. 2003). While several modestly metal-poor T dwarfs ([M/H] ~ -0.5) were found early on by wide-field surveys (A. J. Burgasser et al. 2002b; B. Burningham et al. 2014; D. J. Pinfield et al. 2014; K. Kellogg et al. 2018) and as companions to metal-poor stars (R. Scholz 2010a; D. N. Murray et al. 2011; D. J. Pinfield et al. 2012; B. Burningham et al. 2013; G. N. Mace et al. 2013a), significantly metal-poor substellar T subdwarfs with [M/H] $\lesssim -1$ were initially elusive.

The first examples of true T subdwarfs were uncovered through the deep infrared photometry, multiepoch astrometry, and search efforts of citizen scientists deployed by the Backyward Worlds: Planet 9 program (BYW; M. J. Kuchner et al. 2017). This project aims to build the census of low-temperature brown dwarfs in the solar neighborhood by providing multiepoch unWISE images (D. Lang 2014; A. M. Meisner et al. 2018; E. F. Schlafly et al. 2019) to citizen scientists who visually identify faint moving sources. This approach is particularly well suited for finding low-temperature, nearby thick disk and halo brown dwarfs, whose large velocities translate into large proper motions. A. C. Schneider et al. (2020) reported the discovery of WISEA J041451.67–585456.7 and WISEA J181006.18–101000.5 (hereafter J0414–5854 and J1810–1010), whose near-infrared spectra are indicative of both low temperatures ($T_{\rm eff} \lesssim 1300$ K) and significantly subsolar metallicities ([M/H] $\lesssim -1$). A. M. Meisner et al. (2020, 2021) subsequently reported three additional T subdwarf candidates in BYW data, one (WISE J155349.96+693355.2; hereafter J1553+6933) that exhibits spectroscopic evidence of modest subsolar metallicity ([M/H] ≈ -0.5). H. Brooks et al. (2022) reported the BYW T subdwarf candidate, CWISE J052306.42–015355.4 (hereafter J0523−0153) whose distinct $J-$W2 and W1 $-$ W2 colors and large proper motion suggest it is a metal-poor member of the thick disk or halo. Finally, WISEA J153429.75−104303.3 (hereafter WISE J1534−1043; aka, "The Accident") may be the first known metal-poor Y subdwarf (J. D. Kirkpatrick et al. 2021a). Candidate thick disk and halo T subdwarfs have also been identified in deep multiband imaging and spectroscopic surveys conducted with JWST (K. Glazebrook et al. 2023; M. Nonino et al. 2023; P.-Y. Wang et al. 2023; A. J. Burgasser et al. 2024; K. N. Hainline et al. 2024; B. W. Holwerda et al. 2024).

Low-temperature subdwarf candidates are exceptionally faint, and most lack the spectroscopic validation or astrometric follow-up necessary to assess physical properties. Indeed, N. Lodieu et al. (2022) used improved spectroscopy, photometry, and a parallax measurement for J1810−1010 to conclude that it is both colder ($T_{\rm eff} = 800 \pm 100$ K, equivalent to a T7 dwarf) and more metal-poor ([Fe/H] $= -1.5 \pm 0.5$ dex) than originally estimated. This study also found evidence that J1810−1010 lacks methane absorption even in the strong 3.3 μm band, a defining trait for T dwarfs, suggesting significantly modified atmospheric chemistry. Separately, A. J. Burgasser et al. (2024) have claimed evidence for modified PH_3/CO_2 chemistry in the distant T subdwarf UNCOVER-BD-3 identified with JWST, drawing an analogy to variations in CaH/TiO chemistry among metal-poor M subdwarfs, although this claim has yet to be verified (S. A. Beiler et al. 2024).

In this article, we report spectroscopic follow-up of a sample of late-L and -T subdwarf candidates uncovered by Backyward Worlds: Planet 9. In Section 2 we describe the selection of candidate T subdwarfs and summarize their associated photometric and astrometric properties. We also estimate distances for metal-poor candidates using new empirical color–magnitude relations based on late-L and -T subdwarfs with parallax distance measurements. In Section 3 we describe new near-infrared spectroscopic observations of 24 candidates and three metal-poor L and T dwarf benchmarks. We also define comparison samples of solar metallicity and metal-poor brown dwarf spectra from the literature, including sources that match our selection criteria. In Section 4 we analyze these data, reporting classifications from dwarf standards and spectral indices, K I equivalent widths, spectral model fits, and radial velocities (RVs) from forward modeling. We also use estimated distances, proper motions, and RVs to compute 3D velocities and assess Galactic population membership. In Section 5 we

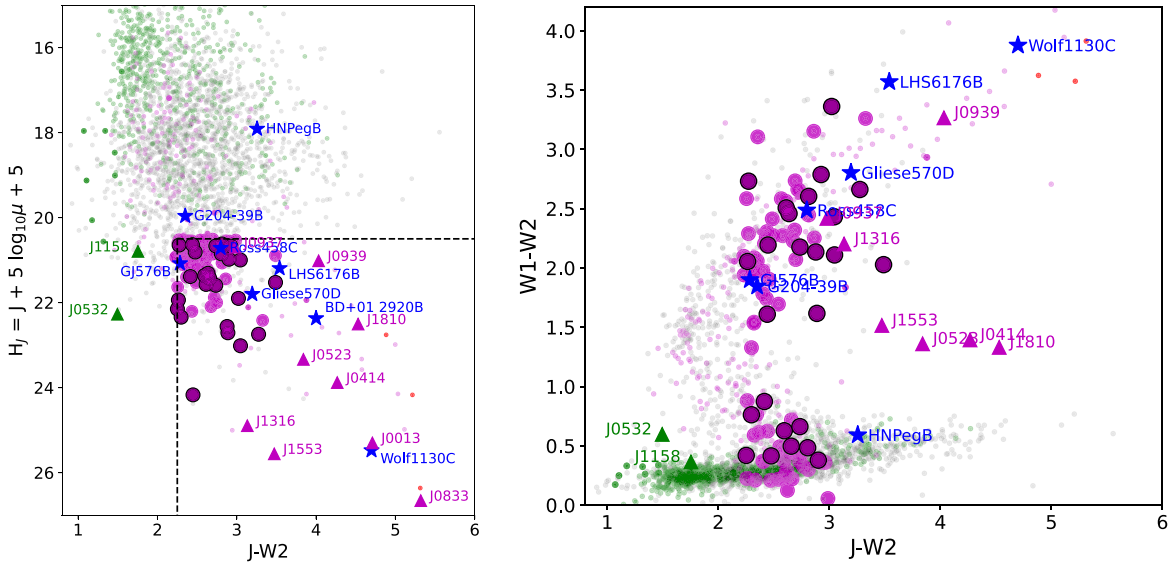

Figure 1. Left panel: selection of candidate T subdwarfs from BYW targets (small gray dots). Semitransparent circles indicate disk late-M and -L dwarfs (green), T dwarfs (magenta), and Y dwarfs (red) from the compilation of W. M. J. Best et al. (2018), while opaque circles indicate metal-poor objects from that compilation and from Z. H. Zhang et al. (2018a). We label previously identified late-L (green triangles) and -T (magenta triangles) subdwarf comparison sources and some of the benchmark companions (blue stars) from our spectroscopic sample (Tables 2 and 3). We delineate our selection criteria of $J - \mathrm{W2} \geqslant 2.25$ mag and $H_J \geqslant 20.5$ mag with dashed lines. All candidates are indicated by large magenta circles, while those with spectroscopic observations reported in this study are further highlighted by black outlines. Right panel: W1 − W2 vs. J − W2 color–color diagram of the same sample. Note that sources without W1 detections are not shown in this plot.

assess the status of our candidates, identifying three new T subdwarfs, 19 new slightly metal-poor T dwarfs, two brown dwarfs with exceptional Galactic orbits, and three apparently metal-rich brown dwarfs with thick disk kinematics. In Section 6 we use our full spectral sample to define anchors for a 2D classification scheme for T dwarfs, extending the existing dwarf sequence to include mild subdwarfs (d/sdT), subdwarfs (sdT), and extreme subdwarfs (esdT). We also construct a calibrated metallicity index that correlates with model-fit metallicities and the iron abundances of the stellar primaries of benchmark T dwarf companions. In Section 7 we examine metallicity dependence in the temperature scale of T dwarfs, continued challenges in modeling T subdwarf spectra, and prospects for expanding the known cold subdwarf population. In Section 8 we summarize our results.

2. BYW T Subdwarf Candidates

2.1. Color and Reduced Proper-motion Selection

The Backyard Worlds: Planet 9 program uses multiepoch imaging data from the Wide-field Infrared Survey Explorer (WISE) mission to find faint, infrared moving sources, which are identified by a community of over 80,000 citizen scientists. Objects identified as moving point sources are matched to optical and near-infrared photometry and astrometry from 2MASS, UKIDSS, CatWISE2020 (F. Marocco et al. 2021), Pan-STARRS DR1 (K. C. Chambers et al. 2016), Gaia DR3 (Gaia Collaboration et al. 2021), the UKIRT Hemisphere Survey (UHS; S. Dye et al. 2018), and the Vista Hemisphere Survey (VHS/VIKING; R. G. McMahon et al. 2013). There are currently over 4000 motion-confirmed cool brown dwarf candidates in the BYW sample, most without existing spectroscopic data. Of these, roughly 3400 sources have well-measured J-band (2MASS, UHS/UKIRT, and VHS/VIKING) and W2-band (WISE) photometry, as well as proper motions from CatWISE2020 or Gaia.

Guided by the photometric and astrometric properties of previously identified L and T subdwarfs compiled in Z. H. Zhang et al. (2018a), A. M. Meisner et al. (2021), and H. Brooks et al. (2022), and "normal" field ultracool dwarfs compiled in W. M. J. Best et al. (2018), we identified a series of selection criteria to isolate high-probability T subdwarf candidates. We imposed a color limit of $J - \mathrm{W2} \geqslant 2.25$ mag to select sufficiently low-temperature objects, and applied a reduced proper-motion (RPM) constraint

$$H_J \equiv J + 5\log_{10}\frac{\mu}{\mathrm{arcsec\ yr^{-1}}} + 5 = M_J + 5\log_{10}\frac{V_{\tan}}{4.74\ \mathrm{km\ s^{-1}}} \geqslant 20.5\ \mathrm{mag} \quad (1)$$

to select sources with large tangential velocities, indicative of thick disk and halo objects (Figure 1). Note unlike A. M. Meisner et al. (2021) and H. Brooks et al. (2022), we do not impose a W1 − W2 color constraint, using H_J to segregate potential T subdwarfs from contaminant field late-L and -T dwarfs. We further required $\mu/\sigma_\mu > 5$, $J \leqslant 18.5$ mag and decl. $\delta \geqslant -35°$ to facilitate follow-up from Keck Observatory. We identified 95 candidate T subdwarfs, including 19 "high-priority" sources with measured $J - K < -0.5$ mag and/or estimated $V_{\tan} > 150\ \mathrm{km\ s^{-1}}$, the latter based on color/absolute magnitude relations from J. D. Kirkpatrick et al. (2021a) or measured parallaxes. These candidates include the previously identified T subdwarfs J1810−1010 and the sdT5 CWISE J113019.19-115811.3 (hereafter J1130−1158; J. D. Kirkpatrick et al. 2021a). Here, we investigate a subset of 31 candidates with infrared spectroscopy.

2.2. Photometric Distance Estimation

The majority of our sample lacks trigonometric parallaxes, and assessment of physical properties (temperature, radius) and population membership (kinematics) requires a distance

estimate. E. C. Gonzales et al. (2018) derived linear relationships between spectral type and absolute 2MASS JHK_s and WISE W1W2 magnitudes for late-M and -L subdwarfs, but these do not extend into the T dwarf regime. Z. H. Zhang et al. (2019b) derived separate linear relationships between spectral type and absolute MKO *YJHK* and WISE W1W2 magnitudes for L and for mid/late-T subdwarfs (the latter encompassing relatively modest subsolar metallicities), but were unable to connect these due to the lack of L/T transition subdwarfs known at the time of that study. With several more cool subdwarfs now known, we revisited these analyses with a sample of 18 metal-poor late-L and -T dwarfs with measured parallactic distances, either of the source or its primary companion[21] (Table 1). Figure 2 compares absolute J, $W1$, and $W2$ magnitudes to $J - W2$ and $W1 - W2$ colors for this sample, as well as empirical relationships for subdwarfs from E. C. Gonzales et al. (2018) and Z. H. Zhang et al. (2019b), and for dwarfs from T. J. Dupuy & M. C. Liu (2012). There are reasonably linear trends between color and absolute magnitude for these combinations, and good overlap with prior empirical relations for most of the metal-poor T dwarfs. However, the metal-poor late-L dwarfs show considerable scatter, particularly in absolute W1 and $W2$ magnitudes where empirical dwarf relations become nearly vertical (a large range of absolute magnitudes over nearly constant color). In addition, both the esdT J1810−1010 and the putative Y subdwarf J1534−1043 are significantly offset from the bulk of the sample in M_{W1} versus $J - W2$, while J1534−1043 and the T subdwarf companion Wolf 1130C are offset in all of the absolute-magnitude versus $W1 - W2$ color samples. We therefore chose to estimate distances from M_J and M_{W2} versus $J - W2$ color–magnitude trends, fitting 16 sources over 1 mag $\leqslant J - W2 \leqslant 8.5$ mag to second-order polynomials by linear least-squares regression:

$$M_J = 11.4103901 + 1.55433844[J - W2] - 0.01643861[J - W2]^2 \quad (2)$$

$$M_{W2} = 11.41790678 + 0.53871427[J - W2] - 0.01195053[J - W2]^2. \quad (3)$$

Both relations have a scatter of 0.44 mag, or 22% error in distance. For our analysis, we used the average of both relations to estimate distances, and include in our uncertainty estimates a 0.3 mag scatter in addition to the photometric uncertainties. We emphasize that these relations are based on a limited sample and require validation with a larger parallax sample of verified low-temperature subdwarfs.

3. Spectroscopic Observations

3.1. Keck/NIRES

We obtained moderate-resolution near-infrared spectroscopy of 20 of our T subdwarf candidates with the Near-Infrared Echellette Spectrometer (NIRES; J. C. Wilson et al. 2004) on the Keck II 10 m telescope. NIRES is a cross-dispersed spectrograph providing $\lambda/\Delta\lambda \approx 2700$ spectra spanning 0.90–2.45 μm over four spectral orders, with a fixed $0\farcs55 \times 18''$ slit. Data were obtained between 2019 October and 2024 January in various conditions (Table 2). All sources were observed with individual exposure times of 300 s in multiple ABBA nodding sets separated by $10''$ along the slit for background subtraction. One candidate, J0623+0715, resides in a crowded field, so we obtained six exposures at one slit position, and offset to measure the sky background at the start, middle, and end of the sequence. For all sources, we observed a nearby A0 V calibrator star at equivalent airmass to measure telluric and instrumental throughput. We also obtained calibration dome flat lamp exposures at the start of both nights. We observed three additional benchmarks for comparative analysis: the late-L subdwarf 2MASS J05325346+8246465 (hereafter J0532+8246; A. J. Burgasser et al. 2003) and the metal-poor T dwarf benchmark companions GJ 576B (T5p, [Fe/H] = −0.37 ± 0.09; R. Scholz 2010a; A. Arentsen et al. 2019) and LHS 6176B (T8p, [Fe/H] = −0.30 ± 0.10; B. Burningham et al. 2013).

All NIRES data were reduced using a modified version of the Spextool package (M. C. Cushing et al. 2004) with standard settings. In brief, we used the dome flat lamps to rectify the spectral orders and correct for pixel-to-pixel response variations, computed the wavelength calibration from OH emission lines in deep exposures, optimally extracted spectra from the rectified 2D traces, averaged multiple spectra for each source order-by-order with a sigma-clipped weighted mean (individual cosmic-ray hits were removed by hand), and corrected the spectra for telluric absorption and instrumental response using the A0 V star spectra following the methodology of W. D. Vacca et al. (2003). We chose to stitch the individual spectral orders into a single spectrum manually to correct for slight inter-order flux scaling variations not accounted for in the Spextool package. The final data have median signal-to-noise ratios (SNRs) between 23 and 275 at the 1.27 μm peak at native resolution.

3.2. IRTF/SpeX

Two candidates, J0140+0150 and J0843+2904, were observed with the SpeX spectrograph on the 3 m NASA Infrared Telescope Facility (J. T. Rayner et al. 2003). J0140+0150 was observed on 2020 Dec 24 (UT) in clear conditions at an average airmass of 1.25; J0843+2904 was observed on 2022 Feb 22 (UT) in partly cloudy conditions at an average airmass of 1.18. Both sources were observed in prism mode with the $0\farcs8 \times 15''$ slit, providing a resolution of $\lambda/\Delta\lambda \approx 75$ spanning 0.75–2.5 μm in a single order, with 10 exposures of 180 s each obtained in an ABBA nodding pattern along the slit for background subtraction. A0 V stars were observed immediately after each source, as well as internal flat field and arc lamp exposures. Data were reduced using Spextool version 4.1 with standard settings, following the procedures described above.

3.3. APO/TripleSpec

One candidate, J0045+7958, was observed on 2018 January 21 (UT) with the TripleSpec spectrograph (TSpec; J. C. Wilson et al. 2004) on the 3.5 m Astrophysical Research Consortium Telescope at Apache Point Observatory (APO). Like NIRES, TSpec is a cross-dispersed spectrograph spanning

[21] We exclude three sources from this sample: the **esdL6** J0616-6407 and the sdT1 J0301 − 2319, whose measured parallaxes from J. K. Faherty et al. (2012) and W. M. J. Best et al. (2020) were deemed too low quality for this analysis; and the subdwarf candidate J0055+5947, a comoving companion to the white dwarf LSPM J0055+5948 (A. M. Meisner et al. 2020), which does not appear to be significantly metal-poor. We also excluded previously reported subdwarfs J0004 − 2604 and J1055+5443 as our analysis and that of G. Robbins et al. (2023) indicate they are not significantly metal-poor.

Table 1
Late-L and -T Subdwarf Absolute Magnitude Standards

Name	SpT[a]	J (mag)	$J - W2$ (mag)	W1 − $W2$ (mag)	π (mas)	M_J (mag)	M_{W1} (mag)	M_{W2} (mag)	Ref.
2MASS J085039.11−022154.3	d/sdL6.5	15.44 ± 0.04	2.34 ± 0.05	0.282 ± 0.016	28.2 ± 1.3	12.70 ± 0.11	10.64 ± 0.10	10.36 ± 0.10	[1];[2]
2MASS J11582077+0435014	d/sdL8	15.61 ± 0.06	2.10 ± 0.06	0.286 ± 0.023	37 ± 3	13.47 ± 0.16	11.65 ± 0.16	11.37 ± 0.16	[1];[2]
2MASS J053253.46+824646.5	esdL8:	15.18 ± 0.06	1.50 ± 0.06	0.596 ± 0.016	40.71 ± 0.15	13.23 ± 0.06	12.328 ± 0.013	11.732 ± 0.014	[1];[2]
2MASS J06453153−6646120	d/sdT0	15.525 ± 0.009	2.227 ± 0.017	0.441 ± 0.023	54 ± 3	14.18 ± 0.12	12.39 ± 0.12	11.95 ± 0.12	[3];[4]
WISEA 181006.18−101000.5[b]	esdT3:	17.29 ± 0.04	4.71 ± 0.06	1.34 ± 0.05	112 ± 8	17.54 ± 0.16	14.17 ± 0.16	12.83 ± 0.16	[5];[5]
HD 65486B	d/sdT4.5	15.78 ± 0.02	1.92 ± 0.03	1.91 ± 0.04	54.157 ± 0.018[c]	14.45 ± 0.02	14.44 ± 0.04	12.531 ± 0.017	[6];[2]
WISE J044853.28−193548.6	sdT5[d]	16.608 ± 0.011	2.378 ± 0.019	2.07 ± 0.03	58 ± 3	15.41 ± 0.11	15.10 ± 0.12	13.03 ± 0.11	[3];[4]
GJ 576B	d/sdT5.5	16.59 ± 0.02	2.284 ± 0.023	1.90 ± 0.03	52.51 ± 0.02[c]	15.192 ± 0.016	14.81 ± 0.03	12.908 ± 0.017	[7];[2]
2MASS 09373487+2931409	sdT6	14.65 ± 0.04	2.46 ± 0.04	2.432 ± 0.017	169.4 ± 1.8	15.79 ± 0.04	15.76 ± 0.03	13.33 ± 0.02	[1];[8]
WISE J030919.67−501614.3	d/sdT7.5	17.10 ± 0.02	3.437 ± 0.021	3.06 ± 0.05	67 ± 4	16.22 ± 0.13	15.85 ± 0.13	12.79 ± 0.13	[3];[9]
ULAS J141623.94+134836.3	sdT7	17.26 ± 0.02	4.428 ± 0.020	3.21 ± 0.03	107.7 ± 0.2[c]	17.421 ± 0.018	16.21 ± 0.03	12.993 ± 0.012	[7];[2]
LHS 6176B	d/sdT7.5	18.05 ± 0.04	3.55 ± 0.04	3.33 ± 0.10	51.00 ± 0.03[c]	16.58 ± 0.04	16.36 ± 0.10	13.03 ± 0.02	[7];[2]
HD 126053B	sdT7.5	18.71 ± 0.05	3.93 ± 0.06	3.11 ± 0.12	57.27 ± 0.04[c]	17.50 ± 0.05	16.67 ± 0.12	13.57 ± 0.03	[10];[2]
WISE J083641.10−185947.0	sdT8[d]	19.10 ± 0.12	3.97 ± 0.09	2.50 ± 0.09	44.2 ± 2.2	17.33 ± 0.16	15.85 ± 0.14	13.36 ± 0.11	[3];[4]
2MASS J09393548−2448279	d/sdT8	15.700 ± 0.007	4.082 ± 0.011	3.31 ± 0.02	196 ± 10	17.16 ± 0.12	16.39 ± 0.12	13.08 ± 0.12	[1],[7];[8]
Wolf 1130C	sdT6:	19.64 ± 0.09	4.50 ± 0.09	2.01 ± 0.04	60.30 ± 0.03[c]	18.54 ± 0.09	16.06 ± 0.04	14.04 ± 0.02	[11];[2]
WISE J083337.82+005214.1	d/sdT8	20.28 ± 0.10	5.37 ± 0.10	⋯	83 ± 5	19.86 ± 0.15	⋯	14.49 ± 0.12	[12];[13]
WISEA J153429.75−104303.3	(e)sdY:[e]	24.5 ± 0.3	8.4 ± 0.3	2.04 ± 0.21	61 ± 5	23.4 ± 0.3	17.1 ± 0.3	15.09 ± 0.19	[14],[4]

Notes. W1W2 photometry is from CATWISE2020 (F. Marocco et al. 2021) as provided by the Vizier catalog service (F. Ochsenbein et al. 2000), with exceptions noted.
[a] Spectral type from this paper unless otherwise noted; see Table 10.
[b] Using WISE photometry as reported in N. Lodieu et al. (2022).
[c] Parallax from primary.
[d] Based on Z. H. Zhang et al. (2019b).
[e] Based on J. D. Kirkpatrick et al. (2021a).

References– The first reference is for J-band photometry, the second reference is for parallax; [1] 2MASS (R. M. Cutri et al. 2003); [2] Gaia EDR3 (Gaia Collaboration et al. 2021); [3] VISTA VHS DR5 (R. G. McMahon et al. 2013); [4] J. D. Kirkpatrick et al. (2021b); [5] N. Lodieu et al. (2022); [6] W. M. J. Best et al. (2021); [7] UKIDSS DR9 (A. Lawrence et al. 2013); [8] J. K. Faherty et al. (2012); [9] J. D. Kirkpatrick et al. (2019); [10] D. J. Pinfield et al. (2012); [11] G. N. Mace et al. (2013a); [12] D. J. Pinfield et al. (2014); [13] J. D. Kirkpatrick et al. (2019); [14] A. M. Meisner et al. (2023)

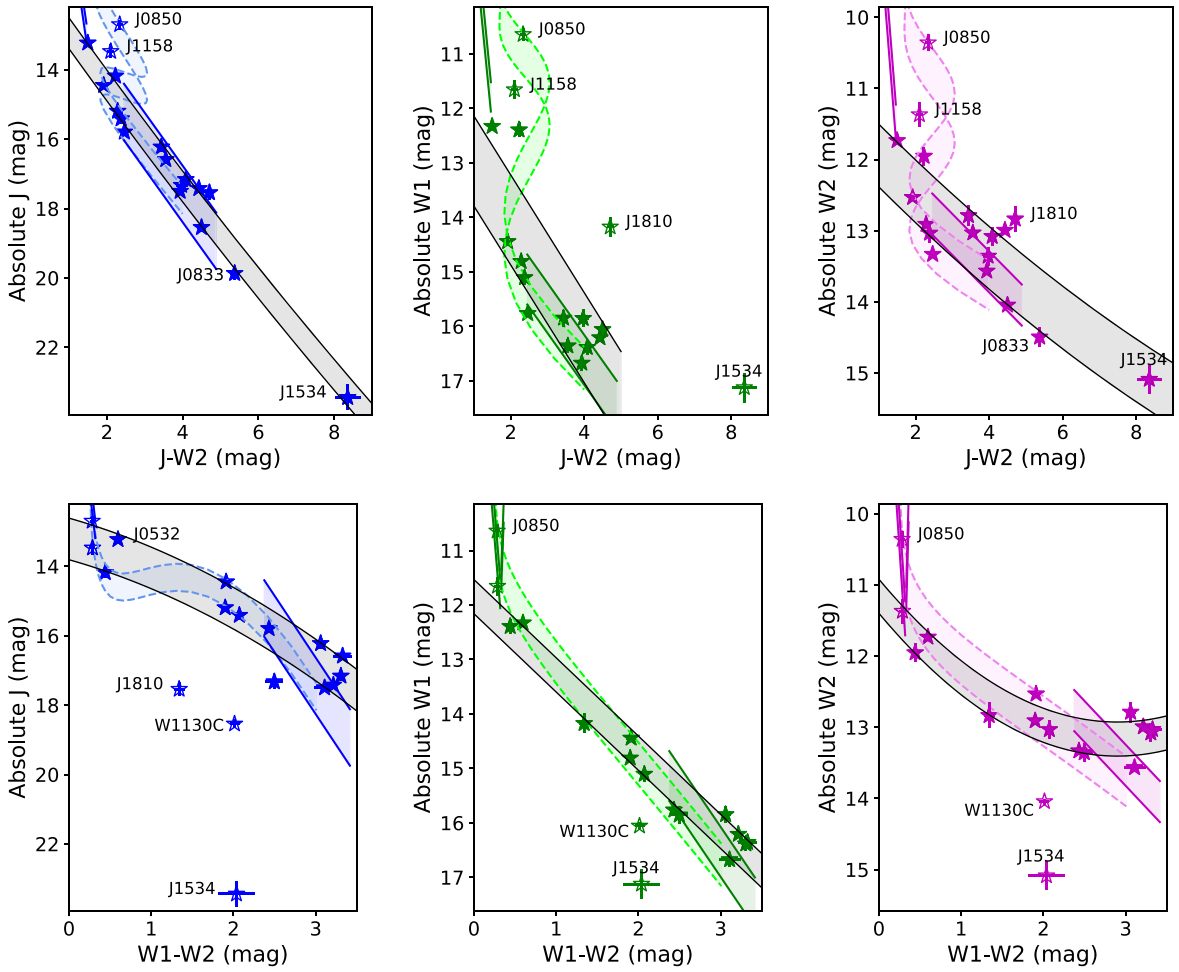

Figure 2. Absolute magnitudes in J (left, in blue), W1 (middle, in green), and $W2$ (right, in magenta) bands as a function of $J - W2$ (top) and W1 $-$ $W2$ (bottom) colors. Symbols display measurements for metal-poor late-L and -T dwarfs with parallax measurements (Table 1) compared to empirical relations for dwarfs (light colored shaded regions with dashed lines: T. J. Dupuy & M. C. Liu 2012) and subdwarfs (dark colored shaded regions with solid lines; E. C. Gonzales et al. 2018; Z. H. Zhang et al. 2019b). Some individual sources are labeled. Gray shaded regions delineate our empirical relationships computed over the ranges 1 mag $\leqslant J - W2 \leqslant 8.5$ mag and 0 mag $\leqslant$W1 $-$ $W2 \leqslant 3.5$ mag. Sources not included in each color–magnitude fit are indicated by open symbols.

0.95–2.46 μm at a resolution of $\lambda/\Delta\lambda \approx 3500$ for a 1.″1-wide slit. Conditions were clear with 1.″5 seeing. We acquired 12 exposures lasting 300 s each in an ABBA nod pattern at an average airmass of 1.53, followed by observations of the B8 IV standard HD 9612 ($V = 6.57$) at an airmass of 1.42. We also obtained quartz lamp flat field and NeAr arc lamp exposures illuminated on the dome at the start of the night. Data were reduced using a modified version of Spextool that incorporates instrument parameters for APO/TSpec (see S. J. Schmidt et al. 2012) following the procedures described above.

3.4. Magellan/FIRE

One candidate, J1515−2157, was observed on 2024 May 29 (UT) with the Folded-port InfraRed Echellette (FIRE; R. A. Simcoe et al. 2013) on the 6.5 m Magellan Baade Telescope at Las Campanas Observatory. FIRE was operated in its prism-dispersed mode, providing 0.82–2.51 μm spectra at an average resolution of $\lambda/\Delta\lambda \approx 300$ for the deployed 0.″8-wide slit. We acquired eight 50 s exposures in an ABBA nod pattern at an average airmass of 1.03, followed by observations of the A0 V standard HD 139273 ($V = 10.13$) at the same airmass. We obtained quartz lamp flat field exposures reflected off the Baade flat field screen at two settings to obtain uniform illumination for pixel calibation at the start of the night, and NeAr arc lamp exposures after the science observation for wavelength calibration. Data were reduced using a custom version of the FIREHOSE package (J. Gagné et al. 2015), which is based on the MASE pipeline (J. J. Bochanski et al. 2009) and Spextool, following procedures described in T. P. Bickle et al. (2024).

3.5. Gemini-North/GNIRS

One candidate, J1138+7212, was observed on 2013 December 3 (UT) with the Gemini Near-Infrared Spectrograph (GNIRS; J. H. Elias et al. 2006) on the 8 m Gemini-North telescope. Data were obtained as part of program GN-2013B-Q-91 in queue service mode, and were obtained through light clouds and seeing of 0.″7. The cross-dispersed mode of GNIRS was used with the 0.″675 slit, short 0.″15 pix^{-1} camera, and 31.7 lines mm^{-1} grating, yielding a 0.9–2.4 μm spectrum at an average resolution of $\lambda/\Delta\lambda \approx 800$. A series of 12 exposures of 180 s each were obtained in an ABBA nod pattern at an average airmass of 1.71, preceded by observations the A5 V star HIP 57348 (V = 10.67) at similar airmass. Data were reduced using the pipeline described in P. Delorme et al. (2008) and L. Albert et al. (2011), following similar procedures as

Table 2
Spectroscopic Observations

Name	Designation (J2000)	J (mag)	Instrument	UT Date	Exposure (s)	Airmass	Seeing (″)	Calibrator	J SNR
Metallicity Benchmarks and Comparison Sources									
J0532+8246	J053310.53+824620.5	15.18 ± 0.06	Keck/NIRES	2022 Jan 19	2400	2.67	0.″7	HD 48049	277
GJ 576B	J150457.52+053759.8	16.59 ± 0.02	Keck/NIRES	2022 Jun 11	2400	1.03	0.″6	HD 123233	224
LHS 6176B	J095047.39+011731.6	18.05 ± 0.04	Keck/NIRES	2022 Jan 20	3600	1.06	0.″4[b]	HD 74721	91
Subdwarf Candidates									
J0045+7958	J004556.21+795847.8	16.97 ± 0.21	APO/TSpec	2018 Jan 21	3600	1.53	1.″5	HD 9612	5
J0140+0150	J014016.91+015054.7[a]	17.20 ± 0.02	IRTF/SpeX	2020 Dec 24	1800	1.25	0.″5	HD 1154	23
…	…	…	Keck/NIRES	2021 Jan 02	2400	1.09	0.″8	HD 18571	64
J0411+4714	J041102.42+471422.6	17.67 ± 0.02	Keck/NIRES	2023 Dec 27	1200	1.34	0.″5	BD+45 981	90
J0429+3201	J042941.12+320125.4	18.28 ± 0.08	Keck/NIRES	2023 Nov 03	2400	1.02	0.″4[b]	BD+43 1021	37
J0623+0715	J062316.20+071506.3	17.75 ± 0.03	Keck/NIRES	2022 Jan 19	1800	1.46	0.″5	HD 37887	46
J0659+1615	J065919.43+161552.0	17.97 ± 0.06	Keck/NIRES	2024 Jan 30	2400	1.24	0.″5	HD 47540	69
J0843+2904	J084325.37+290435.8	17.21 ± 0.02	IRTF/SpeX	2022 Feb 22	1800	1.18	0.″8	HD 71906	15
J1110 − 1747	J111055.13−174738.8	17.68 ± 0.02	Keck/NIRES	2022 Jan 19	2400	1.27	0.″5	HD 98884	76
J1130+3139	J113010.21+313947.0	17.79 ± 0.05	Keck/NIRES	2022 Jan 20	2400	1.05	0.″5	HD 98989	90
J1138+7212	J113833.47+721207.8	17.08 ± 0.23	Gemini/GNIRS	2013 Dec 03	2160	1.71	0.″7	HIP 57348	13
J1204 − 2359	J120444.33−235927.4	17.91 ± 0.03	Keck/NIRES	2022 Jan 19	2400	1.40	0.″5	HD 110649	44
J1304+2819	J130440.45+281927.7	18.10 ± 0.04	Keck/NIRES	2022 Jul 11	2400	1.30	0.″6	HD 109055	40
J1308 − 0321	J130841.33−032157.8	18.07 ± 0.02	Keck/NIRES	2022 Jan 20	1800	1.09	0.″5	HD 114381	72
J1401+4325	J140118.31+432553.6	18.40 ± 0.08	Keck/NIRES	2022 Jan 23	1800	1.09	0.″6	HD 128039	36
J1458+1734	J145837.85+173450.2	18.39 ± 0.07	Keck/NIRES	2022 Jul 11	3600	1.15	0.″5	HD 124773	58
J1515 − 2157	J151521.28−215737.3	17.48 ± 0.03	Magellan/FIRE	2024 May 29	400	1.03	0.″6	HD 139273	33
J1524 − 2620	J152443.15−262001.8	18.42 ± 0.10	Keck/NIRES	2022 Jun 11	2400	1.45	0.″5	HD 147384	25
J1710+4537	J171003.01+453756.4	18.23 ± 0.06	Keck/NIRES	2022 Jun 11	3600	1.17	0.″7	HD 123299	60
J1801+4717	J180122.59+471741.4	18.49 ± 0.09	Keck/NIRES	2021 Aug 23	2400	1.15	0.″5	HD 164899	33
J2013 − 0326	J201342.30−032643.4	18.24 ± 0.12	Keck/NIRES	2021 Aug 23	2400	1.10	0.″5	HD 192230	49
J2021+1524	J202130.11+152418.3	17.18 ± 0.02	Keck/NIRES	2023 Jul 03	2400	1.01	0.″9	HD 333145	70
J2112 − 0529	J211250.14−052924.7	17.50 ± 0.03	Keck/NIRES	2022 Jun 11	2400	1.11	0.″5	HD 203769	62
J2112+3030	J211255.59+303037.6	18.18 ± 0.06	Keck/NIRES	2023 Jul 03	3600	1.02	0.″9	HD 333145	42
J2251 − 0740	J225109.56−074037.4	18.47 ± 0.08	Keck/NIRES	2023 Jul 10	2400	1.16	0.″5	HD 203769	41

Notes. All designations are from the CatWISE2020 catalog (F. Marocco et al. 2021) and are proper-motion corrected to epoch 2015 May 28 except for noted sources.
[a] Astrometry from UKIDSS DR9 (A. Lawrence et al. 2007) epoch 2010.716.
[b] Seeing significantly less than the NIRES 0.″55 slit width, hence systematic radial velocity offsets are possible (see Section 4.5).

noted above, with wavelength calibration achieved using a combination of Ar arc lamps and bright OH telluric emission lines.

3.6. Additional Spectra

In addition to these newly observed candidates, we included in our analysis spectra of late-L and -T dwarfs and subdwarfs previously published in the literature. A sample of 199 L7–T8 spectra were obtained from the SpeX Prism Library Analysis Toolkit (SPLAT; A. J. Burgasser & Splat Development Team 2017), which excluded known resolved and candidate binaries and young brown dwarfs (Table 15 in Appendix A). We also included previously published spectra of T dwarf companions to primary stars with independent iron abundance measurements ranging over $-0.64 \leqslant [\mathrm{Fe/H}] \leqslant +0.25$, and previously identified metal-poor late-L and -T dwarfs (Table 3). For the late-L subdwarf J0532+8246, we stitched our Keck/NIRES spectrum with the Keck/LRIS (J. B. Oke et al. 1995) optical spectrum reported in A. J. Burgasser et al. (2003) by matching in the overlapping region of 0.98–1.0 μm. For the T subdwarf J1810−1010, we stitched together the Palomar/TripleSpec (J. C. Wilson et al. 2004) near-infrared spectrum reported by A. C. Schneider et al. (2020) with the GTC/OSIRIS (J. Cepa et al. 2000) optical and GTC/EMIR (F. Garzón et al. 2007) *YJ* spectra reported by N. Lodieu et al. (2022) by matching in the overlapping region of 0.98–1.32 μm.

For those sources observed with cross-dispersed spectrographs (Keck/NIRES, APO/TSpec, Palomar/TripleSpec, SOAR/ARCoIRIS) and with well-measured J, H, and K magnitudes, we re-evaluated the relative scaling of the spectral orders to ensure they align with photometry. We computed synthetic spectrophotometric $J - H$ and $J - K$ colors by integrating the spectra over the relevant filter profiles from 2MASS JHK_s, UKIRT/WFCam JHK, or VISTA JHK[22] using SPLAT tools, with inter-order gaps filled in using a BT-Settl atmospheric model (F. Allard et al. 2012) at an appropriate temperature, surface gravity, and metallicity (see Section 4.4). For the majority of our sources, the inter-order flux calibration

[22] Filter profiles were obtained from the Spanish Virtual Observatory (SVO) Filter Profile Service (C. Rodrigo et al. 2012; C. Rodrigo & E. Solano 2020) at http://svo2.cab.inta-csic.es/theory/fps/.

Table 3
Additional Spectral Data

Name	Designation (J2000)	J (mag)	Lit. SpT	Instrument	J SNR	[Fe/H] (dex)	References
Metallicity Benchmarks							
HD 3651B	J003918.91+211516.8[a]	16.31 ± 0.03	T8	IRTF/SpeX	73	+0.14	[1], [2]
HD 65486B	J07580132−2538587	16.12 ± 0.08	T4.5	IRTF/SpeX	34	−0.28	[30], [31],[34][d]
Ross 458C	J130041.40+122114.3	16.69 ± 0.02	T8.5p	Magellan/FIRE	67	+0.25	[28], [29]
HD 126053B	J142320.90+011635.3	18.71 ± 0.05	T8p	Gemini/GNIRS	24	−0.38	[25]
Gliese 570D	J145716.21−212216.5	15.32 ± 0.05	T7.5	IRTF/SpeX	37	+0.05	[3], [4]
GJ 576B	J150457.34+053757.0	16.59 ± 0.02	sdT5.5	Gemini/GNIRS	56	−0.37	[5], [6]
…	…	…	…	VLT/X-Shooter	21	…	[7]
G 204-38B	J175805.45+463319.8	16.15 ± 0.09	T6.5	IRTF/SpeX	75	−0.04	[8], [9]
Wolf 1130C	J200519.70+542428.5	19.64 ± 0.09	sdT8	Keck/NIRSPEC	78	−0.70	[10], [11]
…	…	…	…	Keck/MOSFIRE	…	…	[10]
HN Peg B	J214428.67+144606.0[b]	15.86 ± 0.03	T2.5	IRTF/SpeX	114	−0.08	[12], [12]
Wolf 940B	J214638.70−001042.3	18.02 ± 0.06	T8	Magellan/FIRE	69	+0.08	[26], [6]
Metal-poor Comparison Sources							
J0004−1336	J000458.59−133655.2	16.84 ± 0.17	T2p	IRTF/SpeX	18	…	[19]
J0004−2604	J000430.67−260403.6	16.49 ± 0.13	sdT2	IRTF/SpeX	40	…	[19]
J0013+0634	J001354.85+063445.4	19.75 ± 0.05	T8p	Gemini/GNIRS	22	…	[18]
J0021+1552	J002135.97+155226.8	17.88 ± 0.04	T4p	VLT/X-Shooter	9	…	[7]
J0055+5947[c]	J005559.94+594744.4	17.90 ± 0.04	T8	Keck/NIRES	13	…	[22]
J0057+2013	J005757.95+201302.8	16.32 ± 0.10	sdL7	IRTF/SpeX	40	…	[24]
J0301−2319	J030119.47−231921.8	16.64 ± 0.14	sdT1	IRTF/SpeX	25	…	[19]
J0309−5016	J030919.92−501614.0	17.17 ± 0.03	T7p	Magellan/FIRE	37	…	[19]
J0348−5620	J034858.85−562016.9	16.52 ± 0.15	T3p	Magellan/FIRE	22	…	[19]
J0414−5854	J041451.86−585455.3	19.63 ± 0.11	esdT	Magellan/FIRE	6	…	[13]
J0433+1009[c]	J043309.36+100902.3	18.00 ± 0.03	T8	Keck/NIRES	32	…	[15]
J0532+8246	J053310.53+824620.5	15.18 ± 0.06	esdL7	Keck/LRIS	…	−1.6	[14],[16]
J0616−6407	J061643.51−640719.8	16.35 ± 0.01	esdL6	VLT/X-Shooter	26	−1.6	[16]
J0645−6646	J064529.11−664550.7	15.52 ± 0.01	sdL8	VLT/X-Shooter	47	…	[17]
J0833+0052	J083338.11+005206.2	20.28 ± 0.10	T9p	Gemini/GNIRS	15	…	[18]
J0845−3305[c]	J084506.49−330532.1	16.85 ± 0.01	T7	Magellan/FIRE	82	…	[15]
J0850−0221	J085038.99−022155.1	15.44 ± 0.04	sdL7	IRTF/SpeX	83	…	[19]
J0911+2146[c]	J091105.03+214645.4	17.75 ± 0.03	T9	Magellan/FIRE	29	…	[15]
J0937+2931	J093735.65+293127.2	14.65 ± 0.04	T6p	IRTF/SpeX	128	…	[8]
J0939−2448	J093936.13−244844.0	15.67 ± 0.01	T8p	IRTF/SpeX	17	−0.24	[8],[35]
J0953−0943[c]	J095316.33−094318.8	17.01 ± 0.03	T5.5	IRTF/SpeX	24	…	[15],[34][d]
J1019−3911	J101944.47−391150.9	16.03 ± 0.10	sdT3	SOAR/ARCoIRIS	20	…	[19]
J1035−0711	J103534.52−071148.5	16.39 ± 0.09	sdL7	IRTF/SpeX	33	…	[19]
J1055+5443	J105512.03+544328.3	18.87 ± 0.07	sdT8/Y0	Keck/NIRES	29	…	[15],[20]
J1130−1158	J113019.20−115811.5	17.22 ± 0.03	sdT5	SOAR/ARCoIRIS	11	…	[15]
J1158+0435	J115821.40+043446.3	15.61 ± 0.06	sdL7	IRTF/SpeX	103	…	[32]
J1307+1511	J130710.04+151102.4	18.14 ± 0.04	sdL8	VLT/X-Shooter	10	…	[17]
J1316+0755	J131609.68+075553.9	19.29 ± 0.12	sdT6.5	Gemini/GNIRS	13	…	[5]
J1338−0229	J133836.94−022912.2	17.37 ± 0.03	sdL7	Magellan/FIRE	7	…	[16]
J1416+1348B	J141623.96+134837.3	17.26 ± 0.02	T7.5p	IRTF/SpeX	48	−0.35	[21],[35]
J1553+6933	J155347.98+693400.5	19.09 ± 0.07	sdT4	Keck/NIRES	19	…	[22],[33]
J1810−1010[c]	J181005.99−101001.8	17.27 ± 0.02	esdT	Palomar/TripleSpec	33	−1.5	[13],[23]
…	…	…	…	GTC/OSIRIS+EMIR	…	…	[23]
J2105−6235	J210529.52−623604.6	16.85 ± 0.14	sdT1.5	Gemini/Flamingos	69	…	[24]
J2218+1146[c]	J221859.41+114642.9	17.96 ± 0.03	T7p	Keck/NIRES	51	…	[22]

Notes. All designations are from the CatWISE2020 catalog (F. Marocco et al. 2021) and are proper-motion corrected to epoch 2015 May 28 except for noted sources.
[a] Coordinates from J. K. Faherty et al. (2009).
[b] Coordinates from Pan-STARRS DR1 (K. C. Chambers et al. 2016) epoch 2011 Nov 25.
[c] Also identified as a T subdwarf candidate by our selection criteria.
[d] Data re-reduced from the IRSA Legacy Archive.

References– The first reference corresponds to the source of the spectral data; the second reference corresponds to the source of the metallicity (for benchmarks): [1] A. J. Burgasser (2007a); [2] M. Rice & J. M. Brewer (2020); [3] A. J. Burgasser et al. (2004); [4] C. Aguilera-Gómez et al. (2018); [5] B. Burningham et al. (2014); [6] A. Arentsen et al. (2019); [7] Z. H. Zhang et al. (2019b); [8] A. J. Burgasser et al. (2006a); [9] A. Schweitzer et al. (2019); [10] G. N. Mace et al. (2013a); [11] G. N. Mace et al. (2018); [12] K. L. Luhman et al. (2007); [13] A. C. Schneider et al. (2020); [14] A. J. Burgasser et al. (2003); [15] J. D. Kirkpatrick et al. (2021b); [16] Z. H. Zhang et al. (2017); [17] Z. H. Zhang et al. (2018b); [18] D. J. Pinfield et al. (2014); [19] J. J. Greco et al. (2019); [20] G. Robbins et al. (2023); [21] A. J. Burgasser et al. (2010b); [22] A. M. Meisner et al. (2020); [23] N. Lodieu et al. (2022); [24] K. L. Luhman & S. S. Sheppard (2014); [25] D. J. Pinfield et al. (2012); [26] A. J. Burgasser et al. (2011); [27] E. Marfil et al. (2021); [28] A. J. Burgasser et al. (2010c); [29] L. J. Rosenthal et al. (2021); [30] N. R. Deacon et al. (2012a); [31] C. Soubiran et al. (2022); [32] J. D. Kirkpatrick et al. (2010); [33] A. M. Meisner et al. (2021); [34] This paper; [35] M. R. Line et al. (2017).

is generally consistent with the photometric uncertainties. However, for J1810−1010, we found a 50% reduction in K-band flux is required to align the spectrum with its UKIDSS photometry (A. C. Schneider et al. 2020). We used the appropriately scaled spectrum of this source for subsequent analysis.

4. Spectral Analysis

4.1. Comparison to Spectral Templates

Figures 3 and 4 display the reduced spectral data for our subdwarf candidates in both native resolution and smoothed to $\lambda/\Delta\lambda \approx 125$. The smoothed spectra are compared to low-resolution spectra of L and T dwarf near-infrared spectral standards from SPLAT[23] as defined by J. D. Kirkpatrick et al. (2010) and A. J. Burgasser et al. (2006b). A best-fit standard for each source was selected based on comparison over the 0.9–1.4 μm range using a χ^2 statistic (see Equation (4)); these standard types are listed in Table 4. For most of the sources, including the companions GJ 576B and LHS 6176B, we see close agreement with T6–T9 standards, with minor deviations in the *Y*-band (1 μm) and *K*-band (2.1 μm) peaks consistent with slightly subsolar metallicities (A. J. Burgasser et al. 2006a). A handful of sources appear to be late-type L or early-type T dwarfs based on weak or absent 1.6 μm CH_4 absorption, and several exhibit even more suppressed *K*-band peaks relative to their matched standards. For our higher-resolution Keck/NIRES data, we also see variety in the strengths of the 1.2436 μm and 1.2526 μm K I doublet, in many cases weaker than the corresponding NIRES dwarf standard (C. A. Theissen et al. 2022). We quantify these spectral deviations below.

4.2. Spectral Indices

For all of our spectra, we evaluated 10 near-infrared spectral indices that sample molecular features (H_2O and CH_4 bands) and overall spectral shape, defined in A. J. Burgasser et al. (2006a, 2006b) and D. C. Bardalez Gagliuffi et al. (2019). Tables 4 and 15 summarize the index values for our candidates and comparison sources, with uncertainties determined through Monte Carlo sampling of spectral flux errors. We also list index-based spectral classifications based on the index versus spectral type relationships of A. J. Burgasser (2007b), which are defined for spectral types L0–T9. Note that these relationships are defined for solar-metallicity dwarfs and are inaccurate for exceptionally metal-poor sources. Indeed, classifications from matched standards (Figure 3) and from indices can differ by more than three subtypes (e.g., J0532+8246).

4.3. K I Equivalent Widths

The moderate resolution of a subset of our spectra facilitates measurement of line equivalent widths (EWs) of the K I doublets at 1.1692/1.1778 μm and 1.2436/1.2526 μm (Figure 3). We measured these lines by integrating the unsmoothed spectral flux density relative to a linear fit of the local continuum over $\pm$ 0.02 μm windows outside the line regions, and sampled both flux uncertainties and small variations in the integration window through Monte Carlo methods. Table 5 lists the measured EWs. In cases where measurements were less than three times their uncertainties, we report 3σ upper limits.

In Figure 5, we compare these measurements to a compilation of local L and T dwarf spectra from E. C. Martin et al. (2017), which is based on $\lambda/\Delta\lambda \approx 2000$ data from the Keck Near-InfraRed SPECtrometer (NIRSPEC; I. S. McLean et al. 1998). The dwarf data follow previously identified trends for K I absorption, with 1.1692 μm and 1.1778 μm EWs rising from late-L to late-T (largely driven by the drop in continuum as H_2O absorption increases), 1.2436 μm EWs falling over the same range, and 1.2526 μm EWs rising from late-L to mid-T then dropping to zero for the latest T dwarfs. In contrast, many of the previously observed T subdwarfs and metal-poor T benchmarks, and several of our candidates, are either well below these trends or lack detectable K I absorption to limits of 1–2 Å. This is particularly clear for the 1.2526 μm line, which sits near the *J*-band flux peak and shows the greatest dichotomy between dwarfs and subdwarfs for types T1–T7. One notable exception in our candidate sample is J0140+0150, which has exceptionally strong absorption at 1.2436 μm for its T4.5 classification.

4.4. Spectral Model Fits

To obtain initial estimates of the physical properties of our sources, we compared low-resolution versions of our spectra to eight sets of spectral models from A. Burrows et al. (2006, hereafter B06), F. Allard et al. (2012, hereafter Settl and Dusty), M. W. Phillips et al. (2020, hereafter ATMO), M. S. Marley et al. (2021, hereafter Sonora), A. M. Meisner et al. (2021, hereafter LOWZ), S. Mukherjee et al. (2024, hereafter ElfOwl), and E. Alvarado et al. (2024, hereafter SAND). The parameters and parameter ranges explored for these models are summarized in Table 6. These models were chosen as they span both low temperatures and solar and subsolar metallicities, with the LOWZ models currently providing the best metallicity coverage for T subdwarf atmospheres. The observed ($O[\lambda]$) and model ($M[\lambda]$) spectra were resampled onto a common wavelength scale with a constant resolution of $\lambda/\Delta\lambda = 150$ over the range 0.9–2.45 μm using a median filter,[24] and noisy data at the edge of the observed spectral range and in the 1.35–1.45 μm and 1.8–1.95 μm telluric bands were masked from the fit. To identify the best-fitting model, we used a χ^2 goodness-of-fit statistic,

$$\chi^2 = \sum_{i=1}^{N} \frac{(O[\lambda_i] - \beta M[\lambda_i])^2}{\sigma[\lambda_i]^2} \quad (4)$$

where N is the number of unmasked flux values, $\sigma[\lambda_i]$ is the observed uncertainty spectrum, and the optimal scale factor β is computed as

$$\beta = \frac{\sum_{i=1}^{N} \frac{O[\lambda_i]M[\lambda_i]}{\sigma[\lambda_i]^2}}{\sum_{i=1}^{N} \frac{M[\lambda_i]^2}{\sigma[\lambda_i]^2}} \quad (5)$$

(see M. C. Cushing et al. 2008). We report here the reduced chi-square, $\chi^2_r \equiv \chi^2/(N-1)$, as a normalized quality of fit. For sources with measured parallaxes, we scaled the observed spectra to absolute fluxes using their M_J magnitudes, which allows us to estimate the source radius from the scale factor

$$R_\beta = 10\sqrt{\beta} \quad \text{pc} = 2.256 \times 10^{-9}\sqrt{\beta} \quad R_\odot. \quad (6)$$

All other spectra are scaled to apparent *J* magnitudes. No attempt was made to adjust for relative velocity shifts between

[23] Spectral data for late-L and -T dwarf standards are from A. J. Burgasser et al. (2004, 2006b, 2007b); D. L. Looper et al. (2007); and D. C. Bardalez Gagliuffi et al. (2014).

[24] Smoothed uncertainties were computed as median($\{\sigma\}$)/$\sqrt{N-1}$ for the N uncertainty values $\{\sigma\}$ within the sampling region.

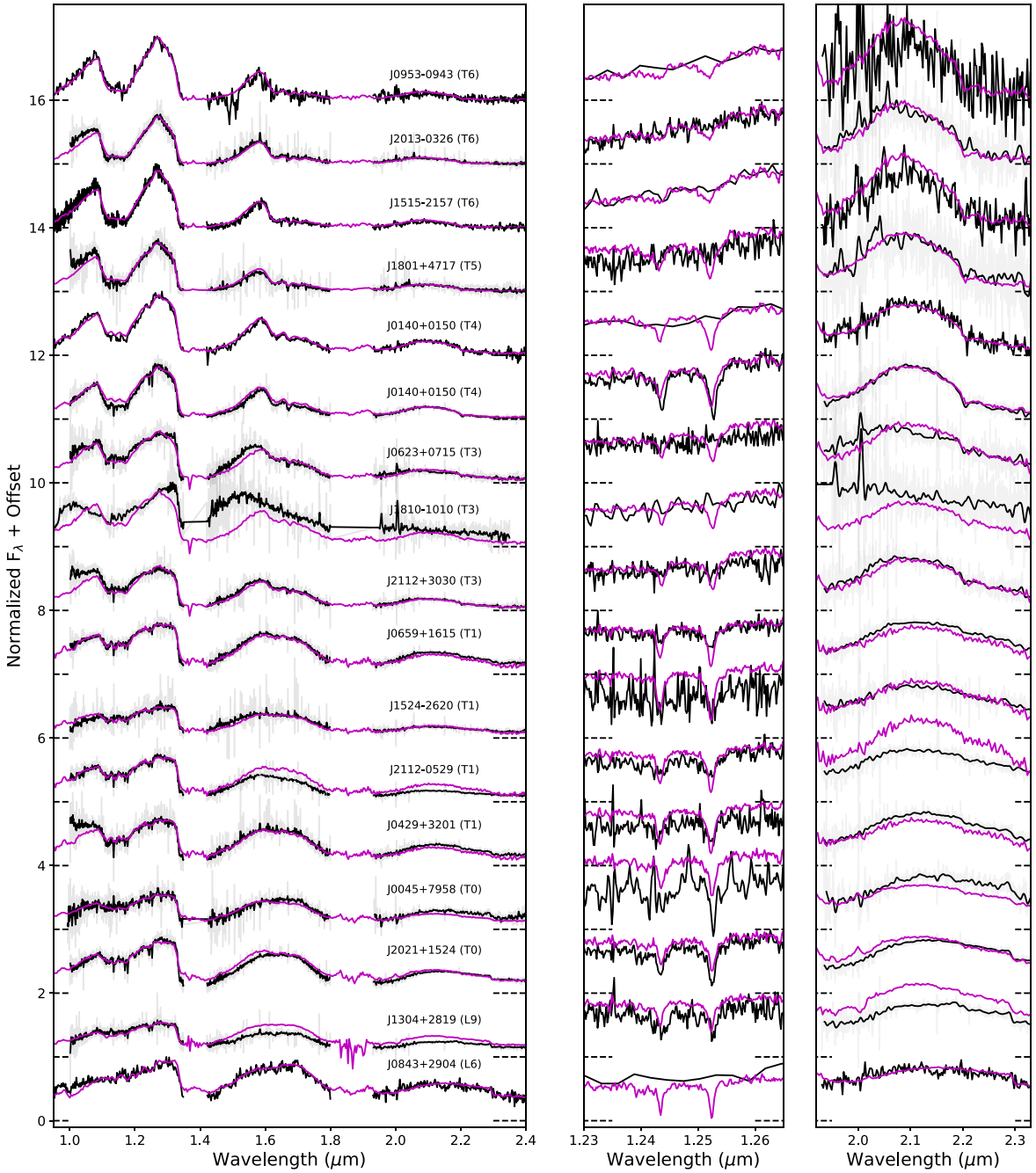

Figure 3. Observed spectra of candidate late-L and -T subdwarfs from Tables 2 and 3. Spectra are normalized at the *J*-band (1.25–1.28 μm) flux peak and offset by a constant (dashed lines on left and right edges). Source are ordered from bottom to top by increasing *H*-band CH_4 band strength. The left panel shows the full 1–2.5 μm spectral data, while the middle and right panels focus on the 1.23–1.265 μm *J*-band and 2.0–2.3 μm *K*-band regions. In the left and right panels, the full-resolution data are shown as gray lines and smoothed spectra ($\lambda/\Delta\lambda \approx 125$) as black lines, and are compared to low-resolution dwarf spectral standards (magenta lines) drawn from J. D. Kirkpatrick et al. (2010) and A. J. Burgasser et al. (2006b), with corresponding types indicated next to each source label. The middle panel shows only the full-resolution data compared to medium-resolution spectral standards from C. A. Theissen et al. (2022) in magenta. Note that IRTF/SpeX and Magellan/FIRE data J0911+2146, and J0953−0943 (the latter three are in Figure 4) are not smoothed, as their native resolution is $\boldsymbol{\lambda/\Delta\lambda \approx}$ 100–300. The *K*-band spectra are re-scaled to highlight structure in this region.

(The data used to create this figure are available in the online article.)

the observed and model spectra, which are expected to be minimal at this low resolution.

For each model set, an initial fit was made to the individual grid models, and the best-fit (lowest χ^2_r) model was used as an initial estimate of the atmosphere parameters. We employed a simple Metropolis-Hastings Markov Chain Monte Carlo (MCMC) algorithm (N. Metropolis et al. 1953; W. K. Hastings 1970) to explore the proximate parameter space. We used a single chain of 2000 steps for each spectrum and model set comparison, varying the continuous variables of effective temperature ($T_{\rm eff}$), surface gravity ($\log g$), and solar-scaled metallicity ([M/H]) for all models, as well as carbon/oxygen abundance ratio (C/O) for LOWZ, Sonora, and ElfOwl models; alpha element enrichment ([α/Fe]) for Settl, Dusty, and SAND models; and adiabatic coefficient $\gamma = (1 - \partial \log T/\partial \log P)^{-1}$ (P. Tremblin et al. 2019) and

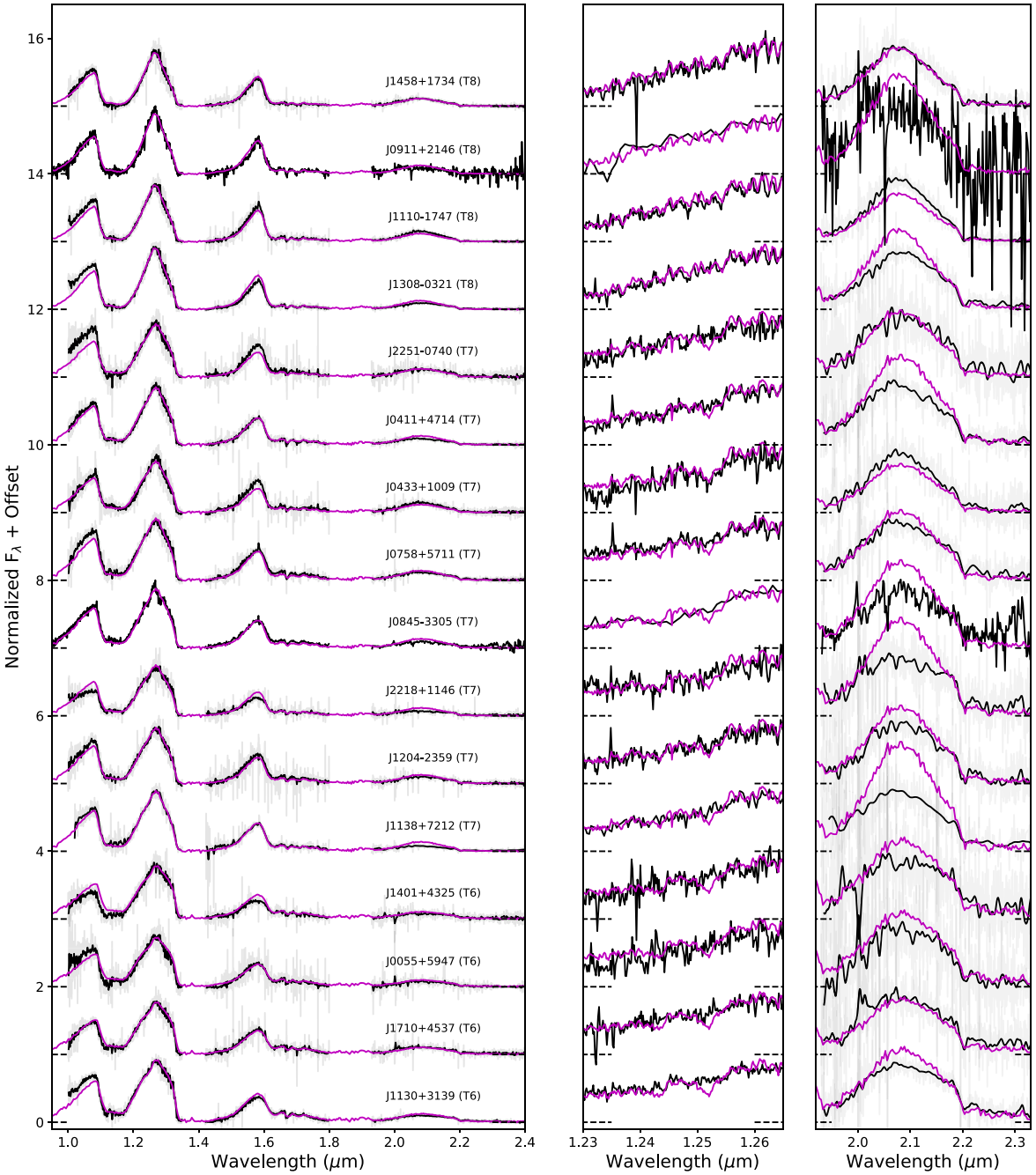

Figure 4. Continuation of Figure 3 for the latest-type sources in our spectral sample.

minimum cloud deck pressure $P_{\rm min}$ for ATMO models. We also varied the disequilibrium mixing diffusion rate $\log \kappa_{zz}$ for the LOWZ, ATMO, and ElfOwl models as a discrete value. Models were linearly interpolated in logarithmic flux units on a logarithmic parameter grid (i.e,. $T_{\rm eff} \Rightarrow \log T_{\rm eff}$). In each iteration, we drew new parameters for the continuous variables using a normal distribution centered on the last parameter values in the chain with pre-defined standard deviations.[25] The discrete variable $\log \kappa_{zz}$ was randomly drawn from the available values. Sequential fits ($i \Rightarrow i + 1$) were compared using the criterion

$$\frac{\chi^2(i+1) - \chi^2(i)}{\rm MIN[\chi^2]} < \mathcal{U}(0, 0.5) \quad (7)$$

where MIN is the minimum of all χ^2 values in the chain and $\mathcal{U}(0, 0.5)$ is a number drawn from a uniform distribution between 0 and 0.5. If the new fit satisfied this criterion, these parameters were added to the chain; otherwise, the previous parameters were added. We also enforced a limit on χ^2 values exceeding 2 × MIN[χ^2], at which point the chain reverted to the minimum χ^2 parameter set. We verified that all fits converged using the convergence diagnostic defined by J. Geweke (1992), requiring that the means of the variable

[25] These standard deviations were $\sigma_{Teff} = 30$ K, $\sigma_{\log g} = 0.1$ dex, $\sigma_{[M/H]} = 0.05$ dex, $\sigma_{C/O} = 0.05$ dex, $\sigma_{[\alpha/Fe]} = 0.05$ dex, and $\sigma_{\gamma} = 0.01$.

Table 4
Index Measurements for New and Literature Spectra

Name	[CH4 − J]	[CH4 − H]	[CH4 − K]	[H2O − J]	[H2O − H]	[H2O − K]	[Y/J]	[K/H]	[K/J]	[H − dip]	SpT[a]	
(numerator)	1.315–1.335	1.635–1.675	2.215–2.255	1.14–1.165	1.48–1.52	1.975–1.995	1.005–1.045	2.06–2.10	2.06–2.10	1.61–1.64	Std	Ind
(denominator)	1.26–1.285	1.56–1.60	2.08–2.12	1.26–1.285	1.56–1.60	2.08–2.12	1.25–1.29	1.25–1.29	1.56–1.60	1.56–1.59,1.66–1.69		
Benchmark Companions												
HD 3651B	0.25 ± 0.01	0.14 ± 0.01	0.04 ± 0.02	0.04 ± 0.01	0.17 ± 0.01	0.32 ± 0.02	0.42 ± 0.01	0.29 ± 0.01	0.14 ± 0.01	0.25 ± 0.02	T8	T7.7
HD 65486B	0.64 ± 0.02	0.50 ± 0.02	0.26 ± 0.07	0.32 ± 0.01	0.37 ± 0.02	0.56 ± 0.09	0.64 ± 0.02	0.30 ± 0.02	0.14 ± 0.01	0.59 ± 0.03	T4.5	
LHS 6176B	0.26 ± 0.01	0.16 ± 0.01	0.12 ± 0.01	0.06 ± 0.01	0.16 ± 0.01	0.39 ± 0.02	0.52 ± 0.01	0.22 ± 0.01	0.11 ± 0.01	0.31 ± 0.01	T8	T7.5
Ross 458C	0.19 ± 0.01	0.12 ± 0.01	0.07 ± 0.01	0.05 ± 0.01	0.19 ± 0.01	0.36 ± 0.01	0.35 ± 0.01	0.45 ± 0.01	0.26 ± 0.01	0.23 ± 0.01	T8	T8.1
HD 126053B	0.27 ± 0.02	0.14 ± 0.01	0.10 ± 0.05	0.05 ± 0.01	0.22 ± 0.02	0.37 ± 0.05	0.54 ± 0.03	0.11 ± 0.01	0.05 ± 0.01	0.40 ± 0.03	T7	T7.5
GJ 570D	0.28 ± 0.01	0.13 ± 0.01	0.11 ± 0.02	0.06 ± 0.01	0.20 ± 0.01	0.34 ± 0.02	0.41 ± 0.01	0.24 ± 0.01	0.11 ± 0.01	0.34 ± 0.02	T8	T7.5
GJ 576B (GNIRS)	0.43 ± 0.01	0.37 ± 0.01	0.21 ± 0.05	0.16 ± 0.01	0.30 ± 0.02	0.47 ± 0.04	0.52 ± 0.01	0.22 ± 0.01	0.10 ± 0.01	0.67 ± 0.03	T6	T5.6
⋯ (XS)	0.43 ± 0.02	0.40 ± 0.02	0.13 ± 0.15	0.15 ± 0.02	0.29 ± 0.02	0.50 ± 0.09	0.54 ± 0.04	0.19 ± 0.03	0.08 ± 0.01	0.64 ± 0.02	T6	T5.5
⋯ (NIRES)	0.44 ± 0.01	0.40 ± 0.01	0.25 ± 0.01	0.15 ± 0.01	0.28 ± 0.01	0.49 ± 0.01	0.45 ± 0.01	0.25 ± 0.01	0.10 ± 0.01	0.61 ± 0.01	T6	T5.5
G 204−39B	0.41 ± 0.01	0.25 ± 0.01	0.10 ± 0.01	0.10 ± 0.01	0.24 ± 0.01	0.40 ± 0.01	0.41 ± 0.01	0.40 ± 0.01	0.20 ± 0.01	0.44 ± 0.01	T6	T6.4
Wolf 1130C	0.82 ± 0.03	0.42 ± 0.01	…[b]	0.01 ± 0.01	0.39 ± 0.01	…[b]	0.74 ± 0.11	…[b]	…[b]	0.75 ± 0.01	T6	T5.4
HN PegB	0.63 ± 0.01	0.84 ± 0.01	0.53 ± 0.01	0.38 ± 0.01	0.43 ± 0.01	0.54 ± 0.01	0.55 ± 0.01	0.46 ± 0.01	0.31 ± 0.01	0.98 ± 0.01	T3	T2.4
Wolf 940B	0.12 ± 0.02	0.08 ± 0.03	−0.03 ± 0.09	0.03 ± 0.02	0.14 ± 0.04	0.29 ± 0.08	…[b]	0.24 ± 0.01	0.13 ± 0.01	0.15 ± 0.06	T8	T8.6
Subdwarf Candidates												
J0045+7958	0.82 ± 0.09	1.12 ± 0.06	0.90 ± 0.05	0.67 ± 0.11	0.60 ± 0.06	0.62 ± 0.04	0.57 ± 0.17	0.63 ± 0.03	0.50 ± 0.04	1.02 ± 0.05	T0	L8.6:
J0055+5947	0.35 ± 0.02	0.27 ± 0.02	0.16 ± 0.05	0.11 ± 0.03	0.25 ± 0.04	0.36 ± 0.08	0.60 ± 0.06	0.23 ± 0.01	0.11 ± 0.01	0.46 ± 0.03	T6	T6.4
J0140+0150 (SpeX)	0.59 ± 0.02	0.58 ± 0.03	0.27 ± 0.05	0.28 ± 0.02	0.34 ± 0.03	0.47 ± 0.05	0.45 ± 0.02	0.44 ± 0.02	0.25 ± 0.01	0.82 ± 0.04	T4	T4.2
⋯ (NIRES)	0.59 ± 0.01	0.56 ± 0.01	0.26 ± 0.01	0.24 ± 0.01	0.32 ± 0.01	0.47 ± 0.01	0.44 ± 0.01	0.44 ± 0.01	0.24 ± 0.01	0.78 ± 0.01	T4	T4.5
J0411+4714	0.27 ± 0.01	0.16 ± 0.01	0.10 ± 0.01	0.08 ± 0.01	0.21 ± 0.01	0.46 ± 0.01	0.46 ± 0.01	0.24 ± 0.01	0.10 ± 0.01	0.33 ± 0.01	T7	T7.4
J0429+3201	0.85 ± 0.02	0.96 ± 0.01	0.77 ± 0.01	0.56 ± 0.01	0.55 ± 0.01	0.59 ± 0.01	0.90 ± 0.03	0.56 ± 0.01	0.45 ± 0.01	1.03 ± 0.01	T1	T1.1
J0433+1009	0.22 ± 0.01	0.16 ± 0.01	0.10 ± 0.02	0.09 ± 0.01	0.22 ± 0.01	0.34 ± 0.02	0.40 ± 0.03	0.34 ± 0.01	0.19 ± 0.01	0.31 ± 0.02	T8	T7.3
J0623+0715	0.82 ± 0.02	0.64 ± 0.01	0.58 ± 0.01	0.50 ± 0.01	0.60 ± 0.02	0.77 ± 0.02	0.72 ± 0.03	0.34 ± 0.01	0.25 ± 0.01	0.89 ± 0.01	T3	T3.4
J0659+1615	0.87 ± 0.01	0.95 ± 0.01	0.76 ± 0.01	0.62 ± 0.01	0.58 ± 0.01	0.61 ± 0.01	0.65 ± 0.02	0.54 ± 0.01	0.44 ± 0.01	1.03 ± 0.01	T1	T1.0
J0758+5711	0.35 ± 0.01	0.26 ± 0.01	0.17 ± 0.01	0.12 ± 0.01	0.23 ± 0.01	0.45 ± 0.02	0.56 ± 0.02	0.27 ± 0.01	0.14 ± 0.01	0.47 ± 0.01	T7	T6.4
J0843+2904	0.93 ± 0.03	1.07 ± 0.04	0.90 ± 0.03	0.83 ± 0.04	0.72 ± 0.04	0.75 ± 0.03	0.66 ± 0.03	0.74 ± 0.03	0.67 ± 0.03	1.00 ± 0.03	L6	L5.9
J0845−3305	0.38 ± 0.01	0.27 ± 0.01	0.22 ± 0.02	0.12 ± 0.01	0.28 ± 0.01	0.42 ± 0.01	0.46 ± 0.01	0.24 ± 0.01	0.12 ± 0.01	0.46 ± 0.01	T7	T6.2
J0911+2146	0.19 ± 0.01	0.13 ± 0.01	…[b]	0.04 ± 0.01	0.17 ± 0.01	0.56 ± 0.05	0.37 ± 0.02	0.19 ± 0.01	0.10 ± 0.01	0.29 ± 0.02	T8	T8.2
J1110−1747	0.20 ± 0.01	0.10 ± 0.01	0.04 ± 0.01	0.05 ± 0.01	0.17 ± 0.01	0.32 ± 0.01	0.46 ± 0.01	0.32 ± 0.01	0.19 ± 0.01	0.22 ± 0.01	T8	T8.2
J1130+3139	0.45 ± 0.01	0.38 ± 0.01	0.26 ± 0.01	0.14 ± 0.01	0.26 ± 0.01	0.47 ± 0.02	0.58 ± 0.01	0.27 ± 0.01	0.11 ± 0.01	0.63 ± 0.01	T6	T5.6
J1138+7212	0.31 ± 0.02	0.23 ± 0.03	0.18 ± 0.08	0.13 ± 0.03	0.26 ± 0.04	0.58 ± 0.10	0.56 ± 0.04	0.21 ± 0.01	0.09 ± 0.01	0.40 ± 0.05	T7	T6.5
J1204−2359	0.31 ± 0.01	0.24 ± 0.01	0.10 ± 0.02	0.09 ± 0.01	0.21 ± 0.02	0.33 ± 0.02	0.50 ± 0.03	0.25 ± 0.01	0.13 ± 0.01	0.42 ± 0.02	T7	T6.8
J1304+2819	0.92 ± 0.02	1.02 ± 0.01	0.90 ± 0.01	0.75 ± 0.02	0.68 ± 0.01	0.69 ± 0.01	0.56 ± 0.02	0.63 ± 0.01	0.44 ± 0.01	0.98 ± 0.01	L9	L7.4
J1308−0321	0.22 ± 0.01	0.12 ± 0.01	0.12 ± 0.01	0.03 ± 0.01	0.16 ± 0.01	0.36 ± 0.01	0.50 ± 0.01	0.24 ± 0.01	0.11 ± 0.01	0.25 ± 0.01	T8	T7.9
J1401+4325	0.42 ± 0.02	0.36 ± 0.01	0.27 ± 0.03	0.09 ± 0.01	0.27 ± 0.02	0.62 ± 0.04	0.38 ± 0.02	0.29 ± 0.01	0.10 ± 0.01	0.60 ± 0.02	T7	T5.6
J1458+1734	0.21 ± 0.01	0.10 ± 0.01	0.05 ± 0.01	0.01 ± 0.01	0.18 ± 0.01	0.36 ± 0.01	0.40 ± 0.02	0.30 ± 0.01	0.15 ± 0.01	0.23 ± 0.01	T8	T8.2
J1515−2157	0.43 ± 0.01	0.28 ± 0.01	0.23 ± 0.02	0.12 ± 0.01	0.18 ± 0.01	0.39 ± 0.02	0.51 ± 0.03	0.23 ± 0.01	0.10 ± 0.01	0.50 ± 0.02	T6	T6.1
J1524−2620	0.87 ± 0.02	0.94 ± 0.01	0.77 ± 0.01	0.67 ± 0.02	0.72 ± 0.02	0.72 ± 0.01	0.48 ± 0.03	0.48 ± 0.01	0.36 ± 0.01	1.01 ± 0.01	L9	L9.3
J1710+4537	0.40 ± 0.01	0.31 ± 0.01	0.26 ± 0.02	0.14 ± 0.01	0.26 ± 0.01	0.44 ± 0.02	0.41 ± 0.02	0.30 ± 0.01	0.15 ± 0.01	0.51 ± 0.01	T6	T5.9
J1801+4717	0.44 ± 0.01	0.43 ± 0.01	0.28 ± 0.03	0.18 ± 0.01	0.33 ± 0.02	0.37 ± 0.03	0.65 ± 0.03	0.34 ± 0.01	0.13 ± 0.01	0.70 ± 0.02	T5	T5.1
J2013−0326	0.40 ± 0.01	0.34 ± 0.01	0.22 ± 0.02	0.13 ± 0.01	0.30 ± 0.01	0.60 ± 0.03	0.58 ± 0.02	0.25 ± 0.01	0.12 ± 0.01	0.57 ± 0.02	T6	T5.8
J2021+1524	0.86 ± 0.01	1.04 ± 0.01	0.91 ± 0.01	0.62 ± 0.01	0.56 ± 0.01	0.59 ± 0.01	0.53 ± 0.01	0.56 ± 0.01	0.39 ± 0.01	1.03 ± 0.01	T0	L9.8
J2112−0529	0.82 ± 0.01	0.88 ± 0.01	0.77 ± 0.01	0.61 ± 0.01	0.60 ± 0.01	0.68 ± 0.01	0.58 ± 0.02	0.42 ± 0.01	0.25 ± 0.01	1.01 ± 0.01	T1	T1.4

Table 4
(Continued)

Name (numerator) (denominator)	[CH4 − J] 1.315–1.335 1.26–1.285	[CH4 − H] 1.635–1.675 1.56–1.60	[CH4 − K] 2.215–2.255 2.08–2.12	[H2O − J] 1.14–1.165 1.26–1.285	[H2O − H] 1.48–1.52 1.56–1.60	[H2O − K] 1.975–1.995 2.08–2.12	[Y/J] 1.005–1.045 1.25–1.29	[K/H] 2.06–2.10 1.25–1.29	[K/J] 2.06–2.10 1.56–1.60	[H − dip] 1.61–1.64 1.56–1.59,1.66–1.69	SpT[a] Std	SpT[a] Ind
J2112+3030	0.78 ± 0.01	0.74 ± 0.01	0.51 ± 0.01	0.53 ± 0.01	0.50 ± 0.01	0.61 ± 0.01	0.93 ± 0.03	0.39 ± 0.01	0.28 ± 0.01	0.93 ± 0.01	T3	T2.6
J2218+1146	0.37 ± 0.01	0.24 ± 0.01	0.14 ± 0.02	0.11 ± 0.01	0.30 ± 0.01	0.51 ± 0.03	0.41 ± 0.02	0.26 ± 0.01	0.10 ± 0.01	0.46 ± 0.02	T7	T6.4
J2251−0740	0.28 ± 0.01	0.19 ± 0.01	0.14 ± 0.02	0.06 ± 0.01	0.16 ± 0.01	0.34 ± 0.03	0.69 ± 0.03	0.26 ± 0.01	0.16 ± 0.01	0.39 ± 0.02	T7	T7.1
Metal-poor Comparison Sources												
J0004−1336	0.76 ± 0.02	0.95 ± 0.03	0.85 ± 0.05	0.57 ± 0.02	0.59 ± 0.04	0.63 ± 0.04	0.55 ± 0.02	0.44 ± 0.02	0.26 ± 0.01	0.96 ± 0.03	T1	T0.6
J0004−2604	0.70 ± 0.01	0.75 ± 0.01	0.57 ± 0.02	0.47 ± 0.01	0.52 ± 0.02	0.59 ± 0.02	0.57 ± 0.01	0.41 ± 0.01	0.27 ± 0.01	0.90 ± 0.02	T3	T2.5
J0013+0634	0.26 ± 0.02	0.32 ± 0.04	0.21 ± 0.09	0.09 ± 0.05	0.17 ± 0.02	…[b]	0.50 ± 0.04	0.09 ± 0.01	0.04 ± 0.01	0.38 ± 0.06	T7	T6.2
J0021+1552	0.67 ± 0.04	0.57 ± 0.03	0.26 ± 0.17	0.39 ± 0.05	0.46 ± 0.04	0.67 ± 0.14	0.52 ± 0.11	0.27 ± 0.04	0.17 ± 0.03	0.83 ± 0.05	T4	T4.0
J0057+2013	0.84 ± 0.01	1.02 ± 0.01	0.95 ± 0.02	0.66 ± 0.01	0.59 ± 0.01	0.70 ± 0.01	0.57 ± 0.01	0.53 ± 0.01	0.38 ± 0.01	0.97 ± 0.01	T0	L8.7
J0301−2319	0.82 ± 0.02	0.98 ± 0.02	0.73 ± 0.02	0.67 ± 0.02	0.67 ± 0.02	0.63 ± 0.02	0.74 ± 0.02	0.49 ± 0.01	0.33 ± 0.01	1.01 ± 0.02	T1	L9.6
J0309−5016	0.20 ± 0.01	0.16 ± 0.01	0.16 ± 0.08	0.05 ± 0.01	0.23 ± 0.01	0.51 ± 0.05	0.56 ± 0.02	0.14 ± 0.01	0.06 ± 0.01	0.30 ± 0.02	T7	T7.7
J0348−5620	0.54 ± 0.02	0.59 ± 0.02	0.30 ± 0.04	0.39 ± 0.02	0.47 ± 0.02	0.61 ± 0.04	0.50 ± 0.02	0.34 ± 0.02	0.20 ± 0.01	0.79 ± 0.03	T4	T4.1
J0414−5854	0.90 ± 0.06	0.58 ± 0.07	…[b]	0.22 ± 0.07	0.81 ± 0.09	…[b]	0.91 ± 0.09	0.04 ± 0.04	0.02 ± 0.02	0.89 ± 0.09	T4	T3.9
J0532+8246	0.85 ± 0.01	0.83 ± 0.01	0.81 ± 0.01	0.83 ± 0.01	0.86 ± 0.01	0.88 ± 0.01	0.56 ± 0.01	0.35 ± 0.01	0.17 ± 0.01	1.00 ± 0.01	L8	L4.6
J0616−6407	0.86 ± 0.03	0.82 ± 0.02	0.95 ± 0.08	0.89 ± 0.03	0.92 ± 0.03	0.84 ± 0.06	0.59 ± 0.03	0.31 ± 0.02	0.15 ± 0.01	0.97 ± 0.02	T0	T1.1
J0645−6646	0.85 ± 0.01	1.01 ± 0.01	0.87 ± 0.02	0.68 ± 0.01	0.63 ± 0.01	0.66 ± 0.01	0.52 ± 0.02	0.48 ± 0.01	0.34 ± 0.01	1.03 ± 0.01	T0	L9.0
J0850−0221	0.89 ± 0.01	1.06 ± 0.01	0.95 ± 0.01	0.77 ± 0.01	0.70 ± 0.01	0.71 ± 0.01	0.48 ± 0.01	0.55 ± 0.01	0.40 ± 0.01	0.98 ± 0.01	L6	L6.5
J0833+0052	0.09 ± 0.02	0.12 ± 0.03	…[b]	−0.04 ± 0.04	0.07 ± 0.04	0.29 ± 0.09	0.51 ± 0.05	0.17 ± 0.02	0.10 ± 0.01	0.30 ± 0.05	T8	…
J0937+2931	0.43 ± 0.01	0.31 ± 0.01	0.18 ± 0.01	0.15 ± 0.01	0.31 ± 0.01	0.53 ± 0.02	0.53 ± 0.01	0.17 ± 0.01	0.07 ± 0.01	0.53 ± 0.01	T6	T5.8
J0939−2448	0.30 ± 0.01	0.14 ± 0.01	0.10 ± 0.04	0.03 ± 0.01	0.17 ± 0.01	0.52 ± 0.05	0.51 ± 0.02	0.13 ± 0.01	0.06 ± 0.01	0.33 ± 0.02	T8	T7.7
J0953−0943	0.50 ± 0.02	0.37 ± 0.03	0.21 ± 0.10	0.21 ± 0.02	−0.18 ± 0.05	0.58 ± 0.13	0.45 ± 0.02	0.25 ± 0.03	0.10 ± 0.01	0.50 ± 0.06	T6	T5.1
J1019−3911	0.66 ± 0.01	0.55 ± 0.01	0.29 ± 0.01	0.44 ± 0.01	0.40 ± 0.01	0.50 ± 0.01	0.48 ± 0.01	0.36 ± 0.01	0.20 ± 0.01	0.77 ± 0.01	T4	T4.0
J1035−0711	0.89 ± 0.02	1.07 ± 0.02	0.94 ± 0.02	0.72 ± 0.01	0.63 ± 0.02	0.66 ± 0.02	0.58 ± 0.01	0.56 ± 0.01	0.38 ± 0.01	1.04 ± 0.02	L9	L7.7
J1055+5443	0.05 ± 0.01	0.06 ± 0.01	0.05 ± 0.03	0.02 ± 0.02	0.11 ± 0.02	0.27 ± 0.03	0.79 ± 0.05	0.31 ± 0.01	0.23 ± 0.01	0.10 ± 0.03	T9	…
J1130−1158	0.49 ± 0.03	0.33 ± 0.03	0.69 ± 0.46	0.21 ± 0.06	0.38 ± 0.05	1.11 ± 0.27	0.49 ± 0.05	0.13 ± 0.02	0.06 ± 0.01	0.62 ± 0.06	T6	T5.4
J1158+0435	0.86 ± 0.01	1.04 ± 0.01	0.89 ± 0.01	0.71 ± 0.01	0.64 ± 0.01	0.69 ± 0.01	0.47 ± 0.01	0.50 ± 0.01	0.32 ± 0.01	1.01 ± 0.01	L7	L8.0
J1307+1510	0.79 ± 0.05	1.03 ± 0.04	0.95 ± 0.12	0.66 ± 0.06	0.58 ± 0.03	0.65 ± 0.06	0.49 ± 0.07	0.52 ± 0.04	0.35 ± 0.03	1.04 ± 0.03	T1	T1.1
J1316+0755	0.40 ± 0.02	0.35 ± 0.03	…[b]	0.13 ± 0.02	0.26 ± 0.04	…[b]	0.69 ± 0.05	0.10 ± 0.01	0.05 ± 0.01	0.51 ± 0.05	T7	T5.7
J1338−0229	0.86 ± 0.06	1.06 ± 0.08	0.83 ± 0.07	0.68 ± 0.05	0.62 ± 0.05	0.70 ± 0.07	0.44 ± 0.04	0.43 ± 0.03	0.28 ± 0.02	1.12 ± 0.07	T0	L9.2:
J1416+1348B	0.30 ± 0.01	0.21 ± 0.01	0.00 ± 0.18	0.04 ± 0.01	0.17 ± 0.01	0.35 ± 0.15	0.60 ± 0.01	0.07 ± 0.01	0.04 ± 0.01	0.42 ± 0.02	T7	T7.0
J1553+6934	0.86 ± 0.03	0.63 ± 0.02	0.65 ± 0.04	0.42 ± 0.03	0.66 ± 0.03	0.86 ± 0.07	0.56 ± 0.05	0.27 ± 0.01	0.16 ± 0.01	0.89 ± 0.02	T4	T3.6
J1810−1010	0.98 ± 0.05	0.75 ± 0.05	…[b]	0.53 ± 0.02	1.06 ± 0.07	…[b]	0.74 ± 0.01	0.37 ± 0.05	0.32 ± 0.04	0.95 ± 0.05	T3	T2.2
J2105−6235	0.80 ± 0.01	0.85 ± 0.01	…[b]	0.55 ± 0.01	0.60 ± 0.01	…[b]	0.53 ± 0.01	…[b]	…[b]	0.98 ± 0.01	T2	T1.8

Notes. Spectral indices are defined as flux ratios, computed as the integral of the spectrum over the defined wavelength ranges in microns. For the [H-dip] index, the denominator is the median of the fluxes computed in the two specified ranges. Further details are provided in A. J. Burgasser et al. (2006a, 2006b) and D. C. Bardalez Gagliuffi et al. (2019).

[a] Spectral type as inferred from direct comparison to spectral standards ("Std") and indices ("Ind").

[b] Missing spectral data or skewed by excess noise.

Table 5
Equivalent Widths

Name	SpT[a]	Instrument	1.1692 μm (Å)	1.1778 μm (Å)	1.2436 μm (Å)	1.2526 μm (Å)
Metallicity Benchmarks						
LHS 6176B	d/sdT7.5	NIRES	16.0 ± 2.4	<9	<1.0	<1.2
HD 126053B	sdT7.5	GNIRS	<63	<93	<2.5	<2.0
GJ 576B	d/sdT5.5	XS	<7	13.3 ± 2.2	<1.3	<1.5
…	…	NIRES	14.7 ± 2.2	10.2 ± 1.5	1.6 ± 0.2	1.8 ± 0.2
Wolf 1130C	(e)sdT6:	Keck	<19	<14	<1.7	<1.6
Subdwarf Candidates						
J0045+7958	d/sdL9	TSpec	<25	6.3 ± 1.1	6.9 ± 1.2	7.8 ± 1.0
J0055+5947	d/sdT6.5	NIRES	<35	<26	<2.1	<1.7
J0140+0150	rT4.5	NIRES	12.8 ± 1.4	13.0 ± 1.5	7.1 ± 0.5	8.9 ± 0.5
J0411+4714	d/sdT7.5	NIRES	14.8 ± 2.5	<8	<1.0	<1.1
J0429+3201	T1	NIRES	8.3 ± 0.9	8.5 ± 0.8	<1.7	3.6 ± 0.5
J0433+1009	T8	NIRES	<41	<65	<1.6	3.3 ± 0.4
J0623+0715	sdT3	NIRES	6.7 ± 1.2	5.5 ± 0.8	<1.1	<1.2
J0659+1615	T1	NIRES	5.4 ± 0.6	7.3 ± 0.5	2.2 ± 0.3	4.6 ± 0.3
J0758+5711	T6.5	NIRES	12.4 ± 1.9	7.7 ± 1.5	2.0 ± 0.3	2.1 ± 0.3
J1110−1747	rT8	NIRES	<12	<22	<1.0	<1.7
J1130+3139	d/sdT5.5	NIRES	13.9 ± 2.0	8.9 ± 1.5	2.0 ± 0.3	<0.8
J1138+7212	d/sdT7	GNIRS	<67	<50	<1.3	<1.2
J1204−2359	d/sdT7	NIRES	16 ± 3	15 ± 3	3.2 ± 0.4	<1.6
J1304+2819	d/sdL9:	NIRES	4.8 ± 0.6	9.5 ± 0.6	6.5 ± 0.6	5.3 ± 0.7
J1308−0321	d/sdT8	NIRES	<51	…[b]	<1.1	<1.8
J1401+4325	d/sdT5.5	NIRES	<18	<9	<1.6	<1.8
J1458+1734	T8	NIRES	<47	…[b]	<1.4	<1.5
J1524−2620	sdT0	NIRES	8.9 ± 1.1	9.4 ± 0.9	5.0 ± 0.7	3.7 ± 0.7
J1710+4537	T6	NIRES	14 ± 3	11.1 ± 1.9	<1.0	<1.0
J1801+4717	d/sdT5	NIRES	17 ± 3	9.8 ± 1.7	<1.4	<1.7
J2013−0326	d/sdT6	NIRES	<10	12.6 ± 2.3	<1.2	<1.1
J2021+1524	d/sdL9	NIRES	9.7 ± 0.7	12.4 ± 0.7	6.3 ± 0.6	8.0 ± 0.5
J2112−0529	sdT1	NIRES	7.9 ± 0.8	10.4 ± 0.6	5.3 ± 0.5	5.9 ± 0.4
J2112+3030	d/sdT2.5	NIRES	5.8 ± 0.9	7.0 ± 0.8	<1.1	3.0 ± 0.4
J2218+1146	d/sdT6.5	NIRES	<12	<8	3.2 ± 0.4	<1.4
J2251−0740	d/sdT7	NIRES	<47	…[b]	<1.7	<1.8
Metal-poor Comparison Sources						
J0021+1552	d/sdT4	XS	<76	<6	<2.3	<1.9
J0532+8246	esdL8:	NIRES	10.1 ± 0.7	13.4 ± 0.7	7.0 ± 0.7	6.3 ± 0.4
J0616−6407	esdT0:	XS	7.3 ± 0.7	10.9 ± 0.8	7.8 ± 0.8	7.2 ± 0.4
J0645−6646	d/sdT0	XS	10.6 ± 0.6	12.2 ± 0.5	6.8 ± 0.5	8.3 ± 0.3
J0833+0052	d/sdT9	GNIRS	<54	<65	<8	<5
J1019-3911	T4	ARCoIRIS2	9.0 ± 1.1	6.3 ± 0.9	3.0 ± 0.4	<0.9
J1055+5443	Y0	NIRES	…[b]	…[b]	<4	<3
J1130−1158	sdT5.5	ARC	<57	<12	<3	<3
J1307+1510	T1	XS	<9	<10	8.1 ± 1.0	8.7 ± 1.0
J1316+0755	sdT6.5	GNIRS	<62	<11	<2.5	<2.5
J1553+6933	sdT4	NIRES	<5	<4	<4	<3
J1810−1010	esdT3:	TSpec	<5	<4	<3	<4

Notes.
[a] Final spectral type as discussed in Section 6.
[b] Affected by excess noise in local continuum.

parameters in the first 10% and last 50% of each chain differ by less than three times their combined variance. We also visually confirmed convergence, and examined each fit to ensure it provided an accurate reproduction of the data.

Table 7 lists the best-fit model parameters for each of the spectra in our sample, while Figures 6–9 display model fits for representative sources. We find excellent agreement with the LOWZ models for most of our spectra, with temperatures appropriate for their spectral classifications. In particular, we find good agreement between the metallicities inferred for our benchmark companions and the metallicities reported for their primaries (Figure 6). Nearly all of the sources with measured parallaxes also have inferred radii consistent with evolved brown dwarfs, with a few cases where radii are either too large

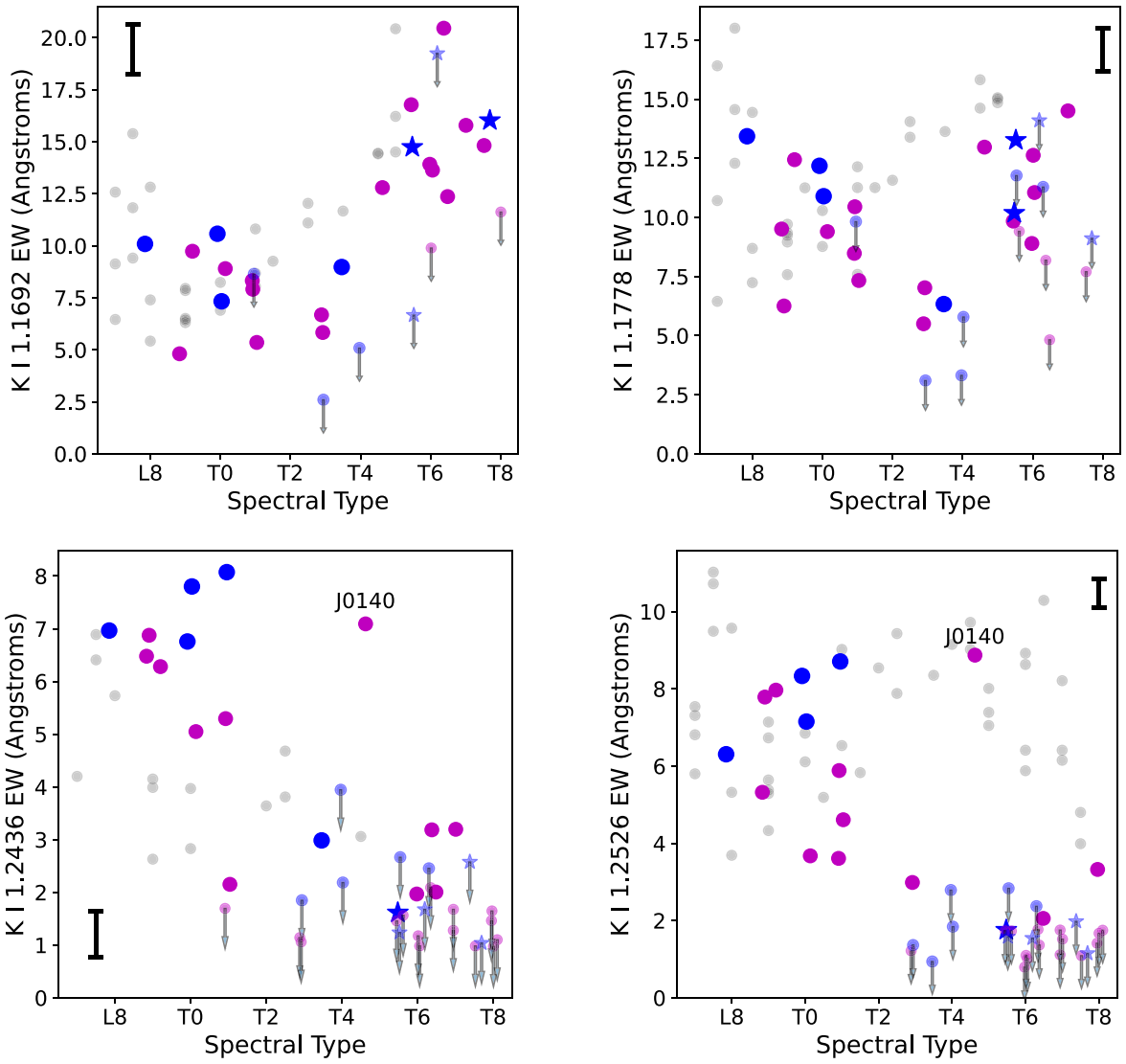

Figure 5. Equivalent width measurements of the 1.1692 μm (top left), 1.1178 μm (top right), 1.2436 μm (bottom left), and 1.2526 μm (bottom right) K I lines based on medium-resolution data in our spectral sample. Subdwarf candidates are indicated by magenta circles, metal-poor comparison sources by blue circles, and benchmark companions by blue stars. Smaller symbols with downward arrows indicate 3σ upper limits. A comparison sample of measurements for local L and T dwarfs with significant detections reported in E. C. Martin et al. (2017) are indicated as gray circles. The typical measurement uncertainties for sources with significant detections are indicated by the black error bar in the corners of each panel. Each source is given a small random offset in spectral type to help differentiate overlapping data points. The unusually red high-velocity T dwarf J0140+0150 is specifically labeled in the bottom two panels.

(e.g., J0055+5947) or too small (e.g., J1316+0755 and J1810−1010), likely reflecting inferred temperatures that are too low or too high, respectively. Fits to three sources (GJ 576B, J0414−5854, and J1316+0755) yield unusually small C/O ratios, which likely offset low temperatures since low C/O reduces the relative strength of CH_4 absorption. The poorest fits for the LOWZ models occur for the late-L and early-T dwarfs in our sample, a consequence of the $T_{\rm eff} = 1600$ K maximum for this model set.

For sources that hit the parameter limits for the LOWZ models or have better fits among the other seven model sets ($|\Delta\chi^2_r| > 5$), we also report in Table 7 the parameters inferred for the best fits among all models. For the highest-temperature sources, these are typically from the SAND models, which yield higher temperatures outside the LOWZ parameter range, and generally higher surface gravities and lower metallicities. An illustrative case is the extreme L subdwarf J0532+8246 (Figure 7) for which the SAND models provide an excellent fit to strong FeH absorption at 1 μm and the smooth near-infrared continuum, while inferring a radius ($R = 0.077^{+0.005}_{-0.003}$ $R_\odot$) in line with theoretical models. On the other hand, SAND model fits to other sources with parallax measurements (e.g., J1158+0435) yield radii too small to be physical, suggesting that the inferred temperatures are too high in these cases. SAND models also provide improved fits for some of the lower-temperature metal-poor sources, including Wolf 1130C for which the inferred metallicity ([M/H] $= -0.65^{+0.10}_{-0.07}$) is consistent with the metallicity of the system's M dwarf primary ([Fe/H] $= -0.70 \pm 0.12$; G. N. Mace et al. 2018); and the extreme T subdwarf J1810−1010 (Figure 8), for which the inferred temperature ($T_{\rm eff} = 869^{+5}_{-13}$ K) and radius ($0.081^{+0.005}_{-0.04}$ $R_\odot$) are consistent with luminosity-based estimates from N. Lodieu et al. (2022). The better agreement in near-infrared spectral morphology and inferred parameters for these sources suggests that the SAND models are well suited for

Table 6
Atmosphere Model Parameters

Model	$T_{\rm eff}$ (K)	$\log g$ (cm s^{-2})	[M/H] (dex)	C/O	$\log \kappa_{zz}$ (cm^2 s^{-1})	Other Parameters	References
LOWZ	500–1600	4.5–5.25	−2.5 to +1.0	0.10–0.85	−1 to +10		[1]
B06	700–2200	4.5–5.5	−0.5 to +0.5	⋯	⋯	Cloud model f100	[2]
Settl	500–2200	4.5–5.5	−0.5 to +0.5	⋯	⋯	$[\alpha/{\rm Fe}] = 0$ to +0.2	[3]
Dusty	1000–2200	4.5–5.5	−2.5 to +0.0	⋯	⋯	$[\alpha/{\rm Fe}] = 0$ to +0.6	[3]
ATMO[a]	600–2000	4.5–5.5	0.0	⋯	4–8, CE[b]	$\log_{10} P_{\rm min} = -8$–0; $\gamma = 1.0$–1.1	[4]
Sonora	500–2200	4.5–5.5	−0.5 to +0.5	0.22–0.83	⋯		[5]
ElfOwl	525–2200	4.5–5.5	−1.0 to +1.0	0.22–0.83	2–8		[6]
SAND	700–2200	4.5–6.0	−2.4 to +0.3	⋯	⋯	$[\alpha/{\rm Fe}] = 0$ to +0.4	[7]

Notes.
[a] ATMO models are further constrained to the K I broadening profile from N. F. Allard et al. (2016) and the condensate rainout prescription described by J. M. Goyal et al. (2019); see M. W. Phillips et al. (2020).
[b] Chemical Equilibrium (no mixing).
References– [1] A. M. Meisner et al. (2021); [2] A. Burrows et al. (2006); [3] F. Allard et al. (2012); [4] M. W. Phillips et al. (2020); [5] M. S. Marley et al. (2021); [6] S. Mukherjee et al. (2024); [7] E. Alvarado et al. (2024).

metal-poor L and T subdwarfs. Other low-temperature T dwarfs with solar/near-solar metallicities are better fit by the ElfOwl models, which have up-to-date opacities for key molecules such as CH_4 and thus better reproduce the strong absorption features present in late-type T dwarf spectra. Nevertheless, these fits yield similar atmosphere parameters as LOWZ ($|\Delta T_{\rm eff}| \lesssim 100$ K, $|\Delta \log g| \lesssim 0.5$, $|\Delta[{\rm M/H}]| \lesssim 0.2$).

Turning to our subdwarf candidates, several show evidence of modest subsolar metallicity ($-0.2 \gtrsim [{\rm M/H}] \gtrsim -0.5$) based on the model fits, with three sources—J0623+0715, J1524−2620, and J2112−0529—being the most metal-poor ([M/H] ≈ -0.7). Remarkably, the candidate J0140+0150 and the previously reported J1055+5443 (G. Robbins et al. 2023) are found to be significantly metal-rich ([M/H] $\gtrsim +0.4$) despite their selection as high-velocity objects. These sources are discussed in further detail in Section 5.

4.5. Radial Velocities

The moderate resolution of our Keck/NIRES data facilitates measurement of the radial velocities of our targets via the forest of H_2O, CH_4, and (for late-L and early-T dwarfs) CO molecular features that are marginally resolved in the data. Our approach is based on the forward-modeling technique using pre-telluric-corrected spectra, as described in A. J. Burgasser et al. (2015) and C.-C. Hsu et al. (2021). We performed separate fits in Y-band (1.11–1.16 μm), J-band (1.26–1.31 μm), H-band (1.52–1.59 μm), and K-band (2.03–2.23 μm) regions that encompass strong molecular features in both source and telluric spectra. We also conducted additional fits in the 1.235–1.285 μm, 1.95–2.40 μm, and 2.26–2.40 μm regions for our earliest-type sources, which encompass K I and CO absorption. Our spectral data model was defined as

$$D[\lambda] = (C[\lambda] \times M[\lambda'] \times T^{\alpha}[\lambda] + \delta_F) \otimes \kappa_G(v_{\rm broad}) \quad (8)$$

where $M[\lambda']$ is a high-resolution ($\lambda/\Delta\lambda = 50{,}000$) BT-Settl atmosphere model (F. Allard et al. 2012), with $\log g = 5.0$ (cgs) and $T_{\rm eff}$ based on the fitting values in Table 7. This model is evaluated at wavelengths $\lambda' = \lambda\left(1 + \frac{v_{\rm bary} + RV}{c}\right)$ where $v_{\rm bary}$ is the barycentric velocity correction for the source at the time of observation, RV is the heliocentric velocity constrained to be within ± 200 km s^{-1}, and c is the speed of light. $T[\lambda]$ is an empirical telluric absorption template from W. Livingston & L. Wallace (1991) scaled by an exponent α to account for varying airmass. $C[\lambda]$ is a fifth-order polynomial continuum correction to the ratio of smoothed versions of the data and the combination $M[\lambda'] \times T^{\alpha}[\lambda]$. δ_F is a constant flux offset. $\kappa_G(v_{\rm broad})$ is a Gaussian instrumental broadening profile of width $v_{\rm broad} = c\frac{\Delta\lambda_I}{\langle\lambda\rangle}$, where $\langle\lambda\rangle$ is the average wavelength over the fitting range, and $\Delta\lambda_I$ is a free parameter. As $v_{\rm broad}$ is typically of the order of 100 km s^{-1}, we ignore stellar rotational broadening in this analysis. We also fit for a constant wavelength offset $\delta_\lambda = \langle\lambda - \lambda_0\rangle$ between the wavelength grid of the data λ_0 and that of the data model to account for slight offsets (up to ± 50 Å) in the original wavelength calibration. These adjustments significantly improve our RV precisions and motivate our use of pre-telluric-corrected spectra (see C.-C. Hsu et al. 2021).

The data model is defined by five free parameters (RV, α, $\Delta\lambda_I$, δ_F, and δ_λ) and six continuum coefficients that are determined at each fitting step. We used a similar reduced χ^2 statistic as Equation (4) to assess the quality of the fit,

$$\chi^2_r = \frac{1}{DOF}\sum_i^N \frac{(O[\lambda_i] - D[\lambda_i])^2}{\sigma^2[\lambda_i]}. \quad (9)$$

where N is the number of unmasked data points and $DOF = N - 11$. Note that the scaling factor β in Equations (4) and (5) is incorporated into the continuum correction $C[\lambda]$. The five free parameters were first optimized using the Nelder-Mead algorithm (J. A. Nelder & R. Mead 1965; F. Gao & L. Han 2012) as implemented in the `scipy` optimize package (P. Virtanen et al. 2020). These parameters were then used to seed an MCMC model with a single chain of 5000 steps for each source and wavelength range, with verification of convergence using the J. Geweke (1992) diagnostic for the RV values and visual confirmation of the chain. We also examined each fit to ensure the presence of distinct spectral structure from both stellar and telluric absorption, and rejected those fits lacking sufficient structure or are in very low signal-to-noise regions.

Table 7
Spectral Model-fit Parameters

Name	SpT	Instrument	$T_{\rm eff}$ (K)	$\log g$ (cm s^{-2})	[M/H] (dex)	C/O	$\log k_{zz}$ (cm^2 s^{-1})	R ($R_\odot$)	MIN χ^2_r	Model
Metallicity Benchmarks										
HD 3651B	T8	SpeX	856^{+23}_{-20}	$4.56^{+0.17}_{-0.06}$	$0.01^{+0.12}_{-0.10}$	$0.48^{+0.11}_{-0.05}$	−1	$0.070^{+0.004}_{-0.004}$	21	LOWZ
…	…	…	834^{+20}_{-31}	$4.53^{+0.15}_{-0.03}$	$0.00^{+0.11}_{-0.05}$	$0.67^{+0.19}_{-0.04}$	4	$0.077^{+0.006}_{-0.004}$	15	ElfOwl
HD 65486B	d/sdT4.5	SpeX	993^{+44}_{-47}	$4.98^{+0.20}_{-0.24}$	$-0.53^{+0.13}_{-0.17}$	$0.38^{+0.15}_{-0.10}$	−1	$0.099^{+0.013}_{-0.010}$	5	LOWZ
LHS 6176B	d/sdT7.5	NIRES	846^{+19}_{-6}	$4.52^{+0.10}_{-0.01}$	$-0.21^{+0.05}_{-0.03}$	$0.49^{+0.04}_{-0.02}$	−1	$0.061^{+0.001}_{-0.004}$	15	LOWZ
Ross 458C	rT8.5	FIRE	790^{+63}_{-10}	$4.61^{+0.13}_{-0.04}$	$0.95^{+0.05}_{-0.08}$	$0.38^{+0.06}_{-0.00}$	−1	$0.080^{+0.000}_{-0.016}$	319	LOWZ
…	…	…	812^{+38}_{-28}	$4.61^{+0.18}_{-0.09}$	$0.78^{+0.09}_{-0.21}$	$1.11^{+0.08}_{-0.15}$	2	$0.075^{+0.005}_{-0.007}$	298	ElfOwl
HD 126053B	sdT7.5	GNIRS	654^{+52}_{-39}	$4.98^{+0.27}_{-0.36}$	$-0.35^{+0.11}_{-0.15}$	$0.56^{+0.16}_{-0.08}$	2	$0.076^{+0.016}_{-0.015}$	40	LOWZ
…	…	…	746^{+36}_{-28}	$4.23^{+0.40}_{-0.15}$	$-0.53^{+0.10}_{-0.04}$	$1.20^{+0.18}_{-0.15}$	2	$0.055^{+0.006}_{-0.007}$	33	ElfOwl
GJ 570D	T7.5	SpeX	837^{+20}_{-17}	$4.62^{+0.18}_{-0.08}$	$-0.11^{+0.07}_{-0.06}$	$0.54^{+0.16}_{-0.07}$	−1	$0.061^{+0.004}_{-0.003}$	10	LOWZ
GJ 576B	sdT5.5	GNIRS	912^{+20}_{-36}	$4.71^{+0.24}_{-0.12}$	$-0.47^{+0.09}_{-0.10}$	$0.37^{+0.07}_{-0.06}$	−1	$0.096^{+0.010}_{-0.006}$	6	LOWZ
…	…	XS	912^{+32}_{-16}	$4.74^{+0.33}_{-0.18}$	$-0.53^{+0.15}_{-0.11}$	$0.32^{+0.05}_{-0.05}$	−1	$0.098^{+0.005}_{-0.010}$	4	LOWZ
…	…	NIRES	966^{+5}_{-36}	$5.25^{+0.02}_{-0.06}$	$-0.24^{+0.06}_{-0.01}$	$0.39^{+0.02}_{-0.03}$	-1	$0.080^{+0.007}_{-0.002}$	62	LOWZ
…	…	…	995^{+19}_{-21}	$5.19^{+0.11}_{-0.22}$	$-0.21^{+0.04}_{-0.07}$	$0.86^{+0.05}_{-0.06}$	…	$0.078^{+0.004}_{-0.004}$	29	Sonora
G 204−39B	T6.5	SpeX	984^{+25}_{-16}	$4.76^{+0.16}_{-0.12}$	$0.43^{+0.15}_{-0.07}$	$0.46^{+0.08}_{-0.03}$	−1	$0.069^{+0.003}_{-0.005}$	26	LOWZ
Wolf 1130C	(e)sdT6:	Multiple	978^{+22}_{-44}	$5.03^{+0.22}_{-0.29}$	$-0.29^{+0.09}_{-0.22}$	$0.60^{+0.05}_{-0.08}$	10	$0.018^{+0.003}_{-0.003}$	97	LOWZ
…	…	…	700^{+15}_{-0}[a]	$5.57^{+0.21}_{-0.11}$	$-0.65^{+0.10}_{-0.07}$	$0.21^{+0.03}_{-0.04}$[b]	…	$0.056^{+0.002}_{-0.003}$	76	SAND
HN PegB	T2.5	SpeX	1284^{+42}_{-23}	$4.76^{+0.24}_{-0.14}$	$-0.11^{+0.23}_{-0.12}$	$0.32^{+0.08}_{-0.04}$	−1	$0.074^{+0.004}_{-0.005}$	90	LOWZ
Wolf 940B	T8.5	FIRE	636^{+32}_{-29}	$5.20^{+0.05}_{-0.28}$	$0.33^{+0.13}_{-0.07}$	$0.81^{+0.04}_{-0.12}$	10	$0.069^{+0.007}_{-0.010}$	6	LOWZ
Subdwarf Candidates										
J0045+7958	d/sdL9	TSpec	1600^{+0}_{-6}[a]	$4.73^{+0.12}_{-0.11}$	$0.79^{+0.10}_{-0.06}$	$0.64^{+0.01}_{-0.02}$	−1	…	6	LOWZ
…	…	…	1637^{+13}_{-14}	$5.47^{+0.03}_{-0.08}$	$-0.05^{+0.09}_{-0.08}$	$0.21^{+0.03}_{-0.06}$[b]	…	…	4	SAND
J0055+5947	d/sdT6.5	NIRES	641^{+82}_{-52}	$5.00^{+0.25}_{-0.32}$	$-0.11^{+0.31}_{-0.25}$	$0.73^{+0.11}_{-0.19}$	−1	$0.143^{+0.048}_{-0.045}$	30	LOWZ
…	…	…	738^{+35}_{-46}	$5.07^{+0.29}_{-0.39}$	$0.04^{+0.19}_{-0.20}$	$0.73^{+0.07}_{-0.12}$	4	$0.094^{+0.017}_{-0.011}$	18	ElfOwl
J0140+0150	rT4.5	SpeX	1149^{+33}_{-27}	$4.77^{+0.34}_{-0.21}$	$0.21^{+0.25}_{-0.22}$	$0.49^{+0.06}_{-0.07}$	−1	…	4	LOWZ
…	…	NIRES	1148^{+19}_{-35}	$5.06^{+0.11}_{-0.30}$	$0.40^{+0.11}_{-0.19}$	$0.48^{+0.04}_{-0.06}$	−1	…	9	LOWZ
J0411+4714	d/sdT7.5	NIRES	860^{+25}_{-21}	$4.63^{+0.19}_{-0.08}$	$-0.20^{+0.08}_{-0.06}$	$0.59^{+0.09}_{-0.06}$	−1	…	10	LOWZ
…	…	…	843^{+15}_{-21}	$4.54^{+0.10}_{-0.36}$	$-0.12^{+0.04}_{-0.05}$	$0.68^{+0.05}_{-0.07}$	4	…	4	ElfOwl
J0429+3201	T1	NIRES	1598^{+2}_{-23}[a]	$4.74^{+0.33}_{-0.16}$	$0.28^{+0.24}_{-0.19}$	$0.59^{+0.03}_{-0.07}$	-1	…	12	LOWZ
…	…	…	1648^{+74}_{-47}	$5.36^{+0.14}_{-0.31}$	$-0.08^{+0.08}_{-0.14}$	…	…	…	11	B06
J0433+1009	T8	NIRES	953^{+47}_{-39}	$4.80^{+0.27}_{-0.20}$	$0.12^{+0.22}_{-0.14}$	$0.60^{+0.09}_{-0.10}$	−1	…	4	LOWZ
J0623+0715	sdT3	NIRES	1277^{+31}_{-40}	$4.81^{+0.26}_{-0.19}$	$-0.68^{+0.12}_{-0.11}$	$0.49^{+0.06}_{-0.07}$	−1	…	6	LOWZ
J0659+1615	T1	NIRES	1600^{+0}_{-28}[a]	$5.20^{+0.05}_{-0.31}$	$0.03^{+0.11}_{-0.09}$	$0.48^{+0.07}_{-0.04}$	2	…	21	LOWZ
…	…	…	1536^{+25}_{-46}	$5.72^{+0.05}_{-0.05}$	$-0.03^{+0.10}_{-0.07}$	$0.08^{+0.02}_{-0.01}$[b]	…	…	6	SAND
J0758+5711	T6.5	NIRES	953^{+12}_{-20}	$4.66^{+0.23}_{-0.13}$	$-0.17^{+0.11}_{-0.09}$	$0.47^{+0.03}_{-0.04}$	−1	…	6	LOWZ
J0843+2904	L6:	SpeX	1600^{+0}_{-19}[a]	$4.69^{+0.25}_{-0.13}$	$0.79^{+0.09}_{-0.22}$	$0.66^{+0.04}_{-0.04}$	−1	…	12	LOWZ
…	…	…	1663^{+37}_{-22}	$5.47^{+0.05}_{-0.03}$	$0.01^{+0.11}_{-0.09}$	$0.08^{+0.01}_{-0.02}$[b]	…	…	2	SAND
J0845−3305	d/sdT6.5	FIRE	933^{+4}_{-24}	$4.51^{+0.17}_{-0.00}$	$-0.23^{+0.03}_{-0.05}$	$0.43^{+0.01}_{-0.03}$	−1	…	173	LOWZ
…	…	…	952^{+3}_{-18}	$4.50^{+0.10}_{-0.01}$	$-0.35^{+0.08}_{-0.01}$	$0.53^{+0.04}_{-0.01}$	2	…	121	ElfOwl
J0911+2146	d/sdT8	FIRE	746^{+71}_{-93}	$4.70^{+0.31}_{-0.16}$	$-0.18^{+0.38}_{-0.20}$	$0.67^{+0.13}_{-0.22}$	−1	…	68	LOWZ
…	…	…	750^{+29}_{-10}	$4.55^{+0.13}_{-0.05}$	$0.00^{+0.11}_{-0.08}$	$0.56^{+0.09}_{-0.03}$	4	…	34	ElfOwl
J1110−1747	rT8	NIRES	909^{+40}_{-26}	$4.74^{+0.32}_{-0.21}$	$0.20^{+0.16}_{-0.20}$	$0.67^{+0.12}_{-0.11}$	−1	…	26	LOWZ
J1130+3139	d/sdT5.5	NIRES	948^{+31}_{-36}	$5.20^{+0.05}_{-0.38}$	$-0.21^{+0.09}_{-0.10}$	$0.37^{+0.04}_{-0.05}$	−1	…	12	LOWZ
…	…	…	1033^{+20}_{-33}	$4.72^{+0.09}_{-0.12}$	$-0.17^{+0.09}_{-0.09}$	$0.53^{+0.06}_{-0.07}$	4	…	7	ElfOwl
J1138+7212	d/sdT7	GNIRS	854^{+34}_{-20}	$4.62^{+0.16}_{-0.10}$	$-0.37^{+0.07}_{-0.06}$	$0.54^{+0.11}_{-0.08}$	−1	$0.113^{+0.006}_{-0.011}$	9	LOWZ
…	…	…	900^{+13}_{-10}	$4.54^{+0.12}_{-0.04}$	$-0.36^{+0.07}_{-0.04}$	$1.05^{+0.11}_{-0.10}$	2	$0.102^{+0.002}_{-0.004}$	5	ElfOwl
J1204−2359	d/sdT7	NIRES	930^{+29}_{-32}	$4.73^{+0.31}_{-0.17}$	$-0.15^{+0.09}_{-0.11}$	$0.47^{+0.09}_{-0.06}$	−1	…	3	LOWZ
J1304+2819	d/sdL9:	NIRES	1600^{+0}_{-20}[a]	$4.63^{+0.17}_{-0.08}$	$0.89^{+0.08}_{-0.10}$	$0.63^{+0.01}_{-0.03}$	−1	…	33	LOWZ
…	…	…	1803^{+47}_{-99}	$5.57^{+0.07}_{-0.06}$	$0.20^{+0.06}_{-0.11}$	$0.06^{+0.02}_{-0.06}$[b]	…	…	8	SAND
J1308−0321	d/sdT8	NIRES	827^{+8}_{-33}	$4.55^{+0.15}_{-0.04}$	$-0.11^{+0.09}_{-0.04}$	$0.50^{+0.13}_{-0.01}$	−1	…	10	LOWZ
J1401+4325	d/sdT5.5	NIRES	896^{+34}_{-38}	$5.19^{+0.06}_{-0.19}$	$-0.13^{+0.12}_{-0.14}$	$0.39^{+0.07}_{-0.06}$	−1	…	4	LOWZ
J1458+1734	T8	NIRES	854^{+34}_{-21}	$4.61^{+0.26}_{-0.08}$	$0.06^{+0.16}_{-0.10}$	$0.72^{+0.09}_{-0.16}$	−1	…	8	LOWZ
…	…	…	790^{+20}_{-16}	$4.14^{+0.09}_{-0.09}$	$0.13^{+0.07}_{-0.05}$	$0.75^{+0.04}_{-0.06}$	4	…	3	ElfOwl
J1515−2157	d/sdT6	FIRE	832^{+40}_{-22}	$4.66^{+0.35}_{-0.16}$	$0.06^{+0.08}_{-0.13}$	$0.57^{+0.05}_{-0.06}$	10	…	62	LOWZ
…	…	…	952^{+43}_{-49}	$4.68^{+0.10}_{-0.08}$	$-0.08^{+0.07}_{-0.07}$	$0.87^{+0.10}_{-0.09}$	4	…	36	ElfOwl
J1524−2620	sdT0	NIRES	1600^{+0}_{-9}[a]	$4.81^{+0.37}_{-0.14}$	$-0.38^{+0.09}_{-0.09}$	$0.44^{+0.07}_{-0.08}$	−1	…	63	LOWZ
…	…	…	1565^{+26}_{-37}	$5.35^{+0.09}_{-0.09}$	$-0.69^{+0.09}_{-0.14}$	$0.20^{+0.04}_{-0.03}$[b]	…	…	9	SAND
J1710+4537	T6	NIRES	984^{+22}_{-29}	$5.17^{+0.08}_{-0.19}$	$0.02^{+0.09}_{-0.10}$	$0.45^{+0.04}_{-0.04}$	−1	…	3	LOWZ
J1801+4717	d/sdT5	NIRES	973^{+33}_{-47}	$5.13^{+0.12}_{-0.48}$	$-0.09^{+0.20}_{-0.14}$	$0.36^{+0.06}_{-0.06}$	−1	…	3	LOWZ
J2013−0326	d/sdT6	NIRES	956^{+37}_{-21}	$4.86^{+0.33}_{-0.26}$	$-0.21^{+0.12}_{-0.12}$	$0.42^{+0.05}_{-0.05}$	−1	…	3	LOWZ
J2021+1524	d/sdL9	NIRES	1600^{+0}_{-12}[a]	$4.66^{+0.25}_{-0.12}$	$0.14^{+0.17}_{-0.08}$	$0.46^{+0.06}_{-0.07}$	−1	…	61	LOWZ
…	…	…	1611^{+22}_{-20}	$5.59^{+0.05}_{-0.06}$	$-0.35^{+0.07}_{-0.06}$	$0.34^{+0.04}_{-0.01}$[b]	…	…	8	SAND
J2112−0529	sdT1	NIRES	1594^{+6}_{-59}[a]	$4.63^{+0.27}_{-0.09}$	$-0.92^{+0.17}_{-0.10}$	$0.15^{+0.10}_{-0.05}$	−1	…	27	LOWZ
…	…	…	1520^{+20}_{-17}	$5.63^{+0.05}_{-0.08}$	$-0.74^{+0.10}_{-0.03}$	$0.38^{+0.01}_{-0.01}$[b]	…	…	4	SAND

Table 7
(Continued)

Name	SpT	Instrument	$T_{\rm eff}$ (K)	$\log g$ (cm s^{-2})	[M/H] (dex)	C/O	$\log k_{zz}$ (cm^2 s^{-1})	R ($R_\odot$)	MIN χ^2_r	Model
J2112+3030	d/sdT2.5	NIRES	1325^{+38}_{-35}	$5.00^{+0.20}_{-0.26}$	$-0.43^{+0.12}_{-0.09}$	$0.40^{+0.04}_{-0.06}$	−1	⋯	6	LOWZ
J2218+1146	d/sdT6.5	NIRES	890^{+19}_{-27}	$5.22^{+0.03}_{-0.16}$	$-0.10^{+0.06}_{-0.11}$	$0.55^{+0.06}_{-0.06}$	−1	⋯	3	LOWZ
J2251−0740	d/sdT7	NIRES	930^{+36}_{-34}	$4.71^{+0.23}_{-0.16}$	$-0.00^{+0.09}_{-0.09}$	$0.48^{+0.11}_{-0.07}$	−1	⋯	5	LOWZ
Metal-poor Comparison Sources										
J0004−1336	d/sdT2:	SpeX	1567^{+33}_{-76}[a]	$4.63^{+0.24}_{-0.12}$	$-0.83^{+0.13}_{-0.08}$	$0.14^{+0.10}_{-0.04}$	−1	⋯	9	LOWZ
⋯	⋯	⋯	2011^{+111}_{-92}	$4.80^{+0.21}_{-0.17}$	$-0.56^{+0.15}_{-0.22}$	$0.20^{+0.10}_{-0.11}$[b]	⋯	⋯	7	SAND
J0004−2604	T3	SpeX	1325^{+23}_{-24}	$4.83^{+0.15}_{-0.10}$	$-0.40^{+0.05}_{-0.07}$	$0.36^{+0.05}_{-0.05}$	2	$0.087^{+0.003}_{-0.003}$	19	LOWZ
J0013+0634	sdT7.5	GNIRS	658^{+97}_{-34}	$4.91^{+0.19}_{-0.23}$	$0.00^{+0.15}_{-0.10}$	$0.23^{+0.16}_{-0.13}$	10	⋯	105	LOWZ
⋯	⋯	⋯	727^{+31}_{-30}	$5.03^{+0.09}_{-0.15}$	$-0.61^{+0.90}_{-0.88}$	$0.18^{+0.18}_{-0.13}$[b]	⋯	⋯	80	Settl
J0021+1552	d/sdT4	XS	1149^{+18}_{-20}	$4.88^{+0.33}_{-0.29}$	$-0.49^{+0.11}_{-0.08}$	$0.37^{+0.05}_{-0.04}$	−1	⋯	2	LOWZ
J0057+2013	d/sdL9	SpeX	1590^{+10}_{-45}[a]	$4.73^{+0.33}_{-0.17}$	$-0.24^{+0.19}_{-0.09}$	$0.49^{+0.10}_{-0.11}$	10	⋯	30	LOWZ
⋯	⋯	⋯	1859^{+62}_{-31}	$4.80^{+0.16}_{-0.16}$	$-0.15^{+0.21}_{-0.15}$	$0.10^{+0.04}_{-0.07}$[b]	⋯	⋯	14	Settl
J0301−2319	d/sdT1	SpeX	1550^{+38}_{-72}[a]	$4.79^{+0.40}_{-0.27}$	$-0.65^{+0.16}_{-0.07}$	$0.26^{+0.07}_{-0.10}$	−1	$0.056^{+0.006}_{-0.003}$	18	LOWZ
⋯	⋯	⋯	1488^{+77}_{-73}	$5.65^{+0.09}_{-0.11}$	$-0.44^{+0.09}_{-0.14}$	$0.18^{+0.11}_{-0.10}$[b]	⋯	$0.063^{+0.007}_{-0.008}$	12	SAND
J0309−5016	d/sdT7.5	FIRE	747^{+33}_{-28}	$4.61^{+0.21}_{-0.08}$	$-0.30^{+0.11}_{-0.07}$	$0.57^{+0.13}_{-0.10}$	2	$0.087^{+0.009}_{-0.009}$	48	LOWZ
⋯	⋯	⋯	795^{+55}_{-27}	$4.13^{+0.09}_{-0.09}$	$-0.36^{+0.08}_{-0.08}$	$0.70^{+0.07}_{-0.10}$	2	$0.077^{+0.008}_{-0.012}$	38	ElfOwl
J0348−5620	d/sdT4	FIRE	1195^{+9}_{-22}	$5.25^{+0.02}_{-0.01}$	$0.00^{+0.04}_{-0.03}$	$0.54^{+0.02}_{-0.05}$	2	⋯	15	LOWZ
J0414−5854	esdT6:	FIRE	699^{+66}_{-49}	$4.88^{+0.29}_{-0.25}$	$-1.34^{+0.17}_{-0.15}$	$0.21^{+0.13}_{-0.10}$	−1	⋯	4	LOWZ
J0532+8246	esdL8:	Multiple	1600^{+0}_{-35}[a]	$4.56^{+0.20}_{-0.05}$	$-1.56^{+0.17}_{-0.02}$	$0.11^{+0.13}_{-0.01}$	-1	$0.088^{+0.004}_{-0.001}$	57	LOWZ
⋯	⋯	⋯	1718^{+30}_{-38}	$5.05^{+0.11}_{-0.10}$	$-1.53^{+0.06}_{-0.03}$	$0.33^{+0.01}_{-0.01}$[b]	⋯	$0.077^{+0.005}_{-0.003}$	9	SAND
J0616−6407	esdT0:	XS	1598^{+2}_{-38}[a]	$4.58^{+0.18}_{-0.06}$	$-1.77^{+0.07}_{-0.05}$	$0.11^{+0.11}_{-0.01}$	2	$0.106^{+0.005}_{-0.003}$	21	LOWZ
⋯	⋯	⋯	2181^{+14}_{-26}	$5.20^{+0.20}_{-0.15}$	$-1.13^{+0.08}_{-0.07}$	$0.07^{+0.05}_{-0.06}$[b]	⋯	$0.056^{+0.003}_{-0.003}$	6	Dusty
J0645−6646	d/sdT0	XS	1595^{+5}_{-22}[a]	$4.54^{+0.23}_{-0.02}$	$-0.63^{+0.16}_{-0.02}$	$0.33^{+0.04}_{-0.03}$	−1	$0.033^{+0.003}_{-0.003}$	73	LOWZ
⋯	⋯	⋯	1594^{+25}_{-20}	$5.49^{+0.04}_{-0.05}$	$-0.46^{+0.07}_{-0.05}$	$0.29^{+0.02}_{-0.04}$[b]	⋯	$0.063^{+0.001}_{-0.003}$	65	SAND
J0833+0052	d/sdT9	GNIRS	528^{+129}_{-28}	$5.03^{+0.22}_{-0.34}$	$-0.08^{+0.15}_{-0.16}$	$0.42^{+0.24}_{-0.16}$	2	$0.050^{+0.010}_{-0.025}$	13	LOWZ
J0850−0221	d/sdL6	SpeX	1600^{+0}_{-19}[a]	$4.57^{+0.45}_{-0.07}$	$-0.24^{+0.08}_{-0.07}$	$0.64^{+0.00}_{-0.13}$	10	$0.131^{+0.003}_{-0.003}$	175	LOWZ
⋯	⋯	⋯	1852^{+48}_{-81}	$5.53^{+0.11}_{-0.09}$	$0.17^{+0.08}_{-0.27}$	$0.05^{+0.02}_{-0.06}$[b]	⋯	$0.099^{+0.008}_{-0.007}$	46	SAND
J0937+2931	sdT6	SpeX	859^{+28}_{-15}	$4.70^{+0.14}_{-0.11}$	$-0.59^{+0.06}_{-0.07}$	$0.49^{+0.04}_{-0.06}$	−1	$0.088^{+0.004}_{-0.007}$	33	LOWZ
J0939−2448	d/sdT8	SpeX	682^{+51}_{-40}	$4.75^{+0.32}_{-0.16}$	$-0.35^{+0.12}_{-0.09}$	$0.73^{+0.10}_{-0.17}$	−1	$0.080^{+0.015}_{-0.016}$	6	LOWZ
J0953−0943	d/sdT6	SpeX	881^{+48}_{-62}	$4.81^{+0.36}_{-0.21}$	$-0.43^{+0.16}_{-0.13}$	$0.52^{+0.21}_{-0.15}$	−1	⋯	7	LOWZ
J1019−3911	T4	ARC	1200^{+2}_{-19}	$5.25^{+0.00}_{-0.00}$	$0.00^{+0.06}_{-0.00}$	$0.55^{+0.01}_{-0.05}$	−1	⋯	58	LOWZ
J1035−0711	d/sdL9	SpeX	1600^{+0}_{-34}[a]	$4.65^{+0.29}_{-0.10}$	$-0.35^{+0.10}_{-0.05}$	$0.37^{+0.05}_{-0.08}$	10	⋯	29	LOWZ
⋯	⋯	⋯	1695^{+3}_{-28}	$5.59^{+0.02}_{-0.07}$	$0.01^{+0.04}_{-0.16}$	$0.17^{+0.06}_{-0.01}$[b]	⋯	⋯	10	SAND
J1055+5443	Y0	NIRES	670^{+105}_{-79}	$4.77^{+0.29}_{-0.19}$	$0.70^{+0.21}_{-0.17}$	$0.34^{+0.29}_{-0.15}$	2	$0.021^{+0.008}_{-0.006}$	8	LOWZ
J1130−1158	sdT5.5	ARC	918^{+31}_{-33}	$4.86^{+0.26}_{-0.24}$	$-0.56^{+0.15}_{-0.13}$	$0.44^{+0.09}_{-0.07}$	−1	⋯	25	LOWZ
J1158+0435	d/sdL8	SpeX	1600^{+0}_{-33}[a]	$4.66^{+0.27}_{-0.13}$	$-0.56^{+0.17}_{-0.08}$	$0.25^{+0.08}_{-0.08}$	−1	$0.085^{+0.003}_{-0.003}$	112	LOWZ
⋯	⋯	⋯	1870^{+40}_{-64}	$5.50^{+0.09}_{-0.04}$	$-0.19^{+0.08}_{-0.02}$	$0.09^{+0.01}_{-0.02}$[b]	⋯	$0.062^{+0.004}_{-0.002}$	30	SAND
J1307+1510	T1	XS	1549^{+51}_{-76}[a]	$4.79^{+0.31}_{-0.18}$	$-0.14^{+0.27}_{-0.23}$	$0.39^{+0.08}_{-0.09}$	2	⋯	3	LOWZ
⋯	⋯	⋯	1633^{+14}_{-53}	$5.45^{+0.12}_{-0.08}$	$-0.42^{+0.05}_{-0.07}$	$0.35^{+0.03}_{-0.03}$[b]	⋯	⋯	1	SAND
J1316+0755	sdT6.5	GNIRS	765^{+55}_{-50}	$4.69^{+0.29}_{-0.14}$	$-0.65^{+0.11}_{-0.09}$	$0.29^{+0.11}_{-0.11}$	−1	⋯	24	LOWZ
J1338−0229	sdL9	FIRE	1592^{+8}_{-39}[a]	$4.60^{+0.18}_{-0.07}$	$-0.71^{+0.06}_{-0.05}$	$0.25^{+0.05}_{-0.07}$	−1	⋯	2	LOWZ
⋯	⋯	⋯	1639^{+26}_{-26}	$5.51^{+0.07}_{-0.10}$	$-0.50^{+0.10}_{-0.08}$	$0.22^{+0.06}_{-0.04}$[b]	⋯	⋯	1	SAND
J1416+1348B	sdT7	SpeX	635^{+68}_{-42}	$4.62^{+0.29}_{-0.10}$	$-0.67^{+0.14}_{-0.09}$	$0.38^{+0.20}_{-0.11}$	−1	$0.102^{+0.026}_{-0.029}$	11	LOWZ
J1553+6933	sdT4	NIRES	1225^{+70}_{-75}	$4.78^{+0.35}_{-0.20}$	$-0.96^{+0.21}_{-0.26}$	$0.42^{+0.13}_{-0.17}$	−1	⋯	2	LOWZ
J1810−1010	esdT3:	Multiple	1300^{+116}_{-99}	$5.00^{+0.23}_{-0.31}$	$-0.91^{+0.34}_{-0.27}$	$0.34^{+0.32}_{-0.20}$	-1	$0.020^{+0.004}_{-0.003}$	32	LOWZ
⋯	⋯	⋯	869^{+5}_{-13}	$5.87^{+0.08}_{-0.11}$	$-1.27^{+0.01}_{-0.04}$	$0.34^{+0.01}_{-0.01}$[b]	⋯	$0.081^{+0.005}_{-0.004}$	9	SAND
J2105−6235	d/sdT2:	Flamingos	1282^{+22}_{-14}	$4.72^{+0.23}_{-0.15}$	$-0.32^{+0.18}_{-0.09}$	$0.66^{+0.05}_{-0.05}$	10	⋯	65	LOWZ

Notes. Model parameters are listed for best-fit LOWZ models by default (A. M. Meisner et al. 2021), Sources that reached the LOWZ $T_{\rm eff}$ parameter limit or had a significantly better fits ($|\Delta\chi^2_r| > 5$) to an alternate model are also listed with the alternative model parameters. Model names are given in shorthand notation as B06 (A. Burrows et al. 2006, assuming cloud model f100), Settl and Dusty (F. Allard et al. 2012), ATMO (M. W. Phillips et al. 2020), Sonora (M. S. Marley et al. 2021), ElfOwl (S. Mukherjee et al. 2024), or SAND (E. Alvarado et al. 2024). Instrument names are given in shorthand notation as ARC = SOAR/ARCoIRIS, TSpec = APO/TripleSpec or Palomar/TripleSpec, and XS = VLT/X-Shooter. Multiple instruments contribute to spectra used for Wolf 1130C (Keck/NIRSPEC and Keck/MOSFIRE), J0532+8246 (Keck/LRIS and Keck/NIRES), and J1810−1010 (GTC/OSIRIS, GTC/EMIR, and Palomar/TripleSpec)

[a] Reaches $T_{\rm eff}$ parameter limit for given model set.

[b] Alpha element enrichment [α/Fe] relative to the Sun for Settl and Dusty models.

Figure 10 illustrates fits for GJ 576B, demonstrating how the combination of telluric and stellar absorption are well reproduced by the forward model. For our highest signal-to-noise data, these fits provide robust constraints on RV ($\sigma_{RV} \approx 5\,{\rm km\,s^{-1}}$, equivalent to roughly 0.2 pixels at native resolution) and consistency between the four fit regions. For lower signal-to-noise data, RV errors increase to tens of kilometers per second. Variations in the RV fit value across the spectral regions are generally consistent with the measurement uncertainties.

Table 8 summarizes the individual fit RVs, with median values and uncertainties computed as weighted 16%, 50%, and

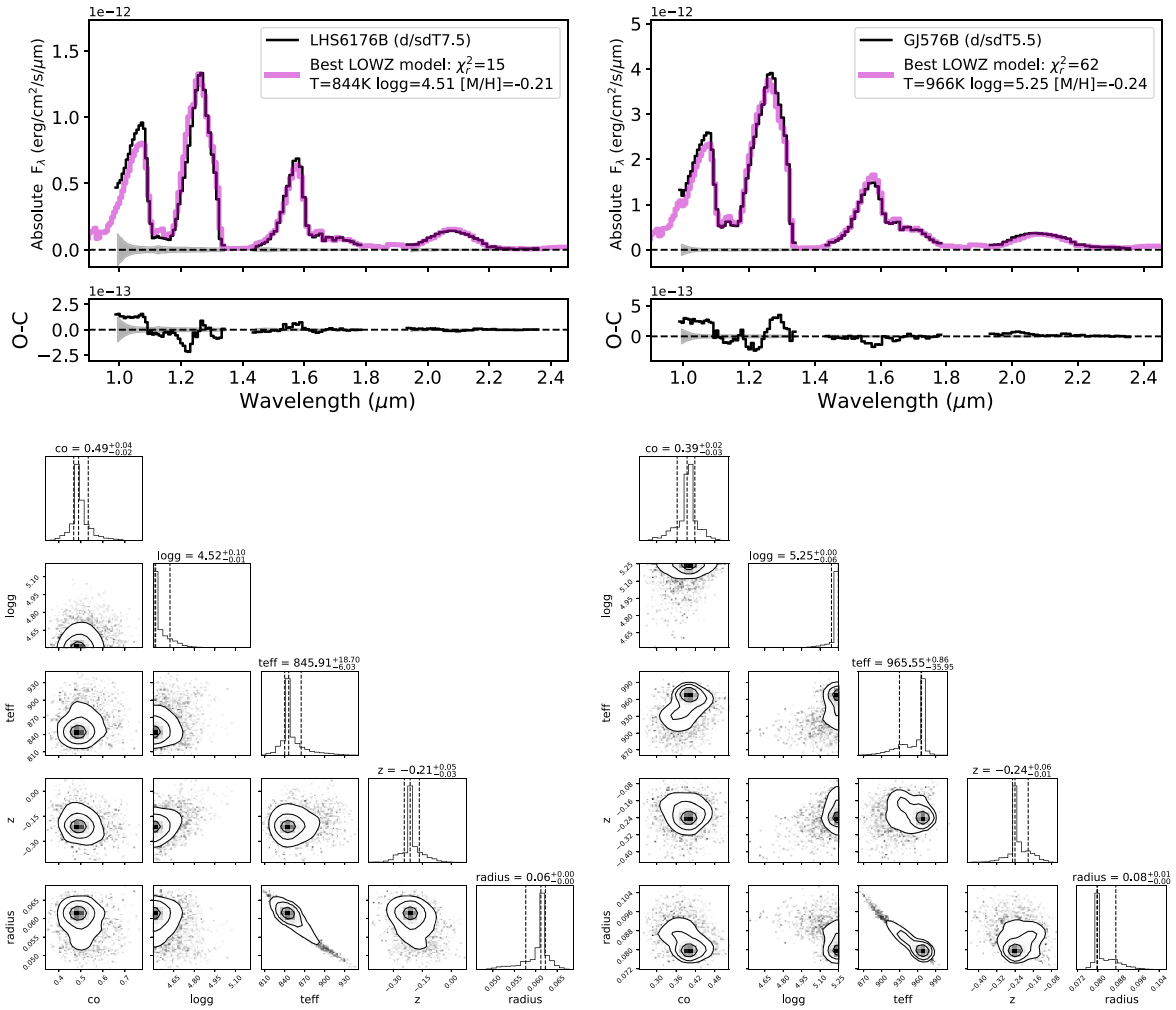

Figure 6. Best-fit LOWZ models and model parameter distributions for Keck/NIRES data for the metallicity benchmarks LHS 6176B (left) and GJ 576B (right). The top panels compare the observed spectra in absolute flux density (black lines) to the best-fit model (magenta line). The bottom panels show parameter distributions for $T_{\rm eff}$, $\log g$, [M/H], C/O, and radius. Plots along the diagonal axis show the marginalized posterior distributions for each parameter, with 16%, 50%, and 84% quantiles indicated as vertical dashed lines (see Table 7). The remaining contour plots display 2D distributions of parameter pairs in the posterior solutions, highlighting parameter correlations. Note that parameter distributions are weighted by their χ^2 value following Equation 10.

84% quantiles, using the weighting factor

$$w_i = \frac{DOF}{DOF + \chi^2_i - \mathrm{MIN}(\chi^2)}. \quad (10)$$

For sources with at least two viable RV measurements, we computed a weighted mean RV and uncertainty by adopting the larger of the lower and upper RV error estimates, σ_{RV}, as a weighting factor:

$$\langle RV \rangle = \frac{\sum_i^M RV_i/\sigma^2_{RV,i}}{\sum_i^M 1/\sigma^2_{RV,i}} \quad (11)$$

$$\sigma^2_{\langle RV \rangle} = \frac{1 + \sum_i^M (RV_i - \langle RV \rangle)^2/\sigma^2_{RV,i}}{\sum_i^M 1/\sigma^2_{RV,i}}. \quad (12)$$

The sums are over the $M = 2$–4 combined measurements, and the form of Equation (12) accounts for the size of the individual measurement uncertainties. The final RVs are reported in Table 8.

For two of the three sources with previously published RVs, LHS 6176B (from its primary) and J0532+82346, we find excellent agreement with our Keck/NIRES RV measurements. For GJ 576B, we measure a precise RV $= -25 \pm 4$ km s^{-1} that is nevertheless highly discrepant with its primary RV of -84.79 ± 0.12 km s^{-1} (J. L. Halbwachs et al. 2018). As the latter value is validated by Gaia DR3 measurements (-83.9 ± 0.2 km s^{-1}; Gaia Collaboration et al. 2021), this deviation cannot be explained by unresolved multiplicity in the primary, and is too large of a magnitude to be explained by unresolved multiplicity of the brown dwarf companion.[26] Instead, this discrepancy is likely due to an observational bias. Both LHS 6176B and J0429+3201 were observed in conditions of excellent seeing ($\lesssim$0.″4), smaller than the fixed slit width of NIRES. A slight offset of the source from the slit center by a single pixel (0.″15, approximately one-third of a resolution element or $\sim$40 km s^{-1}) would shift the dispersed spectrum by an amount sufficient to explain this discrepancy. Unfortunately, this systematic bias is uncorrectable with the present data. We therefore exclude the RV of this source and that of J0429+3201 from our analysis.

[26] The shortest-period very-low-mass binary currently known, LP 413-53AB with $P = 17$ hr, has an RV semiamplitude of 24 km s^{-1} (C.-C. Hsu et al. 2023).

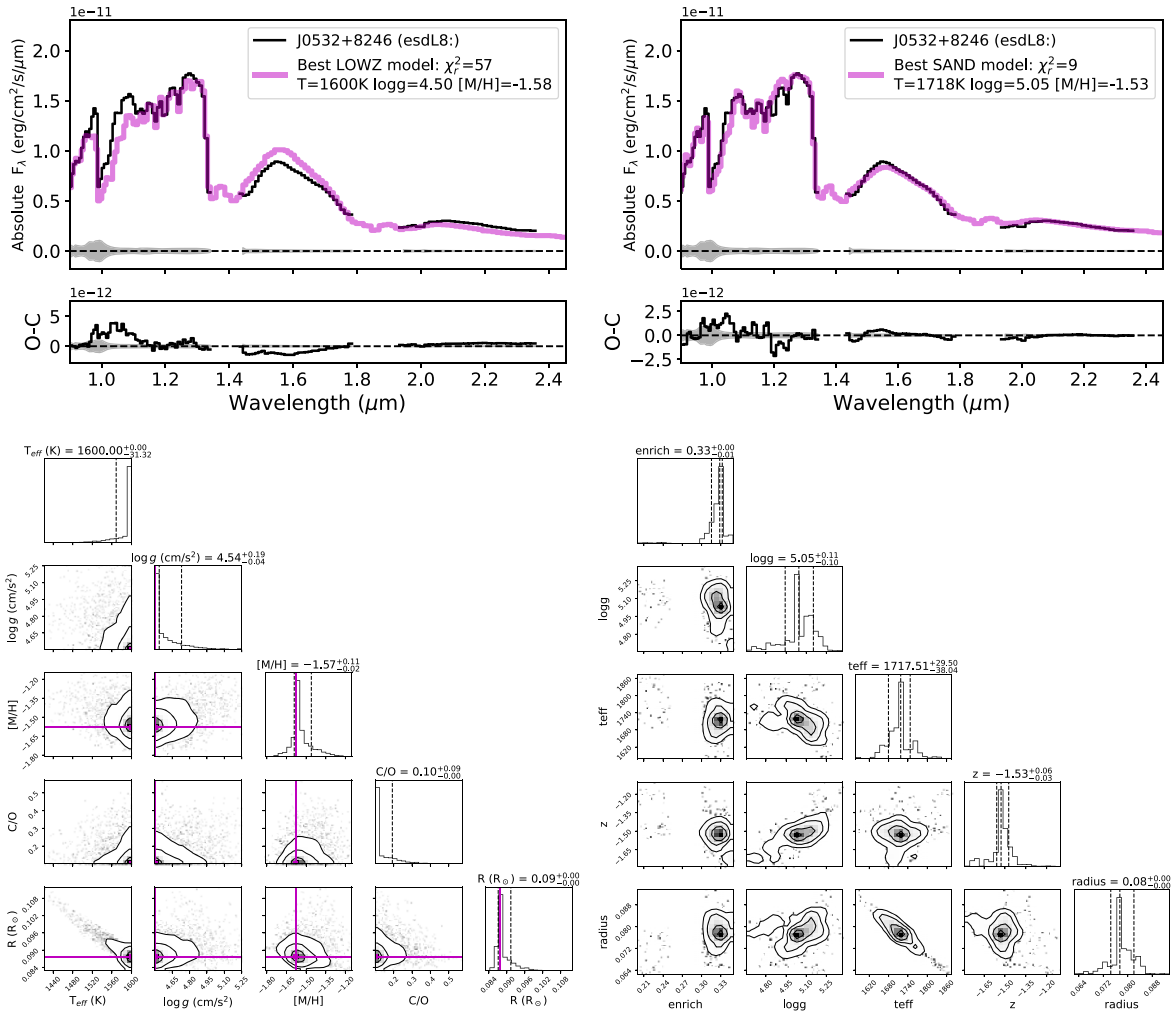

Figure 7. Same as Figure 6 comparing LOWZ (left) and SAND (right) model fits for J0532+8246. The former converges to the $T_{\rm eff}$ upper limit of the LOWZ grid, while the latter provides a significantly better fit at a higher $T_{\rm eff}$, higher surface gravity, and comparable metallicity.

Using the measured proper motions and radial velocities, and parallax or estimated distances, we computed Galactic U, V, W velocities in the local standard of rest (LSR) assuming an LSR solar velocity of (11.10, 12.24, 7.25) km s^{-1} (R. Schönrich et al. 2010). Uncertainties were propagated by the Monte Carlo method assuming normal distributions. These values are listed in Table 9 and plotted in Figure 11 along with the local late-L and -T dwarf kinematic sample of C.-C. Hsu et al. (2021). As expected for our kinematic selection, this sample is more widely dispersed than the local dwarf population, with dispersions of σ_U = 63 km s^{-1}, σ_V = 60 km s^{-1}, and σ_W = 48 km s^{-1}, and a mean azimuthal drift velocity of $\langle V\rangle$ = −17 km s^{-1}. Two candidates, J1130+3139 and J2112+3030, stand out for their large negative V velocities, with J1130 +3139 showing retrograde motion with respect to the Galactic rest frame. The candidates J1204−2359, J2112+3030, and J2251−0740 show large vertical velocities with $|W|$ > 75 km s^{-1}. Our RV measurement and estimated distance of the T subdwarf J1553+6933 places this source in a particularly unusual position in *UVW* velocity space, with a total LSR speed of ≈330 km s^{-1}, comparable to J0532+8246 but with distinct *UVW* component velocities. Overall, we find that the majority of our targets lie outside the 1σ velocity sphere for thin disk sources defined by B. Anguiano et al. (2020).

From the *UVW* velocities, we computed the kinematic probabilities of membership in the Galactic thin disk ($p_{\rm thin}$), thick disk ($p_{\rm thick}$), and halo ($p_{\rm halo}$) following T. Bensby et al. (2003), assuming $p_{\rm thin} + p_{\rm thick} + p_{\rm halo} = 1$. A high probability of thin disk membership does not rule out thick disk or halo membership (see J1810−1010), while a high probability of thick disk or halo membership likely rules out thin disk membership. Three sources in our sample, the previously identified subdwarfs J0532+8246 and J1553+6933, and the subdwarf candidate J1130+3139, all have high probabilities of halo membership (>90%) due to their extreme LSR velocities; while eight of our subdwarf candidates have thick disk probabilities exceeding 90%.

5. Assessment of T Subdwarf Candidates

5.1. New T Subdwarfs

With a thorough assessment of the spectral and kinematic properties of our candidate T subdwarfs, we qualitatively evaluated their likelihood of being a metal-poor brown dwarf by considering four criteria: (1) the degree of deviation of the near-infrared spectrum from the dwarf standards, (2) the presence and strength of 1.25 μm K I absorption compared to solar-metallicity field dwarfs for sources with medium-

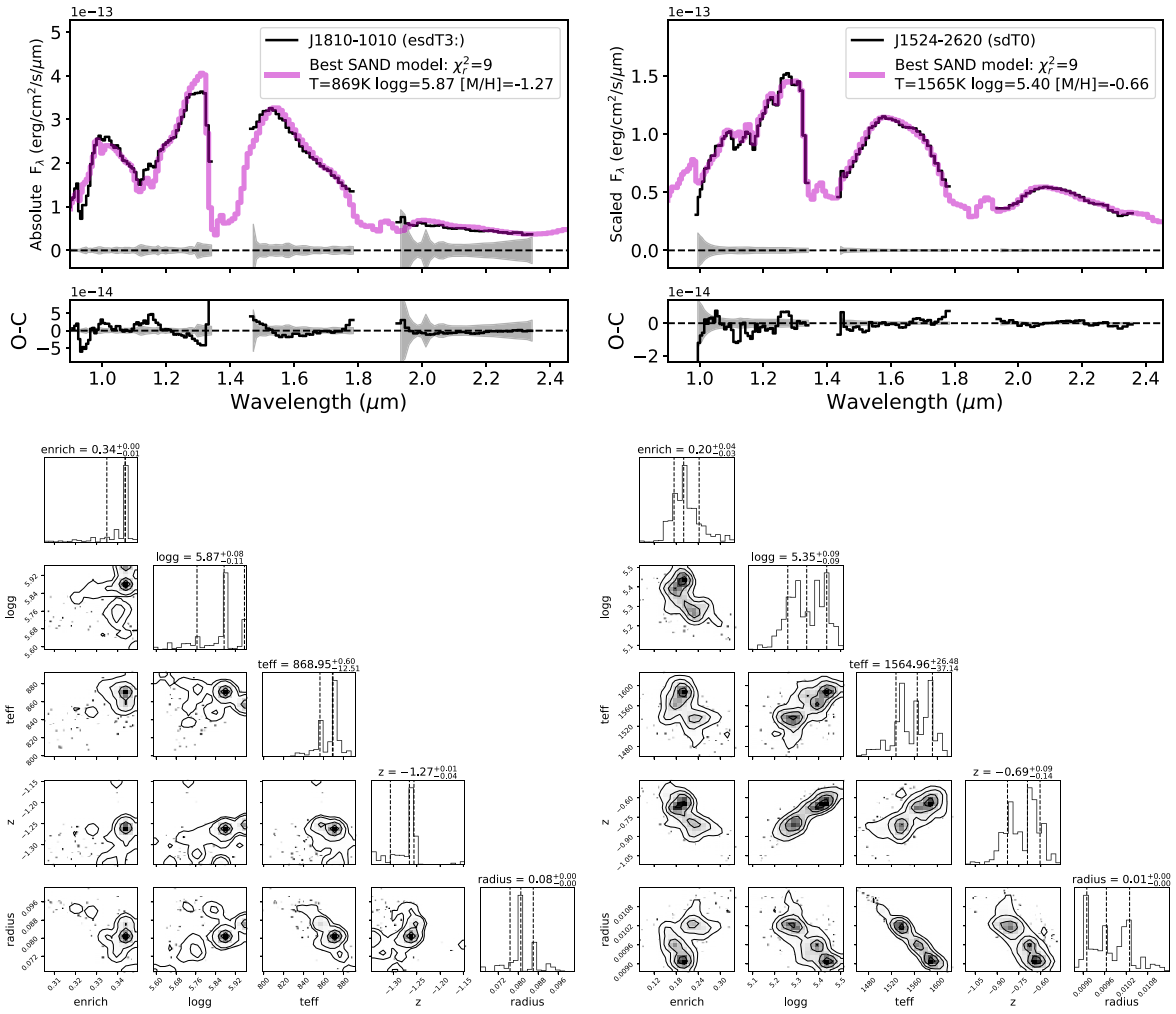

Figure 8. Same as Figure 6, showing best-fit SAND model and parameter distributions for the extreme T subdwarf J1810−0010 (left) and the T subdwarf candidate J1524−2620 (right).

resolution data and spectral types $\leqslant$T7, (3) the metallicity inferred from model fitting, and (4) *UVW* kinematics and the probability of thick disk or halo membership for sources with RV measurements. We treated these criteria in a holistic manner, noting that some criteria vary across spectral type (e.g., metallicity deviations are more pronounced among cloudy late-L and early-T dwarfs) and some may not clarify subdwarf status (e.g., thin disk kinematics does not rule out halo membership). We identified three broad categories for our candidates: likely subdwarfs (sd and esd), "mild" subdwarfs (d/sd), and not subdwarfs. Table 10 summarizes our assessments for both candidates and metal-poor comparison sources.

From our candidate sample, we identify J0623+0715, J1524−2620, and J2112−0529 as high-probability early-type T subdwarfs, as all three exhibit strong deviations from dwarf templates, [M/H] $\lesssim -0.7$ from model fits, and thick disk kinematics. J0623+0715 also lacks detectable K I absorption, while J1524−2620 and J2112−0529 have weak K I absorption compared to dwarf L/T transition objects. We identify a further 19 candidates as mild subdwarfs, predominantly late-type T dwarfs with *K*-band suppression, modestly subsolar metallicities ([M/H] ≈ -0.3) from model fits, and a mixture of population assignments. The remaining nine candidates appear to be normal late-L and -T dwarfs, although a few of these sources warrant further scrutiny as discussed below.

We also assessed the subdwarf status of our comparison sample following the same rubric. While the majority are found to be true subdwarfs, several sources appear to be normal T dwarfs. We reclassify J0004−2604 and J1019−3911, classified sdT2 and sdT3 by J. J. Greco et al. (2019), as T3 and T4 dwarfs based on their excellent agreement with the dwarf standards. We find J1307+1510, classified sdL8 by Z. H. Zhang et al. (2018b), to be well matched to the T1 dwarf standard with strong K I absorption. We also confirm the analysis of G. Robbins et al. (2023) that J1055+5443 is not an sdT8, as photometrically estimated by J. D. Kirkpatrick et al. (2021b), but rather a nearby (6.9 $\pm$ 0.7 pc) Y0 dwarf with unusual colors. Indeed, our spectral model fits suggests this source is highly metal-rich: [M/H] $= +0.70^{+0.21}_{-0.17}$ from LOWZ model fits and [M/H] $= +0.78^{+0.19}_{-0.28}$ from equivalently matching ElfOwl model fits. However, both fits predict small radii ($\sim$0.02 $R_\odot$) that are not physical, indicating an overestimated temperature and a likely unreliable metallicity. Our inferred radial velocity of 39 $\pm$ 22 km s^{-1} for this source has insufficient precision to confirm or rule out membership in the $\sim$180 Myr Crius 197

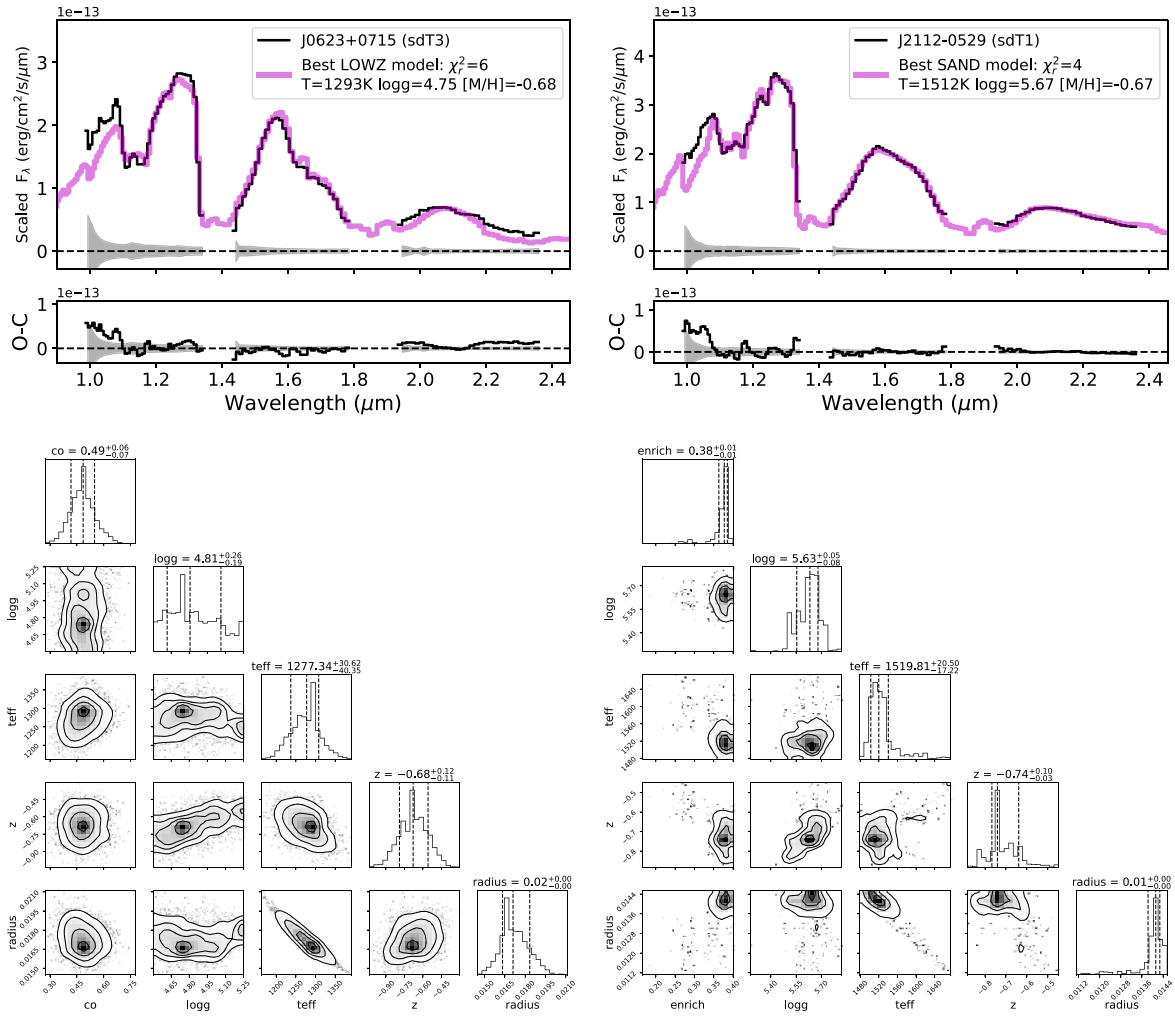

Figure 9. Same as Figure 6, showing best-fit models to the spectra of the T subdwarf candidates J0623+0715 (left, compared to LOWZ models) and J2112−0529 (right, compared to SAND models).

association (L. Moranta et al. 2022), as proposed by G. Robbins et al. (2023).

5.2. The Remarkable Galactic Orbits of J1130+3139 and J1553+6933

Our *UVW* analysis identified three sources that stand out in their Galactic motion. The L subdwarf J0532+8246 has previously been recognized as an object on a retrograde Galactic orbit (A. J. Burgasser et al. 2008b). The subdwarf candidate J1130+3139 was found to have similar *UV* component velocities that place it on a nearly radial Galactic orbit. The orbits for both objects are illustrated in Figure 12, and were computed using the `galpy` package (J. Bovy 2015) assuming the MWPotential2014 potential, solar motion from R. Schönrich et al. (2010), a solar radius of 8 kpc, and a local circular velocity of 220 km s^{-1}. These Figures display 100 orbit realizations sampling uncertainties in distance, proper motion, and radial velocity, all of which dominate over possible model uncertainties for J1130+3139 (e.g., choice of Galactic potential). Both sources are currently near apogal, with J0532+8246 reaching an inner radius of 2.6 kpc and J1130+3139 reaching an inner radius of 0.4–1.8 kpc, well within the bulge. Both sources are also closely aligned in velocity space with the Thamnos streams identified by H. H. Koppelman et al. (2019), whose members span a broad range of metallicities that encompass those inferred from model fits for these two sources.

The other T subdwarf with unusual kinematics is J1553+6933, previously reported in A. M. Meisner et al. (2021). This source's *UVW* velocities are distinct from all of the other sources in our sample. Its large inferred Galactic radial (U) velocity places it on an orbit that reaches $R > 25$ kpc at apogal, with distribution tails extending as far as 200 kpc from the Galactic center. However, this source also has the most poorly measured RV in our sample, $+110 \pm 90$ km s^{-1}, due to the lack of clear spectral features across the near-infrared region and very low SNR. Nevertheless, with a $V_{\rm tan} > 300$ km s^{-1} (similar to J0532+8246), and a velocity that aligns it with the prograde Helmi streams (A. Helmi et al. 1999), this source warrants further kinematic study.

5.3. Metal-rich Thick-disk Sources

Three sources in our sample, J0140+0150, J1110−1747, and J1458+1734 show evidence of kinematic membership in the Galactic thick disk population but have spectra best fit by solar or supersolar metallicity models. J0140+0150, with 99% thick disk membership probability, is found to be the most metal-rich at [M/H] = $+0.40^{+0.11}_{-0.19}$, and has the strongest K I lines in the sample (see Table 5 and Figure 5). J1110−1747 is

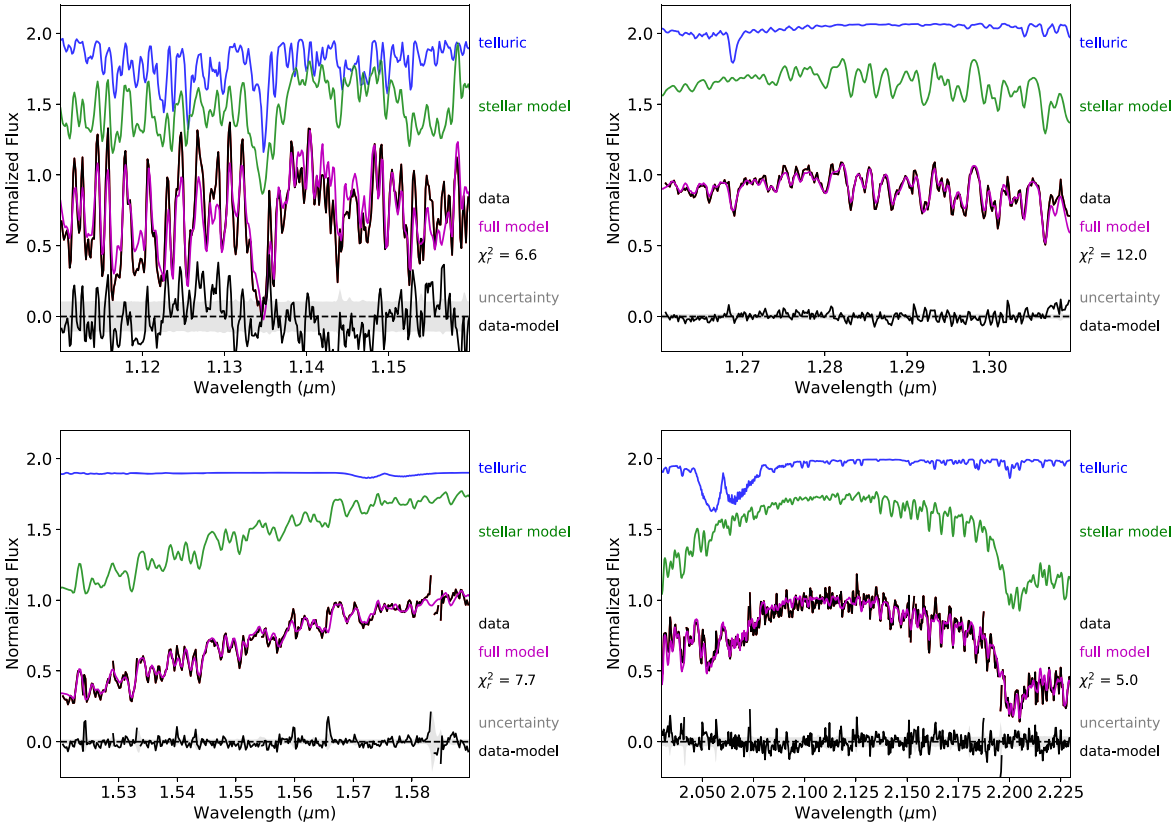

Figure 10. Forward model fits to $Y-$ (top left), $J-$ (top right), $H-$ (bottom left), and $K-$band (bottom right) spectra of GJ 576B. Each panel displays from top to bottom: the best-fit telluric model (blue), the best-fit stellar model (green), the observed data (black) compared to the full data model (magenta), and the difference of these (black) compared to the data uncertainty (gray band, $\pm1\sigma$). The reduced χ^2_r (Equation (9)) is listed along the right axis.

one of the few sources to show excess flux at the K band compared to its closest-match dwarf standard (Figure 3). The nature of these sources suggests that they may be members of the high-velocity thick disk, which have high LSR speeds ($v_{\rm tot} > 220\,{\rm km\,s^{-1}}$) and supersolar metallicities of up to [Fe/H] $\sim +0.5$ (Y. Yan et al. 2020; H. Zhu et al. 2021). A. Bonaca et al. (2017) demonstrated that these stars likely formed in the inner Milky Way and scattered outward through radial migration. Indeed, the Galactic orbit of J0140+0150 is modestly eccentric ($e = 0.45$), extending over a radius range of 4–11 kpc (Figure 12). All three sources have relatively large vertical velocities, $|W| > 50\,{\rm km\,s^{-1}}$, pushing them to maximum displacements of $\pm$1–2 kpc. While not formally part of the "high" velocity tail, these sources demonstrate that thick disk kinematics are not sufficient evidence for subsolar metallicity.

6. Establishing a T Dwarf Metallicity Classification System

6.1. Building a Temperature and Metallicity Grid

Our comprehensive spectral sample of solar- and subsolar-metallicity T dwarfs provides the opportunity to establish an empirical classification system for cold brown dwarfs that encapsulates both temperature and metallicity effects. We followed prior approaches to qualifying and quantifying metallicity effects in M dwarfs (e.g., J. E. Gizis 1997; S. Lépine et al. 2007; S. Zhang et al. 2019a) and L dwarfs (e.g., A. J. Burgasser et al. 2007a; Z. H. Zhang et al. 2017, 2018b; J. J. Greco et al. 2019). In particular, we aimed to define T subdwarf metallicity classes that roughly align with the metallicities of the existing M and L subdwarf classes.

J. E. Gizis (1997) originally proposed two metallicity classes for metal-poor M subdwarfs with [M/H] ≈ -1.2 for sdMs and [M/H] ≈ -2 for edMs. Subsequent expansion of this system into dM, sdM, esdM, and usdM classes by S. Lépine et al. (2007), and calibration of metallicity scales using companions of metal-poor FGK primaries and improved spectral models have refined these estimates. A recent analysis of over 1500 M dwarf and subdwarf optical spectra by N. Hejazi et al. (2020) with classifications on the S. Lépine et al. (2007) system yields median metallicities of [M/H] $= 0.15 \pm 0.27$ for dM, [M/H] $= -0.75 \pm 0.43$ for sdM, [M/H] $= -1.42 \pm 0.40$ for esdM, and [M/H] $= -1.88 \pm 0.18$ for usdM (see also V. M. Woolf et al. 2009; N. Lodieu et al. 2019). Z. H. Zhang et al. (2017) used model fits to optical and infrared spectra to argue for a similar metallicity scale for their defined L dwarf metallicity classes: [M/H] $\gtrsim -0.3$ for dL, $-1.0 \lesssim$ [M/H] $\lesssim -0.3$ for sdL, $-1.7 \lesssim$ [M/H] $\lesssim -1.0$ for esdL, and [M/H] $\lesssim -1.7$ for usdL sources. Given the range of metallicities inferred from our own model fits of the T dwarfs examined here, we restrict our metallicity grid to dT, sdT, and esdT classes, and introduce a mild subdwarf class d/sdT to identify sources with modest subsolar metallicities, which are nevertheless distinguishable from solar-metallicity dwarfs (see R. M. Catchpole et al. 1967; A. J. Burgasser et al. 2007a; B. P. Bowler et al. 2009).

We adopted a qualitative empirical approach to define temperature and metallicity subclasses, based on principles inherent to the W. W. Morgan et al. (1943) stellar classification system. Our system is defined by a grid of standard spectra covering a common wavelength range and resolution (see

Table 8
Radial Velocity Measurements (Keck/NIRES)

Name	*Y* RV (km s^{-1})	*Y* χ^2_r	*J* RV (km s^{-1})	*J* χ^2_r	*H* RV (km s^{-1})	*H* χ^2_r	*K* RV (km s^{-1})	*K* χ^2_r	Adopted RV (km s^{-1})	Prior RV (km s^{-1})	Ref
Metallicity Benchmarks											
LHS 6176B	⋯	⋯	10^{+4}_{-4}	4	-9^{+15}_{-13}	5	-2^{+11}_{-12}	2	8 ± 7	11.7 ± 2.1[c]	[1]
GJ 576B	-32^{+8}_{-10}	7	-23^{+5}_{-5}	12	-24^{+6}_{-5}	7	-25^{+9}_{-12}	5	(-25 ± 4)[d]	-84.79 ± 0.12	[2]
Subdwarf Candidates											
J0055+5947	⋯	⋯	38^{+20}_{-34}	1	30^{+45}_{-31}	1	27^{+60}_{-36}	4	34 ± 25	⋯	
J0140+0150	84^{+24}_{-23}	2	96^{+12}_{-11}	2	90^{+9}_{-9}	2	86^{+15}_{-13}	4	91 ± 7	⋯	
J0411+4714	⋯	⋯	37^{+5}_{-5}	137	17^{+12}_{-11}	175	40^{+14}_{-20}	118	34 ± 8	⋯	
J0429+3201	⋯	⋯	-117^{+29}_{-21}[a]	2	⋯	⋯	-63^{+9}_{-11}[b]	6	(-70 ± 21)[d]	⋯	
J0433+1009	⋯	⋯	21^{+8}_{-8}	2	15^{+18}_{-30}	2	21^{+20}_{-19}	2	21 ± 7	⋯	
J0623+0715	⋯	⋯	-14^{+28}_{-21}	2	18^{+34}_{-23}	2	-2^{+27}_{-24}[b]	3	-1 ± 27	⋯	
J0659+1615	-41^{+13}_{-13}	1	-46^{+51}_{-25}	2	-29^{+10}_{-12}	2	-38^{+12}_{-11}[c]	7	-36 ± 9	⋯	
J0758+5711	⋯	⋯	81^{+8}_{-7}	3	75^{+12}_{-13}	2	72^{+17}_{-19}	2	79 ± 7	⋯	
J1110−1747	⋯	⋯	-46^{+4}_{-4}	3	-55^{+9}_{-10}	5	-44^{+10}_{-9}	5	-47 ± 5	⋯	
J1130+3139	64^{+13}_{-11}	3	76^{+9}_{-9}	3	76^{+13}_{-10}	2	68^{+18}_{-17}	2	72 ± 8	⋯	
J1204−2359	⋯	⋯	-41^{+10}_{-10}	2	-76^{+25}_{-17}	3	-57^{+29}_{-20}	2	-47 ± 15	⋯	
J1304+2819	45^{+20}_{-37}	1	35^{+31}_{-21}	2	⋯	⋯	51^{+8}_{-8}[c]	6	50 ± 9	⋯	
J1308−0321	⋯	⋯	-40^{+4}_{-4}	3	-52^{+12}_{-12}	3	-51^{+11}_{-10}	2	-42 ± 6	⋯	
J1401+4325	⋯	⋯	-68^{+25}_{-21}	3	-79^{+38}_{-36}	2	⋯	⋯	-71 ± 21	⋯	
J1458+1734	⋯	⋯	19^{+6}_{-6}	4	16^{+12}_{-13}	3	24^{+14}_{-13}	4	19 ± 6	⋯	
J1524−2620	34^{+42}_{-26}	1	⋯	⋯	⋯	⋯	28^{+19}_{-17}	4	29 ± 17	⋯	
J1710+4537	-1^{+16}_{-15}	3	-2^{+9}_{-8}	2	-13^{+27}_{-23}	3	⋯	⋯	-3 ± 8	⋯	
J1801+4717	⋯	⋯	-27^{+21}_{-22}	2	-33^{+19}_{-26}	2	-22^{+91}_{-16}	4	-29 ± 17	⋯	
J2013−0326	⋯	⋯	-20^{+10}_{-11}	2	-22^{+26}_{-28}	2	23^{+33}_{-49}	3	-18 ± 13	⋯	
J2021+1524	11^{+22}_{-10}	1	⋯	⋯	10^{+15}_{-17}	2	-7^{+5}_{-5}[c]	5	-5 ± 7	⋯	
J2112−0529	-42^{+24}_{-19}	2	-24^{+46}_{-36}[a]	2	⋯	⋯	-37^{+10}_{-17}[b]	4	-37 ± 14	⋯	
J2112+3030	⋯	⋯	⋯	⋯	⋯	⋯	-125^{+62}_{-40}	4	-125 ± 62	⋯	
J2218+1146	-23^{+16}_{-23}	5	-22^{+8}_{-9}	3	-15^{+22}_{-47}	3	-43^{+52}_{-33}	2	-22 ± 9	⋯	
J2251−0740	⋯	⋯	-133^{+16}_{-17}	4	⋯	⋯	-197^{+49}_{-26}	3	-140 ± 25	⋯	
Comparison Sources											
J0532+8246	-155^{+42}_{-36}	99	-205^{+22}_{-35}[a]	56	⋯	⋯	-128^{+31}_{-21}[b]	42	-160 ± 39	-172 ± 1	[3]
J1055+5443	⋯	⋯	36^{+11}_{-13}	4	3^{+33}_{-27}	3	75^{+19}_{-27}	4	39 ± 22	⋯	
J1553+6933	⋯	⋯	⋯	⋯	⋯	⋯	110^{+46}_{-90}	5	110 ± 90	⋯	

Notes.
References– [1] M. Steinmetz et al. (2020); [2] J. L. Halbwachs et al. (2018); [3] A. Reiners & G. Basri (2006).
[a] Based on fits to alternative spectral range 1.235–1.280 μm.
[b] Based on fits to alternative spectral range 1.95–2.40 μm.
[c] Based on fits to alternative spectral range 2.26-2.40 μm.
[d] Due to unusually good seeing at the time of observation, offsets of tens of kilometers per second are possible; values should be treated with skepticism and are reported here only for completeness.

W. W. Morgan & P. C. Keenan 1973; J. D. Kirkpatrick 2005). We resampled our entire spectral sample onto a common wavelength scale spanning 1.0–2.4 μm at a fixed resolution $\lambda/\Delta\lambda = 300$, and normalized all data at the peak flux between 1.2 and 1.3 μm. At this resolution, we are primarily focused on the behavior of broad molecular absorption bands and overall spectral shape, rather than atomic lines. To anchor our system to the existing T dwarf classification system (A. J. Burgasser et al. 2006b), we used numerical subtypes that parallel the evolution of molecular features through the dwarf track, notably the 1.6 μm CH_4 and 1.15 μm H_2O+CH_4 absorption features, and the gradual narrowing of the 1.25 and 1.6 μm spectral peaks. Metallicity types were then segregated based on deviations associated with metallicity effects: unusually blue near-infrared spectral energy distributions driven by reduced cloud opacity in late-L and early-T dwarfs, and enhanced H_2 in later T dwarfs; a "muting" of H_2O and CH_4 bands beyond 1.3 μm as H_2 dominates near-infrared opacities; and a broadening of the 1.1 μm spectral trough, possibly driven by enhanced pressure-broadening of the 0.77 μm K I alkali line wings. Mild subdwarfs have spectra similar to their dwarf counterparts but with a slightly enhanced 1.05 μm peak and suppressed 2.1 μm peak. Extreme subdwarfs have highly distinct spectra from their closest dwarf counterpart, which were assigned by matching the depth of the 1.1 μm trough.

Table 9
Sample Kinematics

Name	d[a] (pc)	μ_α (mas yr^{-1})	μ_δ (mas yr^{-1})	V_{tan} (km s^{-1})	RV (km s^{-1})	U (km s^{-1})	V (km s^{-1})	W (km s^{-1})	Probabilities			Ref
									Thin	Thick	Halo	
Metallicity Benchmarks												
HD 3651B[b]	11.108 ± 0.006	−461.95 ± 0.07	−369.62 ± 0.03	31.150 ± 0.017	−32.898 ± 0.005	51.149 ± 0.015	−7.205 ± 0.004	15.664 ± 0.008	99%	1%	0%	[1],[2]
HD 65486B[b]	18.465 ± 0.006	362.409 ± 0.012	−245.786 ± 0.016	38.326 ± 0.013	−8.19 ± 0.12	46.17 ± 0.05	4.24 ± 0.10	22.816 ± 0.006	99%	1%	0%	
LHS 6176B[b]	19.607 ± 0.010	234.47 ± 0.03	−360.66 ± 0.02	39.98 ± 0.02	12 ± 2	38.7 ± 0.9	−18.3 ± 1.3	13.7 ± 1.3	99%	1%	0%	[1],[3]
Ross 458C[b]	11.507 ± 0.015	−628.72 ± 0.18	−33.47 ± 0.13	34.34 ± 0.05	−12.3 ± 0.3	−18.46 ± 0.07	−6.02 ± 0.07	−3.9 ± 0.3	99%	1%	0%	
HD 126053B[b]	17.461 ± 0.011	2243.53 ± 0.05	−478.28 ± 0.03	43.69 ± 0.03	−19.21 ± 0.14	32.78 ± 0.07	−3.052 ± 0.017	−32.43 ± 0.12	93%	7%	0%	
GJ 570D[b]	5.886 ± 0.002	1031.47 ± 0.07	−1724.62 ± 0.06	56.04 ± 0.02	26.987 ± 0.002	59.36 ± 0.01	−9.792 ± 0.006	−25.244 ± 0.019	93%	7%	0%	[1],[2]
GJ 576B[b]	19.046 ± 0.009	−607.63 ± 0.02	−506.51 ± 0.02	71.41 ± 0.03	−84.79 ± 0.12	−47.25 ± 0.07	−62.79 ± 0.03	−49.81 ± 0.09	0%	99%	0%	[1],[4]
G 204 − 39B[b]	13.987 ± 0.003	−15.07 ± 0.02	578.14 ± 0.02	38.343 ± 0.008	−31.150 ± 0.002	−33.704 ± 0.008	−7.164 ± 0.002	−0.288 ± 0.002	99%	1%	0%	[1],[5]
Wolf 1130C[b]	16.585 ± 0.007	−1159.52 ± 0.04	−904.01 ± 0.03	115.58 ± 0.05	−33.2 ± 1.3[c]	117.46 ± 0.05	−31.7 ± 1.2	42.2 ± 0.2	18%	81%	0%	[1],[6]
HN PegB[b]	18.133 ± 0.011	231.11 ± 0.03	−113.20 ± 0.03	22.12 ± 0.014	−16.7230 ± 0.0013	−3.340 ± 0.006	−8.848 ± 0.005	−3.510 ± 0.012	99%	1%	0%	[1],[2]
Wolf 940B[b]	12.386 ± 0.008	769.37 ± 0.05	−505.68 ± 0.03	54.05 ± 0.03	−28.4 ± 0.3	−21.27 ± 0.12	−33.11 ± 0.18	−17.72 ± 0.17	92%	8%	0%	
Subdwarf Candidates												
J0055+5947[b]	22.84 ± 0.03	408 ± 25	−24 ± 25	44 ± 3	34 ± 25	−44 ± 15	16 ± 23	4 ± 3	96%	4%	0%	[1],[7]
J0140+0150	27 ± 2	971 ± 13	−90 ± 19	123 ± 11	91 ± 7	−117 ± 8	−45 ± 8	−53 ± 7	0%	99%	1%	[7]
J0411+4714	22 ± 2	440 ± 25	−143 ± 26	49 ± 5	34 ± 8	−40 ± 8	−13 ± 6	26 ± 3	97%	3%	0%	[7]
J0429+3201[d]	35 ± 3	30 ± 31	−458 ± 31	75 ± 8	(− 70 ± 21)	(75 ± 21)	(− 62 ± 8)	(− 25 ± 7)	15%	85%	0%	[7]
J0433+1009	29 ± 3	174 ± 34	−384 ± 36	58 ± 7	21 ± 7	3 ± 6	−46 ± 7	−12 ± 6	83%	17%	0%	[7]
J0623+0715	25 ± 2	7 ± 32	−980 ± 37	117 ± 11	−1 ± 27	56 ± 22	−82 ± 12	−46 ± 6	0%	99%	1%	[7]
J0659+1615	31 ± 3	−115 ± 8	−445 ± 8	68 ± 6	−36 ± 9	55 ± 9	−27 ± 5	−42 ± 4	43%	57%	0%	[7]
J0758+5711	27 ± 2	−120 ± 31	−342 ± 33	46 ± 6	79 ± 7	−75 ± 6	−3 ± 5	34 ± 5	84%	16%	0%	[7]
J1110−1747	26 ± 2	24 ± 28	−395 ± 27	49 ± 5	−47 ± 5	37 ± 4	23 ± 5	−55 ± 5	28%	71%	0%	[7]
J1130+3139	32 ± 3	−1185 ± 35	−1476 ± 38	284 ± 25	72 ± 8	−82 ± 8	−265 ± 24	32 ± 8	0%	0%	100%	[7]
J1204−2359	31 ± 3	−263 ± 37	−473 ± 38	79 ± 9	−47 ± 15	−6 ± 6	−4 ± 11	−82 ± 10	1%	98%	0%	[7]
J1304+2819	31 ± 3	−356 ± 19	18 ± 22	52 ± 5	50 ± 9	−31 ± 4	−13 ± 4	60 ± 9	49%	51%	0%	[7]
J1308−0321	21 ± 2	−454 ± 26	189 ± 29	50 ± 5	−42 ± 6	−49 ± 5	16 ± 4	−16 ± 5	96%	4%	0%	[7]
J1401+4325	34 ± 3	−172 ± 33	−659 ± 34	110 ± 11	−71 ± 21	62 ± 8	−104 ± 11	−25 ± 21	0%	98%	2%	[7]
J1458+1734	32 ± 3	−476 ± 20	163 ± 17	75 ± 7	19 ± 6	−37 ± 6	−14 ± 4	62 ± 6	38%	62%	0%	[7]
J1524−2620	40 ± 4	−372 ± 38	−107 ± 45	73 ± 10	29 ± 17	3 ± 15	−57 ± 10	44 ± 10	35%	65%	0%	[7]
J1710+4537	36 ± 3	−404 ± 36	80 ± 41	69 ± 9	−3 ± 8	−12 ± 8	−26 ± 9	61 ± 10	39%	61%	0%	[7]
J1801+4717	48 ± 4	109 ± 56	478 ± 63	111 ± 17	−29 ± 17	−102 ± 18	19 ± 17	−10 ± 15	56%	44%	0%	[7]
J2013−0326	29 ± 3	−649 ± 39	−625 ± 40	124 ± 12	−18 ± 13	83 ± 13	−81 ± 11	50 ± 8	1%	99%	1%	[7]
J2021+1524	22 ± 2	−547 ± 3	−441 ± 3	72 ± 6	−5 ± 7	69 ± 7	−25 ± 7	31 ± 3	90%	10%	0%	[7]
J2112−0529	30 ± 3	−556 ± 24	−748 ± 25	131 ± 12	−37 ± 14	89 ± 12	−95 ± 10	42 ± 8	0%	99%	1%	[7]
J2112+3030	39 ± 3	−431 ± 15	79 ± 15	80 ± 8	−125 ± 62	28 ± 15	−102 ± 61	100 ± 15	0%	66%	34%	[7]
J2218+1146	27 ± 2	224 ± 31	−267 ± 33	45 ± 6	−22 ± 9	1 ± 4	−31 ± 8	−16 ± 8	92%	8%	0%	[7]
J2251−0740	29 ± 3	696 ± 41	163 ± 41	97 ± 10	−140 ± 25	−117 ± 10	−66 ± 11	88 ± 19	0%	93%	7%	[7]

Table 9
(Continued)

Name	d[a] (pc)	μ_α (mas yr^{-1})	μ_δ (mas yr^{-1})	V_{tan} (km s^{-1})	RV (km s^{-1})	U (km s^{-1})	V (km s^{-1})	W (km s^{-1})	Probabilities			Ref
									Thin	Thick	Halo	
Metal-poor Comparison Sources												
J0532+8246	24.6 ± 0.3	2038.8 ± 0.6	−1663.0 ± 0.5	306 ± 3	−172 ± 1	−55 ± 2	−328 ± 2	66 ± 2	0%	0%	100%	[1],[8]
J0937+2931	6.12 ± 0.07	973 ± 6	−1298 ± 5	47.1 ± 0.5	−4.3 ± 0.4	42.1 ± 0.4	−21.5 ± 0.5	18.9 ± 0.4	98%	2%	0%	[9],[10]
J1055+5443	6.9 ± 0.7	−1519 ± 2	−223 ± 2	50 ± 5	39 ± 22	−50 ± 12	1 ± 6	21 ± 18	93%	7%	0%	[11],[7]
J1416+1348B[b]	9.282 ± 0.019	86.7 ± 0.3	128.0 ± 0.2	6.799 ± 0.017	−42 ± 5	−7 ± 2	18.02 ± 0.12	−31 ± 5	93%	7%	0%	[1],[12]
J1553+6933	34 ± 3	−1451 ± 33	1327 ± 29	321 ± 28	110 ± 90	−299 ± 31	−29 ± 73	137 ± 62	0%	4%	96%	[7]
J1810−1010	8.9 ± 0.6	−1027 ± 4	−264 ± 4	45 ± 3	46 ± 4	62 ± 4	−2 ± 3	43 ± 3	91%	9%	0%	[13]

Notes.
[a] Distance based on parallax measurement of source or primary companion, or estimated from Equations 2 and 3.
[b] Analysis based on kinematics of the primary component of this system.
[c] Center of mass motion of the Wolf 1130AC binary based on orbit fits (G. N. Mace et al. 2018).
[d] RV and *UVW* velocities may be systematically biased by the slit-seeing effect and should be treated with caution.

References– [1] Gaia EDR3 (Gaia Collaboration et al. 2021); [2] C. Soubiran et al. (2018); [3] M. Steinmetz et al. (2020); [4] J. L. Halbwachs et al. (2018); [5] P. Fouqué et al. (2018); [6] G. N. Mace et al. (2018); [7] This paper; [8] A. Reiners & G. Basri (2006); [9] J. K. Faherty et al. (2012); [10] C.-C. Hsu et al. (2021); [11] J. D. Kirkpatrick et al. (2021b); [12] R. Scholz (2010b); [13] N. Lodieu et al. (2022)

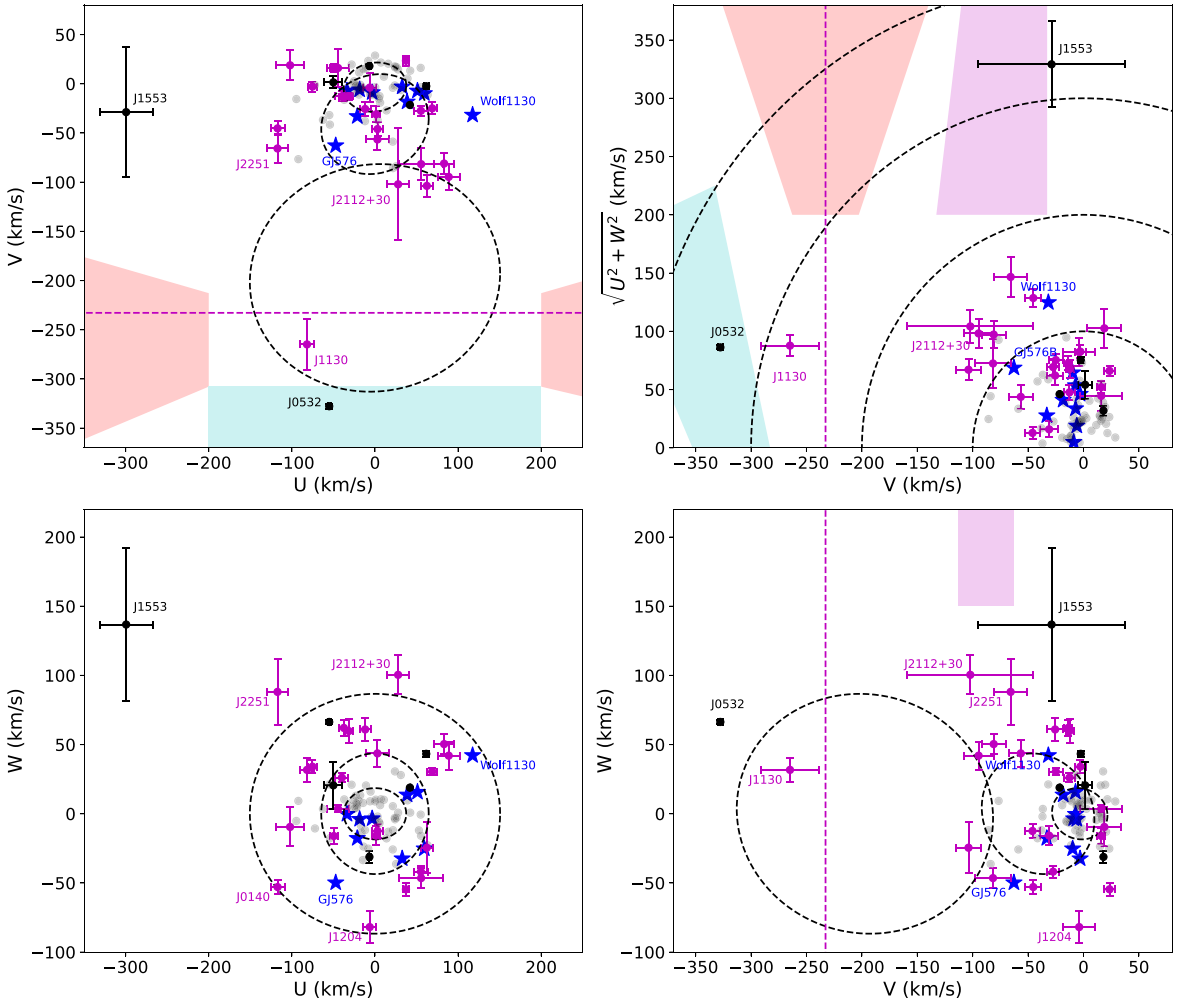

Figure 11. Local standard of rest *UVW* velocities of sources in our Keck/NIRES sample, along with comparison velocities of nearby late-L and -T dwarfs from C.-C. Hsu et al. (2021; gray dots). Symbol colors segregate subdwarf candidates (magenta), metal-poor comparison sources (black circles), and metallicity benchmarks (blue stars). In the upper-left, lower-left, and lower-right panels, we compare pairs of velocity components, with dashed lines indicating the 1σ velocity dispersion spheres for chemically selected thin disk, thick disk, and halo stars (in increasing size) based on the APOGEE and Gaia DR2 compilation of B. Anguiano et al. (2020). The upper-right panel displays a Toomre plot with circles indicating total speeds in steps of 100 km s^{-1}. In the plots containing the V velocity, we indicate the threshold between prograde and retrograde motion in the Galactic frame of rest (i.e., $L_z = 0$) by the dashed magenta lines at $V = -232.8$ km s^{-1} (P. J. McMillan 2017). We also show schematic regions in the Toomre plot for the Gaia-Enceladus (red), Thamnos (cyan), and Helmi streams (magenta) based on H. H. Koppelman et al. (2019) for velocity pairs where these populations are distinct. Sources discussed in the text are labeled.

(The data used to create this figure are available in the online article.)

We iteratively evaluated these variations by direct comparison between spectra. We then built a 2D grid of representative standards that spanned our available sample. Selection of these standards favored sources with high signal-to-noise spectra and/or accessible declinations when more than one option was available. These standards are listed in Table 11 and displayed in sequence in Figure 13. There are gaps among subclasses in the sd and esd sequences where a clear standard was not available. However, as illustrated in Figure 14, those subtypes with representatives across metallicity classes display continuous variations in spectral features tied to metallicity (e.g., near-infrared slope, breadth of the 1.15 μm feature), while maintaining agreement with the dwarf standards in spectral features tied to temperature (e.g., strength of the 1.6 μm CH_4 band, depth of the 1.15 μm H_2O+CH_4 feature). The highly distinct spectra of the extreme subdwarfs J0532+8246, J0616−6407, J1810−1010, and J0414−5854 make their numerical classifications, anchored to the 1.1 μm trough, highly uncertain and are indicated as such with a ":" suffix.

We used these standards to determine revised classifications for the remainder of our candidate and comparison sample, listed in Table 10. Note that this analysis resulted in several significant changes in the classifications of previously identified metal-poor late-L and -T dwarfs. In addition to reclassifying the previously reported subdwarfs J0004−2604, J1019−3911, and J1307+1510 as normal early-T dwarfs, we reassigned several sources as mild subdwarfs given their relatively weak metallicity signatures. We also reclassified the L subdwarfs J0616−6407 and J0645−6646 as early-T subdwarfs based on the presence of weak CH_4 absorption in their *H*- or *K*-band spectra. For J0616−6407, this is a substantial shift from its prior esdL6 classification (Z. H. Zhang et al. 2017), but we assert this reclassification is warranted given the emergent CH_4 feature at 1.6 μm present in its spectrum, a defining trait for T dwarfs (A. J. Burgasser et al. 2006b). For sources with incomplete 1–2.5 μm coverage (e.g., Wolf 1130C, J2105−6235), we indicate uncertainty in their classifications with a ":" suffix.

Table 10
Assessment of T Subdwarf Candidates and Comparison Sources

Name	Assessment Metrics				ζ_T[a]	Spectral Type	
	Deviant?	K I?	Model?	*UVW*?		Prior	Adopted
Confirmed T Subdwarfs							
J0623+0715	Y	Y	Y	y	0.79 ± 0.09	⋯	sdT3
J1524−2620	y?	y	Y	y	0.74 ± 0.09	⋯	sdT0
J2112−0529	Y	n	Y	y	0.79 ± 0.13	⋯	sdT1
Mild T Subdwarfs							
J0045+7958	y	N	y?	⋯	0.99 ± 0.17	⋯	d/sdL9:
J0055+5947	y?	y	n?	n	0.78 ± 0.11	T8	d/sdT6.5
J0411+4714	y	y	y	n	0.95 ± 0.18	⋯	d/sdT7.5
J0845−3305	y	⋯	y	⋯	0.85 ± 0.11	T7	d/sdT6.5
J0911+2146	y	⋯	y?	⋯	0.70 ± 0.14	T9	d/sdT8
J0953−0943	y	⋯	y	⋯	0.78 ± 0.13	T5.5	d/sdT6
J1130+3139	y	Y	y	Y	0.86 ± 0.11	⋯	d/sdT5.5
J1138+7212	Y	⋯	y	⋯	0.76 ± 0.17	⋯	d/sdT7
J1204−2359	y	y	y	y	0.90 ± 0.15	⋯	d/sdT7
J1304+2819	y	n	n	y?	0.90 ± 0.13	⋯	d/sdL9:
J1308−0321	y	⋯	y	n	1.08 ± 0.22	⋯	d/sdT8
J1401+4325	y?	Y	y	y	0.87 ± 0.08	⋯	d/sdT5.5
J1515−2157	y?	n	y?	⋯	0.71 ± 0.11	⋯	d/sdT6
J1801+4717	n	Y	y?	n?	0.93 ± 0.08	⋯	d/sdT5
J2013−0326	y	Y	y	y	0.79 ± 0.08	⋯	d/sdT6
J2021+1524	Y	n	Y	n	0.94 ± 0.15	⋯	d/sdL9
J2112+3030	y?	Y	y	Y	0.96 ± 0.13	⋯	d/sdT2.5
J2218+1146	y	y	y?	n	0.85 ± 0.09	T7p	d/sdT6.5
J2251−0740	y?	y	n?	y	0.99 ± 0.19	⋯	d/sdT7
Not Subdwarfs							
J0140+0150	n	N	N	y	1.11 ± 0.11	⋯	rT4.5
J0429+3201	n	y	y	⋯	1.04 ± 0.11	⋯	T1
J0433+1009	n	⋯	n?	n?	1.12 ± 0.17	T8	T8
J0659+1615	n	n	y?	y?	0.97 ± 0.10	⋯	T1
J0758+5711	n	n	y	n?	0.93 ± 0.12	⋯	T6.5
J0843+2904	n	⋯	n?	⋯	0.93 ± 0.11	⋯	L6:
J1110−1747	n	⋯	n	y	1.28 ± 0.14	⋯	rT8
J1458+1734	n	⋯	n?	y?	1.20 ± 0.17	⋯	T8
J1710+4537	n	y	n?	y?	1.00 ± 0.11	⋯	T6
Metal-poor Comparison Sources							
HD 65486B	n	⋯	Y	n	0.95 ± 0.11	T4.5	d/sdT4.5
LHS 6176B	y	y	y	n	0.76 ± 0.12	T8p	d/sdT7.5
HD 126053B	Y	⋯	Y	n	0.38 ± 0.05	T8p	sdT7.5
GJ 576B	y	Y	y	y	0.78 ± 0.05[b]	sdT5.5	d/sdT5.5
Wolf 1130C	Y	Y	y	y	⋯	T8p	(e)sdT6:
J0004−1336	y	⋯	Y	⋯	0.91 ± 0.11	T2p	d/sdT2:
J0004−2604	n	⋯	y	⋯	0.91 ± 0.06	sdT2	T3
J0013+0634	Y	⋯	n	⋯	0.33 ± 0.18	T8p	sdT7.5
J0021+1552	n	Y	y	⋯	0.81 ± 0.13	T4p	d/sdT4
J0057+2013	Y	⋯	y?	⋯	⋯	sdL7	d/sdL9
J0301−2319	y	⋯	y	⋯	0.89 ± 0.11	sdT1	d/sdT1
J0309−5016	y	⋯	y	⋯	0.49 ± 0.08	T7p	d/sdT7.5
J0348−5620	y	⋯	n	⋯	0.89 ± 0.08	T3p	d/sdT4
J0414−5854	Y	⋯	Y	⋯	0.32 ± 0.16	esdT	esdT6:
J0532+8246	Y	n	Y	Y	0.58 ± 0.07	esdL7	esdL8:
J0616−6407	Y	n	Y	⋯	0.54 ± 0.06	esdL6	esdT0:
J0645−6646	y	N	y?	⋯	⋯	sdL8	d/sdT0
J0833+0052	y	⋯	y?	⋯	0.62 ± 0.13	T9p	d/sdT9
J0850−0221	y	⋯	y	⋯	⋯	sdL7	d/sdL6
J0937+2931	Y	⋯	Y	n	0.64 ± 0.18	T6p	sdT6
J0939−2448	y	⋯	y	⋯	0.45 ± 0.09	T8p	d/sdT8
J1019−3911	y?	⋯	n	⋯	1.00 ± 0.17	sdT3	T4

Table 10
(Continued)

Name	Assessment Metrics					Spectral Type	
	Deviant?	K I?	Model?	*UVW*?	ζ_T[a]	Prior	Adopted
J1035−0711	Y	⋯	y	⋯	⋯	sdL7	d/sdL9
J1055+5443	N	⋯	N	n	⋯	sdT8	Y0
J1130−1158	Y	Y	Y	⋯	0.45 ± 0.18	sdT5.5	sdT5.5
J1158+0435	Y	⋯	y	⋯	⋯	sdL7	d/sdL8
J1307+1510	n	N	y?	⋯	⋯	sdL8	T1
J1316+0755	Y	⋯	Y	⋯	0.37 ± 0.17	sdT6.5	sdT6.5
J1338−0229	y	⋯	y	⋯	⋯	sdL7	sdL9
J1416+1348B	Y	⋯	Y	n	0.23 ± 0.06	T7.5p	sdT7
J1553+6933	Y	Y	Y	Y	0.65 ± 0.05	sdT4	sdT4
J1810−1010	Y	Y	Y	n	0.49 ± 0.07	esdT	esdT3:
J2105−6235	y?	⋯	y	⋯	0.89 ± 0.05	sdT1.5	d/sdT2:

Notes. The qualitative assessment metrics are as follows: "Y": strong positive evidence, "y": marginal positive evidence, "n": marginal negative evidence, "N": strong negative evidence, and "...": unmeasured or unable to evaluate for this source (e.g., K I for ⩾T8 sources and low-resolution spectra).
[a] Metallicity index from infrared indices; see Section 6.2 and Table 13.
[b] Weighted average from multiple spectra.

As with any empirical stellar classification system, the relationship between $T_{\rm eff}$ and spectral type can vary with metallicity, as discussed below. Nevertheless, our model fits indicate that model-fit metallicities of the metallicity class standards align with the metallicity ranges for M and L subdwarf classes, with uncertainty-weighted means of [M/H] = −0.36 ± 0.09 for d/sdT standards, [M/H] = −0.63 ± 0.09 for sdT standards, and [M/H] = −1.32 ± 0.13 for esdT standards. We present this initial grid as a starting point, with the expectation of future expansion and/or reorganization as the known T subdwarf population expands.

6.2. Defining a Metallicity Index

While direct comparison to standards is the optimal method for determining metallicity classifications, metallicity-sensitive spectral indices can be used as estimators of the quantified metallicity of a source. For M subdwarfs, metallicity-sensitive spectral features in the optical (e.g., CaH/TiO; V. M. Woolf & G. Wallerstein 2006; S. Lépine et al. 2007; V. M. Woolf et al. 2009; S. Dhital et al. 2012; V. Neves et al. 2014) or infrared (e.g., Na/H_2O/CO/FeH; B. Rojas-Ayala et al. 2012; R. C. Terrien et al. 2012; A. W. Mann et al. 2013; E. R. Newton et al. 2014) are calibrated with sources of known metallicity, typically companions to FGK dwarfs and resolved binaries (A. W. Mann et al. 2013; D. Montes et al. 2018; D. Qiu et al. 2024). We applied the same approach to our T dwarf sample. We first identified spectral indices in the near-infrared that clearly segregate spectroscopically identified T subdwarfs and low-metallicity benchmark companions from the predominantly solar-metallicity local T dwarf population. The 10 spectral indices reported in Section 4.2 provide 45 unique index pairings, of which six demonstrate consistent separation between dwarfs and subdwarfs. These pairs as listed in Table 12 and displayed in Figures 15 and 16. We combined two index pairings, [H2O-J] versus [Y/J] and [CH4-J] versus [Y/J] into a composite index. For the three pairings with ordinate indices [H2O-H] and [Y/J], the subdwarfs were found to lie above the dwarf sequence, consistent with weakened H_2O absorption at 1.5 μm and a brighter *Y*-band peak, both noted previously as metallicity indicators. The other three pairings with the ordinate index [K/H] have subdwarfs lying below the dwarf sequence, consistent with suppressed *K*-band peaks due to enhanced CIA H_2 absorption. A. J. Burgasser et al. (2006b) had previously proposed use of the [K/J] color index as an indicator of enhanced CIA H_2 absorption, but probable errors in the order-to-order flux calibration of the multiorder spectral data in our sample (see Section 3.6) result in higher scatter for this color index; hence ,we excluded them from our metallicity index set.

For each of these pairings, we fit second-order polynomials to the index values of the local T dwarf sample over an abscissa range that had the clearest offset from the T subdwarfs. In some cases, the abscissa range encompasses a subset of our sample; e.g., only early-type or only late-type T dwarfs. Fit parameters and scatter about the best fits are listed in Table 12 and displayed in Figures 15 and 16.

To guide our interpretation of these trends, we also show the same spectral indices measured on the LOWZ atmosphere models over the temperature range 600 K ⩽ $T_{\rm eff}$ ⩽ 1600 K, surface gravities 4.0 ⩽ log g ⩽ 5.25 (cgs), metallicities −2.5 ⩽ [M/H] ⩽ +0.5, C/O = 0.55, and log κ_{zz} = 2. We find that five of these index pairs show good separation of metallicity and temperature and reasonable overlap with our measured values. The [Y/J] versus ⟨H2O-J,CH4-J⟩ pair shows the most discrepant values between models and measurements, and poor metallicity separation in the models for [M/H] ⩽ −0.5, so we reject this pair as a viable metallicity diagnostic. Of the remaining indices, [H2O-H] versus [CH4-H], [H2O-H] versus [H2O-J], and [K/H] versus [H2O-J] show reasonably orthogonal metallicity and temperature trends in the models, although there is disagreement between models and measurements for the last index for the late-L and early-T dwarfs, likely due to unincorporated cloud opacity effects. The [K/H] versus [H-dip] and [K/H] versus [CH4-H] pairings show greater degeneracy between metallicity and temperature, while [K/H] versus [H-dip] shows greater dynamic range; we therefore prioritize this index pair over [K/H] versus [CH4-H].

Based on these analyses, we defined four metallicity indices, $\zeta_{T,i}$, as the ratio between the metallicity-sensitive index [H2O-H] or [K/H] and their expected values based on the solar-

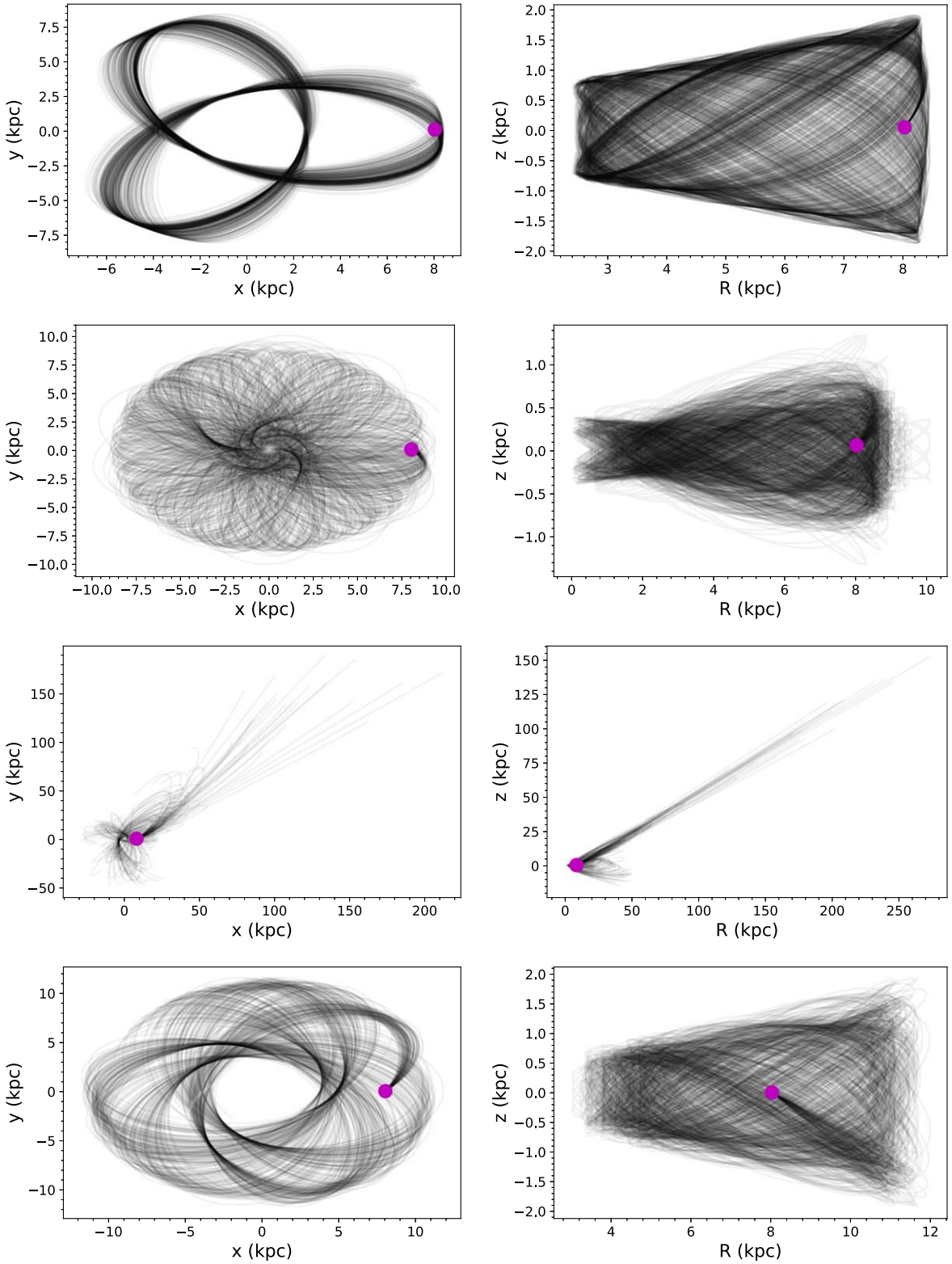

Figure 12. Galactic orbits for the high-velocity sources (from top to bottom): J0532+8246, J1130+3139, J1553+6933, and J0140+0150. Orbits were calculated forward in time by 1 Gyr using `galpy` (J. Bovy 2015) with the MWPotential2014 potential. We assumed a solar motion from R. Schönrich et al. (2010), a local circular velocity of 220 km s^{-1}, and $R_\odot = 8$ kpc. For J1553+6933, we extended the integration to 5 Gyr. The current location of each source is indicated by the magenta circle. We show 100 realizations of each object's orbit by sampling uncertainties in distance, proper motion, and RV.

metallicity dwarf sequences:

$$\zeta_{T,1} \equiv \frac{[\mathrm{H2O}-\mathrm{H}]_\odot([\mathrm{CH4}-\mathrm{H}])}{[\mathrm{H2O}-\mathrm{H}]} \quad (13)$$

$$\zeta_{T,2} \equiv \frac{[\mathrm{H2O}-\mathrm{H}]_\odot([\mathrm{H2O}-\mathrm{J}])}{[\mathrm{H2O}-\mathrm{H}]} \quad (14)$$

Table 11
T Subdwarf Spectral Standards

Dwarfs (d)[a]		Mild Subdwarfs (d/sd)		Subdwarfs (sd)		Extreme Subdwarfs (esd)	
SpT	Name	SpT	Name	SpT	Name	SpT	Name
dL8	J1632+1904	d/sdL8	J1158+0435	sdL8	···	esdL8	J0532+8246
dL9	J0255−4700	d/sdL9	J2021+1524	sdL9	J1338−0229	esdL9	···
dT0	J1207+0244	d/sdT0	J0645−6646	sdT0	J1524−2620	esdT0	J0616−6407
dT1	J0837−0000	d/sdT1	J0301−2319	sdT1	J2112−0529	esdT1	···
dT2	J1254−0122	d/sdT2	J0004−1336	sdT2	···	esdT2	···
dT3	J1209−1004	d/sdT2.5	J2112+3030	sdT3	J0623+0715	esdT3	J1810−1010
dT4	J2254+3123	d/sdT4	J0021+1552	sdT4	J1553+6933	esdT4	···
dT5	J1503+2525	d/sdT5.5	GJ 576B	sdT5.5	J1130−1158	esdT5	···
dT6	J1624+0029	d/sdT6	J2013-0326	sdT6	J0937+2931	esdT6	J0414−5854
dT7	J0727+1710	d/sdT7.5	LHS 6176B	sdT7	J1416+1348B	esdT7	···
dT8	J0415−0935	d/sdT8	J0939−2448	sdT7.5	J0013+0634	esdT8	···
dT9	J0722−0540	d/sdT9	J0833+0052	sdT9	···	esdT9	···

Notes.
[a] Dwarf standards from J. D. Kirkpatrick et al. (1999, 2010) for L dwarfs and A. J. Burgasser et al. (2006b) for T dwarfs; see these references for full source designations.

$$\zeta_{T,3} \equiv \frac{[\mathrm{K/H}]}{[\mathrm{K/H}]_{\odot}([\mathrm{H2O}-\mathrm{J}])} \tag{15}$$

$$\zeta_{T,4} \equiv \frac{[\mathrm{K/H}]}{[\mathrm{K/H}]_{\odot}([\mathrm{H}-\mathrm{dip}])}. \tag{16}$$

Here, the notation $[\mathrm{SP}_y]_{\odot}([\mathrm{SP}_x])$ is the polynomial fit for the dwarf sequence for the index pairings $[\mathrm{SP}_x]$ and $[\mathrm{SP}_y]$ listed in Table 12. These relationships are defined such that subsolar-metallicity objects are expected to have $\zeta_{T,i} \lesssim 1$.

Table 13 lists the individual $\zeta_{T,i}$ values for our spectral sample, as well as the combined index ζ_T, while Figure 17 displays the distributions of these indices. Uncertainties for the individual $\zeta_{T,i}$ values were estimated from the original spectral index uncertainties and the scatter in the dwarf sequence fits using Monte Carlo methods, and are typically 0.1–0.2. Note that $\zeta_{T,3}$ shows larger uncertainties due to the greater scatter of its dwarf sequence fit. We rejected all values of $\zeta_{T,i}$ with uncertainties >0.4, then computed ζ_T as the uncertainty-weighted mean (Equation (10)). For some sources, the scatter among $\zeta_{T,i}$ values exceeded their individual uncertainties (i.e., $\chi^2_r > 1$), in which case we adopted a straight mean with uncertainty equal to the standard deviation of the $\zeta_{T,i}$ values. The combined ζ_T index has a typical uncertainty of 0.1–0.2. Metallicity index values for sources with multiple spectra (GJ 576B and J0140+0150) agree within these uncertainties. Several sources in our sample, including the benchmark companions Wolf 940B and Wolf 1130C, fall outside the fit ranges in Table 12 or had incomplete spectral coverage, and thus, ζ_T values were unable to be measured.

We found excellent alignment between ζ_T and our metallicity classifications. Sources with dwarf classifications, including our local T dwarf sample, have $\zeta_{T,i} = 1$ within 10%–15%, while subdwarfs and extreme subdwarfs typically having $\zeta_{T,i} \lesssim 0.8$ and $\zeta_{T,i} \lesssim 0.6$, respectively. All three of our new subdwarf discoveries, J0623+0715, J1524−2620, and J2112−0529 have $\zeta_T \approx 0.8$. On the other hand, there are outliers among our late-type T dwarfs, notably the d/sdT9 J0833+0052 with $\zeta_T = 0.62$, the d/sdT8 J0939−2448 with $\zeta_T = 0.45$, and the sdT7 standard J1416+1348B with $\zeta_T = 0.23$, all smaller than expected for their metallicity classifications. In addition, the peculiar red T8.5 Ross 458C, which has an unusually bright *K*-band peak, has a large $\zeta_T = 1.71$. These sources have only the $\zeta_{T,4}$ index measured, which is based on the [K/H] versus [H-dip] index pairing. As noted above, the LOWZ models show a coupling between temperature and metallicity for these index pairs at low temperatures (Figure 16) and, in the case of Ross 458C, may not account for enhanced cloud opacity (A. J. Burgasser et al. 2010c; C. V. Morley et al. 2012). Thus, the discrepant ζ_T values of these sources, and potentially other very late-type T dwarfs, may reflect a temperature bias in this particular metallicity index.

To further assess the reliability of the ζ_T index, Figure 18 compares this index to total metallicity [M/H] based on the best-fit spectral models (Table 7), and to the iron abundances [Fe/H] of the primaries of our benchmark companions (Tables 2 and 3). The majority of our sample shows a roughly linear trend between ζ_T and [M/H], with a Pearson *r* correlation of 0.46 ± 0.07. The dispersion becomes larger at the lowest metallicities and ζ_T values, and may reflect the temperature–metallicity coupling for the $\zeta_{T,4}$ index for very late-type T dwarfs. Excluding the L dwarfs in our sample and the unusually red T8.5p dwarf Ross 458C, we find a roughly linear trend between ζ_T and [M/H] for 57 sources:

$$[\mathrm{M/H}] = 1.03611\zeta_T - 1.12491 \tag{17}$$

spanning $0.24 \leqslant \zeta_T \leqslant 1.2$ and $-1.34 \leqslant [\mathrm{M/H}] \leqslant +0.43$, with a metallicity scatter of 0.29 dex. We emphasize that this is a model-dependent correlation, and may be skewed by inaccuracies in the model fitting. However, this trend also accurately reproduces the correlation between ζ_T and [Fe/H] measurements for the primaries of our benchmark companions, with two key exceptions: the aforementioned Ross 458C and the sdT7.5 HD 1260538B, which has a low value of $\zeta_T = 0.38$ for its primary $[\mathrm{Fe/H}] = -0.38$. Excluding these sources, we find a tight correlation among the nine remaining benchmarks (Pearson $r = 0.52 \pm 0.23$) with a similar linear trend

$$[\mathrm{Fe/H}] = 0.99844\zeta_T - 1.07333 \tag{18}$$

for $0.71 \leqslant \zeta_T \leqslant 1.11$ and $-0.37 \leqslant [\mathrm{M/H}] \leqslant +0.14$, with a metallicity scatter of 0.12 dex. The small number of benchmark companions with both [Fe/H] and ζ_T measurements, and the

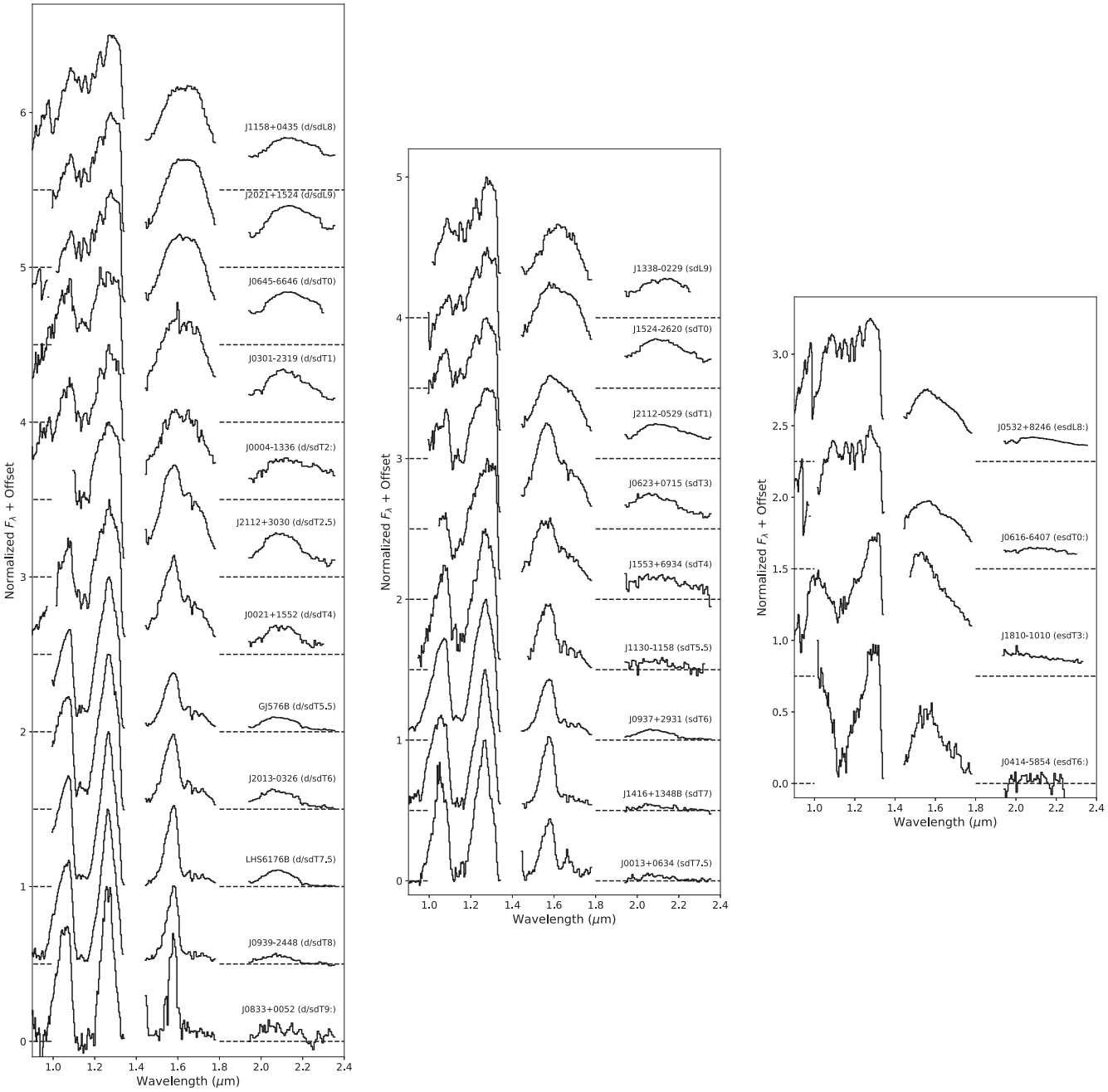

Figure 13. Spectral sequences for mild subdwarfs (d/sd; left), subdwarfs (sd; middle) and extreme subdwarfs (esd; right) for late-L and -T dwarfs in our spectral sample. All data are smoothed to an equivalent resolution of $\lambda/\Delta\lambda = 300$, normalized at the 1.25 μm peak and offset by constants (dashed lines; 0.5 steps for d/sd and sd, 0.75 steps for esd). Standards are identified by name and spectral type.

limited metallicity range of this sample, warrant some caution in the use of this relationship. Nevertheless, these comparisons indicate an overall self-consistency between the metallicity classifications, the ζ_T index, and the actual metallicities of our sources, whether inferred from spectral model fits or stellar primaries.

7. Discussion

7.1. Effective Temperature Trends for T Subdwarfs

The classification of a star is a proxy for its physical parameters, including temperature, luminosity, surface gravity, and (in the case of metallicity classes) composition. For cool stars and brown dwarfs, there are numerous relations linking dwarf numerical spectral types to luminosities and effective temperatures, the latter either requiring a measured or estimated radius inferred from atmospheric model fitting (F. Marocco et al. 2013; M. J. Pecaut & E. E. Mamajek 2013; J. C. Filippazzo et al. 2015; T. J. Dupuy & M. C. Liu 2017; J. D. Kirkpatrick et al. 2021b; A. Sanghi et al. 2023). There are well-documented metallicity offsets in the spectral type/temperature relations of M and L dwarfs, with subdwarfs typically found to be warmer by several 100 K than their equivalently classified dwarf counterparts (A. J. Burgasser & J. D. Kirkpatrick 2006; A. J. Burgasser et al. 2007a; A. S. Rajpurohit et al. 2014; Z. H. Zhang et al. 2017). It is thus useful to explore how effective temperature trends vary with metallicity in the T dwarf regime.

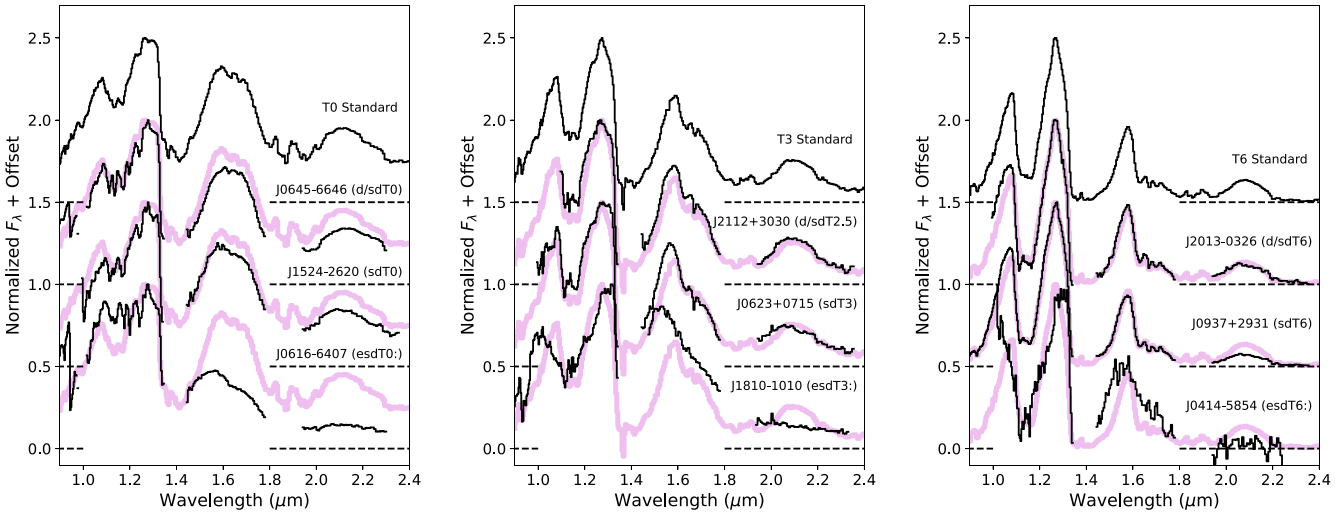

Figure 14. Metallicity sequences of spectral type standards for the T0 (left), T3 (middle), and T6 (right) subclasses, showing from top to bottom dwarf, mild subdwarf (d/sd), subdwarf (sd), and extreme subdwarf (esd) standards. All data are smoothed to an equivalent resolution of $\lambda/\Delta\lambda = 300$, normalized at the 1.25 μm peak and offset by constants (dashed lines). The dwarf standard is repeated in magenta to compare to the d/sd, sd, and esd standards.

Table 12
Spectral Index Pairings That Segregate Metal-poor Late-L and -T Dwarfs

$\zeta_{T,i}$	Abscissa (x)		Ordinate (y)	Solar-metallicity Sequence Polynomial Fit			
	Index	Range	Index	c_2	c_1	c_0	σ_y
$\zeta_{T,1}$	[CH4-H]	0.55–1.00	[H2O-H]	0.52753311	−0.28280498	0.37088006	0.053
$\zeta_{T,2}$	[H2O-J]	0.05–0.60	[H2O-H]	0.44401774	0.38492182	0.20196172	0.033
$\zeta_{T,3}$	[H2O-J]	0.05–0.65	[K/H]	1.23813044	−0.23225536	0.31791332	0.097
$\zeta_{T,4}$	[H-dip]	0.20–0.90	[K/H]	0.01818876	0.17387556	0.22533516	0.046
…[a]	[CH4-H]	0.10–0.65	[K/H]	−0.78127813	0.92425434	0.1014752	0.043
…[a]	⟨[H2O-J],[CH4-J]⟩	0.15–0.75	[Y/J]	0.19243998	0.16534304	0.3675336	0.048

Notes. $\langle SP_1, SP_2 \rangle$ indicates an average of two indices, or the value of one index if the other is unmeasured. Fit relations for the dwarf standards are defined as $y = \sum_{i=0}^{2} c_i x^i$ for indices (x, y) over the ranges specified. The quantity σ_y measures the rms deviation of y-values about this relation. See Figures 15 and 16 for visualization of these fits.
[a] Not used as a metallicity index.

Our first approach was to compare effective temperatures from our model fits to assigned spectral classifications, as illustrated in Figure 19. We see the expected decline of $T_{\rm eff}$ with later spectral type, although many of our sources—including our local comparison sample—are warmer than previously established dwarf empirical relations. These offsets are particularly large for the late-L and early-T dwarfs. For example, our model-fit temperature for J0616−6407, $T_{\rm eff} = 2181^{+14}_{-26}$ K, is over 800 K warmer than the equivalent solar-metallicity T0 dwarf ($T_{\rm eff} \approx 1250$ K; J. C. Filippazzo et al. 2015). As this source has a measured parallax, we can also deduce that its model-fit temperature is overestimated based on the nonphysically small radius required to match its absolute fluxes. Similar scaling issues are seen for other sources in our sample with trigonometric parallaxes (Table 7).

We therefore considered an alternative estimate for $T_{\rm eff}$ based on bolometric magnitude

$$T_B = T_\odot \sqrt{\frac{R_\odot}{R}}\, 10^{(M_{\rm bol,\odot} - M_{\rm bol})} \quad (19)$$

where $T_\odot = 5772$ K, $R_\odot = 6.957 \times 10^{10}$ cm, and $M_{\rm bol,\odot} = 4.74$ are the temperature, radius, and bolometric magnitude of the Sun (E. E. Mamajek et al. 2015). Ignoring interstellar absorption, the bolometric magnitude can be inferred from the absolute magnitude in filter x via the bolometric correction (BC)

$$\mathrm{BC}_x = M_{\rm bol} - M_x = M_{\rm bol} - m_x + 5\log_{10}\left(\frac{d}{10\ \ \mathrm{pc}}\right). \quad (20)$$

While empirical BCs for solar-metallicity T dwarfs exist in the literature (e.g., M. C. Liu et al. 2010; J. C. Filippazzo et al. 2015; A. Sanghi et al. 2023), we chose to compute BCs from the LOWZ atmospheric models to incorporate metallicity effects. For models computed in surface fluxes,

$$\mathrm{BC}_x = 4.74 - 10\log_{10}\left(\frac{T}{T_\odot}\right) - 5\log_{10}\left(\frac{R_\odot}{10\ \ \mathrm{pc}}\right) - m_x \quad (21)$$

(L. Casagrande & D. A. VandenBerg 2014), where m_x is the apparent magnitude computed directly from the model spectra. As our available photometry is on the Vega system, we computed spectrophotometric model magnitudes as

$$m_x = -2.5\log_{10}\left(\frac{\int \lambda f_\lambda(\lambda) T_x(\lambda) d\lambda}{\int \lambda f_\lambda^V(\lambda) T_x(\lambda) d\lambda}\right) \quad (22)$$

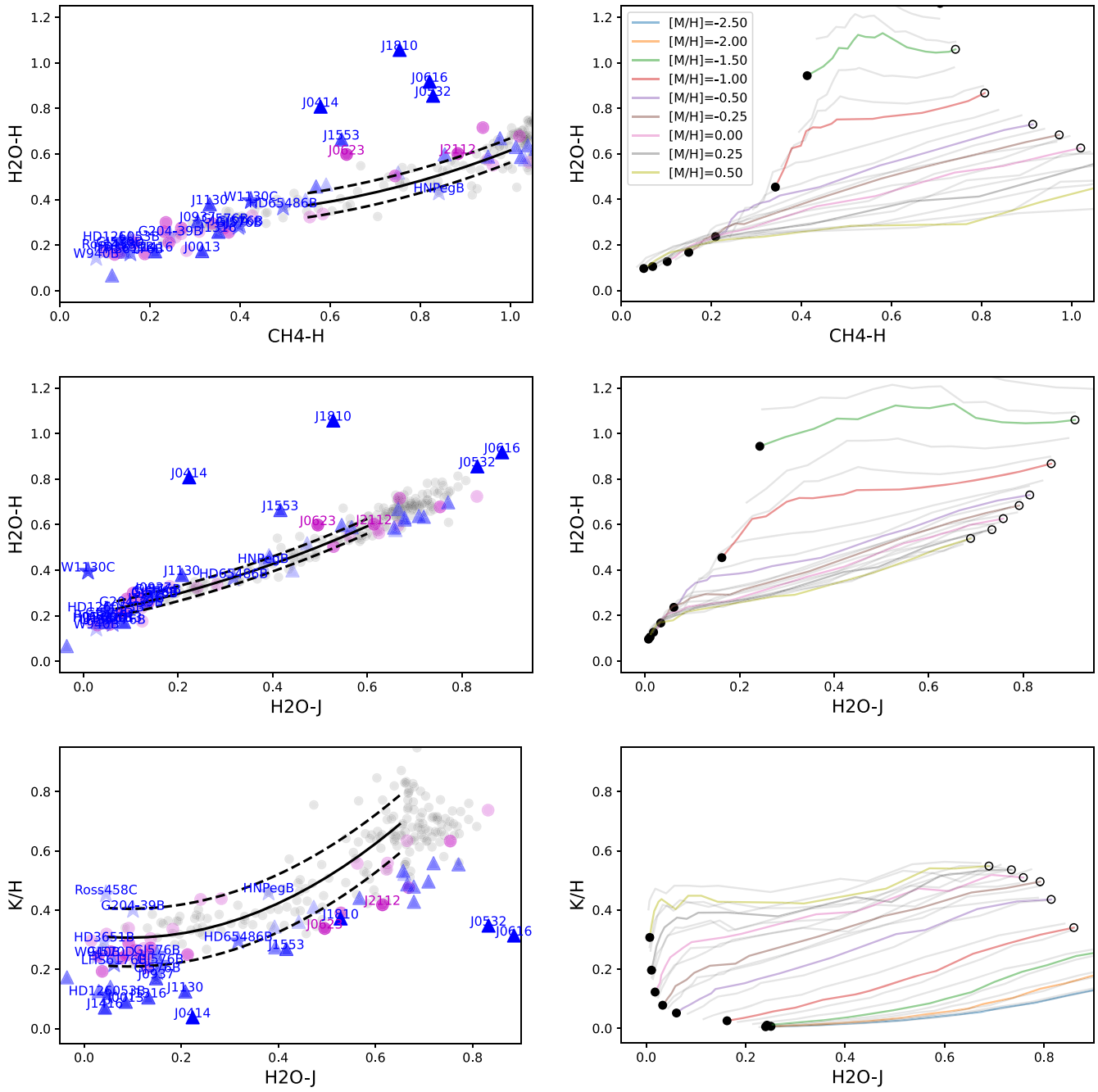

Figure 15. Left panels: three of the spectral index pairings that segregate metal-poor and solar-metallicity late-L and -T dwarfs. Previously classified subdwarfs are indicated by blue triangles, T dwarf benchmarks are indicated by blue stars, local T dwarfs are indicated by gray circles, and observed candidates are indicated by magenta circles. The transparency of each symbol is based on the metallicity class, with dwarfs being most transparent and extreme subdwarfs being most opaque. Sources identified as sdT or esdT and all benchmarks are labeled. Solid and dashed lines trace the mean and $\pm 1\sigma$ standard deviation for second-order polynomial fits to the local T dwarf sample over the ranges specified in Table 12. Right panels: same index pairings measured on LOWZ models for 600 K $\leqslant T_{\rm eff} \leqslant$ 1600 K (filled to open circles) and $-2.5 \leqslant$ [M/H] $\leqslant +0.5$ (colored lines). The color lines trace $\log g = 5.0$ (cgs), while the semitransparent gray lines trace $\log g = 4.0$ and 5.25.

using a model spectrum of Vega f_λ^V from R. L. Kurucz (1993) and filter profiles T_x from the Spanish Virtual Observatory Filter Profile Service[27](C. Rodrigo et al. 2012; C. Rodrigo & E. Solano 2020). Appendix B provides a list of bolometric corrections for various infrared filters for the LOWZ models; here, we focus on J and W2 photometry for sources with measured parallaxes. As the bolometric corrections are inherently dependent on the physical properties of the atmosphere, we assumed $\log g = 5.0$ (cgs), $\log k_{zz} = 2$ (cgs), C/O = 0.55, and a metallicity based on the classification: [M/H] = 0 for dT, [M/H] = −0.25 for d/sdT, [M/H] = −0.75 for sdT, and [M/H] = −1.5 for esdT. We also assumed a theoretical radius of $R_{\rm th} = 0.077\ R_\odot$ based on the solar-metallicity evolutionary models of A. Burrows et al. (2001) and I. Baraffe et al. (2003), and assumed a 10% uncertainty on this value. We iteratively converged to a self-consistent bolometric temperature starting from the model-fit temperature, and estimated the uncertainty in T_B as the greater of the combined

[27] http://svo2.cab.inta-csic.es/theory/fps/

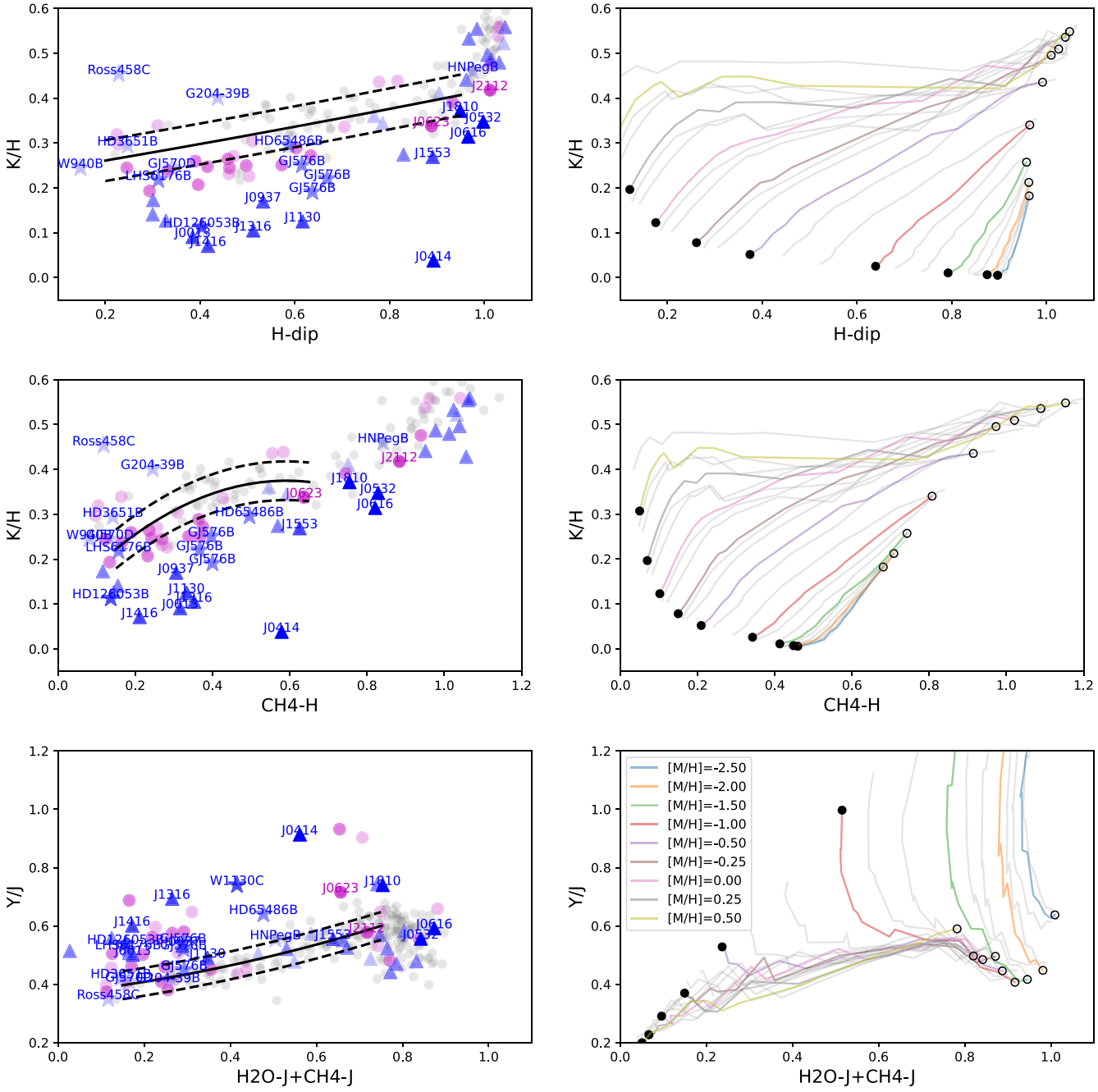

Figure 16. Same as Figure 15 for three additional index pairings.

formal uncertainty from both filters,

$$\left(\frac{\sigma_{T_B}}{T_B}\right)^2 = \left(\frac{1}{2}\frac{\sigma_{R_{\rm th}}}{R_{\rm th}}\right)^2 + \left(\frac{1}{2}\frac{\sigma_\pi}{\pi}\right)^2 + \left(\frac{0.1}{\ln 10}\sigma_x\right)^2 \qquad (23)$$

(here π is parallax, $x \in \{J, \mathrm{W2}\}$), and half of the difference between the temperatures inferred from J and W2.

Table 14 lists the resulting bolometric temperatures, which are displayed in Figure 19. These temperatures are generally lower than those inferred from the model fits, in some cases by hundreds of degrees kelvin (e.g., J0616–6407), in alignment with the underestimated radii from the model fits for these sources. Nevertheless, the bolometric temperatures for the late-L and early-T subdwarfs remain warmer than the dwarf sequence. The mid- and late-type T subdwarfs, on the other hand, appear to be cooler than their equivalently classified dwarf counterparts, notably so for J1810–1010 (T_B = 790 K compared to 1150 K for a typical T3 dwarf) and Wolf 1130C (T_B = 645 K compared to 940 K for a typical T6 dwarf). This apparent reversal in the metallicity-induced temperature offset may be caused by a flattening of the H_2O and CH_4 features by enhanced H_2 absorption, or reduced absorption from these molecules due to reduced C and O abundances. Both cases lead to earlier spectral classifications at a given temperature. We also note that this temperature reversal occurs around the L/T transition, where dwarf spectra evolve due to changes in photospheric cloud properties (or equivalently the adiabatic gradient; P. Tremblin et al. 2016), producing a flat temperature/spectral type relation; i.e., large changes in spectral morphology with minimal change in $T_{\rm eff}$ (A. J. Burgasser et al.

Table 13
Metallicity Indices for the T Subdwarf Sample

Name	SpT	$\zeta_{T,1}$	$\zeta_{T,2}$	$\zeta_{T,3}$	$\zeta_{T,4}$	ζ_T	Prior [Fe/H]	Model [M/H][a]
Benchmark Companions								
HD 3651B	T8	⋯	⋯	⋯	1.09 ± 0.20	1.09 ± 0.20	+0.14	0.00
HD 65486B	d/sdT4.5	⋯	1.01 ± 0.11	0.80 ± 0.29	0.89 ± 0.16	0.95 ± 0.11	−0.28	−0.53
LHS 6176B	d/sdT7.5	⋯	⋯	0.71 ± 0.34	0.77 ± 0.13	0.76 ± 0.12	−0.30	−0.21
Ross 458C	rT8.5	⋯	⋯	⋯	1.71 ± 0.30	1.71 ± 0.30	+0.25	+0.95
HD 126053B	sdT7.5	⋯	⋯	⋯	0.38 ± 0.08	0.38 ± 0.08	−0.38	−0.35
GJ 570D	T7.5	⋯	⋯	⋯	0.85 ± 0.16	0.85 ± 0.16	+0.05	−0.11
GJ 576B (GNIRS)	d/sdT5.5	⋯	0.92 ± 0.12	0.71 ± 0.26	0.63 ± 0.10	0.75 ± 0.16	−0.37	−0.47
⋯ (XS)	d/sdT5.5	⋯	0.94 ± 0.14	0.61 ± 0.41	0.56 ± 0.10	0.71 ± 0.21	−0.37	−0.53
⋯ (NIRES)	d/sdT5.5	⋯	0.96 ± 0.11	0.81 ± 0.43	0.74 ± 0.09	0.83 ± 0.13	−0.37	−0.21
G 204-39B	T6.5	⋯	1.01 ± 0.15	⋯	1.32 ± 0.21	1.11 ± 0.19	−0.04	+0.43
HN PegB	T2.5	1.17 ± 0.13	0.95 ± 0.07	1.13 ± 0.33	⋯	1.01 ± 0.11	−0.08	−0.11
Subdwarf Candidates								
J0055+5947	d/sdT6.5	⋯	0.99 ± 0.21	0.75 ± 0.34	0.75 ± 0.12	0.81 ± 0.15	⋯	+0.04
J0140+0150 (SpeX)	rT4.5	1.14 ± 0.22	1.03 ± 0.17	1.25 ± 0.40	1.16 ± 0.16	1.12 ± 0.11	⋯	+0.21
⋯ (NIRES)	rT4.5	1.16 ± 0.16	0.99 ± 0.10	⋯	1.17 ± 0.16	1.07 ± 0.11	⋯	+0.40
J0411+4714	d/sdT7.5	⋯	1.12 ± 0.17	0.77 ± 0.32	0.83 ± 0.14	0.95 ± 0.18	⋯	−0.12
J0429+3201	T1	1.07 ± 0.10	1.01 ± 0.06	0.96 ± 0.17	⋯	1.02 ± 0.06	⋯	⋯
J0433+1009	T8	⋯	1.08 ± 0.16	⋯	1.21 ± 0.40	1.10 ± 0.16	⋯	+0.12
J0623+0715	sdT3	0.68 ± 0.09	0.84 ± 0.06	0.67 ± 0.14	0.86 ± 0.12	0.79 ± 0.09	⋯	−0.68
J0659+1615	T1	1.00 ± 0.09	⋯	0.82 ± 0.14	⋯	0.95 ± 0.11	⋯	−0.03
J0758+5711	T6.5	⋯	1.09 ± 0.16	⋯	0.87 ± 0.14	0.97 ± 0.12	⋯	−0.17
J0845−3305	d/sdT6.5	⋯	0.92 ± 0.11	0.79 ± 0.28	0.79 ± 0.18	0.85 ± 0.11	⋯	−0.35
J0911+2146	d/sdT8	⋯	⋯	⋯	0.70 ± 0.17	0.70 ± 0.17	⋯	0.00
J1110−1747	rT8	⋯	⋯	⋯	1.20 ± 0.24	1.20 ± 0.24	⋯	+0.20
J1130+3139	d/sdT5.5	⋯	1.03 ± 0.15	⋯	0.79 ± 0.11	0.88 ± 0.12	⋯	−0.17
J1138+7212	d/sdT7	⋯	1.00 ± 0.24	0.67 ± 0.34	0.70 ± 0.12	0.76 ± 0.17	⋯	−0.36
J1204−2359	d/sdT7	⋯	1.13 ± 0.20	0.81 ± 0.39	0.82 ± 0.15	0.91 ± 0.18	⋯	−0.15
J1308−0321	d/sdT8	⋯	⋯	⋯	0.91 ± 0.18	0.91 ± 0.18	⋯	−0.11
J1401+4325	d/sdT5.5	⋯	0.88 ± 0.13	⋯	0.86 ± 0.14	0.87 ± 0.10	⋯	−0.13
J1458+1734	T8	⋯	⋯	⋯	1.12 ± 0.18	1.12 ± 0.18	⋯	+0.13
J1515−2157	d/sdT6	⋯	⋯	0.73 ± 0.31	0.71 ± 0.11	0.71 ± 0.11	⋯	−0.08
J1524−2620	sdT0	0.80 ± 0.08	⋯	⋯	⋯	0.80 ± 0.08	⋯	−0.69
J1710+4537	T6	⋯	1.01 ± 0.13	0.98 ± 0.40	0.95 ± 0.15	0.98 ± 0.10	⋯	+0.02
J1801+4717	d/sdT5	⋯	0.87 ± 0.10	⋯	0.94 ± 0.12	0.91 ± 0.09	⋯	−0.09
J2013−0326	d/sdT6	⋯	0.88 ± 0.11	⋯	0.76 ± 0.12	0.83 ± 0.10	⋯	−0.21
J2021+1524	d/sdL9	⋯	⋯	0.85 ± 0.13	⋯	0.85 ± 0.13	⋯	−0.35
J2112−0529	sdT1	0.89 ± 0.08	⋯	0.65 ± 0.14	⋯	0.79 ± 0.13	⋯	−0.74
J2112+3030	d/sdT2.5	0.90 ± 0.11	1.05 ± 0.07	0.72 ± 0.16	⋯	0.95 ± 0.14	⋯	−0.43
J2218+1146	d/sdT6.5	⋯	0.83 ± 0.13	⋯	0.86 ± 0.15	0.84 ± 0.09	⋯	−0.10
J2251−0740	d/sdT7	⋯	⋯	0.84 ± 0.39	0.88 ± 0.17	0.88 ± 0.16	⋯	0.00
Metal-poor Comparison Sources								
J0004−1336	d/sdT2:	0.98 ± 0.11	0.96 ± 0.08	0.75 ± 0.13	⋯	0.91 ± 0.11	⋯	−0.56
J0004−2604	T3	0.88 ± 0.10	0.93 ± 0.07	0.85 ± 0.18	⋯	0.91 ± 0.06	⋯	−0.40
J0013+0634	sdT7.5	⋯	1.37 ± 0.36	⋯	0.31 ± 0.06	0.32 ± 0.15	⋯	−0.61
J0021+1552	d/sdT4	0.83 ± 0.15	0.92 ± 0.13	0.65 ± 0.22	0.72 ± 0.14	0.81 ± 0.13	⋯	−0.44
J0301−2319	d/sdT1	0.89 ± 0.09	⋯	⋯	⋯	0.89 ± 0.09	⋯	−0.37
J0309−5016	d/sdT7.5	⋯	0.96 ± 0.16	⋯	0.50 ± 0.09	0.63 ± 0.22[b]	⋯	−0.36
J0348−5620	d/sdT4	0.83 ± 0.13	0.90 ± 0.09	0.82 ± 0.35	0.92 ± 0.13	0.89 ± 0.08	⋯	0.00
J0414−5854	esdT6:	0.48 ± 0.10	0.38 ± 0.08	0.12 ± 0.14	0.10 ± 0.10	0.27 ± 0.16[b]	⋯	−1.34
J0532+8246	esdL8:	0.58 ± 0.07	⋯	⋯	⋯	0.58 ± 0.07	−1.6	−1.53
J0616−6407	esdT0:	0.54 ± 0.06	⋯	⋯	⋯	0.54 ± 0.06	−1.6	−1.13
J0833+0052	d/sdT9	⋯	⋯	⋯	0.62 ± 0.12	0.62 ± 0.12	⋯	−0.08
J0937+2931	sdT6	⋯	0.88 ± 0.09	0.55 ± 0.33	0.52 ± 0.08	0.64 ± 0.18	⋯	−0.59
J0939−2448	d/sdT8	⋯	⋯	⋯	0.45 ± 0.10	0.45 ± 0.10	−0.24	−0.35
J0953−0943	d/sdT6	⋯	⋯	0.77 ± 0.24	0.79 ± 0.16	0.78 ± 0.13	⋯	−0.43
J1019−3911	T4	⋯	1.15 ± 0.15	0.79 ± 0.24	0.98 ± 0.13	1.00 ± 0.17	⋯	0.00
J1130−1158	sdT5.5	⋯	0.79 ± 0.15	0.39 ± 0.15	0.37 ± 0.10	0.52 ± 0.19[b]	⋯	−0.56
J1316+0755	sdT6.5	⋯	1.01 ± 0.23	0.34 ± 0.18	0.33 ± 0.06	0.56 ± 0.32[b]	⋯	−0.65

Table 13
(Continued)

Name	SpT	$\zeta_{T,1}$	$\zeta_{T,2}$	$\zeta_{T,3}$	$\zeta_{T,4}$	ζ_T	Prior [Fe/H]	Model [M/H][a]
J1416+1348B	sdT7	⋯	⋯	⋯	0.23 ± 0.05	0.23 ± 0.05	−0.35	−0.67
J1553+6933	sdT4	0.60 ± 0.08	0.66 ± 0.07	0.62 ± 0.17	0.68 ± 0.09	0.65 ± 0.05	⋯	−0.96
J1810−1010	esdT3:	0.43 ± 0.06	0.50 ± 0.05	0.69 ± 0.18	⋯	0.49 ± 0.07	−1.5	−1.27
J2105−6235	d/sdT2:	0.86 ± 0.09	0.91 ± 0.05	⋯	⋯	0.89 ± 0.05	⋯	−0.32

Notes.
[a] Based on best-fit spectral model; see Table 7.
[b] Individual $\zeta_{T,i}$ values differ by more than the uncertainties; reported ζ_T value and uncertainty are the unweighted mean and standard deviation of the individual $\zeta_{T,i}$ values.

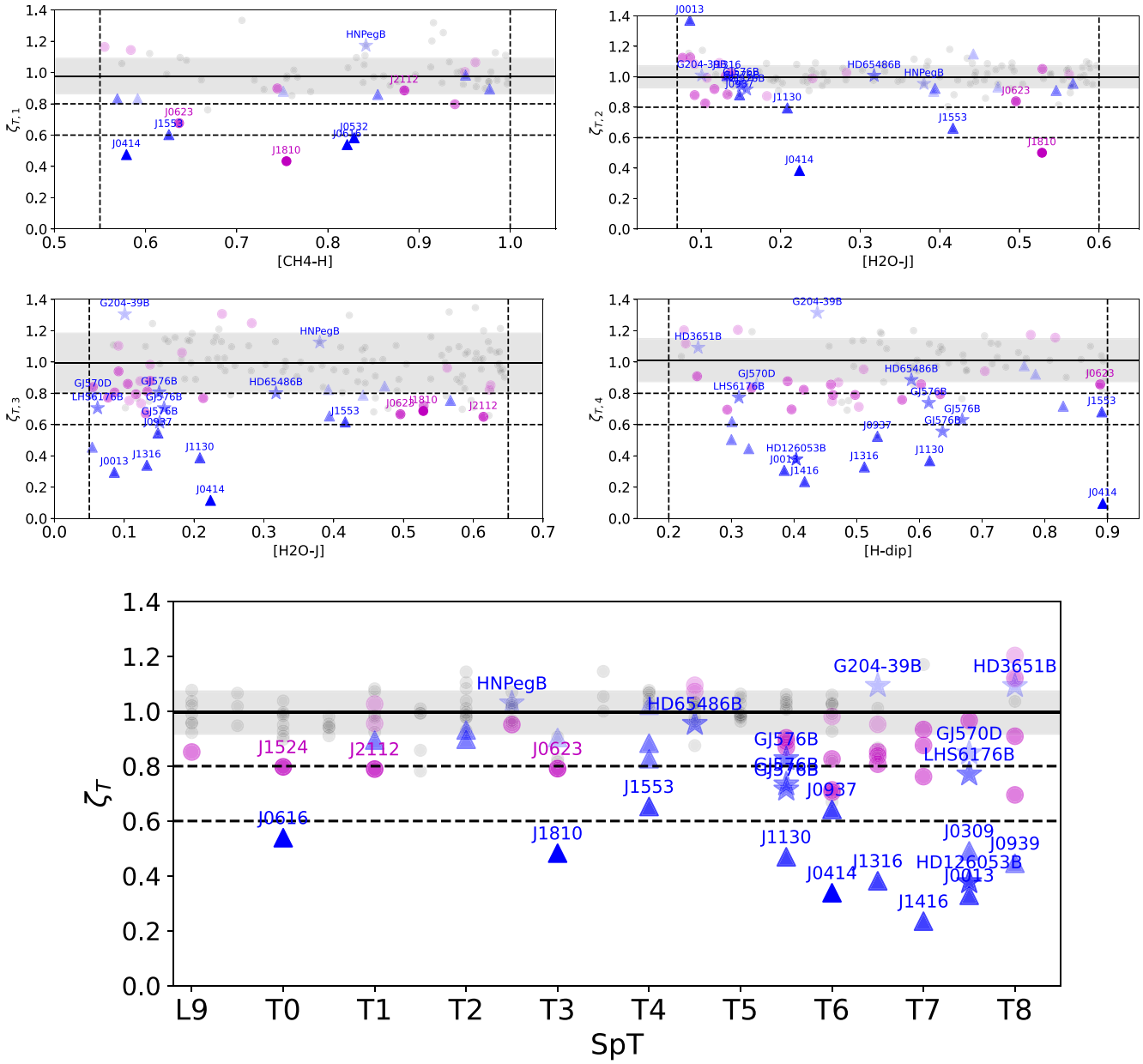

Figure 17. Individual metallicity indices $\zeta_{T,i}$ (top four panels) and mean metallicity index ζ_T (bottom panel) for our spectral sample. Symbols are the same as Figure 15. Each panel shows the median (solid line) and $\pm 1\sigma$ standard deviation (gray band) for local T dwarfs, with vertical dashed lines in the top four panels indicating the abscissa index range over which the solar-metallicity relation is defined (see Table 12). Horizontal dashed lines in each panel indicate threshold values of $\zeta_T = 0.8$ and 0.6. sdT and esdT candidates and comparison sources are labeled, as are all benchmark companions.

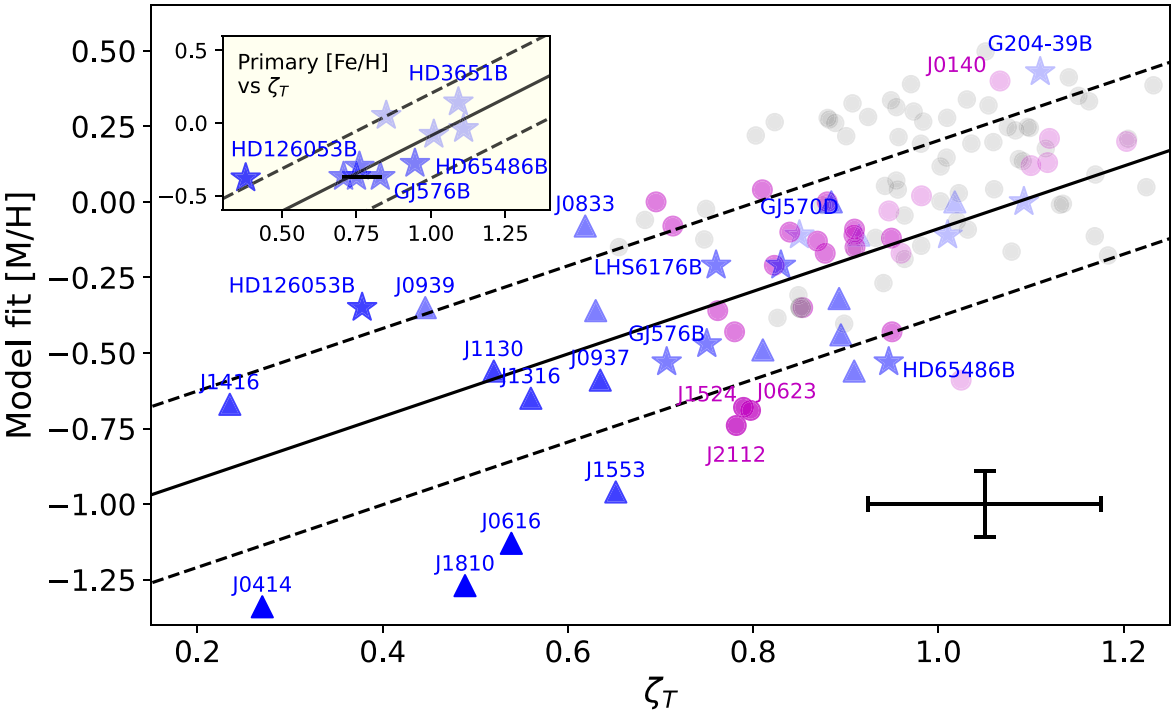

Figure 18. Main panel: comparison of ζ_T to total metallicity [M/H] from spectral model fits (Table 7). Symbols are the same as Figure 15. The error bar at bottom right indicates the median uncertainties in ζ_T and [M/H] for the entire sample. We include values for local T dwarfs (gray dots) based on best-fit LOWZ grid model fits, requiring model $T_{\rm eff} < 1600$ K and robust ζ_T measurements; an additional Gaussian scatter of 0.05 in ζ_T and [M/H] has been added to these values for clarity. The diagonal solid and dashed lines delineate the linear correlation between ζ_T and [M/H] and its 1σ uncertainty of 0.29 dex. Specific sources discussed in the text are labeled. Inset panel: comparison of ζ_T to iron abundance [Fe/H] for the primaries of our benchmark companions. HD 3651B, HD 65486B, HD 126053B, and GJ 576B are labeled. Note that Wolf 1130C and Wolf 940B do not appear on this plot as they lack measured ζ_T values. The diagonal solid and dashed lines delineate the linear correlation between ζ_T and primary [Fe/H] and its 1σ uncertainty of 0.12 dex.

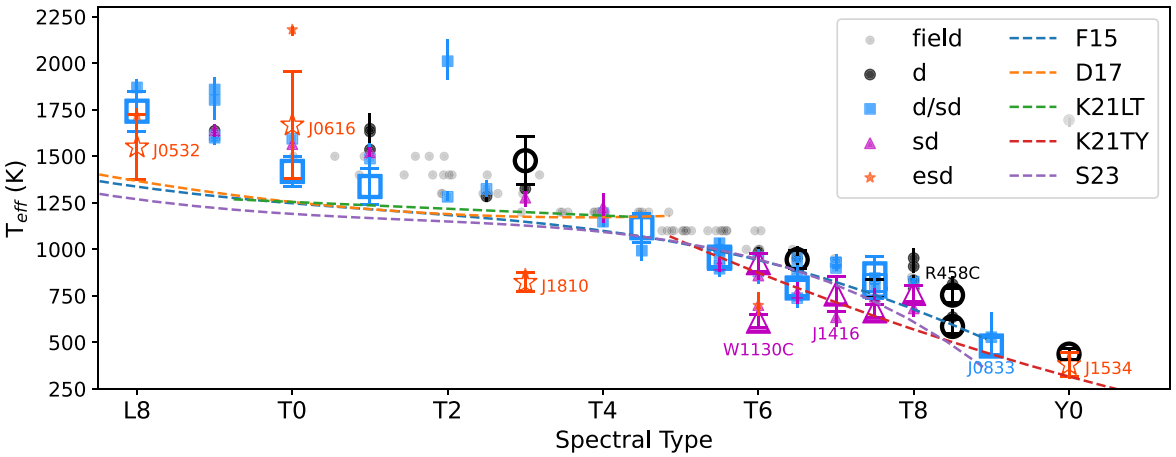

Figure 19. Inferred effective temperatures of sources in our spectral sample based on model fits as a function of numerical spectral type. Symbol shapes and colors encode the metallicity class, with small symbols representing temperatures from spectral model fits (Table 7) and large symbols representing bolometric temperatures for sources with measured parallaxes (Table 14). The light-gray circles represent spectral model-fit temperatures for our local T dwarf sample. Five spectral type/temperature relations for solar-metallicity dwarfs are shown for comparison: J. C. Filippazzo et al. (2015, F15), T. J. Dupuy & M. C. Liu (2017, D17), J. D. Kirkpatrick et al. (2021b, K21LT and K21TY), and A. Sanghi et al. (2023, S23).

2002a; T. J. Dupuy & M. C. Liu 2012). The absence of significant condensate opacity in metal-poor brown dwarf atmospheres could also modify the relationship between temperature and the evolution of spectral morphology. This discussion highlights the nontrivial systematic effects that may be present when inferring subdwarf temperatures from either spectral types or model fitting, and emphasizes the need for additional parallax measurements to infer robust atmospheric properties.

7.2. Prospects for Growing the Sample of T Subdwarfs

To deepen our understanding of the formation, evolution, and atmosphere properties of metal-poor brown dwarfs, it is necessary to expand the known sample of T and Y subdwarfs. Increasing the local sample (e.g., $d \lesssim 20$ pc) is a challenge given the sparsity of metal-poor stars in general and metal-poor brown dwarfs in particular, the latter estimated to be as low as 0.1% (A. C. Schneider et al. 2020). Nevertheless, this study's focus on relatively bright sources ($J < 18.5$) accessible from

Table 14
Bolometric Temperatures for T and Y Dwarf Benchmarks and Subdwarfs

Name	SpT	MKO J				WISE $W2$				Adopted	Model
		M_J (mag)	BC_J[a] (mag)	M_{bol} (mag)	T_B (K)	M_{W2} (mag)	BC_{W2}[a] (mag)	M_{bol} (mag)	T_B (K)	T_B (K)	T_B (K)
T Dwarf Benchmarks											
HD 3651B	T8	16.08 ± 0.03	2.73	18.81	801 ± 80	…[b]	…	…	…	801 ± 80	824^{+20}_{-31}
HD 65486B	d/sdT4.5	14.79 ± 0.08	2.29	17.08	1193 ± 119	12.53 ± 0.02	5.15	17.68	1039 ± 104	1116 ± 77	993^{+44}_{-47}
LHS 6176B	d/sdT7.5	16.56 ± 0.03	2.61	19.17	738 ± 74	13.03 ± 0.02	5.44	18.47	867 ± 87	802 ± 64	846^{+19}_{-6}
Ross 458C	rT8.5	15.02 ± 0.05	2.73	17.75	1023 ± 102	13.59 ± 0.02	5.52	19.10	750 ± 75	887 ± 137	812^{+38}_{-28}
HD 126053B	sdT7.5	17.50 ± 0.05	2.20	19.69	654 ± 65	13.57 ± 0.03	5.93	19.49	685 ± 69	670 ± 34	746^{+36}_{-28}
GJ 570D	T7.5	16.47 ± 0.05	2.67	19.15	742 ± 74	13.29 ± 0.01	5.34	18.63	836 ± 84	789 ± 47	837^{+20}_{-17}
GJ 576B	d/sdT5.5	15.19 ± 0.02	2.71	17.90	988 ± 99	12.91 ± 0.02	5.32	18.23	917 ± 92	953 ± 48	995^{+19}_{-21}
G 204−39B	T6.5	15.42 ± 0.09	2.66	18.09	947 ± 95	13.11 ± 0.01	5.18	18.28	905 ± 91	926 ± 46	984^{+25}_{-16}
Wolf 1130C	(e)sdT6:	18.54 ± 0.09	1.25	19.79	640 ± 64	13.77 ± 0.05	5.97	19.74	648 ± 65	644 ± 32	700^{+15}_{-0}[c]
Wolf 940B	T8.5	17.56 ± 0.06	2.36	19.92	621 ± 62	14.40 ± 0.06	6.05	20.45	550 ± 55	586 ± 35	636^{+32}_{-29}
HN PegB	T2.5	14.57 ± 0.03	2.19	16.75	1288 ± 129	…[b]	…	…	…	1288 ± 129	1284^{+42}_{-23}
T and Y Subdwarfs											
J0301−2319	d/sdT1	14.49 ± 0.26	2.24	16.74	1292 ± 130	11.95 ± 0.22	4.49	16.44	1383 ± 139	1338 ± 96	1488^{+77}_{-73}
J0309−5016	d/sdT7.5	16.29 ± 0.13	2.66	18.96	775 ± 78	12.75 ± 0.13	5.27	18.02	961 ± 96	868 ± 93	795^{+55}_{-27}
J0532+8246	esdL8:	13.23 ± 0.06	2.26	15.48	1725 ± 173	11.73 ± 0.03	4.73	16.47	1376 ± 138	1550 ± 175	1730^{+43}_{-46}
J0616−6407	esdT0:	12.8 ± 0.7	2.3	15.10	1884 ± 197	11.7 ± 0.7	4.58	16.2	1452 ± 152	1668 ± 288	2181^{+14}_{-26}[d]
J0645−6646	d/sdT0	14.18 ± 0.12	2.04	16.21	1458 ± 146	11.96 ± 0.12	4.49	16.45	1380 ± 138	1419 ± 81	1594^{+25}_{-20}
J0833+0052	d/sdT9	19.86 ± 0.15	1.62	21.49	433 ± 43	14.49 ± 0.12	6.13	20.63	528 ± 53	480 ± 48	528^{+129}_{-28}[d]
J0850−0221	d/sdL6.5	12.70 ± 0.11	1.96	14.66	2086 ± 209	10.36 ± 0.10	4.23	14.58	2121 ± 212	2104 ± 115	1852^{+48}_{-81}
J0937+2931	sdT6	15.71 ± 0.04	2.57	18.28	906 ± 91	12.74 ± 0.03	5.33	18.07	952 ± 95	929 ± 47	859^{+28}_{-15}
J0939−2448	d/sdT8	17.13 ± 0.12	2.37	19.50	683 ± 68	13.10 ± 0.12	5.44	18.54	853 ± 85	768 ± 85	682^{+51}_{-40}
J1158+0435	d/sdL8	13.47 ± 0.16	1.96	15.43	1745 ± 175	11.22 ± 0.16	4.23	15.45	1739 ± 174	1742 ± 107	1870^{+40}_{-64}
J1416+1348B	sdT7	17.42 ± 0.02	2.20	19.62	666 ± 67	12.94 ± 0.04	5.59	18.54	854 ± 85	760 ± 94	635^{+68}_{-42}
J1810−1010	esdT3:	17.52 ± 0.16	1.42	18.95	777 ± 78	12.84 ± 0.16	5.50	18.34	893 ± 90	835 ± 58	869^{+5}_{-13}
J1534−1043	(e)sdY:	23.4 ± 0.3	−0.56[d]	22.9	314 ± 32	15.09 ± 0.19	6.26[e]	21.35	447 ± 45	381 ± 67	…

Notes.
[a] Bolometric corrections computed from the LOWZ models assuming $\log g = 5.0$ (cgs), $\log k_{zz} = 2$ (cgs), C/O = 0.55, a metallicity based on the source classification ([M/H] = 0 for dwarfs, [M/H] = −0.25 for mild subdwarfs, [M/H] = −0.75 for subdwarfs, and [M/H] = −1.5 for extreme subdwarfs), and the closest temperature to T_B in the model grid. See Appendix B for the full list of bolometric corrections.
[b] The proximity of a bright stellar companion prevents WISE detection of this source.
[c] Fit T_{eff} at limit of model parameters.
[d] Model fit produces nonphysically small radius ($R \lesssim 0.05\ R_\odot$), suggesting an overestimated T_{eff}.
[e] Using the BC value for $T_{eff} = 500$ K and [M/H] = −1.5.

the northern hemisphere means that several promising T subdwarf candidates remain to be characterized in the BYW sample alone (see H. Brooks et al. 2022; A. M. Meisner et al. 2023).

Current and forthcoming deep imaging and spectroscopic surveys are also expected to substantially increase the number of halo brown dwarfs with photometric, spectroscopic, and astrometric characterization. In addition to the individual discoveries now being made in deep pointings with JWST to limiting magnitudes of ≈30 AB (M. Nonino et al. 2023; K. Glazebrook et al. 2023; P.-Y. Wang et al. 2023; A. J. Burgasser et al. 2024; K. N. Hainline et al. 2024; B. W. Holwerda et al. 2024), the recently launched Euclid mission is expected to detect of the order of 10^4 thick disk and 10^3 halo T dwarfs in its 15,000 deg^2 wide-field survey, reaching $YJH \approx 24.5$ AB (R. Laureijs et al. 2011; Z. H. Zhang et al. 2019b; E. Solano et al. 2021). A significant fraction of these sources will also be observed with Euclid's slitless spectroscopic mode, yielding 1.25–1.85 μm spectra at $\lambda/\Delta\lambda \approx 250$ for potentially hundreds of metal-poor brown dwarfs. Starting in the late 2020s, the Nancy Grace Roman Space Telescope's High Latitude Wide Area Imaging Survey, spanning 2000 deg^2 to $YJH \approx 27$ AB (M. A. Troxel et al. 2021), is expected to detect 5×–10× more sources than Euclid (Z. H. Zhang et al. 2019b). This survey is also matched to a spectroscopic survey that will acquire 1.0–1.93 μm spectra at $\lambda/\Delta\lambda \approx 400$–800, covering many of the metallicity-sensitive features examined in this study. These infrared surveys will be complemented by optical photometry from the Vera Rubin Observatory Large Survey of Space and Time (LSST; Ž. Ivezić et al. 2019). While this survey will detect few halo brown dwarfs due to its poor sensitivity at low temperatures (10–100 s over the Southern sky; Z. H. Zhang et al. 2019b), it will provide useful color limits and y-band dectections for refining candidate samples.

The multiepoch astrometry of all three surveys will enable identification of candidate nearby halo brown dwarfs through reduced proper-motion constraints, candidates that can be spectroscopically confirmed with JWST or planned 30-meter class ground-based facilities. In short, the limited sample presented here is a small fraction of the halo brown dwarf

population expected to be discovered and explored over the next decade, primarily by space-based infrared surveys that continue the legacy of WISE.

8. Summary

This work has presented a comprehensive study of the spectroscopic properties of currently known metal-poor T dwarfs, augmented with new discoveries from the Backyard Worlds: Planet 9 program. Our key results are as follows:

1. Using photometric and astrometric data from several wide-field infrared surveys, most notably the CatWISE2020 catalog, and imposing color and reduced proper-motion constraints, we identified a sample of 95 high-probability, bright ($J \leqslant 18.5$) T subdwarf candidates visible from the northern hemisphere, which includes several previously reported metal-poor brown dwarfs (A. C. Schneider et al. 2020; A. M. Meisner et al. 2020; J. D. Kirkpatrick et al. 2021b, 2024).
2. Near-infrared spectroscopic follow-up with Keck/NIRES, IRTF/SpeX, APO/TSpec, Magellan/FIRE, and Gemini-N/GNIRS of a subset of these candidates has allowed us to identify three new T subdwarfs: the sdT0 J1524−2620, the sdT1 J2112−0529, and the sdT3 J0623+0715. We also identify 19 new mildly metal-poor T dwarfs. These identifications are based on metallicity-sensitive spectral features, including a broadened 1.1 μm absorption band, suppressed 2.1 μm peak emission, and weak or absent K I lines at 1.17 and 1.25 μm.
3. Atmospheric model fits to the spectra of candidate and previously reported late-L and -T subdwarfs and benchmark companions allowed us to validate the metal-poor nature of our candidates, as well as identify several prior discoveries as normal dwarfs. Comparing to several sets of spectral models, we find that the LOWZ models (A. M. Meisner et al. 2021) typically provide the best fits for all brown dwarfs with 800 K $\lesssim T_{\rm eff} \lesssim$ 1600 K, the SAND models (E. Alvarado et al. 2024) perform better at higher temperatures and low metallicities, and the ElfOwl models (S. Mukherjee et al. 2024) perform better at lower temperatures and near-solar metallicities. Notably, the SAND models provide self-consistent fits to the spectra of extreme L subdwarfs (e.g., J0532+8246) and T subdwarfs (e.g., J1810–1010), indicating that these models are well suited for metal-poor brown dwarfs.
4. By forward-modeling moderate-resolution Keck/NIRES spectral data, we measured the radial velocities of 27 candidate and comparison late-L and -T subdwarfs. The corresponding *UVW* velocities are more dispersed than the local T dwarfs, and several sources have velocities consistent with the thick disk or halo populations. Two subdwarfs, the esdL8 J0532+8246 and the d/sdT5.5 J1130+3139, have retrograde Galactic orbits potentially consistent with the Thamnos stream; while the sdT4 J1553+6933 has a motion potentially consistent with the Helmi stream. We also identify three sources with thick disk kinematics that appear to be metal-rich, and may be part of the high-velocity thick disk that originated in the inner Milky Way.
5. We used our spectral sample to construct a metallicity classification system for T dwarfs anchored to spectral standards. Our scheme encompasses classes of mild subdwarfs (d/sdT), subdwarfs (sdT), and extreme subdwarfs (esdT), with estimated metallicities of [M/H] ≈ -0.4, [M/H] ≈ -0.6, and [M/H] ≈ -1.3, respectively, matching the metallicity scales of M and L subdwarfs. We have defined a near-infrared index to quantify metallicity, ζ_T, and demonstrated that this index correlates with the metallicities inferred from spectral model fitting and the iron abundances measured from the primaries of a small sample of benchmark T dwarf companions.
6. We examined the relationship between effective temperature and spectral type for brown dwarfs of differing metallicities, and find that late-L and early-T subdwarfs are generally warmer, and mid- and late-T subdwarfs are generally cooler than equivalently classified solar-metallicity dwarfs. The latter offset may be due to the enhanced H_2 absorption and reduced C and O abundances weakening the molecular bands used for spectral classification, while the switch from warmer to cooler may be driven by a reduction in condensate opacity in subdwarfs.

The sample explored here encompasses nearly all of the lowest-temperature, metal-poor brown dwarfs currently known, but it is in no way complete. In addition to T subdwarf candidates identified at southern decls. and fainter magnitudes by the BYW program, additional yields from JWST, Euclid, LSST, and the Nancy Grace Roman Space Telescope are expected to dramatically expand our sample of T subdwarfs from tens to thousands. Adding these discoveries to the known T subdwarf sample will provide a more robust assessment of the diversity of metal-poor brown dwarf atmospheres, including variations in individual elemental abundances that are tied to distinct Milky Way populations. Both near-infrared spectroscopy and parallax measurements for these sources will be crucial, the latter providing an essential constraint on bolometric luminosity to calibrate spectral model fits. Indeed, our study demonstrates that advances in metal-poor atmosphere modeling, as illustrated by the SAND models, yield more reliable fits and self-consistent radii for absolute flux densities. We anticipate that our assessment of the currently known T subdwarf population and this first approach at T dwarf metallicity classification will require revision as future searches, observations, and modeling are undertaken.

Acknowledgments

We thank our telescope operators and instrument scientists at Keck Observatory, the NASA Infrared Telescope Facility, and Apache Point Observatory for their assistance in the acquisition of the spectral data reported here. APO/TSpec data were acquired and reduced by Katelyn Allers. We thank Ben Burningham, Nicolas Lodieu, Kevin Luhman, Greg Mace, David Pinfield, and Zenghua Zhang for making digital versions of their published data available; we thank Michael Cushing for providing modified versions of Spextool available for Keck/NIRES and APO/TSpec reduction. We also thank our referee, Zenghua Zhang, for a careful review of our manuscript and constructive feedback that improved the analysis. The Backyard Worlds: Planet 9 team acknowledges the many Zooniverse volunteers who have participated in this project, from providing feedback during the beta review stage to classifying

flipbooks to contributing to discussions on TALK. This material is based upon work supported by the National Science Foundation under grant No. 2009136. This research has made use of the Spanish Virtual Observatory (https://svo.cab.inta-csic.es) project funded by MCIN/AEI/10.13039/501100011033/ through grant PID2020-112949GB-I00 Data presented herein were obtained at the W.M. Keck Observatory, which is operated as a scientific partnership among the California Institute of Technology, the University of California, and the National Aeronautics and Space Administration. The Observatory was made possible by the generous financial support of the W.M. Keck Foundation. This publication makes use of data products from the Wide-field Infrared Survey Explorer, which is a joint project of the University of California, Los Angeles, and the Jet Propulsion Laboratory/California Institute of Technology, and NEOWISE, which is a project of the Jet Propulsion Laboratory/California Institute of Technology. WISE and NEOWISE are funded by the National Aeronautics and Space Administration. Part of this research was carried out at the Jet Propulsion Laboratory, California Institute of Technology, under a contract with the National Aeronautics and Space Administration. This research has benefitted from the SpeX Prism Spectral Libraries, maintained by Adam Burgasser at https://splat.physics.ucsd.edu/splat/. This research has made use of the SIMBAD database (M. Wenger et al. 2000), the Aladin sky atlas (F. Bonnarel et al. 2000), and the VizieR catalog access tool developed and operated at CDS, Strasbourg, France. The authors recognize and acknowledge the significant cultural role and reverence that the summit of Maunakea has with the indigenous Hawaiian community, and that the W. M. Keck Observatory stands on Crown and Government Lands that the State of Hawaii is obligated to protect and preserve for future generations of indigenous Hawaiians. Portions of this work were conducted at the University of California, San Diego, which was built on the unceded territory of the Kumeyaay Nation, whose people continue to maintain their political sovereignty and cultural traditions as vital members of the San Diego community.

Facility: Keck:II (NIRES), IRTF (SpeX), ARC (TripleSpec), Magellan:Baade (FIRE), Gemini:Gillett (GNIRS).

Software: astropy (Astropy Collaboration et al. 2013, 2018, 2022), Matplotlib (J. D. Hunter 2007), NumPy (S. van der Walt et al. 2011), pandas (W. McKinney 2010), SciPy (P. Virtanen et al. 2020), SpeXTool (M. C. Cushing et al. 2004), SPLAT (A. J. Burgasser & Splat Development Team 2017).

Appendix A
IRTF/SpeX Comparison Sample

The following Tables provide the measured spectral indices (Table 15) and LOWZ model-fit parameters (Table 16) for a sample of 184 late-L and -T dwarfs with low-resolution near-infrared spectra obtained with the IRTF/SpeX instrument (J. T. Rayner et al. 2003) and curated in the SPLAT archive (A. J. Burgasser & Splat Development Team 2017). Data references for the individual spectra are included in the Table endnotes. The model fits for these data were conducted exclusively on the individual grid models without interpolation.

Table 15
Index Measurements for Dwarf Late-L and -T Dwarf Sample

Designation	SpT[a]	[CH4-J]	[CH4-H]	[CH4-K]	[H2O-J]	[H2O-H]	[H2O-K]	[Y/J]	[K/H]	[K/J]	[H-dip]	$\langle\zeta_T\rangle$	References
J00001354+2554180	T4.5	0.549 ± 0.015	0.548 ± 0.006	0.259 ± 0.005	0.327 ± 0.002	0.349 ± 0.005	0.480 ± 0.004	0.476 ± 0.005	0.352 ± 0.002	0.197 ± 0.001	0.738 ± 0.008	1.00 ± 0.09	[3]
J00062785+1857288	L7	1.011 ± 0.021	1.056 ± 0.018	1.001 ± 0.013	0.727 ± 0.018	0.781 ± 0.017	0.809 ± 0.013	0.508 ± 0.013	0.711 ± 0.011	0.691 ± 0.011	0.995 ± 0.012	0.93 ± 0.12	[29]
J00150206+2959323	L7	0.982 ± 0.013	1.047 ± 0.016	0.924 ± 0.009	0.773 ± 0.011	0.743 ± 0.012	0.770 ± 0.011	0.585 ± 0.011	0.658 ± 0.008	0.583 ± 0.007	0.983 ± 0.010	0.85 ± 0.10	[12]
J00164396+2304267	T0.0	0.704 ± 0.012	1.005 ± 0.013	0.798 ± 0.015	0.559 ± 0.010	0.534 ± 0.011	0.675 ± 0.013	0.578 ± 0.010	0.573 ± 0.009	0.449 ± 0.006	1.010 ± 0.012	1.04 ± 0.06	[28]
…	…	0.752 ± 0.012	1.046 ± 0.015	0.796 ± 0.011	0.555 ± 0.011	0.564 ± 0.012	0.668 ± 0.012	0.602 ± 0.013	0.594 ± 0.008	0.465 ± 0.006	1.045 ± 0.011	0.99 ± 0.07	[29]
J00185151+5153306	L7.0	0.845 ± 0.020	1.122 ± 0.019	1.011 ± 0.013	0.662 ± 0.017	0.710 ± 0.018	0.798 ± 0.011	0.481 ± 0.016	0.829 ± 0.017	0.893 ± 0.016	1.015 ± 0.016	1.20 ± 0.15	[28]
J00311004+5749363	L8	0.900 ± 0.009	1.030 ± 0.009	0.843 ± 0.007	0.653 ± 0.007	0.658 ± 0.007	0.687 ± 0.007	0.582 ± 0.009	0.655 ± 0.007	0.591 ± 0.005	1.028 ± 0.007	0.99 ± 0.15	[20]
…	…	0.940 ± 0.007	1.073 ± 0.007	0.837 ± 0.005	0.653 ± 0.005	0.656 ± 0.007	0.678 ± 0.005	0.600 ± 0.006	0.651 ± 0.005	0.570 ± 0.004	1.021 ± 0.005	0.98 ± 0.15	[34]
J00325937+1410371	L8	0.884 ± 0.014	1.032 ± 0.014	0.840 ± 0.013	0.635 ± 0.013	0.673 ± 0.014	0.693 ± 0.012	0.591 ± 0.014	0.656 ± 0.009	0.626 ± 0.009	1.033 ± 0.011	0.99 ± 0.13	[11]
…	…	0.876 ± 0.010	1.034 ± 0.010	0.838 ± 0.009	0.695 ± 0.010	0.664 ± 0.009	0.714 ± 0.009	0.669 ± 0.013	0.655 ± 0.007	0.570 ± 0.006	1.023 ± 0.009	0.95 ± 0.13	[11]
J00345157+0523050	T6.5	0.420 ± 0.007	0.227 ± 0.004	0.120 ± 0.007	0.102 ± 0.001	0.209 ± 0.006	0.427 ± 0.009	0.450 ± 0.005	0.217 ± 0.002	0.100 ± 0.001	0.485 ± 0.015	0.82 ± 0.21	[1]
J00440332+0228112	L7p (red)	0.857 ± 0.012	1.215 ± 0.017	1.140 ± 0.010	0.664 ± 0.011	0.703 ± 0.012	0.888 ± 0.013	0.437 ± 0.010	0.834 ± 0.012	0.814 ± 0.010	1.017 ± 0.011	1.21 ± 0.18	[33]
…	…	0.936 ± 0.021	1.212 ± 0.026	1.110 ± 0.015	0.660 ± 0.022	0.729 ± 0.020	0.872 ± 0.013	0.454 ± 0.018	0.830 ± 0.016	0.768 ± 0.019	0.996 ± 0.016	1.18 ± 0.19	[32]
J00454256+3611391	T5	0.408 ± 0.009	0.393 ± 0.008	0.201 ± 0.013	0.197 ± 0.003	0.325 ± 0.007	0.457 ± 0.010	0.555 ± 0.007	0.379 ± 0.005	0.175 ± 0.002	0.616 ± 0.013	1.02 ± 0.13	[21]
J00492826+0440575	L9	0.916 ± 0.008	1.031 ± 0.008	0.854 ± 0.006	0.728 ± 0.007	0.708 ± 0.007	0.695 ± 0.007	0.599 ± 0.006	0.662 ± 0.004	0.639 ± 0.005	1.011 ± 0.006	0.91 ± 0.15	[16]
J00550564+0134365	L7	0.920 ± 0.009	1.152 ± 0.011	1.101 ± 0.007	0.759 ± 0.007	0.786 ± 0.009	0.870 ± 0.009	0.491 ± 0.006	0.735 ± 0.006	0.624 ± 0.005	1.007 ± 0.008	0.93 ± 0.12	[33]
J00575764+2013040	sdL7	0.837 ± 0.012	1.024 ± 0.015	0.948 ± 0.017	0.657 ± 0.011	0.587 ± 0.014	0.700 ± 0.016	0.569 ± 0.014	0.533 ± 0.009	0.382 ± 0.007	0.967 ± 0.012	0.85 ± 0.13	[25]
…	…	0.717 ± 0.006	1.049 ± 0.006	0.908 ± 0.006	0.694 ± 0.004	0.670 ± 0.008	0.668 ± 0.006	0.523 ± 0.006	0.598 ± 0.004	0.392 ± 0.003	0.989 ± 0.004	0.87 ± 0.11	[23]
J01020186+0355405	L9	0.937 ± 0.019	1.050 ± 0.016	0.815 ± 0.014	0.637 ± 0.018	0.592 ± 0.014	0.656 ± 0.012	0.628 ± 0.040	0.666 ± 0.011	0.632 ± 0.010	1.042 ± 0.014	1.07 ± 0.19	[29]
J01352531+0205232	L9.5	1.045 ± 0.009	1.094 ± 0.010	0.900 ± 0.009	0.674 ± 0.009	0.606 ± 0.011	0.616 ± 0.012	0.609 ± 0.008	0.636 ± 0.007	0.555 ± 0.006	1.054 ± 0.008	0.98 ± 0.13	[33]
J01365662+0933473	T2.5	0.754 ± 0.004	0.840 ± 0.003	0.552 ± 0.003	0.493 ± 0.001	0.482 ± 0.003	0.590 ± 0.002	0.531 ± 0.004	0.448 ± 0.001	0.307 ± 0.001	0.970 ± 0.003	1.03 ± 0.07	[9]
J01383658−0322212	T3	0.638 ± 0.008	0.760 ± 0.008	0.684 ± 0.011	0.410 ± 0.006	0.541 ± 0.008	0.632 ± 0.011	0.552 ± 0.008	0.472 ± 0.005	0.308 ± 0.003	0.901 ± 0.009	0.83 ± 0.06	[16]
J01414839−1601196	L7:	0.984 ± 0.016	1.080 ± 0.022	0.942 ± 0.019	0.720 ± 0.019	0.651 ± 0.028	0.690 ± 0.017	0.562 ± 0.020	0.715 ± 0.017	0.636 ± 0.012	0.961 ± 0.018	1.03 ± 0.15	[12]
J01453520−0314117	L9	0.686 ± 0.011	1.003 ± 0.010	0.849 ± 0.008	0.703 ± 0.009	0.715 ± 0.010	0.722 ± 0.010	0.681 ± 0.010	0.674 ± 0.007	0.627 ± 0.006	1.031 ± 0.008	0.94 ± 0.13	[33]
J01501089+3827241	T0	0.848 ± 0.010	0.973 ± 0.006	0.795 ± 0.006	0.670 ± 0.005	0.662 ± 0.006	0.674 ± 0.005	0.594 ± 0.007	0.596 ± 0.004	0.516 ± 0.003	1.006 ± 0.005	0.89 ± 0.07	[16]
…	…	0.904 ± 0.032	0.997 ± 0.021	0.807 ± 0.013	0.706 ± 0.025	0.661 ± 0.018	0.676 ± 0.012	0.622 ± 0.030	0.634 ± 0.012	0.597 ± 0.016	1.000 ± 0.015	0.93 ± 0.07	[31]
J01514155+1244300	T1	0.821 ± 0.011	0.949 ± 0.008	0.707 ± 0.007	0.671 ± 0.005	0.625 ± 0.008	0.615 ± 0.008	0.608 ± 0.008	0.512 ± 0.004	0.431 ± 0.002	1.026 ± 0.007	0.85 ± 0.10	[1]
J02022929+2305139	L7	0.974 ± 0.022	1.188 ± 0.019	1.050 ± 0.013	0.669 ± 0.018	0.676 ± 0.015	0.753 ± 0.011	0.467 ± 0.014	0.798 ± 0.014	0.778 ± 0.013	1.004 ± 0.016	1.17 ± 0.19	[32]
J02062527+2640236	L9p (red)	0.890 ± 0.012	1.076 ± 0.008	0.935 ± 0.007	0.680 ± 0.008	0.683 ± 0.008	0.731 ± 0.006	0.574 ± 0.010	0.816 ± 0.007	0.854 ± 0.008	1.031 ± 0.007	1.19 ± 0.14	[16]
J02101025+4008296	T4.5	0.536 ± 0.010	0.502 ± 0.011	0.248 ± 0.017	0.331 ± 0.005	0.365 ± 0.013	0.472 ± 0.014	0.477 ± 0.009	0.366 ± 0.006	0.197 ± 0.003	0.670 ± 0.012	1.02 ± 0.07	[21]
J02260916−1610004	L7p (red)	0.965 ± 0.023	1.198 ± 0.026	1.067 ± 0.013	0.686 ± 0.024	0.748 ± 0.023	0.900 ± 0.012	0.425 ± 0.024	0.948 ± 0.022	0.995 ± 0.022	0.992 ± 0.019	1.31 ± 0.16	[32]
J02303885−0225471	L8:p	0.924 ± 0.015	1.057 ± 0.017	0.840 ± 0.012	0.633 ± 0.013	0.613 ± 0.015	0.705 ± 0.011	0.658 ± 0.018	0.708 ± 0.012	0.720 ± 0.011	1.051 ± 0.013	1.12 ± 0.17	[34]
J02431371−2453298	T6	0.403 ± 0.006	0.332 ± 0.005	0.157 ± 0.005	0.141 ± 0.002	0.282 ± 0.005	0.455 ± 0.007	0.446 ± 0.005	0.386 ± 0.003	0.191 ± 0.001	0.538 ± 0.009	1.07 ± 0.15	[1]
J02550357−4700509	L8	0.830 ± 0.013	1.034 ± 0.004	0.837 ± 0.005	0.681 ± 0.003	0.680 ± 0.005	0.686 ± 0.003	0.567 ± 0.005	0.647 ± 0.004	0.593 ± 0.003	1.026 ± 0.004	0.94 ± 0.14	[3]
J02572581−3105523	L8	0.915 ± 0.010	1.054 ± 0.010	0.899 ± 0.007	0.717 ± 0.006	0.733 ± 0.007	0.723 ± 0.007	0.583 ± 0.007	0.712 ± 0.006	0.685 ± 0.008	1.015 ± 0.010	0.97 ± 0.10	[5]
J03162759+2650277	T2.5	0.640 ± 0.010	0.767 ± 0.009	0.577 ± 0.012	0.438 ± 0.005	0.478 ± 0.009	0.541 ± 0.011	0.565 ± 0.009	0.432 ± 0.005	0.282 ± 0.003	0.931 ± 0.009	0.95 ± 0.06	[31]
J03230186+5625580	L7	0.929 ± 0.012	1.103 ± 0.010	1.009 ± 0.009	0.667 ± 0.012	0.688 ± 0.010	0.767 ± 0.007	0.489 ± 0.012	0.772 ± 0.008	0.770 ± 0.008	1.015 ± 0.008	1.13 ± 0.18	[25]
J03244023−1919056	L8p (blue)	0.950 ± 0.014	1.020 ± 0.013	0.884 ± 0.013	0.733 ± 0.013	0.687 ± 0.015	0.715 ± 0.011	0.587 ± 0.011	0.630 ± 0.009	0.572 ± 0.007	0.999 ± 0.013	0.88 ± 0.12	[32]
J03255322+0425406	T5.5	0.499 ± 0.005	0.367 ± 0.008	0.224 ± 0.012	0.202 ± 0.005	0.311 ± 0.011	0.455 ± 0.014	0.445 ± 0.011	0.286 ± 0.005	0.144 ± 0.003	0.590 ± 0.011	0.90 ± 0.09	[2]
J03284265+2302051	L8	0.907 ± 0.010	0.997 ± 0.011	0.828 ± 0.009	0.645 ± 0.008	0.636 ± 0.011	0.652 ± 0.008	0.601 ± 0.010	0.617 ± 0.006	0.573 ± 0.006	1.005 ± 0.008	0.96 ± 0.07	[9]
J03490944+1514360	L7p	1.107 ± 0.020	1.181 ± 0.021	1.086 ± 0.013	0.678 ± 0.020	0.731 ± 0.019	0.905 ± 0.011	0.469 ± 0.019	0.983 ± 0.015	1.200 ± 0.025	1.020 ± 0.017	1.38 ± 0.20	[28]
J04070885+1514565	T5	0.521 ± 0.010	0.369 ± 0.006	0.167 ± 0.005	0.236 ± 0.003	0.349 ± 0.008	0.418 ± 0.009	0.415 ± 0.011	0.402 ± 0.003	0.204 ± 0.002	0.591 ± 0.016	1.02 ± 0.16	[1]
J04151954−0935066	T8	0.232 ± 0.005	0.106 ± 0.003	0.054 ± 0.006	0.038 ± 0.002	0.159 ± 0.004	0.319 ± 0.007	0.348 ± 0.005	0.274 ± 0.002	0.150 ± 0.001	0.220 ± 0.007	1.20 ± 0.20	[1]
J04373705+2331080	L7.0	1.018 ± 0.021	1.189 ± 0.031	1.140 ± 0.019	0.792 ± 0.019	0.766 ± 0.024	0.974 ± 0.017	0.606 ± 0.025	0.760 ± 0.018	0.706 ± 0.015	1.000 ± 0.019	0.96 ± 0.11	[24]
J04574602−0207179	T2	0.708 ± 0.006	0.822 ± 0.005	0.522 ± 0.005	0.456 ± 0.002	0.480 ± 0.006	0.583 ± 0.005	0.487 ± 0.005	0.472 ± 0.003	0.305 ± 0.002	0.918 ± 0.005	0.99 ± 0.05	[34]
J05065020+5236312	T4.5	0.515 ± 0.009	0.496 ± 0.011	0.248 ± 0.012	0.254 ± 0.004	0.320 ± 0.011	0.458 ± 0.015	0.450 ± 0.008	0.372 ± 0.007	0.190 ± 0.003	0.724 ± 0.017	1.03 ± 0.07	[28]
J05160945−0445499	T5.5	0.480 ± 0.007	0.336 ± 0.005	0.159 ± 0.007	0.194 ± 0.003	0.296 ± 0.005	0.416 ± 0.007	0.394 ± 0.005	0.363 ± 0.003	0.182 ± 0.001	0.510 ± 0.009	1.06 ± 0.10	[9]
J05591914−1404488	T4.5	0.592 ± 0.004	0.482 ± 0.009	0.240 ± 0.007	0.347 ± 0.004	0.401 ± 0.012	0.502 ± 0.008	0.460 ± 0.005	0.351 ± 0.004	0.184 ± 0.001	0.671 ± 0.011	0.97 ± 0.07	[3]
J06020638+4043588	T4.5	0.572 ± 0.009	0.461 ± 0.008	0.252 ± 0.016	0.302 ± 0.005	0.344 ± 0.009	0.469 ± 0.013	0.471 ± 0.008	0.355 ± 0.005	0.179 ± 0.002	0.716 ± 0.014	1.01 ± 0.07	[6]
J06073865+2429535	L8	0.930 ± 0.004	1.020 ± 0.002	0.847 ± 0.002	0.687 ± 0.001	0.673 ± 0.003	0.701 ± 0.002	0.534 ± 0.003	0.680 ± 0.002	0.656 ± 0.002	1.013 ± 0.002	0.99 ± 0.16	[22]
…	…	0.893 ± 0.006	1.003 ± 0.003	0.839 ± 0.002	0.700 ± 0.002	0.683 ± 0.004	0.703 ± 0.003	0.581 ± 0.004	0.644 ± 0.002	0.597 ± 0.002	1.016 ± 0.002	0.92 ± 0.12	[19]
J06113513−0410240	T0	0.810 ± 0.015	0.925 ± 0.015	0.743 ± 0.018	0.584 ± 0.013	0.600 ± 0.015	0.662 ± 0.017	0.566 ± 0.016	0.553 ± 0.010	0.433 ± 0.007	1.021 ± 0.017	0.95 ± 0.05	[16]
J06272007−1114280	T6	0.399 ± 0.008	0.324 ± 0.007	0.155 ± 0.013	0.158 ± 0.003	0.278 ± 0.009	0.452 ± 0.011	0.425 ± 0.007	0.358 ± 0.005	0.168 ± 0.003	0.493 ± 0.013	1.05 ± 0.11	[16]
J06420559+4102000	L8.0	0.822 ± 0.011	1.048 ± 0.012	0.838 ± 0.008	0.565 ± 0.009	0.600 ± 0.011	0.677 ± 0.008	0.589 ± 0.011	0.769 ± 0.010	0.761 ± 0.008	1.009 ± 0.012	0.96 ± 0.10	[28]
J07053400−1839256	L8	0.959 ± 0.025	1.063 ± 0.026	0.939 ± 0.013	0.768 ± 0.021	0.728 ± 0.022	0.792 ± 0.014	0.638 ± 0.020	0.682 ± 0.015	0.670 ± 0.014	1.054 ± 0.017	0.90 ± 0.11	[32]
J07271824+1710012	T7	0.296 ± 0.005	0.183 ± 0.005	0.061 ± 0.007	0.085 ± 0.003	0.206 ± 0.010	0.348 ± 0.009	0.403 ± 0.008	0.341 ± 0.003	0.160 ± 0.002	0.333 ± 0.013	1.19 ± 0.12	[4]
J07414920+2351275	T5	0.508 ± 0.008	0.362 ± 0.008	0.167 ± 0.012	0.196 ± 0.003	0.299 ± 0.009	0.441 ± 0.012	0.428 ± 0.007	0.318 ± 0.005	0.148 ± 0.002	0.587 ± 0.017	0.97 ± 0.07	[11]

Table 15
(Continued)

Designation	SpT[a]	[CH4-J]	[CH4-H]	[CH4-K]	[H2O-J]	[H2O-H]	[H2O-K]	[Y/J]	[K/H]	[K/J]	[H-dip]	$\langle\zeta_T\rangle$	References
J07420130+2055198	T5	0.481 ± 0.007	0.399 ± 0.005	0.195 ± 0.011	0.245 ± 0.003	0.317 ± 0.007	0.477 ± 0.010	0.448 ± 0.007	0.316 ± 0.003	0.157 ± 0.001	0.597 ± 0.010	0.97 ± 0.08	[11]
J07483861+1743329	L7	0.984 ± 0.010	1.084 ± 0.013	0.972 ± 0.010	0.735 ± 0.009	0.679 ± 0.010	0.735 ± 0.009	0.490 ± 0.011	0.665 ± 0.010	0.575 ± 0.006	0.968 ± 0.010	0.93 ± 0.14	[26]
J07554795+2212169	T5	0.498 ± 0.012	0.403 ± 0.006	0.209 ± 0.015	0.233 ± 0.004	0.327 ± 0.011	0.489 ± 0.015	0.459 ± 0.009	0.340 ± 0.006	0.155 ± 0.003	0.596 ± 0.014	0.99 ± 0.08	[3]
J07584037+3247245	T2	0.682 ± 0.005	0.927 ± 0.005	0.629 ± 0.005	0.445 ± 0.002	0.448 ± 0.005	0.562 ± 0.003	0.567 ± 0.005	0.503 ± 0.003	0.356 ± 0.001	1.006 ± 0.004	1.09 ± 0.12	[9]
J08070023+4130268	L8p	0.943 ± 0.007	1.056 ± 0.005	0.927 ± 0.005	0.761 ± 0.004	0.772 ± 0.005	0.750 ± 0.004	0.564 ± 0.006	0.692 ± 0.004	0.631 ± 0.003	1.005 ± 0.004	0.89 ± 0.11	[22]
J08195805−0335285	T4	0.634 ± 0.010	0.645 ± 0.008	0.360 ± 0.009	0.385 ± 0.004	0.378 ± 0.007	0.495 ± 0.011	0.479 ± 0.006	0.346 ± 0.004	0.206 ± 0.002	0.834 ± 0.009	1.00 ± 0.11	[16]
J08203013+1037372	L9.5:	0.793 ± 0.012	1.060 ± 0.017	0.880 ± 0.012	0.610 ± 0.016	0.624 ± 0.017	0.684 ± 0.010	0.604 ± 0.013	0.648 ± 0.012	0.583 ± 0.010	1.010 ± 0.020	1.04 ± 0.17	[2]
J08300825+4828482	L8	0.928 ± 0.010	1.078 ± 0.009	0.872 ± 0.006	0.604 ± 0.008	0.590 ± 0.007	0.563 ± 0.005	0.532 ± 0.008	0.666 ± 0.006	0.633 ± 0.006	1.037 ± 0.006	1.10 ± 0.17	[9]
…	…	0.847 ± 0.008	1.067 ± 0.006	0.875 ± 0.004	0.642 ± 0.004	0.586 ± 0.006	0.567 ± 0.004	0.618 ± 0.005	0.648 ± 0.004	0.585 ± 0.003	1.037 ± 0.005	1.04 ± 0.15	[9]
J08304878+0128311	T4.5	0.499 ± 0.009	0.457 ± 0.007	0.232 ± 0.012	0.259 ± 0.003	0.341 ± 0.009	0.484 ± 0.014	0.454 ± 0.007	0.333 ± 0.004	0.164 ± 0.002	0.675 ± 0.011	0.95 ± 0.06	[11]
J08371718−0000179	T1	0.858 ± 0.012	0.984 ± 0.012	0.721 ± 0.013	0.588 ± 0.010	0.535 ± 0.012	0.622 ± 0.013	0.632 ± 0.013	0.505 ± 0.007	0.386 ± 0.006	1.017 ± 0.010	1.07 ± 0.09	[34]
J08523490+4720359	L9.5:	0.867 ± 0.010	1.022 ± 0.009	0.845 ± 0.009	0.639 ± 0.009	0.647 ± 0.010	0.672 ± 0.010	0.628 ± 0.011	0.639 ± 0.006	0.549 ± 0.005	1.016 ± 0.009	0.98 ± 0.15	[11]
J08575849+5708514	L8	0.949 ± 0.005	1.106 ± 0.005	0.926 ± 0.004	0.639 ± 0.004	0.635 ± 0.005	0.700 ± 0.003	0.525 ± 0.005	0.819 ± 0.003	0.871 ± 0.004	1.028 ± 0.004	1.27 ± 0.17	[11]
J08583467+3256275	T1	0.810 ± 0.011	0.995 ± 0.011	0.899 ± 0.011	0.589 ± 0.009	0.551 ± 0.010	0.624 ± 0.008	0.650 ± 0.013	0.642 ± 0.006	0.554 ± 0.006	0.980 ± 0.009	1.08 ± 0.06	[11]
…	…	0.813 ± 0.014	0.979 ± 0.017	0.905 ± 0.018	0.565 ± 0.011	0.597 ± 0.016	0.624 ± 0.017	0.570 ± 0.022	0.630 ± 0.012	0.554 ± 0.007	0.996 ± 0.015	0.97 ± 0.06	[2]
J09002368+2539343	L7	0.938 ± 0.009	1.067 ± 0.009	0.932 ± 0.010	0.741 ± 0.008	0.667 ± 0.009	0.680 ± 0.008	0.532 ± 0.008	0.581 ± 0.006	0.445 ± 0.004	1.001 ± 0.008	0.81 ± 0.10	[26]
J09025899+6708331	L7p (red)	1.044 ± 0.008	1.178 ± 0.012	1.121 ± 0.006	0.678 ± 0.008	0.670 ± 0.009	0.770 ± 0.006	0.398 ± 0.008	0.765 ± 0.007	0.748 ± 0.007	0.997 ± 0.007	1.12 ± 0.18	[32]
J09293364+3429527	L8	0.902 ± 0.012	1.099 ± 0.015	0.946 ± 0.010	0.693 ± 0.011	0.694 ± 0.011	0.726 ± 0.008	0.616 ± 0.014	0.801 ± 0.010	0.806 ± 0.009	1.042 ± 0.010	1.14 ± 0.17	[11]
J09310955+0327331	L7.5 ± 1.5	0.826 ± 0.012	1.102 ± 0.011	0.977 ± 0.016	0.672 ± 0.009	0.585 ± 0.011	0.653 ± 0.013	0.489 ± 0.010	0.532 ± 0.007	0.346 ± 0.004	1.031 ± 0.009	0.84 ± 0.12	[34]
J09373487+2931409	T6p	0.430 ± 0.011	0.306 ± 0.007	0.183 ± 0.012	0.148 ± 0.002	0.305 ± 0.006	0.532 ± 0.022	0.532 ± 0.009	0.170 ± 0.003	0.074 ± 0.001	0.533 ± 0.011	0.62 ± 0.16	[4]
J09553336−0208403	L7p (red)	0.904 ± 0.022	1.096 ± 0.026	0.982 ± 0.015	0.677 ± 0.026	0.711 ± 0.026	0.757 ± 0.013	0.516 ± 0.023	0.827 ± 0.019	0.884 ± 0.021	1.022 ± 0.024	1.18 ± 0.19	[32]
J09560810−1447065	L9.5	0.825 ± 0.011	1.038 ± 0.012	0.808 ± 0.009	0.579 ± 0.010	0.540 ± 0.011	0.653 ± 0.009	0.609 ± 0.010	0.658 ± 0.008	0.586 ± 0.006	1.018 ± 0.009	1.07 ± 0.07	[31]
J10071185+1930563	L8:	0.893 ± 0.026	1.036 ± 0.014	0.835 ± 0.020	0.640 ± 0.015	0.656 ± 0.016	0.684 ± 0.016	0.630 ± 0.016	0.633 ± 0.015	0.541 ± 0.015	1.043 ± 0.018	0.97 ± 0.14	[2]
…	…	0.900 ± 0.011	1.061 ± 0.014	0.857 ± 0.012	0.621 ± 0.011	0.643 ± 0.013	0.651 ± 0.010	0.598 ± 0.014	0.736 ± 0.010	0.703 ± 0.008	1.057 ± 0.012	1.15 ± 0.19	[11]
J10255227+3212349	L7.5::	0.903 ± 0.019	1.027 ± 0.014	0.943 ± 0.012	0.690 ± 0.019	0.703 ± 0.013	0.715 ± 0.016	0.554 ± 0.017	0.693 ± 0.008	0.656 ± 0.009	0.991 ± 0.011	0.98 ± 0.19	[2]
…	…	0.913 ± 0.016	1.052 ± 0.016	0.908 ± 0.014	0.728 ± 0.020	0.736 ± 0.014	0.740 ± 0.013	0.587 ± 0.019	0.704 ± 0.011	0.698 ± 0.011	1.004 ± 0.012	0.95 ± 0.11	[26]
J10271549+5445175	L7	0.985 ± 0.021	1.146 ± 0.019	1.105 ± 0.013	0.809 ± 0.018	0.793 ± 0.016	0.917 ± 0.016	0.577 ± 0.013	0.682 ± 0.011	0.572 ± 0.012	1.006 ± 0.011	0.83 ± 0.08	[33]
J10302678+0213057	L9.5:	0.912 ± 0.015	1.023 ± 0.013	0.858 ± 0.013	0.664 ± 0.011	0.624 ± 0.012	0.706 ± 0.012	0.543 ± 0.014	0.622 ± 0.008	0.562 ± 0.008	1.003 ± 0.013	0.96 ± 0.11	[11]
J10430758+2225236	L8	0.911 ± 0.015	1.107 ± 0.010	0.857 ± 0.009	0.615 ± 0.010	0.606 ± 0.010	0.675 ± 0.007	0.562 ± 0.013	0.772 ± 0.007	0.786 ± 0.007	1.039 ± 0.009	1.25 ± 0.19	[5]
J10433508+1213149	L9	0.932 ± 0.011	1.038 ± 0.010	0.855 ± 0.008	0.661 ± 0.011	0.673 ± 0.011	0.697 ± 0.008	0.617 ± 0.010	0.664 ± 0.008	0.628 ± 0.008	1.020 ± 0.009	0.98 ± 0.15	[12]
…	…	0.903 ± 0.007	1.031 ± 0.006	0.842 ± 0.005	0.675 ± 0.005	0.646 ± 0.006	0.669 ± 0.005	0.582 ± 0.007	0.679 ± 0.004	0.664 ± 0.004	1.019 ± 0.004	1.02 ± 0.16	[11]
J10440942+0429376	L7	0.890 ± 0.009	1.031 ± 0.006	0.874 ± 0.005	0.710 ± 0.006	0.684 ± 0.006	0.706 ± 0.006	0.545 ± 0.007	0.667 ± 0.004	0.631 ± 0.004	1.017 ± 0.006	0.95 ± 0.14	[11]
J10475385+2124234	T6.5	0.404 ± 0.005	0.261 ± 0.005	0.122 ± 0.009	0.119 ± 0.002	0.251 ± 0.006	0.424 ± 0.010	0.435 ± 0.006	0.237 ± 0.003	0.109 ± 0.001	0.487 ± 0.011	0.83 ± 0.12	[9]
J10482926+0919373	T2.5	0.743 ± 0.013	0.831 ± 0.010	0.558 ± 0.015	0.491 ± 0.008	0.457 ± 0.012	0.576 ± 0.014	0.581 ± 0.012	0.410 ± 0.006	0.288 ± 0.004	0.947 ± 0.013	1.06 ± 0.10	[11]
J10491557 −5319061A	L8	0.930 ± 0.007	1.112 ± 0.006	0.928 ± 0.004	0.603 ± 0.005	0.639 ± 0.006	0.692 ± 0.003	0.488 ± 0.005	0.846 ± 0.005	0.913 ± 0.005	1.027 ± 0.003	1.35 ± 0.24	[18]
J10491557−5319061B	T0.5	0.832 ± 0.008	1.059 ± 0.006	0.834 ± 0.005	0.611 ± 0.004	0.551 ± 0.006	0.659 ± 0.003	0.634 ± 0.005	0.609 ± 0.004	0.515 ± 0.003	1.045 ± 0.004	1.03 ± 0.19	[18]
J10595185+3042059	T4	0.624 ± 0.014	0.523 ± 0.009	0.277 ± 0.012	0.384 ± 0.007	0.387 ± 0.011	0.476 ± 0.014	0.470 ± 0.010	0.402 ± 0.007	0.240 ± 0.005	0.725 ± 0.012	1.08 ± 0.07	[10]
J11220826−3512363	T2	0.786 ± 0.013	0.781 ± 0.008	0.505 ± 0.009	0.530 ± 0.005	0.537 ± 0.012	0.547 ± 0.009	0.547 ± 0.007	0.386 ± 0.004	0.283 ± 0.002	0.926 ± 0.007	0.92 ± 0.11	[3]
J11472421−2040204	L7	0.935 ± 0.029	1.255 ± 0.030	1.108 ± 0.014	0.549 ± 0.027	0.672 ± 0.026	0.779 ± 0.012	0.419 ± 0.027	0.986 ± 0.028	1.098 ± 0.029	1.056 ± 0.025	0.86 ± 0.20	[30]
J11555389+0559577	L7.5	0.889 ± 0.008	1.061 ± 0.006	0.911 ± 0.007	0.716 ± 0.005	0.691 ± 0.006	0.702 ± 0.005	0.558 ± 0.007	0.647 ± 0.004	0.555 ± 0.004	1.011 ± 0.005	0.91 ± 0.12	[11]
J11582077+0435014	sdL7	0.862 ± 0.009	1.039 ± 0.007	0.889 ± 0.008	0.709 ± 0.005	0.638 ± 0.007	0.686 ± 0.007	0.470 ± 0.006	0.496 ± 0.005	0.321 ± 0.002	1.006 ± 0.006	0.73 ± 0.09	[12]
J12010457+5730042	L9	0.959 ± 0.018	1.103 ± 0.028	0.871 ± 0.017	0.614 ± 0.020	0.598 ± 0.022	0.619 ± 0.014	0.623 ± 0.020	0.655 ± 0.016	0.597 ± 0.012	1.057 ± 0.019	1.07 ± 0.16	[32]
J12060248+2813293	T3	0.716 ± 0.006	0.668 ± 0.011	0.429 ± 0.013	0.457 ± 0.007	0.548 ± 0.018	0.540 ± 0.018	0.617 ± 0.014	0.321 ± 0.006	0.210 ± 0.003	0.892 ± 0.019	0.79 ± 0.10	[2]
J12144089+6316434	T3.5:	0.597 ± 0.015	0.706 ± 0.016	0.421 ± 0.016	0.278 ± 0.005	0.326 ± 0.011	0.502 ± 0.013	0.492 ± 0.007	0.385 ± 0.007	0.244 ± 0.003	0.932 ± 0.016	1.12 ± 0.15	[2]
J12195156+3128497	L8	0.898 ± 0.009	1.065 ± 0.009	0.848 ± 0.005	0.637 ± 0.006	0.638 ± 0.009	0.657 ± 0.005	0.564 ± 0.007	0.717 ± 0.006	0.683 ± 0.005	1.009 ± 0.006	1.11 ± 0.14	[11]
J12314753+0847331	T5.5	0.446 ± 0.013	0.357 ± 0.005	0.154 ± 0.007	0.182 ± 0.002	0.264 ± 0.005	0.370 ± 0.006	0.451 ± 0.005	0.322 ± 0.004	0.155 ± 0.002	0.565 ± 0.010	1.02 ± 0.09	[1]
J12545393−0122474	T2	0.775 ± 0.009	0.914 ± 0.006	0.594 ± 0.005	0.470 ± 0.005	0.460 ± 0.007	0.545 ± 0.006	0.528 ± 0.006	0.490 ± 0.004	0.361 ± 0.003	1.015 ± 0.005	1.09 ± 0.09	[1]
J13072984−0558146	L8	0.950 ± 0.010	1.020 ± 0.012	0.898 ± 0.010	0.723 ± 0.013	0.694 ± 0.014	0.738 ± 0.008	0.599 ± 0.011	0.665 ± 0.008	0.623 ± 0.006	1.017 ± 0.011	0.93 ± 0.12	[29]
J13184567+3626138	L7	0.936 ± 0.019	1.151 ± 0.028	1.130 ± 0.023	0.744 ± 0.021	0.785 ± 0.025	0.893 ± 0.026	0.487 ± 0.016	0.709 ± 0.017	0.651 ± 0.016	0.987 ± 0.017	0.91 ± 0.10	[33]
J13240767+1906259	T3.5	0.643 ± 0.007	0.623 ± 0.006	0.356 ± 0.009	0.434 ± 0.003	0.404 ± 0.006	0.488 ± 0.009	0.605 ± 0.007	0.394 ± 0.004	0.214 ± 0.002	0.858 ± 0.010	1.05 ± 0.09	[13]
J13262981−0038314	L8:	0.984 ± 0.010	1.094 ± 0.008	0.998 ± 0.007	0.667 ± 0.010	0.710 ± 0.010	0.792 ± 0.007	0.516 ± 0.013	0.795 ± 0.006	0.806 ± 0.009	0.999 ± 0.007	1.14 ± 0.20	[11]
J13464634−0031501	T6.5	0.405 ± 0.009	0.279 ± 0.007	0.123 ± 0.010	0.130 ± 0.004	0.266 ± 0.007	0.425 ± 0.010	0.419 ± 0.009	0.340 ± 0.005	0.154 ± 0.002	0.456 ± 0.018	1.05 ± 0.11	[4]
J13480699+6603284	L9	1.012 ± 0.013	1.062 ± 0.015	0.850 ± 0.012	0.592 ± 0.012	0.616 ± 0.014	0.633 ± 0.015	0.557 ± 0.013	0.654 ± 0.010	0.650 ± 0.009	0.996 ± 0.013	0.96 ± 0.07	[16]
J13585269+3747137	T4.5:	0.566 ± 0.005	0.376 ± 0.011	0.303 ± 0.017	0.252 ± 0.003	0.347 ± 0.010	0.510 ± 0.036	0.482 ± 0.012	0.267 ± 0.006	0.122 ± 0.003	0.668 ± 0.012	0.84 ± 0.10	[2]
J14002320+4338222	L7:	0.952 ± 0.013	1.041 ± 0.008	0.888 ± 0.007	0.776 ± 0.009	0.748 ± 0.008	0.750 ± 0.006	0.594 ± 0.010	0.733 ± 0.006	0.724 ± 0.007	0.999 ± 0.007	0.95 ± 0.13	[11]
J14321117+3244338	L7	0.986 ± 0.026	1.173 ± 0.022	1.044 ± 0.014	0.734 ± 0.021	0.659 ± 0.021	0.776 ± 0.014	0.487 ± 0.021	0.772 ± 0.013	0.702 ± 0.018	0.994 ± 0.016	1.10 ± 0.13	[32]

Table 15
(Continued)

Designation	SpT[a]	[CH4-J]	[CH4-H]	[CH4-K]	[H2O-J]	[H2O-H]	[H2O-K]	[Y/J]	[K/H]	[K/J]	[H-dip]	$\langle\zeta_T\rangle$	References
J14564268+6450097	L7p (red)	1.034 ± 0.016	1.156 ± 0.015	1.086 ± 0.011	0.703 ± 0.015	0.699 ± 0.014	0.763 ± 0.010	0.470 ± 0.015	0.785 ± 0.011	0.809 ± 0.013	0.964 ± 0.010	1.11 ± 0.16	[32]
J15031961+2525196	T5	0.465 ± 0.013	0.411 ± 0.004	0.201 ± 0.006	0.238 ± 0.001	0.319 ± 0.006	0.453 ± 0.005	0.459 ± 0.005	0.324 ± 0.002	0.151 ± 0.001	0.590 ± 0.006	0.98 ± 0.07	[1]
J15050237−2853452	T1.5	0.785 ± 0.010	0.861 ± 0.007	0.669 ± 0.009	0.539 ± 0.005	0.530 ± 0.009	0.617 ± 0.009	0.575 ± 0.007	0.493 ± 0.005	0.388 ± 0.004	0.984 ± 0.008	1.00 ± 0.06	[13]
J15131461+4019356	L8	0.910 ± 0.017	1.059 ± 0.022	0.917 ± 0.018	0.666 ± 0.020	0.646 ± 0.021	0.735 ± 0.016	0.600 ± 0.027	0.741 ± 0.016	0.712 ± 0.015	1.032 ± 0.021	1.12 ± 0.15	[22]
J15150607+4436483	L7.5:	0.951 ± 0.011	1.106 ± 0.010	0.944 ± 0.008	0.679 ± 0.008	0.691 ± 0.009	0.732 ± 0.009	0.504 ± 0.011	0.739 ± 0.007	0.704 ± 0.008	1.018 ± 0.009	1.07 ± 0.16	[11]
J15164306+3053443	T0.5:	0.750 ± 0.014	1.145 ± 0.014	0.843 ± 0.013	0.473 ± 0.011	0.507 ± 0.014	0.600 ± 0.010	0.537 ± 0.013	0.755 ± 0.011	0.673 ± 0.008	1.058 ± 0.011	0.98 ± 0.13	[11]
J15203974+3546210	T0:	0.939 ± 0.020	1.020 ± 0.015	0.795 ± 0.011	0.716 ± 0.016	0.693 ± 0.016	0.690 ± 0.010	0.643 ± 0.016	0.613 ± 0.009	0.543 ± 0.009	1.017 ± 0.012	0.86 ± 0.11	[34]
…	…	0.926 ± 0.005	1.018 ± 0.005	0.808 ± 0.004	0.705 ± 0.005	0.688 ± 0.005	0.675 ± 0.004	0.590 ± 0.005	0.632 ± 0.004	0.575 ± 0.004	1.010 ± 0.004	0.90 ± 0.13	[11]
J15210327+0131426	T2:	0.719 ± 0.009	0.841 ± 0.013	0.482 ± 0.014	0.444 ± 0.008	0.456 ± 0.013	0.558 ± 0.013	0.530 ± 0.010	0.463 ± 0.008	0.303 ± 0.005	0.975 ± 0.012	1.04 ± 0.08	[11]
J15232263+3014562	L8	0.913 ± 0.014	1.030 ± 0.011	0.879 ± 0.009	0.665 ± 0.011	0.667 ± 0.011	0.710 ± 0.009	0.589 ± 0.013	0.708 ± 0.008	0.715 ± 0.008	0.986 ± 0.009	1.05 ± 0.16	[11]
J15261405+2043414	L7	0.920 ± 0.008	1.072 ± 0.006	0.935 ± 0.005	0.762 ± 0.005	0.719 ± 0.007	0.724 ± 0.005	0.537 ± 0.007	0.653 ± 0.005	0.550 ± 0.004	0.996 ± 0.007	0.87 ± 0.12	[1]
J15335852+4757069	L8:	1.012 ± 0.027	1.091 ± 0.025	0.962 ± 0.015	0.667 ± 0.022	0.718 ± 0.018	0.695 ± 0.015	0.561 ± 0.019	0.746 ± 0.015	0.709 ± 0.017	1.012 ± 0.020	1.07 ± 0.15	[32]
J15400942+3742316	L9:	0.822 ± 0.022	1.045 ± 0.019	0.884 ± 0.015	0.624 ± 0.016	0.675 ± 0.017	0.672 ± 0.010	0.631 ± 0.014	0.706 ± 0.015	0.633 ± 0.013	1.070 ± 0.013	1.07 ± 0.20	[2]
…	…	0.891 ± 0.010	1.082 ± 0.011	0.891 ± 0.009	0.655 ± 0.009	0.671 ± 0.009	0.614 ± 0.008	0.638 ± 0.010	0.686 ± 0.006	0.620 ± 0.006	1.034 ± 0.008	1.02 ± 0.16	[11]
J15423630−0045452	L7	0.802 ± 0.012	1.143 ± 0.021	1.025 ± 0.022	0.772 ± 0.012	0.610 ± 0.018	0.706 ± 0.021	0.641 ± 0.015	0.560 ± 0.014	0.360 ± 0.008	1.002 ± 0.017	0.80 ± 0.12	[15]
J15450901+3555271	L7.5	0.988 ± 0.018	1.017 ± 0.014	0.907 ± 0.014	0.736 ± 0.016	0.696 ± 0.014	0.749 ± 0.013	0.603 ± 0.017	0.690 ± 0.012	0.708 ± 0.011	0.992 ± 0.012	0.95 ± 0.13	[34]
J15461460+4932113	T2.5:	0.679 ± 0.010	0.755 ± 0.010	0.493 ± 0.011	0.445 ± 0.005	0.475 ± 0.009	0.556 ± 0.011	0.506 ± 0.009	0.398 ± 0.006	0.280 ± 0.003	0.893 ± 0.011	0.96 ± 0.07	[11]
J15462718−3325111	T5.5	0.507 ± 0.008	0.377 ± 0.009	0.179 ± 0.011	0.220 ± 0.003	0.285 ± 0.010	0.436 ± 0.012	0.403 ± 0.007	0.332 ± 0.004	0.152 ± 0.002	0.627 ± 0.015	1.02 ± 0.09	[9]
J16241436+0029158	T6	0.461 ± 0.008	0.303 ± 0.005	0.161 ± 0.006	0.151 ± 0.001	0.270 ± 0.008	0.412 ± 0.009	0.406 ± 0.006	0.307 ± 0.003	0.141 ± 0.001	0.495 ± 0.010	0.99 ± 0.08	[4]
J16272565+3255246	T6	0.405 ± 0.007	0.294 ± 0.004	0.180 ± 0.014	0.136 ± 0.002	0.296 ± 0.008	0.449 ± 0.013	0.414 ± 0.006	0.232 ± 0.003	0.105 ± 0.001	0.476 ± 0.010	0.79 ± 0.09	[16]
J16291855+0335355	T2	0.738 ± 0.006	0.916 ± 0.006	0.618 ± 0.005	0.441 ± 0.003	0.420 ± 0.006	0.561 ± 0.006	0.562 ± 0.005	0.492 ± 0.003	0.354 ± 0.002	1.014 ± 0.006	1.14 ± 0.11	[17]
J16303054+4344032	L7:	0.919 ± 0.012	1.062 ± 0.010	0.879 ± 0.007	0.696 ± 0.010	0.670 ± 0.008	0.706 ± 0.006	0.602 ± 0.010	0.729 ± 0.007	0.698 ± 0.006	1.022 ± 0.007	1.06 ± 0.17	[11]
J16322911+1904407	L8	0.943 ± 0.009	1.059 ± 0.011	0.883 ± 0.010	0.710 ± 0.012	0.677 ± 0.009	0.693 ± 0.010	0.594 ± 0.008	0.747 ± 0.007	0.742 ± 0.008	1.025 ± 0.009	1.06 ± 0.13	[8]
J16323934+4150048	T1:	0.883 ± 0.015	0.896 ± 0.015	0.592 ± 0.015	0.597 ± 0.012	0.549 ± 0.013	0.568 ± 0.016	0.553 ± 0.014	0.468 ± 0.010	0.382 ± 0.007	0.992 ± 0.016	1.02 ± 0.10	[11]
J16471557+5632083	L9p (red)	0.839 ± 0.014	1.095 ± 0.013	0.943 ± 0.010	0.669 ± 0.012	0.702 ± 0.012	0.712 ± 0.009	0.560 ± 0.011	0.805 ± 0.008	0.817 ± 0.010	1.005 ± 0.011	1.16 ± 0.17	[16]
J17342104+5023508	T4	0.483 ± 0.009	0.520 ± 0.007	0.249 ± 0.009	0.400 ± 0.004	0.427 ± 0.008	0.486 ± 0.010	0.428 ± 0.007	0.402 ± 0.004	0.223 ± 0.002	0.714 ± 0.010	1.03 ± 0.09	[21]
J17385927+6142421	L9p	0.896 ± 0.021	1.088 ± 0.020	0.943 ± 0.011	0.564 ± 0.019	0.626 ± 0.019	0.717 ± 0.010	0.530 ± 0.019	0.969 ± 0.018	1.225 ± 0.024	1.034 ± 0.017	0.93 ± 0.17	[21]
J17502385+4222373	T2	0.852 ± 0.015	0.913 ± 0.012	0.619 ± 0.013	0.504 ± 0.011	0.534 ± 0.013	0.609 ± 0.010	0.524 ± 0.009	0.508 ± 0.007	0.364 ± 0.004	1.021 ± 0.012	0.97 ± 0.07	[3]
J17503293+1759042	T3.5	0.714 ± 0.010	0.661 ± 0.008	0.348 ± 0.013	0.460 ± 0.004	0.435 ± 0.009	0.520 ± 0.012	0.518 ± 0.008	0.365 ± 0.006	0.230 ± 0.003	0.870 ± 0.012	0.99 ± 0.11	[1]
J17545447+1649196	T5.5	0.482 ± 0.006	0.405 ± 0.005	0.216 ± 0.008	0.191 ± 0.002	0.299 ± 0.006	0.430 ± 0.007	0.455 ± 0.006	0.363 ± 0.004	0.175 ± 0.001	0.630 ± 0.010	1.02 ± 0.09	[9]
J17551028+1803202	T2	0.755 ± 0.010	0.850 ± 0.010	0.548 ± 0.011	0.584 ± 0.006	0.527 ± 0.010	0.537 ± 0.011	0.597 ± 0.008	0.422 ± 0.005	0.308 ± 0.004	0.968 ± 0.010	1.02 ± 0.14	[25]
J18002660+0134531	L7.5	0.907 ± 0.005	1.039 ± 0.003	0.882 ± 0.003	0.727 ± 0.002	0.708 ± 0.004	0.714 ± 0.002	0.604 ± 0.004	0.716 ± 0.002	0.693 ± 0.002	1.023 ± 0.002	0.98 ± 0.13	[14]
J18095253−0448125	T0.5	0.835 ± 0.009	0.964 ± 0.007	0.731 ± 0.007	0.625 ± 0.005	0.615 ± 0.007	0.630 ± 0.007	0.602 ± 0.007	0.534 ± 0.005	0.428 ± 0.004	1.007 ± 0.007	0.94 ± 0.09	[21]
…	…	0.861 ± 0.015	0.976 ± 0.012	0.723 ± 0.009	0.661 ± 0.010	0.635 ± 0.011	0.641 ± 0.011	0.656 ± 0.012	0.554 ± 0.006	0.438 ± 0.006	1.010 ± 0.011	0.92 ± 0.08	[20]
…	…	0.861 ± 0.014	0.976 ± 0.014	0.723 ± 0.010	0.661 ± 0.010	0.635 ± 0.012	0.641 ± 0.009	0.656 ± 0.012	0.554 ± 0.007	0.438 ± 0.006	1.010 ± 0.011	0.92 ± 0.08	[28]
J18305856+4542574	L9	0.841 ± 0.013	1.055 ± 0.014	0.835 ± 0.012	0.656 ± 0.013	0.669 ± 0.013	0.724 ± 0.011	0.598 ± 0.014	0.692 ± 0.011	0.649 ± 0.010	1.057 ± 0.012	1.03 ± 0.16	[16]
J19010601+4718136	T5	0.553 ± 0.008	0.433 ± 0.007	0.248 ± 0.008	0.282 ± 0.003	0.353 ± 0.008	0.501 ± 0.011	0.490 ± 0.005	0.331 ± 0.004	0.170 ± 0.002	0.675 ± 0.012	0.96 ± 0.07	[1]
J19062474+4508071	T6	0.452 ± 0.009	0.323 ± 0.007	0.200 ± 0.012	0.187 ± 0.003	0.294 ± 0.010	0.471 ± 0.016	0.441 ± 0.006	0.283 ± 0.005	0.129 ± 0.002	0.543 ± 0.012	0.92 ± 0.09	[16]
J19284135+2356049	T6	0.416 ± 0.004	0.347 ± 0.002	0.145 ± 0.003	0.173 ± 0.001	0.272 ± 0.003	0.373 ± 0.002	0.426 ± 0.003	0.364 ± 0.001	0.172 ± 0.001	0.537 ± 0.005	1.08 ± 0.09	[21]
…	…	0.442 ± 0.005	0.342 ± 0.004	0.158 ± 0.004	0.163 ± 0.001	0.278 ± 0.005	0.375 ± 0.006	0.416 ± 0.004	0.354 ± 0.002	0.169 ± 0.001	0.548 ± 0.008	1.05 ± 0.10	[34]
J20304279+0749347	T1.5	0.800 ± 0.004	0.877 ± 0.003	0.568 ± 0.003	0.600 ± 0.002	0.561 ± 0.003	0.578 ± 0.002	0.558 ± 0.003	0.445 ± 0.001	0.336 ± 0.001	0.975 ± 0.003	0.87 ± 0.12	[21]
…	…	0.780 ± 0.008	0.868 ± 0.007	0.557 ± 0.008	0.622 ± 0.007	0.570 ± 0.007	0.576 ± 0.009	0.622 ± 0.009	0.430 ± 0.004	0.320 ± 0.003	0.981 ± 0.007	0.84 ± 0.12	[20]
J20431769−1551031	L9	0.870 ± 0.013	1.040 ± 0.017	0.771 ± 0.015	0.681 ± 0.016	0.666 ± 0.015	0.664 ± 0.015	0.633 ± 0.014	0.635 ± 0.014	0.564 ± 0.011	1.031 ± 0.014	0.93 ± 0.12	[11]
J20435642+6220490	T1.5	0.765 ± 0.013	0.933 ± 0.013	0.622 ± 0.012	0.561 ± 0.009	0.530 ± 0.012	0.605 ± 0.013	0.666 ± 0.017	0.453 ± 0.006	0.335 ± 0.004	0.996 ± 0.014	1.02 ± 0.11	[21]
J20474959−0718176	T0:	0.882 ± 0.014	1.010 ± 0.011	0.789 ± 0.012	0.691 ± 0.011	0.683 ± 0.011	0.692 ± 0.010	0.639 ± 0.014	0.613 ± 0.008	0.562 ± 0.007	1.029 ± 0.011	0.88 ± 0.11	[11]
J20520174−2043119	L8	0.945 ± 0.016	1.039 ± 0.019	0.911 ± 0.015	0.742 ± 0.016	0.747 ± 0.017	0.740 ± 0.010	0.613 ± 0.014	0.652 ± 0.010	0.583 ± 0.009	1.023 ± 0.016	0.86 ± 0.11	[29]
J21171444−2940052	T0:	0.854 ± 0.018	0.963 ± 0.017	0.754 ± 0.020	0.664 ± 0.015	0.646 ± 0.016	0.624 ± 0.019	0.677 ± 0.020	0.563 ± 0.012	0.498 ± 0.011	1.031 ± 0.016	0.90 ± 0.07	[28]
J21241387+0059599	T5	0.584 ± 0.012	0.383 ± 0.008	0.196 ± 0.010	0.239 ± 0.004	0.307 ± 0.012	0.412 ± 0.012	0.436 ± 0.009	0.377 ± 0.004	0.189 ± 0.002	0.634 ± 0.011	1.08 ± 0.08	[3]
J21243865+1849263	L9	0.849 ± 0.012	1.041 ± 0.014	0.798 ± 0.009	0.539 ± 0.007	0.528 ± 0.011	0.596 ± 0.011	0.590 ± 0.009	0.642 ± 0.008	0.576 ± 0.007	1.050 ± 0.012	1.04 ± 0.08	[27]
J21324898−1452544	T4	0.731 ± 0.012	0.638 ± 0.014	0.365 ± 0.017	0.412 ± 0.008	0.370 ± 0.014	0.564 ± 0.022	0.530 ± 0.011	0.348 ± 0.007	0.218 ± 0.004	0.895 ± 0.020	0.98 ± 0.15	[34]
J21392676+0220226	T1.5	0.664 ± 0.010	1.015 ± 0.005	0.691 ± 0.003	0.422 ± 0.002	0.454 ± 0.006	0.575 ± 0.002	0.514 ± 0.004	0.572 ± 0.003	0.405 ± 0.002	1.031 ± 0.003	0.99 ± 0.10	[3]
J21442847+1446077	T2.5	0.630 ± 0.007	0.842 ± 0.008	0.526 ± 0.006	0.380 ± 0.004	0.432 ± 0.010	0.542 ± 0.007	0.554 ± 0.007	0.460 ± 0.004	0.306 ± 0.002	0.976 ± 0.008	1.02 ± 0.12	[7]
J21513839−4853542	T4	0.615 ± 0.008	0.604 ± 0.008	0.307 ± 0.013	0.331 ± 0.004	0.350 ± 0.008	0.471 ± 0.011	0.417 ± 0.008	0.378 ± 0.005	0.192 ± 0.002	0.770 ± 0.012	1.04 ± 0.07	[3]
J21513979+3402444	L7p	0.968 ± 0.013	1.049 ± 0.010	0.943 ± 0.011	0.753 ± 0.010	0.748 ± 0.009	0.770 ± 0.011	0.576 ± 0.012	0.699 ± 0.007	0.661 ± 0.009	0.999 ± 0.009	0.92 ± 0.11	[12]
J21542494−1023022	T4.5	0.585 ± 0.009	0.528 ± 0.007	0.282 ± 0.015	0.353 ± 0.005	0.401 ± 0.008	0.496 ± 0.010	0.455 ± 0.007	0.390 ± 0.006	0.212 ± 0.003	0.758 ± 0.012	1.01 ± 0.07	[6]
J22092183−2711329	T2.5	0.824 ± 0.008	0.719 ± 0.007	0.463 ± 0.009	0.460 ± 0.004	0.463 ± 0.009	0.557 ± 0.009	0.488 ± 0.006	0.430 ± 0.004	0.301 ± 0.003	0.873 ± 0.011	1.00 ± 0.07	[34]
J22153705+2110554	T0	0.814 ± 0.009	0.942 ± 0.009	0.691 ± 0.007	0.576 ± 0.006	0.572 ± 0.009	0.669 ± 0.006	0.502 ± 0.008	0.530 ± 0.004	0.382 ± 0.003	0.996 ± 0.008	0.99 ± 0.05	[31]

Table 15
(Continued)

Designation	SpT[a]	[CH4-J]	[CH4-H]	[CH4-K]	[H2O-J]	[H2O-H]	[H2O-K]	[Y/J]	[K/H]	[K/J]	[H-dip]	$\langle\zeta_T\rangle$	References
…	…	0.785 ± 0.005	0.946 ± 0.005	0.703 ± 0.004	0.581 ± 0.003	0.571 ± 0.006	0.657 ± 0.005	0.532 ± 0.005	0.524 ± 0.003	0.369 ± 0.002	1.002 ± 0.005	1.00 ± 0.05	[27]
J22221993+3026014	L9	0.941 ± 0.015	1.042 ± 0.012	0.841 ± 0.009	0.749 ± 0.012	0.738 ± 0.013	0.709 ± 0.009	0.638 ± 0.011	0.681 ± 0.008	0.633 ± 0.007	1.037 ± 0.012	0.90 ± 0.11	[26]
J22361759+5105519	T5.5	0.466 ± 0.005	0.408 ± 0.004	0.194 ± 0.004	0.228 ± 0.002	0.322 ± 0.006	0.439 ± 0.005	0.436 ± 0.005	0.372 ± 0.002	0.181 ± 0.001	0.636 ± 0.008	1.03 ± 0.09	[20]
J22393755+1617161	T3	0.653 ± 0.007	0.730 ± 0.006	0.553 ± 0.008	0.418 ± 0.004	0.499 ± 0.007	0.580 ± 0.008	0.546 ± 0.006	0.411 ± 0.004	0.263 ± 0.002	0.890 ± 0.007	0.91 ± 0.08	[16]
J22541892+3123498	T4	0.673 ± 0.010	0.574 ± 0.005	0.314 ± 0.005	0.368 ± 0.003	0.362 ± 0.004	0.494 ± 0.005	0.455 ± 0.007	0.382 ± 0.002	0.239 ± 0.002	0.808 ± 0.010	1.05 ± 0.08	[1]
J23032925+3150210	T2p	0.719 ± 0.009	0.755 ± 0.008	0.446 ± 0.011	0.490 ± 0.005	0.468 ± 0.009	0.543 ± 0.011	0.561 ± 0.008	0.368 ± 0.004	0.245 ± 0.002	0.911 ± 0.010	1.00 ± 0.12	[31]
…	…	0.749 ± 0.013	0.763 ± 0.012	0.445 ± 0.013	0.478 ± 0.007	0.455 ± 0.012	0.544 ± 0.014	0.547 ± 0.009	0.345 ± 0.006	0.229 ± 0.004	0.939 ± 0.015	0.99 ± 0.15	[29]
J23185497−1301106	T5	0.699 ± 0.008	0.443 ± 0.008	0.198 ± 0.007	0.317 ± 0.005	0.377 ± 0.009	0.466 ± 0.012	0.344 ± 0.007	0.416 ± 0.005	0.235 ± 0.003	0.704 ± 0.013	1.06 ± 0.11	[34]
J23230708+0541130	L8p (blue)	0.893 ± 0.022	1.007 ± 0.019	0.868 ± 0.015	0.694 ± 0.022	0.688 ± 0.022	0.718 ± 0.015	0.628 ± 0.018	0.671 ± 0.012	0.609 ± 0.014	1.036 ± 0.020	0.96 ± 0.12	[32]
J23254530+4251488	L8	0.872 ± 0.019	1.040 ± 0.015	0.884 ± 0.015	0.697 ± 0.013	0.682 ± 0.012	0.682 ± 0.015	0.581 ± 0.010	0.692 ± 0.012	0.657 ± 0.012	1.016 ± 0.011	0.99 ± 0.14	[11]
J23272874−2730566	L9	0.848 ± 0.009	0.986 ± 0.010	0.806 ± 0.011	0.603 ± 0.009	0.636 ± 0.011	0.678 ± 0.009	0.554 ± 0.010	0.637 ± 0.007	0.590 ± 0.006	0.994 ± 0.009	0.96 ± 0.07	[16]
J23305116−0844533	L8.0	0.915 ± 0.026	1.034 ± 0.020	0.863 ± 0.011	0.693 ± 0.024	0.639 ± 0.017	0.704 ± 0.013	0.634 ± 0.020	0.713 ± 0.013	0.741 ± 0.018	1.013 ± 0.016	1.06 ± 0.15	[34]
J23333346+0251284	L8p (blue)	0.953 ± 0.017	1.075 ± 0.016	1.036 ± 0.013	0.792 ± 0.018	0.813 ± 0.014	0.753 ± 0.011	0.476 ± 0.013	0.706 ± 0.010	0.614 ± 0.010	0.968 ± 0.013	0.86 ± 0.09	[32]
J23352734+4511442	L9p	0.954 ± 0.014	1.130 ± 0.015	0.976 ± 0.009	0.653 ± 0.013	0.657 ± 0.012	0.736 ± 0.007	0.557 ± 0.015	0.871 ± 0.011	0.936 ± 0.010	1.032 ± 0.013	1.32 ± 0.23	[28]
J23391025+1352284	T5	0.514 ± 0.009	0.458 ± 0.006	0.233 ± 0.012	0.244 ± 0.003	0.295 ± 0.009	0.460 ± 0.009	0.469 ± 0.007	0.343 ± 0.004	0.162 ± 0.002	0.647 ± 0.014	1.03 ± 0.09	[3]
J23565477−1553111	T5.5	0.548 ± 0.010	0.365 ± 0.006	0.140 ± 0.009	0.231 ± 0.004	0.314 ± 0.006	0.406 ± 0.012	0.396 ± 0.007	0.383 ± 0.006	0.193 ± 0.002	0.539 ± 0.009	1.08 ± 0.11	[3]

Notes.
[a] Spectral type as inferred from direct comparison to spectral standards.

References. [1] A. J. Burgasser et al. (2004); [2] K. Chiu et al. (2006); [3] A. J. Burgasser et al. (2006b); [4] A. J. Burgasser et al. (2006a); [5] N. Siegler et al. (2007); [6] D. L. Looper et al. (2007); [7] K. L. Luhman et al. (2007); [8] A. J. Burgasser (2007b); [9] A. J. Burgasser et al. (2008a); [10] S. S. Sheppard & M. C. Cushing (2009); [11] A. J. Burgasser et al. (2010a); [12] J. D. Kirkpatrick et al. (2010); [13] N. R. Deacon et al. (2011); [14] J. E. Gizis et al. (2011); [15] K. Geissler et al. (2011); [16] J. D. Kirkpatrick et al. (2011); [17] N. R. Deacon et al. (2012b); [18] A. J. Burgasser et al. (2013); [19] P. J. Castro et al. (2013); [20] W. M. J. Best et al. (2013); [21] G. N. Mace et al. (2013b); [22] M. A. Thompson et al. (2013); [23] J. D. Kirkpatrick et al. (2014); [24] B. P. Bowler et al. (2014); [25] K. L. Luhman & S. S. Sheppard (2014); [26] D. C. Bardalez Gagliuffi et al. (2014); [27] K. Kellogg et al. (2015); [28] W. M. J. Best et al. (2015); [29] A. C. Schneider et al. (2016a); [30] A. C. Schneider et al. (2016b); [31] J. Robert et al. (2016); [32] A. C. Schneider et al. (2017); [33] K. Kellogg et al. (2017); [34] A. J. Burgasser et al. (2025, in preparation)

Table 16
LOWZ Fit Parameters for Local Late-L and -T Dwarfs

Designation	SpT	Best-fit LOWZ Parameters						References
		$T_{\rm eff}$ (K)	$\log g$ (cm s^{-2})	[M/H] (dex)	C/O	$\log k_{zz}$ (cm^2 s^{-1})	χ^2_r	
J00001354+2554180	T4.5	1200	5.2	0.00	0.55	2	111	[3]
J00062785+1857288	L7	1600	4.5	0.75	0.85	10	29	[28]
J00150206+2959323	L7	1600	4.5	0.25	0.85	10	23	[12]
J00164396+2304267	T0.0	1600	4.5	0.00	0.55	2	18	[27]
J00164397+2304265	T0	1600	4.5	0.00	0.55	2	31	[28]
J00185151+5153306	L7.0	1600	4.5	0.75	0.85	10	69	[27]
J00311004+5749363	L8	1600	4.5	0.50	0.85	10	38	[20]
…	…	1600	4.5	0.50	0.85	10	89	[33]
J00325937+1410371	L8	1600	4.5	0.50	0.85	10	10	[11]
…	…	1600	4.5	0.50	0.85	10	32	[11]
J00345157+0523050	T6.5	850	4.5	−0.25	0.55	−1	187	[1]
J00440332+0228112	L7p	1600	4.5	0.75	0.85	10	266	[32]
…	…	1600	4.5	0.75	0.85	10	100	[31]
J00454256+3611391	T5	1100	4.5	0.25	0.55	−1	53	[21]
J00492826+0440575	L9	1600	4.5	0.50	0.85	10	33	[16]
J00550564+0134365	L7	1600	4.5	0.75	0.85	10	297	[32]
J01020186+0355405	L9	1600	4.5	0.50	0.85	10	12	[28]
J01352531+0205232	L9.5	1600	4.5	0.50	0.85	10	143	[32]
J01365662+0933473	T2.5	1400	5.0	0.00	0.55	2	1364	[9]
J01383658−0322212	T3	1400	5.0	0.00	0.55	2	96	[16]
J01414839−1601196	L7:	1600	4.5	0.50	0.85	10	9	[12]
J01453520−0314117	L9	1600	4.5	0.50	0.85	10	76	[32]
J01501089+3827241	T0	1600	4.5	0.00	0.55	2	97	[16]
…	…	1600	4.5	0.25	0.85	10	11	[30]
J01514155+1244300	T1	1600	4.5	−0.25	0.55	−1	26	[1]
J02022929+2305139	L7	1600	4.5	0.75	0.85	10	76	[31]
J02062527+2640236	L9p	1600	4.5	0.75	0.85	10	120	[16]
J02101025+4008296	T4.5	1200	5.2	0.00	0.55	−1	14	[21]
J02260916−1610004	L7p	1600	4.5	0.75	0.85	10	156	[31]
J02303885−0225471	L8:p	1600	4.5	0.75	0.85	10	14	[33]
J02431371−2453298	T6	1000	5.0	0.25	0.55	2	112	[1]
J02550357−4700509	L8	1600	4.5	0.50	0.85	10	125	[3]
J02572581−3105523	L8	1600	4.5	0.75	0.85	10	61	[5]
J03162759+2650277	T2.5	1300	5.0	0.25	0.55	2	48	[30]
J03230186+5625580	L7	1600	4.5	0.75	0.85	10	131	[24]
J03244023−1919056	L8p	1600	4.5	0.50	0.85	10	38	[31]
J03255322+0425406	T5.5	1100	5.2	0.25	0.55	2	14	[2]
J03284265+2302051	L8	1500	4.5	0.25	0.85	10	36	[9]
J03490944+1514360	L7p	1500	4.5	1.00	0.85	10	220	[27]
J04070885+1514565	T5	1100	5.0	0.25	0.55	2	25	[1]
J04151954−0935066	T8	850	4.5	0.00	0.85	−1	133	[1]
J04373705+2331080	L7	1600	4.5	0.75	0.85	10	36	[23]
J04574602−0207179	T2	1400	5.2	0.25	0.55	−1	274	[33]
J05065020+5236312	T4.5	1100	4.5	0.25	0.55	2	20	[27]
J05160945−0445499	T5.5	1100	5.2	0.25	0.55	2	38	[9]
J05591914−1404488	T4.5	1200	5.2	0.00	0.55	−1	64	[3]
J06020638+4043588	T4.5	1100	4.5	0.25	0.55	2	26	[6]
J06073865+2429535	L8	1600	4.5	0.50	0.85	10	1542	[22]
…	…	1600	4.5	0.50	0.85	10	639	[19]
J06113513−0410240	T0	1600	4.5	−0.25	0.55	2	11	[16]
J06272007−1114280	T6	1000	4.5	0.25	0.55	2	23	[16]
J06420559+4102000	L8	1600	4.5	0.75	0.85	10	53	[27]
J07053400−1839256	L8	1600	4.5	0.50	0.85	10	20	[31]
J07271824+1710012	T7	950	4.5	0.25	0.55	2	28	[4]
J07414920+2351275	T5	1100	5.2	0.25	0.55	2	23	[11]
J07420130+2055198	T5	1100	5.2	0.25	0.55	2	35	[11]
J07483861+1743329	L7	1600	4.5	0.50	0.85	10	32	[25]
J07554795+2212169	T5	1100	5.2	0.25	0.55	2	18	[3]
J07584037+3247245	T2	1400	4.5	0.25	0.55	2	391	[9]
J08070023+4130268	L8p	1600	4.5	0.50	0.85	10	119	[22]
J08195805−0335285	T4	1200	5.2	0.25	0.55	2	36	[16]
J08203013+1037372	L9.5 ± 2	1600	4.5	0.50	0.85	10	23	[2]
J08300825+4828482	L8	1500	4.5	0.50	0.85	10	62	[9]
…	…	1600	5.2	0.75	0.55	−1	200	[9]
J08304878+0128311	T4.5	1100	4.5	0.25	0.55	2	36	[11]
J08371718−0000179	T1	1600	4.5	−0.25	0.55	−1	17	[33]
J08523490+4720359	L9.5 ± 1	1600	4.5	0.50	0.85	10	37	[11]
J08575849+5708514	L8	1600	4.5	0.75	0.85	10	700	[11]
J08583467+3256275	T1	1600	4.5	0.50	0.85	10	32	[11]

Table 16
(Continued)

Designation	SpT	Best-fit LOWZ Parameters						References
		$T_{\rm eff}$ (K)	$\log g$ (cm s^{-2})	[M/H] (dex)	C/O	$\log k_{zz}$ (cm^2 s^{-1})	χ^2_r	
…	…	1500	4.5	0.75	0.85	10	19	[2]
J09002368+2539343	L7	1600	4.5	0.00	0.55	2	52	[25]
J09025899+6708331	L7p	1600	4.5	0.75	0.85	10	631	[31]
J09293364+3429527	L8	1600	4.5	0.75	0.85	10	37	[11]
J09310955+0327331	L7.5 ± 1.5	1600	4.5	−0.25	0.55	10	32	[33]
J09553336−0208403	L7p	1600	4.5	0.75	0.85	10	60	[31]
J09560810−1447065	L9.5	1600	4.5	0.50	0.85	10	40	[30]
J10071185+1930563	L8 ± 1.5	1600	4.5	0.00	0.55	2	30	[2]
…	…	1600	4.5	0.75	0.85	10	19	[11]
J10255227+3212349	L7.5 ± 2.5	1600	4.5	0.50	0.85	10	16	[2]
…	…	1600	4.5	0.50	0.85	10	8	[25]
J10271549+5445175	L7	1600	4.5	0.50	0.85	10	93	[32]
J10302678+0213057	L9.5 ± 1	1600	4.5	0.50	0.85	10	16	[11]
J10430758+2225236	L8	1600	4.5	0.75	0.85	10	44	[5]
J10433508+1213149	L9	1600	4.5	0.50	0.85	10	18	[12]
…	…	1600	4.5	0.50	0.85	10	53	[11]
J10440942+0429376	L7	1600	4.5	0.50	0.85	10	55	[11]
J10475385+2124234	T6.5	900	5.0	−0.25	0.55	−1	62	[9]
J10482926+0919373	T2.5	1400	5.0	−0.50	0.10	−1	27	[11]
J10491557−5319061A	L8	1500	4.5	1.00	0.85	10	778	[18]
J10491557−5319061B	T0.5	1600	4.5	0.25	0.55	−1	252	[18]
J10595185+3042059	T4	1200	5.2	0.25	0.55	−1	13	[10]
J11220826−3512363	T2	1300	4.5	−0.25	0.55	2	86	[3]
J11472421−2040204	L7	1500	4.5	1.00	0.85	10	203	[29]
J11555389+0559577	L7.5	1600	4.5	0.50	0.85	10	78	[11]
J12010457+5730042	L9	1600	4.5	0.50	0.85	10	19	[31]
J12060248+2813293	T3	1200	5.2	−0.25	0.55	10	26	[2]
J12144089+6316434	T3.5 ± 1	1200	5.0	0.75	0.55	2	37	[2]
J12195156+3128497	L8	1600	4.5	0.50	0.85	10	61	[11]
J12314753+0847331	T5.5	1100	4.5	0.25	0.55	−1	91	[1]
J12545393−0122474	T2	1400	5.2	0.25	0.55	2	80	[1]
J13072984−0558146	L8	1600	4.5	0.50	0.85	10	30	[28]
J13184567+3626138	L7	1600	4.5	0.75	0.85	10	34	[32]
J13240767+1906259	T3.5	1200	5.2	0.00	0.55	2	118	[13]
J13262981−0038314	L8:	1600	4.5	0.75	0.85	10	196	[11]
J13464634−0031501	T6.5	1000	4.5	0.00	0.55	−1	30	[4]
J13480699+6603284	L9	1600	4.5	0.50	0.85	10	18	[16]
J13585269+3747137	T4.5 ± 1	1000	5.0	−0.50	0.55	−1	36	[2]
J14002320+4338222	L7 ± 1	1600	5.0	0.50	0.85	10	37	[11]
J14321117+3244338	L7	1600	4.5	0.75	0.85	10	52	[31]
J14564268+6450097	L7p	1600	4.5	0.75	0.85	10	154	[31]
J15031961+2525196	T5	1100	5.2	0.25	0.55	2	114	[1]
J15050237−2853452	T1.5	1500	5.0	0.00	0.55	2	55	[13]
J15131461+4019356	L8	1600	4.5	0.75	0.85	10	8	[22]
J15150607+4436483	L7.5 ± 1.5	1600	4.5	0.75	0.85	10	39	[11]
J15164306+3053443	T0.5 ± 1	1500	4.5	0.75	0.85	10	32	[11]
J15203974+3546210	T0 ± 1	1600	5.2	0.00	0.55	2	15	[33]
…	…	1500	4.5	0.25	0.85	10	106	[11]
J15210327+0131426	T2:	1300	5.0	0.25	0.55	2	19	[11]
J15232263+3014562	L8	1600	4.5	0.75	0.85	10	26	[11]
J15261405+2043414	L7	1600	4.5	0.50	0.85	10	102	[1]
J15335852+4757069	L8:	1600	4.5	0.75	0.85	10	29	[31]
J15400942+3742316	L9 ± 1.5	1600	4.5	0.50	0.85	10	20	[2]
…	…	1600	4.5	0.50	0.85	10	26	[11]
J15423630−0045452	L7	1600	4.5	−0.25	0.55	10	26	[15]
J15450901+3555271	L7.5	1600	5.0	0.50	0.85	10	10	[33]
J15461460+4932113	T2.5 ± 1	1300	4.5	−0.25	0.55	2	28	[11]
J15462718−3325111	T5.5	1100	5.2	0.25	0.55	2	26	[9]
J16241436+0029158	T6	1000	5.2	0.00	0.55	−1	64	[4]
J16272565+3255246	T6	900	4.5	−0.50	0.55	−1	33	[16]
J16291855+0335355	T2	1400	5.2	0.25	0.55	2	188	[17]
J16303054+4344032	L7 ± 1.5	1600	4.5	0.75	0.85	10	37	[11]
J16322911+1904407	L8	1600	4.5	0.75	0.85	10	42	[8]
J16323934+4150048	T1:	1400	4.5	−0.25	0.55	2	8	[11]
J16471557+5632083	L9p	1600	4.5	0.75	0.85	10	42	[16]
J17342104+5023508	T4	1200	5.2	0.00	0.55	−1	46	[21]
J17385927+6142421	L9p	1500	4.5	1.00	0.85	10	128	[21]
J17502385+4222373	T2	1500	4.5	−0.25	0.55	2	23	[3]
J17503293+1759042	T3.5	1200	5.2	0.25	0.55	2	37	[1]

Table 16
(Continued)

Designation	SpT	Best-fit LOWZ Parameters						References
		$T_{\rm eff}$ (K)	$\log g$ (cm s^{-2})	[M/H] (dex)	C/O	$\log k_{zz}$ (cm^2 s^{-1})	χ^2_r	
J17545447+1649196	T5.5	1100	4.5	0.25	0.55	−1	58	[9]
J17551028+1803202	T2	1400	4.5	−1.00	0.10	−1	40	[24]
J18002660+0134531	L7.5	1600	4.5	0.75	0.85	10	580	[14]
J18095253−0448125	T0.5	1600	4.5	−0.25	0.55	2	47	[21]
…	…	1600	4.5	−0.25	0.55	2	24	[20]
…	…	1600	4.5	−0.25	0.55	2	24	[27]
J18305856+4542574	L9	1600	4.5	0.50	0.85	10	11	[16]
J19010601+4718136	T5	1100	5.0	0.25	0.55	−1	69	[1]
J19062474+4508071	T6	1000	5.0	−0.25	0.55	−1	24	[16]
J19284135+2356049	T6	1100	5.2	0.25	0.55	2	518	[21]
…	…	1100	5.2	0.25	0.55	−1	121	[33]
J20304279+0749347	T1.5	1400	5.0	0.00	0.55	2	721	[21]
…	…	1400	4.5	−0.50	0.55	2	43	[20]
J20431769−1551031	L9	1500	5.0	0.50	0.85	10	13	[11]
J20435642+6220490	T1.5	1500	5.2	−0.50	0.10	−1	18	[21]
J20474959−0718176	T0:	1600	5.2	0.00	0.55	2	26	[11]
J20520174−2043119	L8	1600	4.5	0.50	0.85	10	28	[28]
J21171444−2940052	T0:	1600	5.2	0.00	0.55	2	5	[27]
J21241387+0059599	T5	1100	5.0	0.25	0.55	−1	26	[3]
J21243865+1849263	L9	1600	4.5	0.50	0.85	10	36	[26]
J21324898−1452544	T4	1200	5.2	0.00	0.55	2	14	[33]
J21392676+0220226	T1.5	1500	4.5	0.25	0.55	−1	882	[3]
J21442847+1446077	T2.5	1300	4.5	0.50	0.55	2	113	[7]
J21513839−4853542	T4	1200	5.2	0.00	0.55	2	35	[3]
J21513979+3402444	L7p	1600	5.0	0.50	0.85	10	24	[12]
J21542494−1023022	T4.5	1200	5.2	0.00	0.55	−1	20	[6]
J22092183−2711329	T2.5	1300	4.5	−0.25	0.55	2	64	[33]
J22221993+3026014	L9	1600	5.2	0.50	0.85	10	25	[25]
J22361759+5105519	T5.5	1100	4.5	0.25	0.55	2	176	[20]
J22393755+1617161	T3	1300	5.0	0.25	0.55	2	106	[16]
J22541892+3123498	T4	1200	4.5	0.00	0.55	2	123	[1]
J23032925+3150210	T2p	1300	5.0	−0.50	0.55	2	44	[30]
…	…	1300	5.0	−0.50	0.55	2	41	[28]
J23185497−1301106	T5	1200	4.5	0.00	0.55	−1	53	[33]
J23230708+0541130	L8p	1600	4.5	0.50	0.85	10	16	[31]
J23254530+4251488	L8	1600	4.5	0.50	0.85	10	13	[11]
J23272874−2730566	L9	1600	4.5	0.50	0.85	10	26	[16]
J23305116−0844533	L8.0	1600	4.5	0.75	0.85	10	25	[33]
J23333346+0251284	L8p	1600	4.5	0.75	0.85	10	31	[31]
J23352734+4511442	L9p	1600	4.5	0.75	0.85	10	157	[27]
J23391025+1352284	T5	1100	5.2	0.25	0.55	2	38	[3]
J23565477−1553111	T5.5	1100	5.2	0.25	0.55	2	29	[3]

References. [1] A. J. Burgasser et al. (2004); [2] K. Chiu et al. (2006); [3] A. J. Burgasser et al. (2006b); [4] A. J. Burgasser et al. (2006a); [5] N. Siegler et al. (2007); [6] D. L. Looper et al. (2007); [7] K. L. Luhman et al. (2007); [8] A. J. Burgasser (2007b); [9] A. J. Burgasser et al. (2008a); [10] S. S. Sheppard & M. C. Cushing (2009); [11] A. J. Burgasser et al. (2010a); [12] J. D. Kirkpatrick et al. (2010); [13] N. R. Deacon et al. (2011); [14] J. E. Gizis et al. (2011); [15] K. Geissler et al. (2011); [16] J. D. Kirkpatrick et al. (2011); [17] N. R. Deacon et al. (2012b); [18] A. J. Burgasser et al. (2013); [19] P. J. Castro et al. (2013); [20] W. M. J. Best et al. (2013); [21] G. N. Mace et al. (2013b); [22] M. A. Thompson et al. (2013); [23] B. P. Bowler et al. (2014); [24] K. L. Luhman & S. S. Sheppard (2014); [25] D. C. Bardalez Gagliuffi et al. (2014); [26] K. Kellogg et al. (2015); [27] W. M. J. Best et al. (2015); [28] A. C. Schneider et al. (2016a); [29] A. C. Schneider et al. (2016b); [30] J. Robert et al. (2016); [31] A. C. Schneider et al. (2017); [32] K. Kellogg et al. (2017); [33] A. J. Burgasser et al. (2025, in preparation)

Appendix B
Bolometric Corrections from LOWZ Models

We provide in this Appendix bolometric corrections computed from a subset of the LOWZ model grid (A. M. Meisner et al. 2021), specifically: $\log g = 5.0$ (in cm s^{-2}); $\log k_{zz} = 2$ (in cm^2 s^{-1}); C/O = 0.55; $-2.5 \leqslant$ [M/H] $\leqslant 1.0$; and 500 K $\leqslant T_{\rm eff} \leqslant$ 1600 K, listed in Table 17. These corrections are for the MKO *YJHK* and WISE W1W2 filters and are computed on the Vega system. See Section 7.1 for details on these calculations.

Table 17
Bolometric Corrections for Brown Dwarfs Based on the LOWZ Models

			Bolometric Correction					
$T_{\rm eff}$ (K)	[M/H] (**dex**)	$M_{\rm bol}$ (mag)	MKO Y (mag)	MKO J (mag)	MKO H (mag)	MKO K (mag)	WISE W1 (mag)	WISE W2 (mag)
500	−2.50	20.86	−0.94	−1.71	−0.13	−5.84	4.58	6.02
500	−2.00	20.86	−0.61	−1.29	0.11	−5.18	4.35	6.13
500	−1.50	20.86	−0.17	−0.56	0.36	−4.19	4.00	6.26
500	−1.00	20.86	0.24	0.33	0.61	−2.82	3.52	6.36
500	−0.50	20.86	0.63	1.25	0.86	−1.34	2.99	6.33
500	−0.25	20.86	0.83	1.62	1.08	−0.72	2.70	6.24
500	0.00	20.86	0.93	1.91	1.22	−0.01	2.46	6.14
500	0.25	20.86	0.92	2.08	1.30	0.61	2.26	6.00
500	0.50	20.86	0.94	2.19	1.35	1.17	2.10	5.84
500	0.75	20.86	0.88	2.16	1.37	1.63	2.01	5.66
500	1.00	20.86	0.90	2.09	1.30	1.90	1.96	5.45
550	−2.50	20.45	−0.44	−1.04	0.26	−4.83	4.56	5.95
550	−2.00	20.45	−0.08	−0.61	0.42	−4.25	4.33	6.06
550	−1.50	20.45	0.25	0.05	0.67	−3.30	4.00	6.19
550	−1.00	20.45	0.43	0.90	0.99	−1.98	3.55	6.27
550	−0.50	20.45	0.95	1.67	1.24	−0.73	3.01	6.20
550	−0.25	20.45	0.99	1.96	1.37	−0.13	2.75	6.13
550	0.00	20.45	0.99	2.16	1.47	0.52	2.54	6.05
550	0.25	20.45	0.96	2.30	1.54	1.08	2.35	5.94
550	0.50	20.45	1.06	2.35	1.53	1.52	2.20	5.82
550	0.75	20.45	1.18	2.31	1.48	1.86	2.09	5.67
550	1.00	20.45	1.09	2.24	1.41	2.07	2.06	5.50
600	−2.50	20.07	−0.08	−0.32	0.55	−3.79	4.57	5.93
600	−2.00	20.07	0.18	0.07	0.79	−3.28	4.35	6.02
600	−1.50	20.07	0.62	0.67	1.04	−2.49	3.99	6.11
600	−1.00	20.07	0.98	1.35	1.25	−1.30	3.54	6.17
600	−0.50	20.07	1.10	1.98	1.51	−0.22	3.02	6.08
600	−0.25	20.07	1.13	2.19	1.62	0.35	2.78	6.01
600	0.00	20.07	1.22	2.36	1.71	0.92	2.58	5.91
600	0.25	20.07	1.19	2.45	1.74	1.43	2.41	5.77
600	0.50	20.07	1.20	2.50	1.75	1.87	2.32	5.61
600	0.75	20.07	1.17	2.46	1.70	2.17	2.29	5.41
600	1.00	20.07	1.13	2.44	1.67	2.35	2.29	5.20
650	−2.50	19.72	0.23	0.10	0.81	−3.12	4.53	5.84
650	−2.00	19.72	0.54	0.48	0.98	−2.58	4.29	5.92
650	−1.50	19.72	0.88	1.02	1.18	−1.79	3.95	6.01
650	−1.00	19.72	1.08	1.66	1.48	−0.78	3.51	6.05
650	−0.50	19.72	1.30	2.20	1.69	0.20	3.02	5.97
650	−0.25	19.72	1.26	2.37	1.79	0.72	2.80	5.90
650	0.00	19.72	1.07	2.38	1.85	1.25	2.61	5.82
650	0.25	19.72	1.24	2.55	1.86	1.70	2.45	5.72
650	0.50	19.72	1.27	2.59	1.85	2.07	2.36	5.61
650	0.75	19.72	1.22	2.55	1.78	2.28	2.30	5.46
650	1.00	19.72	1.24	2.57	1.76	2.43	2.31	5.27
700	−2.50	19.40	0.39	0.67	1.06	−2.27	4.52	5.79
700	−2.00	19.40	0.60	1.00	1.27	−1.79	4.30	5.87
700	−1.50	19.40	0.95	1.42	1.47	−1.13	3.94	5.93
700	−1.00	19.40	1.35	1.95	1.65	−0.36	3.47	5.93
700	−0.50	19.40	1.39	2.37	1.86	0.51	2.99	5.84
700	−0.25	19.40	1.38	2.52	1.95	1.02	2.79	5.78
700	0.00	19.40	1.38	2.59	1.97	1.50	2.62	5.68
700	0.25	19.40	1.35	2.62	1.96	1.93	2.50	5.55
700	0.50	19.40	1.34	2.64	1.95	2.26	2.44	5.39
700	0.75	19.40	1.34	2.67	1.94	2.48	2.45	5.21

Table 17
(Continued)

$T_{\rm eff}$ (K)	[M/H] (**dex**)	$M_{\rm bol}$ (mag)	Bolometric Correction					
			MKO Y (mag)	MKO J (mag)	MKO H (mag)	MKO K (mag)	WISE W1 (mag)	WISE W2 (mag)
700	1.00	19.40	1.41	2.77	1.89	2.59	2.49	5.02
750	−2.50	19.10	0.61	0.91	1.21	−1.79	4.46	5.69
750	−2.00	19.10	0.84	1.26	1.42	−1.31	4.23	5.76
750	−1.50	19.10	1.19	1.68	1.60	−0.70	3.88	5.81
750	−1.00	19.10	1.43	2.12	1.77	−0.02	3.41	5.81
750	−0.50	19.10	1.46	2.49	2.00	0.82	2.98	5.73
750	−0.25	19.10	1.44	2.61	2.05	1.29	2.80	5.63
750	0.00	19.10	1.43	2.67	2.08	1.74	2.65	5.52
750	0.25	19.10	1.46	2.75	2.11	2.17	2.57	5.35
750	0.50	19.10	1.40	2.71	2.07	2.43	2.52	5.16
750	0.75	19.10	1.52	2.84	2.08	2.59	2.53	4.96
750	1.00	19.10	1.39	2.77	2.03	2.71	2.64	4.86
800	−2.50	18.82	0.69	1.20	1.39	−1.27	4.42	5.59
800	−2.00	18.82	0.97	1.49	1.54	−0.84	4.17	5.65
800	−1.50	18.82	1.21	1.85	1.74	−0.29	3.83	5.71
800	−1.00	18.82	1.34	2.24	1.96	0.36	3.40	5.71
800	−0.50	18.82	1.41	2.51	2.10	1.09	2.97	5.63
800	−0.25	18.82	1.53	2.66	2.15	1.51	2.79	5.56
800	0.00	18.82	1.49	2.73	2.12	1.88	2.63	5.48
800	0.25	18.82	1.53	2.81	2.13	2.25	2.55	5.38
800	0.50	18.82	1.56	2.87	2.11	2.48	2.52	5.22
800	0.75	18.82	1.60	2.95	2.13	2.64	2.56	5.05
800	1.00	18.82	1.42	2.79	2.05	2.71	2.62	4.89
850	−2.50	18.56	0.83	1.43	1.50	−0.83	4.36	5.49
850	−2.00	18.56	0.87	1.69	1.74	−0.34	4.16	5.58
850	−1.50	18.56	1.09	1.99	1.94	0.14	3.82	5.63
850	−1.00	18.56	1.40	2.33	2.07	0.63	3.36	5.59
850	−0.50	18.56	1.56	2.65	2.16	1.26	2.92	5.50
850	−0.25	18.56	1.53	2.69	2.20	1.68	2.78	5.44
850	0.00	18.56	1.48	2.67	2.22	2.09	2.68	5.34
850	0.25	18.56	1.59	2.75	2.23	2.42	2.63	5.18
850	0.50	18.56	1.85	3.00	2.33	2.61	2.62	5.02
850	0.75	18.56	1.85	3.16	2.30	2.72	2.65	4.86
850	1.00	18.56	1.63	2.97	2.23	2.80	2.72	4.74
900	−2.50	18.31	0.96	1.55	1.58	−0.54	4.29	5.39
900	−2.00	18.31	1.06	1.83	1.80	−0.09	4.08	5.46
900	−1.50	18.31	1.25	2.12	2.00	0.36	3.74	5.50
900	−1.00	18.31	1.45	2.41	2.14	0.86	3.31	5.49
900	−0.50	18.31	1.48	2.57	2.33	1.56	2.96	5.41
900	−0.25	18.31	1.54	2.70	2.31	1.90	2.81	5.32
900	0.00	18.31	1.65	2.86	2.33	2.25	2.72	5.18
900	0.25	18.31	1.70	2.92	2.34	2.51	2.69	5.00
900	0.50	18.31	1.65	2.84	2.34	2.68	2.72	4.86
900	0.75	18.31	1.78	2.95	2.40	2.79	2.76	4.72
900	1.00	18.31	1.44	2.80	2.33	2.88	2.82	4.60
950	−2.50	18.07	1.08	1.68	1.65	−0.27	4.22	5.28
950	−2.00	18.07	1.09	1.93	1.88	0.16	4.02	5.35
950	−1.50	18.07	1.19	2.17	2.11	0.64	3.70	5.42
950	−1.00	18.07	1.23	2.32	2.37	1.25	3.35	5.45
950	−0.50	18.07	1.54	2.63	2.38	1.70	2.93	5.33
950	−0.25	18.07	1.64	2.68	2.43	2.04	2.81	5.27
950	0.00	18.07	1.60	2.66	2.44	2.39	2.76	5.20
950	0.25	18.07	1.61	2.86	2.35	2.54	2.67	5.05
950	0.50	18.07	1.58	2.83	2.39	2.70	2.70	4.90
950	0.75	18.07	1.63	2.81	2.39	2.79	2.74	4.76
950	1.00	18.07	1.82	2.94	2.52	2.90	2.82	4.64
1000	−2.50	17.85	1.01	1.79	1.77	0.08	4.19	5.20
1000	−2.00	17.85	0.98	1.97	2.04	0.54	4.01	5.30
1000	−1.50	17.85	1.04	2.12	2.28	0.99	3.71	5.37
1000	−1.00	17.85	1.31	2.37	2.41	1.39	3.30	5.34
1000	−0.50	17.85	1.49	2.62	2.46	1.87	2.93	5.24
1000	−0.25	17.85	1.57	2.71	2.47	2.17	2.82	5.15

Table 17
(Continued)

$T_{\rm eff}$ (K)	[M/H] (**dex**)	$M_{\rm bol}$ (mag)	Bolometric Correction					
			MKO Y (mag)	MKO J (mag)	MKO H (mag)	MKO K (mag)	WISE W1 (mag)	WISE W2 (mag)
1000	0.00	17.85	1.60	2.73	2.52	2.48	2.79	5.04
1000	0.25	17.85	1.65	2.78	2.49	2.63	2.76	4.90
1000	0.50	17.85	1.70	2.92	2.52	2.74	2.77	4.75
1000	0.75	17.85	1.86	3.05	2.67	2.88	2.82	4.63
1000	1.00	17.85	1.65	2.86	2.62	2.95	2.89	4.51
1100	−2.50	17.44	1.16	1.94	1.84	0.40	4.04	4.99
1100	−2.00	17.44	1.18	2.11	2.10	0.83	3.87	5.09
1100	−1.50	17.44	1.18	2.28	2.34	1.24	3.58	5.16
1100	−1.00	17.44	1.07	2.22	2.61	1.88	3.33	5.23
1100	−0.50	17.44	1.35	2.47	2.62	2.22	2.97	5.08
1100	−0.25	17.44	1.34	2.45	2.66	2.49	2.91	5.02
1100	0.00	17.44	1.34	2.42	2.69	2.70	2.90	4.93
1100	0.25	17.44	1.61	2.77	2.69	2.72	2.81	4.78
1100	0.50	17.44	1.56	2.72	2.76	2.86	2.86	4.66
1100	0.75	17.44	1.58	2.72	2.87	3.02	2.98	4.41
1100	1.00	17.44	1.73	2.84	2.83	3.04	3.01	4.27
1200	−2.50	17.06	1.13	2.05	1.93	0.75	3.94	4.82
1200	−2.00	17.06	1.02	2.15	2.23	1.23	3.81	4.96
1200	−1.50	17.06	1.08	2.20	2.48	1.65	3.55	5.04
1200	−1.00	17.06	1.20	2.33	2.64	2.00	3.21	5.01
1200	−0.50	17.06	1.14	2.27	2.76	2.54	3.06	4.89
1200	−0.25	17.06	1.16	2.29	2.78	2.71	3.02	4.80
1200	0.00	17.06	1.29	2.42	2.77	2.76	2.95	4.68
1200	0.25	17.06	1.26	2.40	2.83	2.91	2.99	4.58
1200	0.50	17.06	1.58	2.69	2.84	2.89	2.94	4.41
1200	0.75	17.06	1.51	2.61	2.88	3.02	3.01	4.31
1200	1.00	17.06	1.47	2.68	2.85	3.07	3.05	4.18
1300	−2.50	16.71	1.18	2.11	1.96	0.94	3.81	4.65
1300	−2.00	16.71	1.07	2.22	2.27	1.41	3.70	4.78
1300	−1.50	16.71	0.95	2.21	2.55	1.91	3.50	4.89
1300	−1.00	16.71	1.05	2.20	2.72	2.31	3.23	4.88
1300	−0.50	16.71	1.23	2.32	2.79	2.60	3.01	4.72
1300	−0.25	16.71	1.13	2.24	2.82	2.79	3.02	4.66
1300	0.00	16.71	1.05	2.19	2.85	2.94	3.06	4.58
1300	0.25	16.71	1.40	2.49	2.96	2.99	3.02	4.45
1300	0.50	16.71	1.37	2.45	2.99	3.16	3.13	4.26
1300	0.75	16.71	1.48	2.53	2.88	3.06	3.07	4.09
1300	1.00	16.71	1.46	2.47	2.87	3.19	3.18	3.96
1400	−2.50	16.39	1.20	2.16	2.00	1.13	3.71	4.49
1400	−2.00	16.39	1.02	2.25	2.31	1.60	3.62	4.64
1400	−1.50	16.39	0.95	2.23	2.58	2.04	3.41	4.73
1400	−1.00	16.39	0.91	2.19	2.76	2.47	3.20	4.68
1400	−0.50	16.39	0.98	2.13	2.84	2.81	3.13	4.56
1400	−0.25	16.39	0.91	2.08	2.85	2.94	3.14	4.49
1400	0.00	16.39	1.11	2.20	2.89	3.00	3.12	4.39
1400	0.25	16.39	1.03	2.13	2.87	3.15	3.21	4.29
1400	0.50	16.39	1.02	2.12	2.88	3.28	3.32	4.17
1400	0.75	16.39	1.26	2.30	2.91	3.28	3.25	4.02
1400	1.00	16.39	1.24	2.24	2.88	3.39	3.44	3.80
1500	−2.50	16.09	1.22	2.19	2.01	1.24	3.59	4.34
1500	−2.00	16.09	1.08	2.28	2.32	1.69	3.50	4.48
1500	−1.50	16.09	0.89	2.24	2.60	2.19	3.36	4.58
1500	−1.00	16.09	0.85	2.16	2.78	2.57	3.18	4.52
1500	−0.50	16.09	0.80	2.06	2.85	2.90	3.18	4.43
1500	−0.25	16.09	0.79	2.04	2.86	3.02	3.21	4.36
1500	0.00	16.09	0.88	2.02	2.85	3.15	3.28	4.29
1500	0.25	16.09	0.90	2.04	2.87	3.26	3.37	4.15
1500	0.50	16.09	1.02	2.07	2.83	3.31	3.39	4.01
1500	0.75	16.09	1.03	2.06	2.82	3.41	3.53	3.89
1500	1.00	16.09	1.19	2.21	2.81	3.38	3.47	3.72
1600	−2.50	15.81	1.25	2.20	2.01	1.34	3.49	4.22
1600	−2.00	15.81	1.05	2.29	2.34	1.81	3.43	4.35

Table 17
(Continued)

$T_{\rm eff}$ (K)	[M/H] (**dex**)	$M_{\rm bol}$ (mag)	Bolometric Correction					
			MKO Y (mag)	MKO J (mag)	MKO H (mag)	MKO K (mag)	WISE W1 (mag)	WISE W2 (mag)
1600	−1.50	15.81	0.93	2.26	2.61	2.25	3.27	4.41
1600	−1.00	15.81	0.79	2.15	2.79	2.66	3.20	4.37
1600	−0.50	15.81	0.73	2.04	2.85	2.97	3.27	4.27
1600	−0.25	15.81	0.73	1.96	2.84	3.13	3.35	4.23
1600	0.00	15.81	0.77	1.99	2.85	3.21	3.37	4.14
1600	0.25	15.81	0.79	1.98	2.84	3.33	3.49	4.05
1600	0.50	15.81	0.96	2.02	2.81	3.40	3.57	3.95
1600	0.75	15.81	0.96	2.00	2.76	3.43	3.65	3.82
1600	1.00	15.81	1.01	2.04	2.77	3.46	3.73	3.65

Note. Magnitudes are on the Vega system, and evaluation of $M_{\rm bol}$ assumes $R = 0.077\ R_\odot$. We further constrain the LOWZ models to have $\log g = 5$ (cm s^{-2}), $\log \kappa_{zz} = 2$ (cm^2 s^{-1}), and C/O = 0.55.

ORCID iDs

Adam J. Burgasser https://orcid.org/0000-0002-6523-9536
Adam C. Schneider https://orcid.org/0000-0002-6294-5937
Aaron M. Meisner https://orcid.org/0000-0002-1125-7384
Dan Caselden https://orcid.org/0000-0001-7896-5791
Chih-Chun Hsu https://orcid.org/0000-0002-5370-7494
Roman Gerasimov https://orcid.org/0000-0003-0398-639X
Christian Aganze https://orcid.org/0000-0003-2094-9128
Emma Softich https://orcid.org/0000-0002-1420-1837
Preethi Karpoor https://orcid.org/0000-0002-1480-9041
Christopher A. Theissen https://orcid.org/0000-0002-9807-5435
Hunter Brooks https://orcid.org/0000-0002-5253-0383
Thomas P. Bickle https://orcid.org/0000-0003-2235-761X
Jonathan Gagné https://orcid.org/0000-0002-2592-9612
Ètienne Artigau https://orcid.org/0000-0003-3506-5667
Michaël Marsset https://orcid.org/0000-0001-8617-2425
Austin Rothermich https://orcid.org/0000-0003-4083-9962
Jacqueline K. Faherty https://orcid.org/0000-0001-6251-0573
J. Davy Kirkpatrick https://orcid.org/0000-0003-4269-260X
Marc J. Kuchner https://orcid.org/0000-0002-2387-5489
Nikolaj Stevnbak Andersen https://orcid.org/0000-0003-4714-3829
Guillaume Colin https://orcid.org/0000-0002-7630-1243
Jean Marc Gantier https://orcid.org/0000-0002-1044-1112
Leopold Gramaize https://orcid.org/0000-0002-8960-4964
Les Hamlet https://orcid.org/0000-0002-7389-2092
Ken Hinckley https://orcid.org/0000-0002-4733-4927
Martin Kabatnik https://orcid.org/0000-0003-4905-1370
Frank Kiwy https://orcid.org/0000-0001-8662-1622
Arttu Sainio https://orcid.org/0000-0003-4864-5484
Jörg Schümann https://orcid.org/0000-0002-7587-7195
Melina Thévenot https://orcid.org/0000-0001-5284-9231

References

Aguilera-Gómez, C., Ramírez, I., & Chanamé, J. 2018, A&A, 614, A55
Albert, L., Artigau, É., Delorme, P., et al. 2011, AJ, 141, 203
Allard, F., Homeier, D., & Freytag, B. 2012, RSPTA, 370, 2765
Allard, N. F., Spiegelman, F., & Kielkopf, J. F. 2016, A&A, 589, A21
Alvarado, E., Gerasimov, R., Burgasser, A. J., et al. 2024, RNAAS, 8, 134
Anguiano, B., Majewski, S. R., Hayes, C. R., et al. 2020, AJ, 160, 43
Arentsen, A., Prugniel, P., Gonneau, A., et al. 2019, A&A, 627, A138
Astropy Collaboration, Price-Whelan, A. M., Sipőcz, B. M., et al. 2018, AJ, 156, 123
Astropy Collaboration, Price-Whelan, A. M., Lim, P. L., et al. 2022, ApJ, 935, 167
Astropy Collaboration, Robitaille, T. P., Tollerud, E. J., et al. 2013, A&A, 558, A33
Baraffe, I., Chabrier, G., Allard, F., & Hauschildt, P. H. 1997, A&A, 327, 1054
Baraffe, I., Chabrier, G., Barman, T. S., Allard, F., & Hauschildt, P. H. 2003, A&A, 402, 701
Bardalez Gagliuffi, D. C., Burgasser, A. J., Gelino, C. R., et al. 2014, ApJ, 794, 143
Bardalez Gagliuffi, D. C., Burgasser, A. J., Schmidt, S. J., et al. 2019, ApJ, 883, 205
Beiler, S. A., Mukherjee, S., Cushing, M. C., et al. 2024, ApJ, 973, 60
Bensby, T., Feltzing, S., & Lundström, I. 2003, A&A, 410, 527
Best, W. M. J., Liu, M. C., Magnier, E. A., & Dupuy, T. J. 2020, AJ, 159, 257
Best, W. M. J., Liu, M. C., Magnier, E. A., & Dupuy, T. J. 2021, AJ, 161, 42
Best, W. M. J., Liu, M. C., Magnier, E. A., et al. 2013, ApJ, 777, 84
Best, W. M. J., Liu, M. C., Magnier, E. A., et al. 2015, ApJ, 814, 118
Best, W. M. J., Magnier, E. A., Liu, M. C., et al. 2018, ApJS, 234, 1
Bickle, T. P., Schneider, A. C., Gagné, J., et al. 2024, AJ, 168, 66
Bochanski, J. J., Hennawi, J. F., Simcoe, R. A., et al. 2009, PASP, 121, 1409
Bonaca, A., Conroy, C., Wetzel, A., Hopkins, P. F., & Kereš, D. 2017, ApJ, 845, 101
Bonnarel, F., Fernique, P., Bienaymé, O., et al. 2000, A&AS, 143, 33
Bovy, J. 2015, ApJS, 216, 29
Bowler, B. P., Liu, M. C., & Cushing, M. C. 2009, ApJ, 706, 1114
Bowler, B. P., Liu, M. C., Kraus, A. L., & Mann, A. W. 2014, ApJ, 784, 65
Brooks, H., Kirkpatrick, J. D., Caselden, D., et al. 2022, AJ, 163, 47
Burgasser, A. J. 2007a, ApJ, 658, 617
Burgasser, A. J. 2007b, ApJ, 659, 655
Burgasser, A. J. 2009, in IAU Symp. 258, The Ages of Stars, ed. E. E. Mamajek, D. R. Soderblom, & R. F. G. Wyse (Cambridge: Cambridge Univ. Press), 317
Burgasser, A. J., Bezanson, R., Labbe, I., et al. 2024, ApJ, 962, 177
Burgasser, A. J., Burrows, A., & Kirkpatrick, J. D. 2006a, ApJ, 639, 1095
Burgasser, A. J., Cruz, K. L., Cushing, M., et al. 2010a, ApJ, 710, 1142
Burgasser, A. J., Cruz, K. L., & Kirkpatrick, J. D. 2007a, ApJ, 657, 494
Burgasser, A. J., Cushing, M. C., Kirkpatrick, J. D., et al. 2011, ApJ, 735, 116
Burgasser, A. J., Geballe, T. R., Leggett, S. K., Kirkpatrick, J. D., & Golimowski, D. A. 2006b, ApJ, 637, 1067
Burgasser, A. J., Gillon, M., Melis, C., et al. 2015, AJ, 149, 104
Burgasser, A. J., & Kirkpatrick, J. D. 2006, ApJ, 645, 1485
Burgasser, A. J., Kirkpatrick, J. D., Brown, M. E., et al. 2002b, ApJ, 564, 421
Burgasser, A. J., Kirkpatrick, J. D., Burrows, A., et al. 2003, ApJ, 592, 1186
Burgasser, A. J., Liu, M. C., Ireland, M. J., Cruz, K. L., & Dupuy, T. J. 2008a, ApJ, 681, 579
Burgasser, A. J., Looper, D., & Rayner, J. T. 2010b, AJ, 139, 2448
Burgasser, A. J., Looper, D. L., Kirkpatrick, J. D., & Liu, M. C. 2007b, ApJ, 658, 557
Burgasser, A. J., Marley, M. S., Ackerman, A. S., et al. 2002a, ApJL, 571, L151

Burgasser, A. J., McElwain, M. W., Kirkpatrick, J. D., et al. 2004, AJ, 127, 2856
Burgasser, A. J., Sheppard, S. S., & Luhman, K. L. 2013, ApJ, 772, 129
Burgasser, A. J., Simcoe, R. A., Bochanski, J. J., et al. 2010c, ApJ, 725, 1405
Burgasser, A. J. & Splat Development Team 2017, ASInC, 14, 7
Burgasser, A. J., Vrba, F. J., Lépine, S., et al. 2008b, ApJ, 672, 1159
Burningham, B., Smith, L., Cardoso, C. V., et al. 2014, MNRAS, 440, 359
Burningham, B., Cardoso, C. V., Smith, L., et al. 2013, MNRAS, 433, 457
Burrows, A., Heng, K., & Nampaisarn, T. 2011, ApJ, 736, 47
Burrows, A., Hubbard, W. B., Lunine, J. I., & Liebert, J. 2001, RvMP, 73, 719
Burrows, A., Sudarsky, D., & Hubeny, I. 2006, ApJ, 640, 1063
Caiazzo, I., Heyl, J. S., Richer, H., & Kalirai, J. 2017, arXiv:1702.00091
Casagrande, L., & VandenBerg, D. A. 2014, MNRAS, 444, 392
Castro, P. J., Gizis, J. E., Harris, H. C., et al. 2013, ApJ, 776, 126
Catchpole, R. M., Pagel, B. E. J., & Powell, A. L. T. 1967, MNRAS, 136, 403
Cepa, J., Aguiar, M., Escalera, V. G., et al. 2000, Proc. SPIE, 4008, 623
Chambers, K. C., Magnier, E. A., Metcalfe, N., et al. 2016, arXiv:1612.05560
Chiu, K., Fan, X., Leggett, S. K., et al. 2006, AJ, 131, 2722
Cushing, M. C., Kirkpatrick, J. D., Gelino, C. R., et al. 2011, ApJ, 743, 50
Cushing, M. C., Marley, M. S., Saumon, D., et al. 2008, ApJ, 678, 1372
Cushing, M. C., Vacca, W. D., & Rayner, J. T. 2004, PASP, 116, 362
Cutri, R. M., Skrutskie, M. F., van Dyk, S., et al. 2003, yCat, 2246, 0
Deacon, N. R., Liu, M. C., Magnier, E. A., et al. 2011, AJ, 142, 77
Deacon, N. R., Liu, M. C., Magnier, E. A., et al. 2012a, ApJ, 755, 94
Deacon, N. R., Liu, M. C., Magnier, E. A., et al. 2012b, ApJ, 757, 100
Delorme, P., Delfosse, X., Albert, L., et al. 2008, A&A, 482, 961
Dhital, S., West, A. A., Stassun, K. G., et al. 2012, AJ, 143, 67
Dupuy, T. J., & Liu, M. C. 2012, ApJS, 201, 19
Dupuy, T. J., & Liu, M. C. 2017, ApJS, 231, 15
Dye, S., Lawrence, A., Read, M. A., et al. 2018, MNRAS, 473, 5113
Elias, J. H., Rodgers, B., Joyce, R. R., et al. 2006, Proc. SPIE, 6269, 626914
Faherty, J. K., Burgasser, A. J., Cruz, K. L., et al. 2009, AJ, 137, 1
Faherty, J. K., Burgasser, A. J., Walter, F. M., et al. 2012, ApJ, 752, 56
Filippazzo, J. C., Rice, E. L., Faherty, J., et al. 2015, ApJ, 810, 158
Fouqué, P., Moutou, C., Malo, L., et al. 2018, MNRAS, 475, 1960
Gagné, J., Lambrides, E., Faherty, J. K., & Simcoe, R. 2015, FireHose_v2: Firehose v2.0, Zenodo:10.5281/zenodo.18775
Gaia Collaboration, Brown, A. G. A., Vallenari, A., et al. 2021, A&A, 650, C3
Gao, F., & Han, L. 2012, Computational Optimization and Applications, 51, 259
Garzón, F., Abreu, D., Barrera, S., et al. 2007, RMxAC, 29, 12
Geissler, K., Metchev, S., Kirkpatrick, J. D., Berriman, G. B., & Looper, D. 2011, ApJ, 732, 56
Gerasimov, R., Homeier, D., Burgasser, A., & Bedin, L. R. 2020, RNAAS, 4, 214
Geweke, J. 1992, in Bayesian Statistics 4, ed. A. D. J. M. Bernardo, J. O. Berger, & A. Smith (Oxford: Oxford Univ. Press)
Gizis, J. E. 1997, AJ, 113, 806
Gizis, J. E., Burgasser, A. J., Faherty, J. K., Castro, P. J., & Shara, M. M. 2011, AJ, 142, 171
Gizis, J. E., & Harvin, J. 2006, AJ, 132, 2372
Glazebrook, K., Nanayakkara, T., Jacobs, C., et al. 2023, ApJL, 947, L25
Gonzales, E. C., Burningham, B., Faherty, J. K., et al. 2021, ApJ, 923, 19
Gonzales, E. C., Faherty, J. K., Gagné, J. A., Artigau, É., & G. D., B. 2018, ApJ, 864, 100
Goyal, J. M., Wakeford, H. R., Mayne, N. J., et al. 2019, MNRAS, 482, 4503
Greco, J. J., Schneider, A. C., Cushing, M. C., Kirkpatrick, J. D., & Burgasser, A. J. 2019, AJ, 158, 182
Hainline, K. N., Helton, J. M., Johnson, B. D., et al. 2024, ApJ, 964, 66
Halbwachs, J. L., Mayor, M., & Udry, S. 2018, A&A, 619, A81
Hastings, W. K. 1970, Biometrika, 57, 97
Hejazi, N., Lépine, S., Homeier, D., Rich, R. M., & Shara, M. M. 2020, AJ, 159, 30
Helmi, A., White, S. D. M., de Zeeuw, P. T., & Zhao, H. 1999, Natur, 402, 53
Holwerda, B. W., Hsu, C.-C., Hathi, N., et al. 2024, MNRAS, 529, 1067
Hsu, C.-C., Burgasser, A. J., & Theissen, C. A. 2023, ApJL, 945, L6
Hsu, C.-C., Burgasser, A. J., Theissen, C. A., et al. 2021, ApJS, 257, 45
Hunter, J. D. 2007, CSE, 9, 90
Ivezić, Ž., Kahn, S. M., Tyson, J. A., et al. 2019, ApJ, 873, 111
Joy, A. H. 1947, ApJ, 105, 96
Jurić, M., Ivezić, Ž., Brooks, A., et al. 2008, ApJ, 673, 864
Kellogg, K., Kirkpatrick, J. D., Metchev, S., Gagné, J., & Faherty, J. K. 2018, AJ, 155, 87
Kellogg, K., Metchev, S., Geißler, K., et al. 2015, AJ, 150, 182
Kellogg, K., Metchev, S., Miles-Páez, P. A., & Tannock, M. E. 2017, AJ, 154, 112
Kilic, M., Munn, J. A., Harris, H. C., et al. 2017, ApJ, 837, 162
Kirkpatrick, J. D. 2005, ARA&A, 43, 195
Kirkpatrick, J. D., Cushing, M. C., Gelino, C. R., et al. 2011, ApJS, 197, 19
Kirkpatrick, J. D., Gelino, C. R., Faherty, J. K., et al. 2021b, ApJS, 253, 7
Kirkpatrick, J. D., Looper, D. L., Burgasser, A. J., et al. 2010, ApJS, 190, 100
Kirkpatrick, J. D., Martin, E. C., Smart, R. L., et al. 2019, ApJS, 240, 19
Kirkpatrick, J. D., Marocco, F., Caselden, D., et al. 2021a, ApJL, 915, L6
Kirkpatrick, J. D., Marocco, F., Gelino, C. R., et al. 2024, ApJS, 271, 55
Kirkpatrick, J. D., Reid, I. N., Liebert, J., et al. 1999, ApJ, 519, 802
Kirkpatrick, J. D., Schneider, A., Fajardo-Acosta, S., et al. 2014, ApJ, 783, 122
Koppelman, H. H., Helmi, A., Massari, D., Price-Whelan, A. M., & Starkenburg, T. K. 2019, A&A, 631, L9
Kuchner, M. J., Faherty, J. K., Schneider, A. C., et al. 2017, ApJL, 841, L19
Kurucz, R. L. 1993, SYNTHE Spectrum Synthesis Programs And Line Data (Cambridge, MA: Smithsonian Astrophysical Observatory)
Lang, D. 2014, AJ, 147, 108
Laughlin, G., Bodenheimer, P., & Adams, F. C. 1997, ApJ, 482, 420
Laureijs, R., Amiaux, J., Arduini, S., et al. 2011, arXiv:1110.3193
Lawrence, A., Warren, S. J., Almaini, O., et al. 2007, MNRAS, 379, 1599
Lawrence, A., Warren, S. J., Almaini, O., et al. 2013, yCat, 2319, 0
Lépine, S., Rich, R. M., & Shara, M. M. 2007, ApJ, 669, 1235
Line, M. R., Marley, M. S., Liu, M. C., et al. 2017, ApJ, 848, 83
Linsky, J. L. 1969, ApJ, 156, 989
Liu, M. C., Dupuy, T. J., & Leggett, S. K. 2010, ApJ, 722, 311
Livingston, W., & Wallace, L. 1991, An Atlas of the Solar Spectrum in the Infrared from 1850 to 9000 cm-1 (1.1 to 5.4 Micrometer), NSO Technical Rep., National Solar Observatory
Lodieu, N., Allard, F., Rodrigo, C., et al. 2019, A&A, 628, A61
Lodieu, N., Burgasser, A. J., Pavlenko, Y., & Rebolo, R. 2015, A&A, 579, A58
Lodieu, N., Zapatero Osorio, M. R., Martín, E. L., Rebolo López, R., & Gauza, B. 2022, A&A, 663, A84
Lodieu, N., Zapatero Osorio, M. R., Martín, E. L., Solano, E., & Aberasturi, M. 2010, ApJL, 708, L107
Looper, D. L., Kirkpatrick, J. D., & Burgasser, A. J. 2007, AJ, 134, 1162
Luhman, K. L. 2014, ApJL, 786, L18
Luhman, K. L., & Sheppard, S. S. 2014, ApJ, 787, 126
Luhman, K. L., Patten, B. M., Marengo, M., et al. 2007, ApJ, 654, 570
Mace, G. N., Kirkpatrick, J. D., Cushing, M. C., et al. 2013a, ApJ, 777, 36
Mace, G. N., Kirkpatrick, J. D., Cushing, M. C., et al. 2013b, ApJS, 205, 6
Mace, G. N., Mann, A. W., Skiff, B. A., et al. 2018, ApJ, 854, 145
Mamajek, E. E., Torres, G., Prsa, A., et al. 2015, arXiv:1510.06262
Mann, A. W., Brewer, J. M., Gaidos, E., Lépine, S., & Hilton, E. J. 2013, AJ, 145, 52
Marfil, E., Tabernero, H. M., Montes, D., et al. 2021, A&A, 656, A162
Marley, M. S., Saumon, D., Visscher, C., et al. 2021, ApJ, 920, 85
Marocco, F., Andrei, A. H., Smart, R. L., et al. 2013, AJ, 146, 161
Marocco, F., Eisenhardt, P. R. M., Fowler, J. W., et al. 2021, ApJS, 253, 8
Martin, E. C., Mace, G. N., McLean, I. S., et al. 2017, ApJ, 838, 73
McKinney, W. 2010, in Proc. of the 9th Python in Science Conf., ed. S. van der Walt & J. Millman, 56
McLean, I. S., Becklin, E. E., Bendiksen, O., et al. 1998, Proc. SPIE, 3354, 566
McMahon, R. G., Banerji, M., Gonzalez, E., et al. 2013, Msngr, 154, 35
McMillan, P. J. 2017, MNRAS, 465, 76
Meisner, A. M., Lang, D., & Schlegel, D. J. 2018, AJ, 156, 69
Meisner, A. M., Leggett, S. K., Logsdon, S. E., et al. 2023, AJ, 166, 57
Meisner, A. M., Faherty, J. K., Kirkpatrick, J. D., et al. 2020, ApJ, 899, 123
Meisner, A. M., Schneider, A. C., Burgasser, A. J., et al. 2021, ApJ, 915, 120
Metropolis, N., Rosenbluth, A. W., Rosenbluth, M. N., Teller, A. H., & Teller, E. 1953, JChPh, 21, 1087
Montes, D., González-Peinado, R., Tabernero, H. M., et al. 2018, MNRAS, 479, 1332
Moranta, L., Gagné, J., Couture, D., & Faherty, J. K. 2022, ApJ, 939, 94
Morgan, W. W., & Keenan, P. C. 1973, ARA&A, 11, 29
Morgan, W. W., Keenan, P. C., & Kellman, E. 1943, An Atlas of Stellar Spectra, with An Outline of Spectral Classification (Chicago, IL: Univ. Chicago Press),
Morley, C. V., Fortney, J. J., Marley, M. S., et al. 2012, ApJ, 756, 172
Mould, J. R., & McElroy, D. B. 1978, ApJ, 220, 935
Mukherjee, S., Fortney, J. J., Morley, C. V., et al. 2024, ApJ, 963, 73
Murray, D. N., Burningham, B., Jones, H. R. A., et al. 2011, MNRAS, 414, 575
Nelder, J. A., & Mead, R. 1965, CompJ, 7, 308
Neves, V., Bonfils, X., Santos, N. C., et al. 2014, A&A, 568, A121
Newton, E. R., Charbonneau, D., Irwin, J., et al. 2014, AJ, 147, 20
Nonino, M., Glazebrook, K., Burgasser, A. J., et al. 2023, ApJL, 942, L29

Ochsenbein, F., Bauer, P., & Marcout, J. 2000, A&AS, 143, 23
Oke, J. B., Cohen, J. G., Carr, M., et al. 1995, PASP, 107, 375
Pecaut, M. J., & Mamajek, E. E. 2013, ApJS, 208, 9
Phillips, M. W., Tremblin, P., Baraffe, I., et al. 2020, A&A, 637, A38
Pinfield, D. J., Burningham, B., Lodieu, N., et al. 2012, MNRAS, 422, 1922
Pinfield, D. J., Gomes, J., Day-Jones, A. C., et al. 2014, MNRAS, 437, 1009
Qiu, D., Li, J., Zhang, B., et al. 2024, MNRAS, 527, 11866
Rajpurohit, A. S., Reylé, C., Allard, F., et al. 2014, A&A, 564, A90
Rayner, J. T., Toomey, D. W., Onaka, P. M., et al. 2003, PASP, 115, 362
Reiners, A., & Basri, G. 2006, AJ, 131, 1806
Rice, M., & Brewer, J. M. 2020, ApJ, 898, 119
Robbins, G., Meisner, A. M., Schneider, A. C., et al. 2023, ApJ, 958, 94
Robert, J., Gagné, J., Artigau, É., et al. 2016, ApJ, 830, 144
Rodrigo, C., & Solano, E. 2020, in XIV.0 Scientific Meeting (Virtual) of the Spanish Astronomical Society (Barcelona: Spanish Astronomical Society), 182
Rodrigo, C., Solano, E., & Bayo, A. 2012, SVO Filter Profile Service Version 1.0 1015, Int. Virtual Observatory Alliance
Rojas-Ayala, B., Covey, K. R., Muirhead, P. S., & Lloyd, J. P. 2012, ApJ, 748, 93
Rosenthal, L. J., Fulton, B. J., Hirsch, L. A., et al. 2021, ApJS, 255, 8
Sanghi, A., Liu, M. C., Best, W. M. J., et al. 2023, ApJ, 959, 63
Saumon, D., Bergeron, P., Lunine, J. I., Hubbard, W. B., & Burrows, A. 1994, ApJ, 424, 333
Schlafly, E. F., Meisner, A. M., & Green, G. M. 2019, ApJS, 240, 30
Schmidt, S. J., Kowalski, A. F., Hawley, S. L., et al. 2012, ApJ, 745, 14
Schneider, A. C., Burgasser, A. J., Gerasimov, R., et al. 2020, ApJ, 898, 77
Schneider, A. C., Greco, J., Cushing, M. C., et al. 2016a, ApJ, 817, 112
Schneider, A. C., Windsor, J., Cushing, M. C., Kirkpatrick, J. D., & Shkolnik, E. L. 2017, AJ, 153, 196
Schneider, A. C., Windsor, J., Cushing, M. C., Kirkpatrick, J. D., & Wright, E. L. 2016b, ApJL, 822, L1
Scholz, R. 2010a, A&A, 515, A92
Scholz, R. 2010b, A&A, 510, L8
Scholz, R.-D., Lodieu, N., & McCaughrean, M. J. 2004, A&A, 428, L25
Schönrich, R., Binney, J., & Dehnen, W. 2010, MNRAS, 403, 1829
Schweitzer, A., Passegger, V. M., Cifuentes, C., et al. 2019, A&A, 625, A68
Sheppard, S. S., & Cushing, M. C. 2009, AJ, 137, 304
Siegler, N., Close, L. M., Burgasser, A. J., et al. 2007, AJ, 133, 2320
Simcoe, R. A., Burgasser, A. J., Schechter, P. L., et al. 2013, PASP, 125, 270
Sivarani, T., Lépine, S., Kembhavi, A. K., & Gupchup, J. 2009, ApJL, 694, L140
Skrutskie, M. F., Cutri, R. M., Stiening, R., et al. 2006, AJ, 131, 1163
Solano, E., Gálvez-Ortiz, M. C., Martín, E. L., et al. 2021, MNRAS, 501, 281
Soubiran, C., Brouillet, N., & Casamiquela, L. 2022, A&A, 663, A4
Soubiran, C., Jasniewicz, G., Chemin, L., et al. 2018, A&A, 616, A7
Steinmetz, M., Guiglion, G., McMillan, P. J., et al. 2020, AJ, 160, 83
Terrien, R. C., Mahadevan, S., Bender, C. F., et al. 2012, ApJL, 747, L38
Theissen, C. A., Burgasser, A. J., Martin, E. C., et al. 2022, RNAAS, 6, 151
Thompson, M. A., Kirkpatrick, J. D., Mace, G. N., et al. 2013, PASP, 125, 809
Tremblin, P., Amundsen, D. S., Chabrier, G., et al. 2016, ApJL, 817, L19
Tremblin, P., Padioleau, T., Phillips, M. W., et al. 2019, ApJ, 876, 144
Troxel, M. A., Long, H., Hirata, C. M., et al. 2021, MNRAS, 501, 2044
Vacca, W. D., Cushing, M. C., & Rayner, J. T. 2003, PASP, 115, 389
van der Walt, S., Colbert, S. C., & Varoquaux, G. 2011, CSE, 13, 22
Virtanen, P., Gommers, R., Oliphant, T. E., et al. 2020, NatMe, 17, 261
Wang, P.-Y., Goto, T., Ho, S. C. C., et al. 2023, MNRAS, 523, 4534
Wenger, M., Ochsenbein, F., Egret, D., et al. 2000, A&AS, 143, 9
Wilson, J. C., Henderson, C. P., Herter, T. L., et al. 2004, Proc. SPIE, 5492, 1295
Woolf, V. M., Lépine, S., & Wallerstein, G. 2009, PASP, 121, 117
Woolf, V. M., & Wallerstein, G. 2006, PASP, 118, 218
Yan, Y., Du, C., Li, H., et al. 2020, ApJ, 903, 131
York, D. G., Adelman, J., Adelman, J. E., Jr., et al. 2000, AJ, 120, 1579
Zhang, S., Luo, A. L., Comte, G., et al. 2019a, ApJS, 240, 31
Zhang, Z. H., Burgasser, A. J., Gálvez-Ortiz, M. C., et al. 2019b, MNRAS, 486, 1260
Zhang, Z. H., Galvez-Ortiz, M. C., Pinfield, D. J., et al. 2018b, MNRAS, 480, 5447
Zhang, Z. H., Pinfield, D. J., Gálvez-Ortiz, M. C., et al. 2017, MNRAS, 464, 3040
Zhang, Z. H., Pinfield, D. J., Gálvez-Ortiz, M. C., et al. 2018a, MNRAS, 479, 1383
Zhu, H., Du, C., Yan, Y., et al. 2021, ApJ, 915, 9